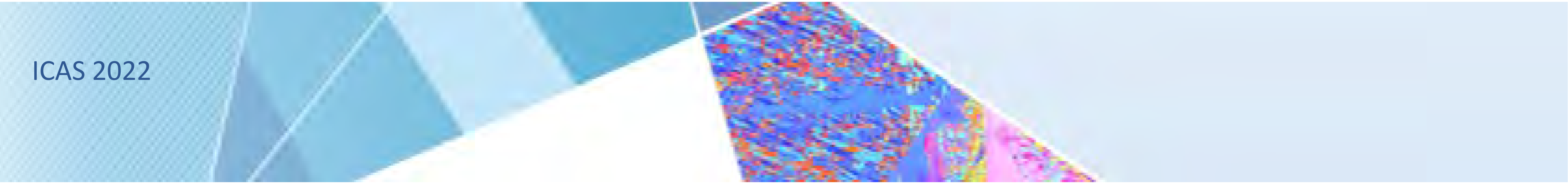

ICAS 2022

The 7th International Conference on Advanced Steels

Proceedings（POSTER)

May 29 - June 1, 2022· in Tsukuba, Japan

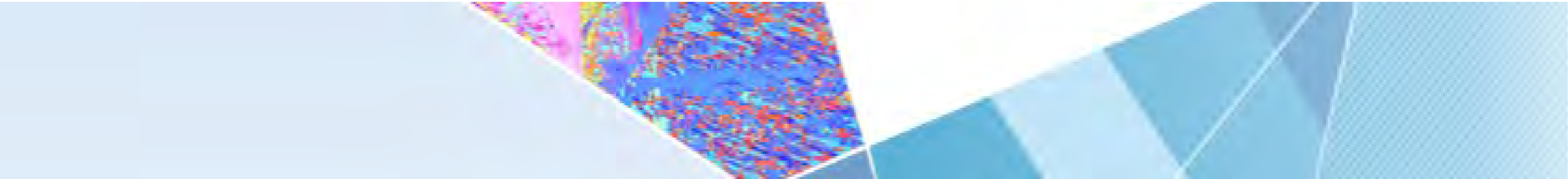

Poster Award

No	page	Symposium	Name	affiliate	Poster Title
S1S01	1-4	1	**Yasuhito Kawahara**	Department of Materials Science and Engineering, Graduate School of Engineering, Kyushu University	Influence of nitrogen addition on the temperature dependences of hardening mechanisms in austenitic stainless steels
S1S02	5-8	1	Satoshi Noguchi	Department of Advanced Interdisciplinary Studies, The University of Tokyo	Characterization and generation of material microstructures by machine learning consistent with metallurgists' way of thinking
S1S03	9-11	1	Ayano Kita	Department of Material Design Innovation Engineering, Nagoya University	Monte Carlo simulation on grain growth in dual phase microstructure, followed by sensitive analysis
S1S05	12-13	1	Yoshihisa Mino	Department of Material Design Innovation Engineering, Nagoya University	Bayesian optimized cellular automaton modeling of austenite-to-ferrite phase transformation in carbon steel
S1S06	14-16	1	Yutaro Suzuki	Division of Material Design Innovation Engineering, Nagoya University	Abnormal Goss grain growth in pure iron by two-way cold rolling and subsequent annealing
S1S10	17-20	1	**Yulin Xie**	Graduate School of engineering, Tohoku University	Surface hardening and nano-sized clustering during low temperature nitriding of Fe-35Ni-X (X=Cr, V, Mo, Al) alloys
S1S11	21-24	1	**Shotaro Jimbo**	Department of Materials Engineering, The University of Tokyo	3-dimensional morphology of upper and lower bainite in the initial stage of transformation
S1S13	25-28	1	Kazuki Okayasu	Chiba Institute of Technology	Spheroidization of Lamellae Cementite in Pearlitic Steel with Kinked Structure
S1S14	29-33	1	Miku Watanabe	Department of Metallurgy, Tohoku University	Heterogeneous chemistry and size of retained austenite and its thermal stability in austempered Fe-2Mn-1.5Si-0.4C alloy
S1S15	34-37	1	Chang Jiang	School of Materials and Science Engineering, Shanghai University	Axial tensile load fatigue testing of SCM435 steel for bolts
S1S16	38	1	Chao Yang	Shanghai University	Elimination of orientation inheritance in a CrNiMoV steel
S1Y01	39-42	1	**Daiki Terazawa**	Steel Research Laboratories, Nippon Steel Corporation	The effect of ♑ recrystallization to B segregation and precipitation behavior after hot rolling proces
S1Y02	43	1	Koyo Ohga	Steel Research Laboratories,R&D Laboratories,Nippon Steel	Characteristics of retained austenite formed by friction stir welding of ultrahigh carbon steels
S1Y03	44	1	Hojun Gwon	Graduate Institute of Ferrous Technology, Pohang University of Science and	Martensitic transformation induced by electro-chemical polishing in metastable austenitic stainless steel
S1Y04	45-48	1	**Yosuke Nonaka**	Steel Research Laboratories, Nippon Steel Corporation	Fracture toughness prediction model for TiN-ferrite steels

No	page	Symposium	Name	affiliate	Poster Title
S1Y05	49	1	Delphic Chen	Steel Product Development Section, Iron & Steel Research & Development Department, China Steel Corp	Abnormal grain growth in martensitic steel
S1Y06	50-53	1	Po-Yu Chen	Iron and Steel Research & Development Department, China Steel Corporation,	The effect of precipitate size on magnetic properties of non-oriented electrical steels
S1Y07	54	1	Xue Bai	Shougang Research Institute of Technology	The influence of pre-plating on the LME phenomenon of advanced high strength steel
S1Y08	55	1	Jingliang Wang	University of Science and Technology Beiing	First-principles study on the P-induced embrittlement and de-embrittling effect of B and C in ferritic steels
S1Y10	56-59	1	Kawamoto Yuzo	Nippon Steel Corporation	Effect of Nb and Mo on the morphology of martensite
S1Y13	60-61	1	Haokai Dong	School of Materials Science and Engineering, Tsinghua University	A comparative study on intrinsic mobility of incoherent and semicoherent interfaces during the austenite to ferrite transformation
S2S01	62-63	2	Simoon Sung	Department of Materials Science and Engineering & Research Institute of Advanced Materials, Seoul National	Molecular Dynamics Approaches for Migrating Boundary Induced Plasticity of Iron
S2S02	64	2	**Kyung Mun Min**	Department of Materials Science and Engineering & RIAM, Seoul National University	Computational approach for predicting anisotropy and formability of thermo-mechanically processed steel sheet in terms of texture control
S2S05	65	2	Woojin Cho	Department of Materials Science and Engineering and Research Institute of Advanced Materials, Seoul	Bake hardening behavior accompanying yield point phenomenon in low carbon steel
S2S06	66	2	Ta-Te Chen	Research Center for Structural Materials, National Institute for Materials Science,	Computer-aided Estimation of Plastic Properties using Instrumented Indentation Tests
S2S07	67-70	2	Yuxiong Zhou	1.Graduate School of Engineering, Kyushu University	Relationship Between Hall-Petch Coefficient and Grain Boundary
S2S08	71-74	2	Sien Liu	Department of Materials Engineering, The University of Tokyo	Numerical study on the effect of interfacial energy on the interfacial strength and toughness of bcc-Fe tilt interfaces

No	page	Symposium	Name	affiliate	Poster Title
S2S09	75	2	**Viola Paul**	Department of Materials Science and Engineering, Kyushu University, Research Center for Structural Materials, National Institute for Materials Science	Nanomechanical Analysis of SUS304LStainless Steel with Bimodal Distribution in Grain Size
S2S10	76-78	2	Tianze Ma	Department of Materials, Graduate school of Engineering, Kyushu University	Grain refinement strengthening in Si-C combined added ferritic steel
S2S11	79-83	2	Chao Lin	School of Materials Science and Engineering, Shanghai University	Microstructure and Mechanical Properties of Resistance Spot Welding Joints Between Two Hot Stamping Boron Steels and DP1180 steel
S2S13	84-87	2	Tinghui Man	School of Materials and Science Engineering, Shanghai University	Deformation behaviors and fracture mechanism in medium Mn forged steels
S2S14	88	2	Ryota Hamana	Toyohashi University of Technology	Mechanical behavior of Si-alloyed interstitial free steels investigated by pop-in analysis during nanoindentation
S2S15	89-91	2	Bo Zi WANG_	School of Materials and Science Engineering, Shanghai University	Effect of aging temperature on microstructure and mechanical properties of microalloyed steel for cold heading bolt
S2Y01	92-95	2	Elango Chandiran	Research Center for Structural Materials, National Institute for Materials Science	Deformation behaviour of two different types of medium carbon bainitic steel designed by Sparse Mixed Regression Model (SMRM)
S2Y02	96-99	2	**Miyuri Kameya**	Steel Research Laboratories, Nippon Steel Corporation	Hydrogen Absorption Behavior and Absorbed Hydrogen Trapping Sites in Rolling Contact Fatigue
S2Y03	100	2	Takayuki Shiraiwa	The University of Tokyo	Exploration of optimal microstructure for improving strength and ductility of dual-phase steels
S2Y04	101	2	**Chiharu Kura**	Applied Physics Research Laboratory, Kobe Steel, Ltd	Atomistic calculations of the interaction between screw dislocations and symmetric tilt grain boundaries in iron
S2Y05	102-105	2	Haruka Yoshida	Research & Development, Nippon Steel Corporation	Effect of hardenability on anisotropic deformation of steel cylinder in carburized quenching process
S2Y06	106-109	2	**Fabien Briffod**	Department of Materials Engineering, The University of Tokyo	Micromechanical investigation of ductile void nucleation in dual-phase steels with varying microstructure
S2Y07	110-113	2	Yuji Sakiyama	Steel Research Lab., Nippon Steel Corporation	Evaluation of residual stress at circular punched end-face and its validity
S2Y08	114-117	2	Kohei Nakada	Nagoya Works, NIPPON STEELCORPORATION	The work-hardening behavior of pearlite under strain path changes
S2Y09	118-120	2	**Seung-Yong Lee**	Department of Materials Science and Engineering, Tokyo Institute of Technology	Characterization of the Portevin-Le Chatelier Effect in Austenitic Stainless Steel using High-Temperature Digital Image Correlation Analysis

No	page	Symposium	Name	affiliate	Poster Title
S2Y10	121-124	2	Hiromi Oyamada	Welding Business, KOBE STEEL, LTD.	Creep Properties of High Chromium Steel Weld Metals
S2Y11	125	2	**Junya Tobata**	Steel Research Laboratory, JFE Steel Corporation	Elastic limit of Martensitic Steel Sheet Containing Retained Austenite
S2Y12	126-127	2	Yoshiyasu Kawasaki	JFE Steel Corporation	Effects of Tensile Testing Temperature on Mechanical Properties and Deformation Behavior in Medium Mn Steels
S2Y13	128	2	Wenqi Mao	Japan Atomic Energy Agency	Effect of ultra-grain refinement on deformation behavior of Fe-24Ni-0.3C metastable
S2Y14	129-131	2	Lavakumar Avala	Department of Materials Science and Engineering, Kyoto University, Institute for Materials Chemistry and Engineering, Kyushu University	Global and local deformation behavior of ferrite + martensite + austenite steel analyzed by in-situ X-ray diffraction and digital image correlation (DIC) method
S3S01	132-135	3	**Gaoge Xue**	Division of Mechanical and Space Engineering, Hokkaido University	Three-dimensional observation of small fatigue cracks growth process in a beta titanium alloy Ti-22V-4Al using multiscale synchrotron radiation computed tomography
S3S02	136-139	3	Takuya Yamazaki	Division of Mechanical and Space Engineering, Hokkaido University,	The formation process of multiple facets in internal fatigue fractures of (α+β) Ti-6Al-4V
S3S03	140-143	3	Sourav Kumar Modi	Division of Mechanical and Space Engineering, Hokkaido University	Estimation of Fatigue life for internal cracks using crack growth rates measured in a vacuum environment
S3Y01	144	3	Satoshi Maeda	Steel Research Laboratory, JFE Steel Corporation,	Influence of shearing condition on delayed fracture at sheared edge in 1470 MPa grade steel
S3Y02	145-148	3	**Fumiyoshi Yoshinaka**	Research Center for Structural Materials, National Institute for Materials Science	Enhanced plastic fatigue durability of Fe-Mn-Cr-Ni-Si bidirectional-TRIP steel
S3Y03	149	3	Rama Srinivas Varanasi	1□Institute for Materials Research, Tohoku University	Hydrogen embrittlement susceptibility of a 1.5GPa class
S3Y04	150-151	3	**Mariko Kadowaki**	Research Center for Structural Materials, National Institute for Materials Science	First-Principles Investigation on the Beneficial Effect of Interstitial Carbon on Steel Corrosion
S3Y05	152-153	3	Naoya Ihara	JFE Steel Corp.	Crack propagation behavior in rotational bending fatigue test of soft-nitrided JIS SCM420 steel

Influence of nitrogen addition on the temperature dependences of hardening mechanisms in austenitic stainless steels

Yasuhito Kawahara[1,*], Shunya Kobatake[1], Chikako Takushima[2], Jun-ichi Hamada[2] and Kenji Kaneko[1]

[1] Department of Materials Science and Engineering, Graduate School of Engineering, Kyushu University, 744 Motooka,
Nishi-ku, Fukuoka, Japan
[2] Research & Development Center, Nippon Steel Stainless Steel Corporation, 3434 Shimata, Hikari, Yamaguchi, Japan
*email: kawahara.yasuhito.766@s.kyushu-u.ac.jp

Keywords: austenitic stainless steel, transmission electron microscopy, nitrogen, stacking-fault energy, work-hardening

Austenitic stainless steels are extensively used in constructions and automobiles because they exhibit excellent strengths over a wide temperature range. Nitrogen is known to play an important role to improve the mechanical properties of steels by, size effect 1), I-S effect 2), reduction of stacking-fault energy (SFE)3), and dislocation planarization4). In practice, it is necessary to optimize temperatures and nitrogen contents separately to achieve an optimal combination. In this study, microstructures of 0.01 wt%-nitrogen and 0.19 wt%-nitrogen added-austenitic stainless steels deformed to 5% strain at 573 K and 973 K were characterized by transmission electron microscopy (TEM) in order to clarify the correlation between the hardening mechanisms, roles of nitrogen and temperature dependences.

Steels in this study were prepared by vacuum melting and their compositions are listed in Table 1. High temperature tensile tests were carried out at 573 K and 973 K with tensile rate at 0.3 %/min, and TEM samples were then prepared after 5% deformations. Thin TEM foils were fabricated by the conventional twin-jet method using a 5 mol% $HClO_4$ - 95 mol% CH_3COOH solution at room temperature with a current of 25 mA and a voltage of 30 V. Conventional TEM observations were carried out by JEM-2100HC, and scanning TEM (STEM) observations by JEM-ARM200F, both operated at 200kV.

Figures 1(a) to (d) show bright-field (BF) STEM images of dislocations viewed along [011] zone axis, in 0.01N and 0.19N deformed at 573 K and 973 K, respectively. In the case of the samples deformed at 573 K, 0.01N-573 and 0.19N-573, dislocations were localized on the slip plane, and nitrogen addition changed the dislocation morphology from curved to linear. Tomota et al. reported that nitrogen-added austenitic stainless steels exhibited both edge-type and screw-type dislocations in the linear form 5). Screw-type dislocations have higher dislocation-self energy than edge-type dislocations in austenitic stainless steels6). In the case of samples deformed at 973 K, 0.01N-973 and 0.19N-973, nitrogen addition strongly promoted that the dislocation localizations on the slip plane. In the case of 0.01N-973, the curved dislocations were uniformly dispersed, while in the case of 0.19N-973, almost all dislocations were localized on the slip plane. In this alloy, it is considered that the nitrogen addition decreased the SFE and suppressed the cross-slip, resulting in the dislocation localizations 7). In the case of 0.01N, the increase in deformation temperature resulted in the uniform dispersion of dislocations, while in 0.19N, there was seen little change of dislocation structures.

Figures 2(a) to (d) show BF-TEM images of dislocations viewed along [111] from four samples, 0.01N-573, 0.19N-573, 0.01N-973 and 0.19N-973, respectively. In the case of 0.01N-573 and 0.19N-573, as seen in Fig.1, dislocations were localized on the slip planes. It is clearly seen that planar dislocations were introduced by addition of nitrogen, as seen in the previous research 5). Additional long liner dislocations were also observed as indicated by arrows in Fig.2(c), which would be different from planar dislocations. In the case of 0.01N-973 and 0.19N-973, nitrogen addition changed the shape of dislocations from curved to linear, as seen in the samples deformed at 573 K as shown in Fig.1. In 0.01N-973, the curved dislocations are uniformly dispersed, indicating that the solute elements dominate the movement of dislocations rather than their climbing. In 0.19N-973, straight dislocations are uniformly dispersed, and dislocation motion is fixed, suggesting that the work-hardening mechanism is different between 0.01N-973 and 0.19N-973. In the case of 0.19N, long liner dislocations disappear as deformation temperature increases, which suggests that the solute drag effect has large influences on the dislocation morphology.

Figure 3 shows $\mathbf{g}\cdot\mathbf{b}$ analysis of 0.19N-973. It can be seen that the contrast between complete and dissociated dislocations disappears by changing the diffraction conditions. In Fig. 3(b), the contrast between the linear dislocations disappears as indicated by the arrows, and the complete dislocations are determined to be edge-type dislocations. This result indicates that nitrogen atoms or N-Cr pairs strongly drag the motions of the edge-type dislocations in the case of 0.19N-973[6]. As shown in Fig.3, edge-type dislocations are clustered, suggesting that this may be caused by the attractive interaction between edge-type dislocations. In addition, the occurrence of clusters in a direction oblique to the dislocation line suggests that edge-type dislocations with different plus/minus signs are clustered. Dissociated dislocations were observed as indicated by dashed line arrow in Fig. 3(b), partial dislocations of dissociated dislocations were no longer observed depending on the diffraction conditions. In addition, curved dislocations were also observed, but as seen in Fig.1(d) and Fig.2(d), curved dislocations are rarely observed, suggesting that both edge-type perfect dislocations and SFs dominate the deformation mechanism of 0.19N-973.

Figures 4 show high-resolution (HR) (S)TEM images of dislocations deformed at 573 K and 973 K, where SFs were observed in the case of 0.01N-573, 0.01N-973 and 0.19N-973. As shown in Fig. 4(a)-(d), Romer-Cottrell-Locked dislocations are formed in the dislocation crossing region where the dislocation reaction occurs.

$$a/6[2\ -1\ 1]+a/6[-1\ 2\ -1]\rightarrow a/6[1\ 1\ 0]$$

The dislocation-self energy is proportional to the square of Burgers vector, so that Romer-Cottrell-Locked dislocations are more stable compared with the SFs. Therefore, the activation energy is required to break the Romer-Cottrell-Locked dislocation, so that dislocation motions must be effectively disturbed. Our previous studies have shown that SFEs decrease with nitrogen addition, expected to promote the effect of these SF interactions on the high-temperature strength[7].

Figure 5(a) shows the stress-strain (S-S) curve at 973 K, where increase of 0.2% proof stress and tensile strength could be easily recognized, as summarized in Table 2. The increase of 0.2% proof stress by nitrogen addition is about 74 MPa, which is explained by the solid solution hardening of nitrogen. The increase in tensile strength due to nitrogen addition is 120 MPa, which is larger than the increase in 0.2% proof stress. The uniform elongation dramatically increased from 26.1% to 43.6% and the local elongation decreased from 28.8% to 4.7% with nitrogen addition. At 973 K, the nitrogen addition resulted in the dislocation localization on the slip planes, which may be responsible for the decrease in local elongation. Figure 5(b) showed the S-S curve up to 15% strain range, where continuous serrated flow was easily recognized from 0.19N. These results indicate that dynamic strain aging contributed to the work-hardenability of 0.01N and 0.19N, and the contribution of dynamic strain aging in 0.19N was superior to that in 0.01N. Figure 5(c) showed the work-hardening rate curves of 0.01N and 0.19N deformed at 973 K, where nitrogen addition dramatically improved the work-hardening rate in the range 7-30% strain. Dastur et al. reported that dynamic strain aging improved the work-hardening rate in carbon-added austenitic stainless steels [8], so that addition of nitrogen also improved the work-hardening rate by dynamic strain aging. Up to 5% strain, work-hardening rate of 0.19N was lower than that of 0.01N, possibly due to the yield drop because of the dynamic strain aging.

(S)TEM investigations and S-S curves indicated that nitrogen addition contributed to the high temperature strengths via dynamic strain aging and SF interactions. Depending on the temperature, the diffusion rate of nitrogen should change, so that the contribution of nitrogen to the strengths should also be changed. Masumura et al. investigated the nitrogen distribution in aged nitrogen-added austenitic stainless steels and found that nitrogen segregates into dislocations at 573 K[9]. The effect of dynamic strain aging on the deformation mechanism was not clear from TEM observations of 0.01N-573 and 0.19N-573 K, suggesting nitrogen alone is insufficient for the dislocation dragging. In the case of samples deformed at 973 K, the Fe matrix and solute elements would diffuse, where deformation mechanisms were apparently changed by nitrogen addition, and the N-Cr pairs must contribute to the deformation mechanisms. On the other hand, the Suzuki effect promotes the effect of nitrogen on SFE because nitrogen addition decreased the SFE in this alloy system, so that decrease of SFE also contribute to the hardening mechanisms at 573 K and 973 K. The quantitative contributions of SFE and dynamic strain aging are still unclear, but both may contribute to the high temperature hardening mechanisms.

In this study, (S)TEM and tensile tests were carried out to clarify the hardening mechanism by nitrogen addition at high temperatures. As a result of (S)TEM observation, it was found that dislocations were localized on the slip plane in the samples deformed at 573K and 973K by addition of nitrogen. In 0.19N-973, edge-type dislocations were dominantly observed, while curved dislocations were uniformly dispersed in 0.01N deformed at 973 K. HRTEM clarified the SF interactions, which also contributed to the high temperature strengths. The S-S curves showed that nitrogen addition improves work hardening and dynamic strain aging at 973K. Nitrogen addition contributed to the high temperature strengths by SF interactions and dynamic strain aging.

Acknowledgement

One of the authors (YK) would like to acknowledge the Research Fellowship for Young Scientists from the Japan Society for Promotion of Science (JSPS) (JSPS KAKENHI Grant Number JP21J20683).

References

1) S. Wakita, M. Kikuchi and R. Tanaka: Tetsu-to-Hagané, 61 (1975), 2418.
2) K. Monma and H. Suto: J. Jpn. Inst. Met., 30 (1966), 558.
3) H. Oikawa: Materia Jpn., 49 (2010), 49.
4) P. Müllner, C. Solenthaler, P. Uggowitzer and M. O. Speidel: Mater. Sci. Eng. A, 164 (1993), 164.
5) S. Kubota, Y. Xia and Y. Tomota: ISIJ int., 38 (1998), 474.
6) H. Suzuki: *Introduction to Dislocation Theory* (Agne, Tokyo, 1967).
7) Y. Kawahara, R. Teranishi, C. Takushima, J. Hamada and K. Kaneko: ISIJ int, 61 (2021), 1029.
8) Y. N. Dastur and W. C. Leslie: Metall. Trans. A, 12A (1981), 749.
9) T. Masumura, T. Honda, K. Naridomi, S. Uranaka, T. Tsuchiyama, G. Miyamoto and S. Yamasaki: Mater. Trans., 63 (2022), 163.

Table.1 Compositions of the samples used in this study

No.	Fe	C	Si	Mn	P	S	Ni	Cr	N
0.01N	Bal.	0.05	3.2	0.8	0.03	0.0007	13.5	19.5	0.01
0.19N	Bal.	0.05	3.1	0.8	0.03	0.0007	13.6	19.8	0.19

Table.2 Mechanical properties of the samples deformed at 973 K.

	0.2% yield point (MPa)	Tensile strength (MPa)	Uniform elongation (%)	Local elongation (%)	Total elongation (%)
0.01N	96.6	242	26.1	28.8	54.9
0.19N	169	361	43.6	4.70	48.3

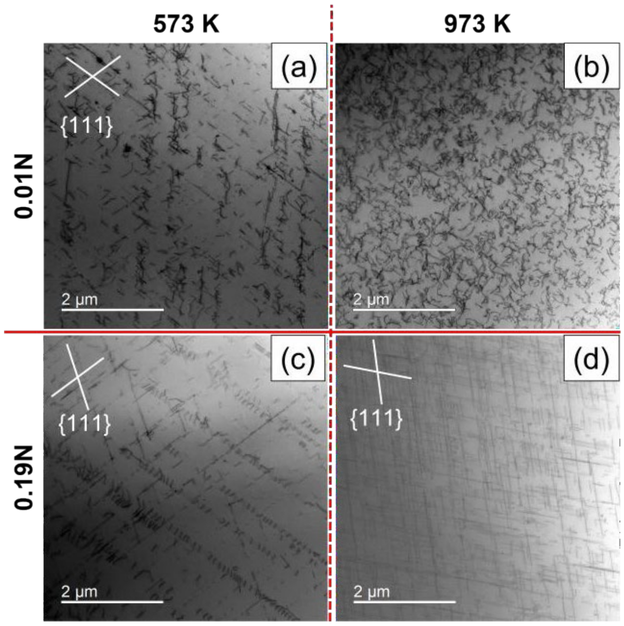

Fig.1 BF-STEM images of dislocation structures viewed along [011] zone axis

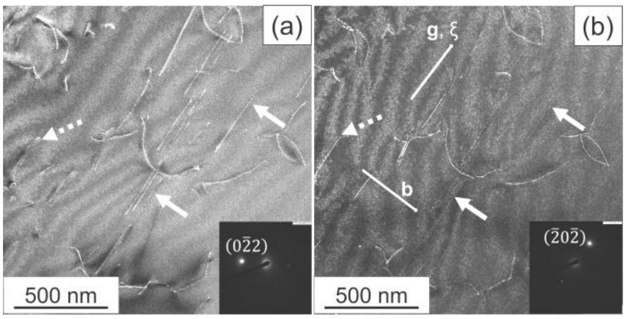

Fig.3 Weak-beam TEM images for **g**·**b** analysis in 0.19N deformed at 973 K

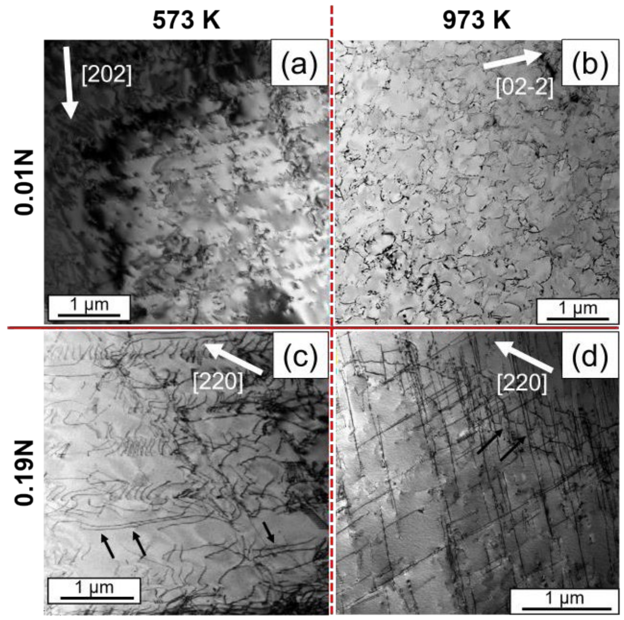

Fig.2 BF-TEM images of dislocation structures viewed along [111]

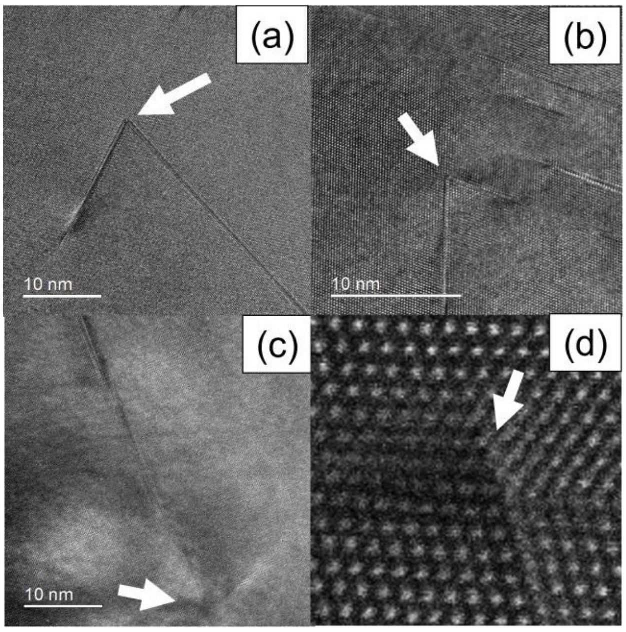

Fig.4 HR-TEM images of stacking-faults in 0.01N-573 (a), 0.19N-573 (b) and 0.19N-973 (c). HAADF-STEM image of stacking-faults in 0.19N-973 (d)

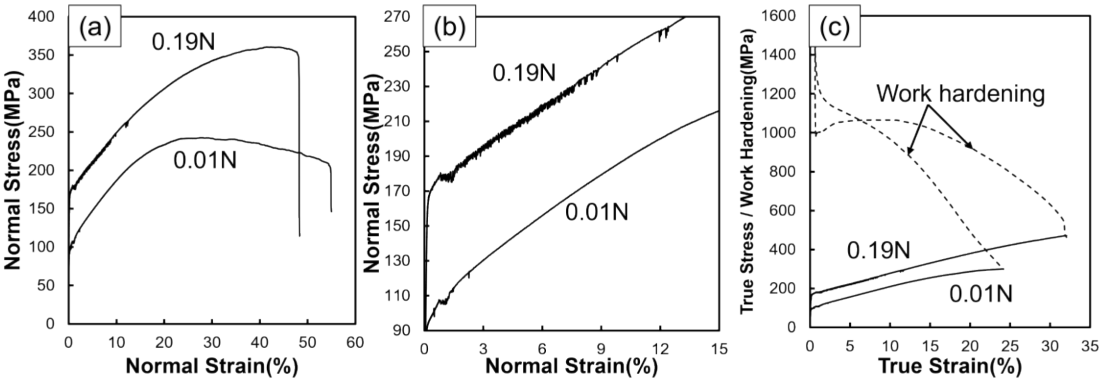

Fig.5 Stress-Strain curves of 0.01N and 0.19N deformed at 973 K

Characterization and generation of material microstructures by machine learning consistent with metallurgists' way of thinking

Satoshi Noguchi[1], and Junya Inoue[2, 3, *]

[1] Department of Advanced Interdisciplinary Studies, The University of Tokyo, 4-6-1 Komaba, Meguro, Tokyo 153-8904, Japan
[2] Institute for Industrial Science, The University of Tokyo, 5-1-5 Kashiwanoha, Kashiwa, Chiba 277-0082, Japan
[3] Department of Materials Engineering, The University of Tokyo, 7-3-1 Hongo, Bunkyo, Tokyo 113-8655, Japan
*email:j-inoue@iis.u-tokyo.ac.jp

Keywords: characterization and generation of microstructures, process–structure–property linkage, inverse analysis, dual-phase steel

I Introduction

The goal of material design is to identify novel material with desired properties, which is called inverse material design. To achieve inverse material design, establishing a process–structure–property (PSP) linkage is essential. For that purpose, a central problem is the analysis, characterization and control of material microstructures since microstructures play a central role in PSP linkage. Thus, as a first step toward developing a framework for establishment of PSP linkage, this work discusses a general methodology for the characterization and generation of material microstructures using deep learning methods.

Authors' group successfully demonstrated that a deep learning framework can be used for automatically generation of material microstructures from process parameters1). The hint of constructing framework we adopted is to imitate metallurgists' way of thinking when interpreting and designing metallic material microstructures. The fundamental idea which metallurgists share in common is that steel microstructures are composed of a finite kind of dissimilar phases such as ferrite, pearlite, bainite, and martensite. Due to the variation of internal structures, steel alloys are widely known to exhibit a wide range of mechanical properties.Also, these microstructures develop competitively with totally different physical processes. Thus, steel microstructures are interpreted as a set of dissimilar phases having certain spatial orders to each other depending on several processing conditions. The guide of construction of deep learning framework adopted in this study is to represent this metallurgists' fundamental interpretation of steel microstructures.

For representing the above interpretation, deep learning methodology should have two key functional components: (i) identification and extraction of dissimilar phases having totally different geometrical features, and (ii) determination of spatial orders among extracted several phases which also should be related to the processing conditions and material properties. To realize these components, we adopted two deep learning algorithms, that is a vector quantized variational autoencoder (VQVAE)2) and a pixel convolutional neural network (PixelCNN)3),4). VQVAE is used for extraction of finite kind of small-scale microstructures included in target steel microstructures, and PixleCNN is used for determination of spatial correlation among them.

II Framework for characterization and generation of material microstructure

In this section, we explain the architecture of the proposed framework1) which is composed of VQVAE and PixelCNN. Also, we show that the proposed method is suitable for representing the above metallurgists' process of thinking.

II.A. Vector quantized variational autoencoder

Here, we describe VQVAE used for characterization of material microstructures by extracting geometrical features. Fig. 1 (a) shows the schematic of VQVAE. VQVAE extracts small-scale microstructures constructing a target material in unsupervised way. It is composed of a convolutional encoder and a convolutional decoder. The encoder maps input microstructure images into corresponding spatial arrangement of characteristic microstructures, and the decoder maps the extracted features back to the original microstructure images. As candidates of the characteristic microstructures of steels, ferrite and martensite phases or their grain boundaries can be considered. Extracted feature is a two-dimensional arrangement of latent vectors, which is understood as a spatial arrangement of small-scale microstructures. One of the important characteristics of VQVAE for imitating the human researchers' way of thinking is that each latent vector is assumed to stem from different manifolds. In other words, they are not assumed to follow an explicit continuous distribution, which enables VQVAE to extract qualitatively different small-scale microstructures in a similar way that human researchers dissolve steel microstructures into a set of several characteristic phases. In this sense, VQVAE is considered to be suitable for representing our interpretation.

II.B. Pixelconvolutional neural network

Next, the architecture of PixelCNN is explained. A schematic of PixelCNN is given in Fig. 1 (b). PixelCNN is used for determination of spatial correlation among extracted characteristic microstructures which is dependent on processing parameters and/or material properties $\mathbf{!}$. PixelCNN is an autoregressive model for building the joint distribution of each component over a spatial arrangement $\text{"} = \{\%_{!}, \%_{\text{"}}, \ldots, \%_{\#!}\}$ as the following product of conditional distributions,

$$)(\text{"}|\mathbf{!}) =)(\%_{!}|\mathbf{!}) \overset{\&\text{"}}{\underset{\text{'()}}{—}})(\%_{\$}|\%_{\text{"}}, \ldots, \%_{\$\%!}, \mathbf{!}), \tag{1}$$

where " represents the two-dimensional list of latent vectors $\%_{\$}$, and $\mathbf{!}$ is the given condition. Since each $\%_{\$}$ can be considered to correspond to small-scale microstructures, Eq. (1) expresses a certain spatial order among them. In addition, the spatial correlation is defied to be stochastic, which enables us to extract stochastic spatial correlation in the target material. This is one of the important advantages of this framework. Owing to this definition, the stochastic nature of material microstructures stemming from the competitive development of several phases can be captured.

II.C. Microstructures generation by the trained VQVAE and PixelCNN

Using the trained network, microstructures can be generated for given conditions such as processing parameters and/or material properties[1), 3)]. First, we obtain the probability distribution of spatial arrangement of characteristic microstructures by giving desired conditions into the trained PixelCNN. Then, a two-dimensional spatial arrangement of microstructures sampled from the distribution can be converted into a corresponding micrograph by the trained decoder. As a result, we can construct a stochastic mapping from desired conditions into material microstructures.

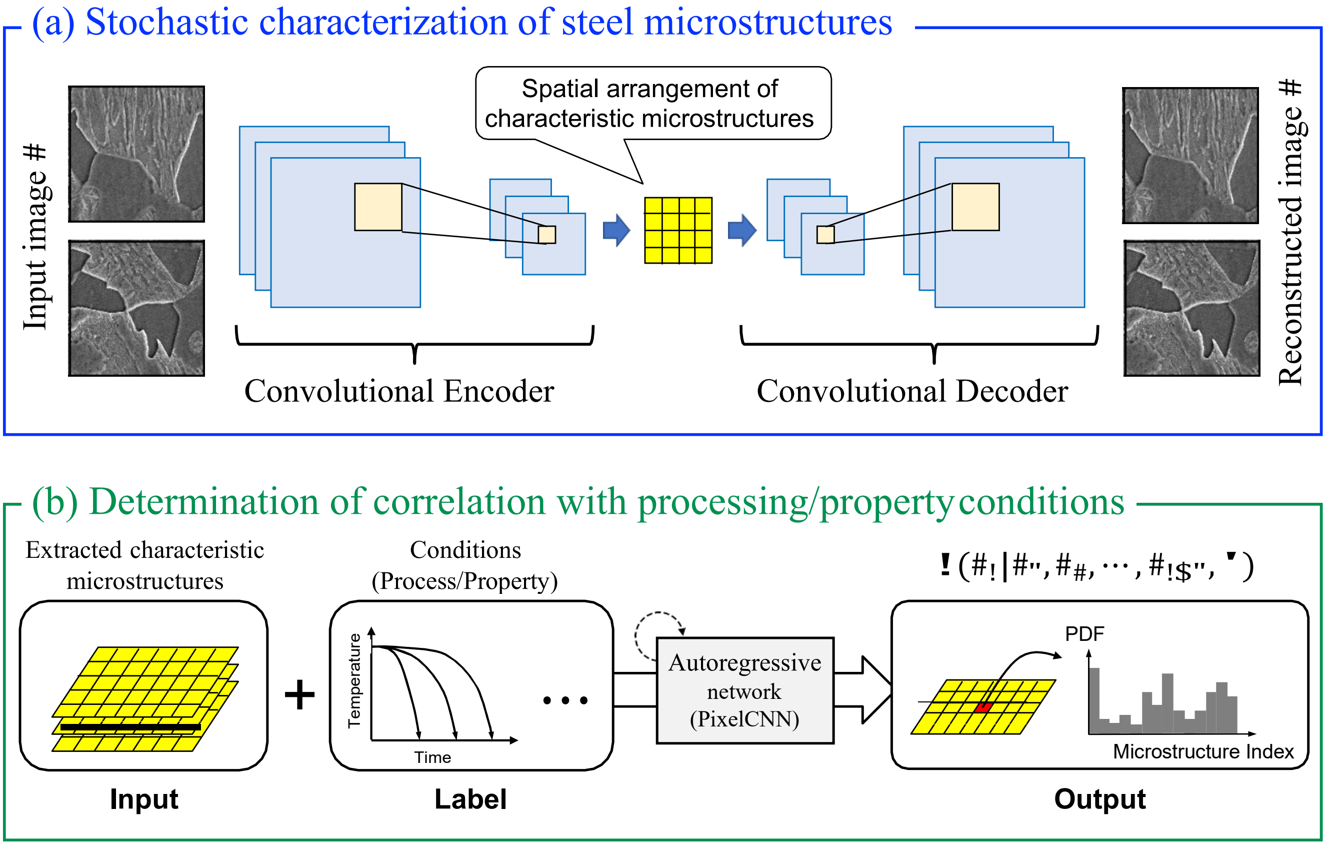

Fig. 1 Schematic of the framework. (a) Stochastic characterization of steel microstructures by VQVAE. VQVAE is composed of a convolutional encoder and decoder. The encoder converts steel microstructure images into the spatial arrangement of characteristic microstructures, and the decoder maps them back to the original images. (b) Determination of correlation between the extracted features and given processing/property conditions by PixelCNN.

III Results of application to dual-phase steel microstructures

In this section, to show the capability of the method, it is applied in the generation of steel microstructures. The example problem is to estimate the dual-phase (DP) steel microstructures corresponding to the given process parameter.

III.A. Training dataset of steel microstructures

As a training dataset, we prepared several micrographs of DP steels which were generated under different process conditions. The steel samples were austenitized at 950 °C and the cooling start temperature were 650, 700, and 750 °C. The example microstructures used for training is shown in Fig. 3. The size of microstructure images is 1260×960 pixel. The total number of prepared images is 300, and they comprise 100 microstructure images for each of the three cooling start temperature, 650, 700, and 750 °C. Table 1 summarize the cooling start temperatures and tensile strength of the prepared steel microstructures.

To create a training dataset, 128×128-pixel square patches are cropped from the original 1260×960-pixel microstructure images. We cropped 495 square images with overlapping each other for each original micrograph. Additionally, the square images flipped horizontally are added into training dataset. The resultant training dataset includes 99000 square images.

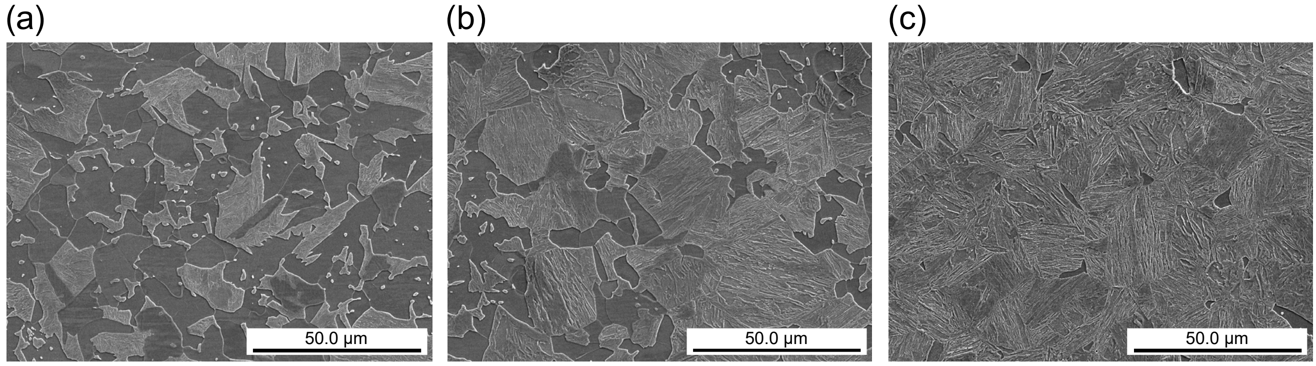

Fig. 2 The examples of microstructures included in the training dataset. (a), (b), and (c) show the steel microstructures cooled at 650, 700, and 750 °C, respectively. The size of the images is 1260×960 pixel.

Table 2 The cooling start temperature and tensile strength of each steel included in training dataset.

Steel index	Cooling start temperatures [°C]	Tensile strength [MPa]
(a)	650	1012
(b)	700	1195
(c)	750	1343

III.B. Results of application to the steel microstructures

We trained each network using the above prepared training dataset. In this application, we consider cooling start temperatures as a condition given to PixelCNN. Fig. 3 illustrates the microstructures generated for the given cooling start temperatures. Comparing with Fig. 2, we can see reasonable agreement between the original microstructures and the generated microstructures in terms of the trend of volume fractions and grain sizes relative to the change in the cooling start temperatures. It should be noted that the microstructures are not included in the training dataset because they are stochastically generated. This result indicates that our framework can capture stochastic dependency of microstructures on the process parameter.

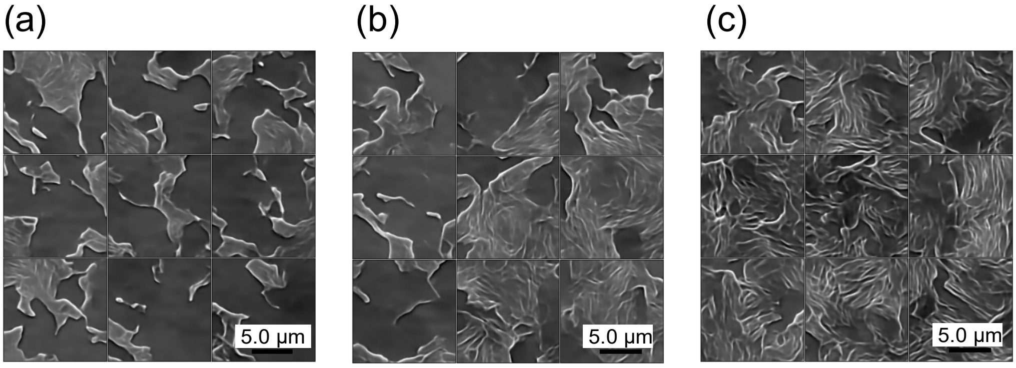

Fig.3 Microstructures generated for the given cooling start temperatures. (a), (b), and (c) are generated for 650, 700, and 750 °C, respectively. Each set shows nine microstructure images.

As mentioned above, Fig. 3 shows that the proposed method can predict the basic topology of steel microstructures such as volume fraction and grain size. Additionally, the volume fraction and the grain size are known as dominant factor for determination of strength of steels[5), 6)]. Thus, the above result implies that the strength also can be predicted from the microstructures, which means that we can capture PSP linkage. To demonstrate a potential of the proposed method for extraction of PSP relationship, we consider a problem of prediction of tensile strength from microstructure images using another convolutional neural network (CNN).

Fig. 4 summarizes the results of the analysis of the example problem. For validation of the training of the CNN, we divided into the dataset into training and test dataset. After training of the CNN using the training dataset, we tested the network

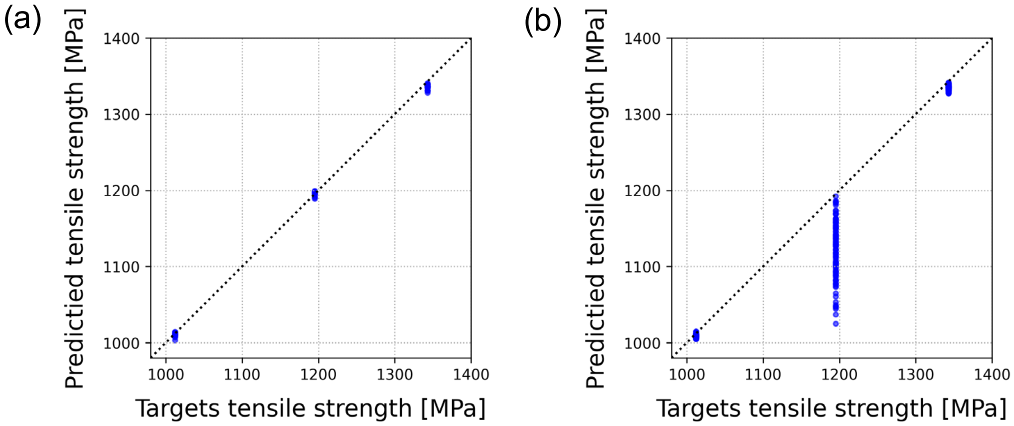

Fig.4 (a) The comparison between the predicted strength and the trus strength for test data. (b) The predicted strength for microstuctures generated for each of the cooling start temperatures, 650, 700, and 750 °C

by comparing the predicted tensile strength and the true tensile strength. Fig. 4 (a) shows the result of validation of the CNN, also the 0" value is 0.999. This result illustrates that the trained network can correctly predict the tensile strength from microstructure images. Then, using the trained CNN, we obtained the predicted strength for the microstructures generated for each of the cooling start temperatures, 650, 700, and 750 °C. Fig. 4 (b) shows the results comparison of the predicted strength of the microstructures generated corresponding to each of the cooling start temperatures and the strength of steels experimentally generated for the same cooling start temperatures. The 0" value is 0.876. The strength of generated microstructures is predicted to exhibit the similar trend to those of microstructures obtained experimentally. As shown in Fig. 3, in steels (a) and (c), the martensite phase tends to be regularly arranged in the cropped square areas. On the other hand, the martensite phase in steel (b) is irregularly arranged in the cropped square patches. In other ward, the martensite volume fractions of each patch of steel (b) vary. This is why the prediction of steel (b) have a trail out to the smaller values than the target strength. In the light of above results, we can conclude that the proposed framework could be a basis for capturing PSP linkage.

IV Conclusion

We propose the methodology for characterization and generation of material microstructures using deep learning methods. The guide for construction of framework we adopted is to imitate metallurgists' process of thinking when designing materials. For representing the way of thinking of human researchers, we chose the deep learning framework composed of VQVAE and PixelCNN. VQVAE is used for the extraction of dissimilar phases having qualitatively different geometrical features and PixelCNN is used for determination of spatial orders among them. In the sense of that this process is consistent with our interpretation that material microstructures are composed of finite kind of characteristic small-scale microstructures, VQVAE and PixelCNN is suitable for representing our way of thinking as a computational method.

For demonstrating the capability of our methodology, we applied it in the generation of steel microstructures from a target condition. The results illustrated that the methodology can capture a general trend of basic topology of steel microstructures relative to the change in the process parameter. Moreover, for validation of the generated microstructures, we trained another CNN for the prediction of tensile strength from microstructure images. Using the trained CNN, we compared between the tensile strengths of the generated microstructures predicted by the CNN and the experimental results. The result demonstrates that the proposed methodology can extract the relationship between the cooling start temperatures and the tensile strength through material microstructures as an intermediate variable. This clearly indicates the potential of the framework for capturing PSP linkage.

Acknowledgement

This work was supported by Council for Science, Technology and Innovation (CSTI), Cross-ministerial Strategic Innovation Promotion Program (SIP), "Materials Integration" for Revolutionary Design System of Structural Materials (Funding agency: JST).

References

1)S. Noguchi and J. Inoue: Phys. Rev. E **104** (2021) 025302 (1-13).
2) Van Oord, O. Vinyals, and K. Kavukcuoglu: *Neural Information Processing System Conference* (NIPS, 2017).
3) Van Oord, N. Kalchbrenner, and K. Kavukcuoglu: *International Conference on Machine Learning* (ICML, 2016).
4) A. Van Oord, N. Kalchbrenner, O. Vinyals, L. Espeholt, A. Graves, and K. Kavukcuoglu: *Neural Information Processing System Conference* (NIPS,2016).
5) C. Peng-Heng and A. Predan: Acta Metall. **33** (1985) 5 (897-903).
6) M. R. Avbarpour and A. Ekrami: Mater. Sci. Eng. A **477** (2008) 1-2 (306-310).

Monte Carlo simulation on grain growth in dual phase microstructure, followed by sensitive analysis

Ayano Kita[1,*], Yoshitaka Adachi[1], Toshio Ogawa[1] and Zhilei Wang[1]

[1] Department of Material Design Innovation Engineering, Nagoya University, Nagoya, Aichi 464-8603, Japan
*email: wh.97z.7760@s.thers.ac.jp

Keywords: steel, dual phase steel, Monte Carlo simulation, machine learning, Artificial Neural Network

1. Introduction

Dual phase steel has an excellent balance of strength and ductility. In this study, the grain growth behavior of the dual phase microstructure is investigated to further improve the mechanical properties[1)]. For example, dual phase stainless steel, which is composed of ferrite and austenite has excellent mechanical properties, such as superplasticity at high temperature and excellent impact properties at low temperature[2)], because their crystal grains are very fine. A precise understanding of the microstructural evolution is extremely essential in further improving the mechanical properties. However, a quantitative analysis of the grain growth behavior in dual phase steel cannot be achieved only through experimental approaches. Therefore, the present study aims to develop a modeling system using the Monte Carlo (MC) method to perform a quantitative analysis of the grain growth behavior in dual phase steel. Furthermore, the dominant factors of grain growth are analyzed by machine learning using the simulation results.

2. Methods

(1) Two-dimensional lattice model of the dual phase microstructure

The first step of the grain growth simulation is the generation of a polycrystalline microstructure for calculation. The crystal orientation was represented by assigning an integer from −1000 to 1000 to each cell in an array of 200 × 200 square unit cells on the computer. Parent and second phases were assigned to positive and negative numbers, respectively. A grain was represented by an aggregation of cells with the same number of orientations. The boundary between cells with different numbers of orientations corresponded to the grain boundary or the interface between different phases. Figure 1 shows the initial microstructure that was generated by randomly assigning an orientation number from −1000 to 1000 to each cell.

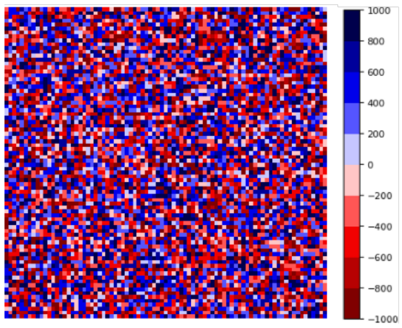

Fig. 1 Initial microstructure for the simulation.

(2) MC simulation model

A simulation model was constructed using the MC method, which is a stochastic calculation method using random numbers. After randomly selecting one cell and calculating the change in the microstructure, the procedure was repeated to represent the grain growth behavior.

Figure 2 presents the specific calculation procedure. First, a cell was selected using a random number. Next, the energy of the selected cell and that of the eight cells adjacent to the selected cell were expressed as follows:

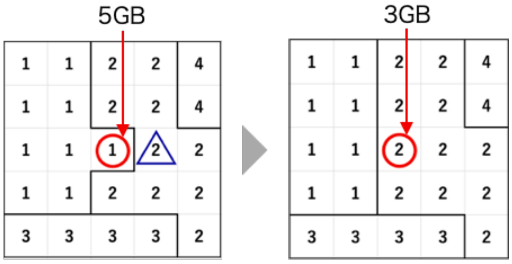

1	1	2	2	4
1	1	2	2	4
1	1	1	2	2
1	1	2	2	2
3	3	3	3	2

1	1	2	2	4
1	1	2	2	4
1	1	2	2	2
1	1	2	2	2
3	3	3	3	2

Fig. 2 Intergranular migration process.

$$E_A = \sum_{A\neq B}^{k} \left[E_{gb1}(1-\delta_{S_AS_B})\zeta_{AB}+E_{pb}(1-\zeta_{AB})\right] \qquad (S_A>0)$$

$$E_A = \sum_{A\neq B}^{k} \left[E_{gb2}(1-\delta_{S_AS_B})\zeta_{AB}+E_{pb}(1-\zeta_{AB})\right] \qquad (S_A<0)$$

where E_{gb1} and E_{gb2} are the grain boundary energies of the parent and second phases, respectively; E_{pb} is the interface energy between the parent and second phases; and S_A and S_B are the orientations of any cell A and its neighboring cell B, respectively. $\delta_{S_AS_B}$ is set to 1 when $S_A = S_B$ and to 0 at other instances. ζ_{AB} was set to 1 when cells A and B are in the same phase and at 0 when in different phases.

The grain boundary migration proceeded during minimization of energy by changing the orientation of a randomly selected cell or exchanging the orientation of the selected cell with any of the eight adjacent cells. Considering the Ostwald ripening of the second phase, the orientation changed when two randomly selected cells belong to different phases and during energy minimization. This operation is effective when the sum of the energies of the two cells decreases or hardly changes after the cell exchange and the change of orientation. The cell state returns to that before the cell exchange occurs when the sum of the energies increases. This simulation was performed using the following variables: grain boundary energy between the parent phase; grain boundary energy between the second phase; interfacial energy between the parent and second phases; second phase volume fraction; frequency of Ostwald ripening; and time. The calculation steps were 3.0×10^5.

The simulation results were used for machine learning. Moreover, a regression model of the input and output parameters was built using an artificial neural network (ANN). The input parameters were the variables used in the simulation. The output parameters were the average grain size. The hyperparameters were determined using Bayesian optimization. Furthermore, a sensitivity analysis was conducted to quantify the influence of the input variables on the grain growth behavior using the regression model.

3. Results and Discussion

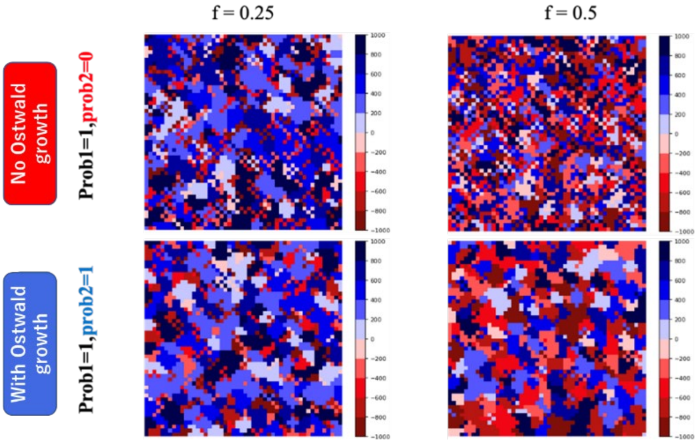

Fig. 3 Results of simulations with different frequencies of Ostwald ripening.

Figure 3 shows the simulation results with different Ostwald ripening frequencies when the volume fraction of the second phase was 25% and 50% (E_{gb1}:E_{gb2}:E_{pb}= 1:1:3). The grain growth was accelerated by the enhancement of the Ostwald ripening, regardless of the volume fraction of the second phase. The grain growth was accelerated by decreasing the pinning effect caused by the Ostwald ripening of the second phase[3)]. The obtained result was in a good agreement with the findings in the previous report. In addition, the grain growth was accelerated by decreasing the volume fraction of the second phase, grain boundary energy between the parent and second phases, and by increasing the interfacial energy between the parent and second phases. This result suggests that the developed simulation model can reproduce the experimental trend.

Table 1 shows the sensitivity analysis results obtained using the model developed by ANN analysis. The calculation result indicates the magnitude of the influence of each parameter. The parameter largely influenced the model when the value was large. Time, interfacial energy between the parent and second phases, and the frequency of Ostwald ripening were substantial.

Table. 1 Sensitivity analysis results obtained using the model developed by ANN

time (t)	3.27
interfacial energy between the parent and second phases (E_{pb})	3.01
Ostwald ripening (prob2)	2.54
second phase volume fraction (f)	1.90
grain boundary energy between the parent phases (E_{gb1})	1.47
grain boundary energy between the second phases (E_{gb2})	1.07

4. Conclusions

In this study, a simulation model of the grain growth behavior in the dual phase microstructure was developed. The model reproduced the same trend as in the experiment. A sensitivity analysis was performed to analyze the dominant factors of the grain growth behavior. The results showed that the interfacial energy between the parent and second phases and the frequency of Ostwald ripening remarkably affected the grain growth behavior.

Acknowledgement

This work was performed under the support of the Managing Researcher, Research Center for Structural Materials of National Institute for Materials Science (NIMS), for many issues regarding the MC model on grain growth in dual phase microstructure.

References

1) Taiji Nishizawa: Grain growth in single- and dual phase steels, Tetsu-to-Hagané, 70 (1984), 1984-1992.
2) Masayuki Abe, Akira Hiura, Kiyohito Ishida and Taiji Nishizawa: Grain growth in duplex stainless steels, Tetsu-to-Hagané, 70 (1984), 2025-2032.

3) Takemori Takayama, Myeong Yong Wey and Taiji Nishizawa: Grain growth in dual phase steel, Tetsu-to-Hagané, 8 (1982), 1016-1023

Bayesian-optimized cellular automaton modeling of austenite-to-ferrite phase transformation in carbon steels

Yoshihisa Mino[1,*], Zhi-Lei Wang[1], Toshio Ogawa[1], Yukinobu Natsume[2] and Yoshitaka Adachi[1]

[1] Department of Material Design Innovation Engineering, Nagoya University, Nagoya, Aichi 464-8603, Japan
[2] Department of Materials Science Faculty of Engineering Science, Akita University, Akita, Akita 010-8502, Japan
*email: mino.yoshihisa.y7@s.mail.nagoya-u.ac.jp

Keywords: steel, cellular automaton, phase transformation, Bayesian optimization, TTT diagram, modeling

1. Introduction

Controlling the microstructure of steel relies on phase transformation. Therefore, many studies concentrating on driving forces and mobility have been conducted to better understand phase transformation behaviors. The simulation of phase transformation events based on thermodynamics is currently represented via phase-field simulation (PF). However, PF is of high cost mainly because microstructural development is related to certain physical parameters. Conversely, cellular automaton (CA) simulation has relatively simple local rules for cell transition, which result in global microstructure evolution1). The optimization modeling parameters, which make simulation plausible2), are one of the topics covered via CA simulation.

Therefore, we attempt to optimize CAparameters by introducing the Bayesian optimization.

2. CA Simulation

This study considered the phase transformation behavior of three types of Fe–C binary systems (Fe–0.20 to 0.50 wt.% C). A Gaussian function with two parameters, T_{max} and dT_{σ}, was employed to represent nucleation behavior, where T_{max} and dT_{σ} are the temperatures of maximum ferrite nucleation rate and its standard deviation, respectively (Fig. 1). In this CA simulation, local equilibrium at an interphase boundary is assumed and carbon diffusion in austenite is calculated using Fick's 2nd law.

Thereafter, a Time–Temperature–Transformation (TTT) diagram was obtained by conducting CA simulation at each temperature. The transformation was conducted until the ferrite volume fraction achieved equilibrium. The CA parameters, T_{max}, dT_{σ}, were determined by minimizing the differences in the TTT diagram between previously reported3) experimental results and CA simulation as shown in Fig. 2. Additionally, root mean squared error (RMSE) was employed to explain these differences.

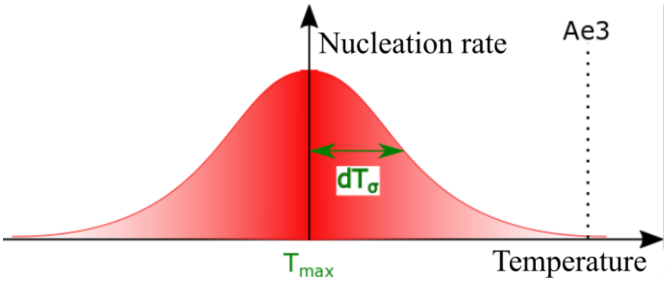

Fig. 1 Setting of ferrite nucleation rate using Gaussian function with two parameters.

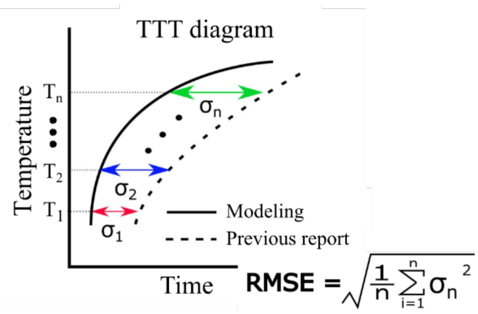

Fig. 2 Calculation of RMSE in TTT diagram.

3. Results and Discussion

Fig. 3 shows (a) initial austenite and (b) microstructures transformed at 950 K in an Fe–0.20 wt.% C alloy. Same color in Fig. 3(b) indicates that ferrite grains have the same orientation and the black regions represent martensite transformed by quenching. Fig. 4 presents the three trustworthy parameters (T_{max} and dT_{σ}) obtained during multiple calculations. Regardless of carbon content, T_{max} was almost constant at approximately 885 K; whereas, dT_{σ} decreased as the carbon content increased.

The TTT diagram obtained using the optimized parameters for the Fe–0.20 wt.% C alloy agreed well with the previous report[3] (Fig. 5(a)). Meanwhile, as the carbon content increased (Fig. 5(b)), the CA-simulated TTT diagram tends to disagree with the literature. It is likely that this agreement is because this CA simulation does not account for the incubation time of nucleation.

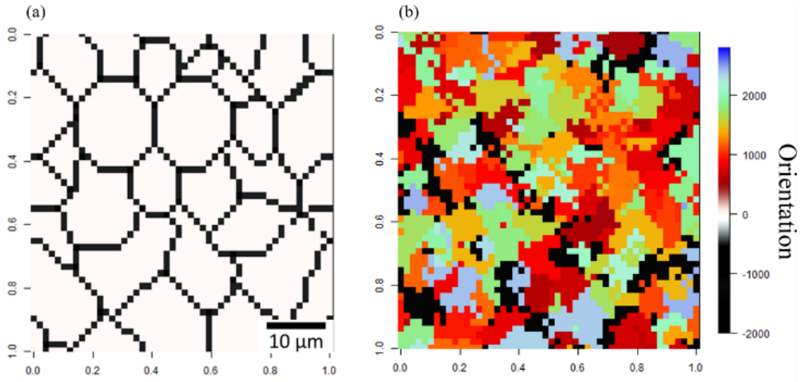

Fig. 3 (a) Initial and (b) transformed microstructures for CA simulation (Fe–0.20 wt.% C, 950 K).

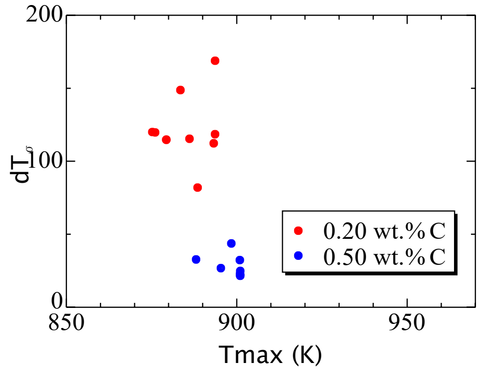

Fig. 4 Optimized CA parameters (T_{max} and dT_σ) for each carbon content.

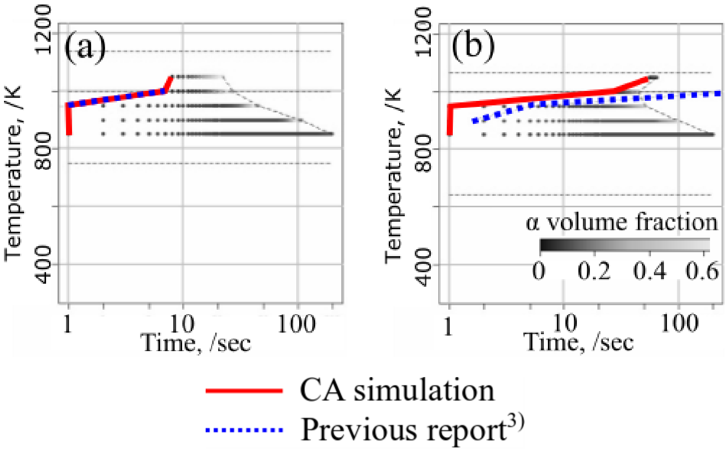

Fig. 5 Comparison of TTT diagrams between simulation and experiment in Fe–(a) 0.20 wt.% C and (b) 0.50 wt.% C.

4. Conclusions

In combination with Bayesian optimization, a high-accuracy CA model of austenite-to-ferrite phase transformation in carbon steels was investigated. By optimizing the CA parameters, T_{max} and dT_σ, a simulated TTT diagram similar to a previously reported diagram was obtained.

References

1) D. An, S. Pan, L. Huang, T. Dai, B. Krakauer and M. Zhu, Modeling of ferrite-austenite phase transformation using a cellular automaton model, ISIJ Int., 54 (2014), 422-429.
2) M. Kumar, R. Sasikumar and P. K. Nair, Competition between nucleation and early growth of ferrite from austenite—studies using cellular automaton simulations, Acta Mater., 46 (1998), 6291-6303.
3) Y. Waseda, Kinzoku-Databook, Maruzen Publishing Co. Ltd. (2004), 453-483.

Abnormal Goss grain growth in pure iron by two-way cold rolling and subsequent annealing

Yutaro Suzuki[1,*], Zhi-Lei Wang [1], Toshio Ogawa[1], Yoshitaka Adachi[1],
Atsushi Yamaguchi[2], and Yukihiro Matsubara[2]

[1] Division of Material Design Innovation Engineering, Nagoya University, Furo-cho, Chikusa-ku,Nagoya, Aichi 464-8603, Japan
[2]Asahi-Seiki Manufacturing Co.,Ltd., Asahimae-cho, Owariasahi, Aichi 488-8655, Japan
*email: suzuki.yutaro.s0@s.mail.nagoya-u.ac.jp

Keywords: steel, texture, Goss orientation, abnormal grain growth, two-way cold rolling, annealing

1. Introduction

Iron and steel are used in several fields, and a minor improvement in their performance has a substantial influence. Controlling the texture of iron is essential to enhance its formability and magnetic properties. The mechanism of recrystallization texture evolution can be changed using chemical composition, cold rolling conditions, and annealing patterns. With regards to cold-rolled, pure iron, and ultra-low-carbon steel, it is common that α-fiber oriented in the < 110 > direction which is parallel to the rolling direction and γ-fiber oriented in the {111} plane which is normal to the sheet surface develop[1)]. In subsequent annealing, recrystallized grains preferentially nucleate in γ-fiber region and grow with consuming α-fiber, eventually γ-fiber is strongly developed[1)].

The introduction of alloying elements is essential in the development of several textures to control the performance of iron; for example, electromagnetic steel is added 3% silicon to pure iron to improve their magnetic properties. In contrast, texture methods of control that does not use alloying elements need special conditions. It has been reported that in the case of pure iron, α-fiber is effectively developed by severely cold rolling at a reduction ratio of 99.8% and subsequent annealing[2)]. As a result, we develop a simpler approach to control the texture of pure iron by two-way cold rolling and annealing.

2. Materials and Methods

A sheet of pure iron (thickness: 1.4 mm) was used as the original specimen. Figure 1 shows a two-way cold rolling procedure. The original specimen was cold-rolled to a thickness of 0.98 mm perpendicular to the rolling direction of the original specimen and then cold-rolled to a thickness of 0.56 mm in the same direction of the original specimen. The final cold rolling ratio was 60%.After the cold rolling, we conducted short-term and long-term annealing to examinethe nucleation of recrystallized grains and the grain growth, respectively. As a result of short-term annealing, the cold-rolled specimens were heated to 800°C at a rate of 5°C/s and subsequently quenched without isothermal holding. For the long-term annealing, the cold-rolled specimens were heated to 850°C, retained isothermally for 3 h (condition A), and then slow-cooling for 1 h (condition B). EBSD measurement was used to evaluate the texture after annealing.

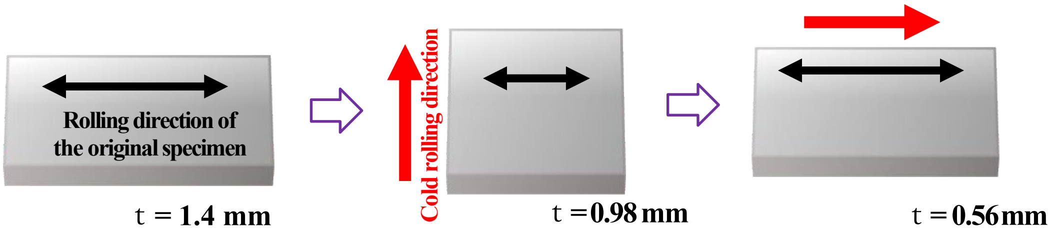

Fig. 1 Schematics of two-way cold rolling process.

3. Results and Discussion

Figure 2 shows the orientation determination function (ODF) maps of the cold-rolled and short-term annealed specimen. Both α-fiber and γ-fiber were developed in cold-rolled specimen, and this result is consistent with the previous study[1)]. On the contrary, recrystallization texture was random in the short-term annealed specimen. Moreover, Goss orientation grains (< 100 > {110}), which are known to be rarely developed in pure iron, were observed. This is a unique texture that differs from previous research.

Inverse pole figure (IPF) maps of long-term annealed specimens are shown in Figure 3. Abnormal Goss grain growth was observed in condition A (Goss grains are expressed as red and green in the rolling and normal directions, respectively). Furthermore, a coarse Goss grain was examined in condition B. In contrast, Goss grains were difficult to identifywhen the original specimen was annealed for long-term (Fig. 4). These results imply that there is a possibility of discovering the new types of recrystallization textures by devising the cold rolling direction.

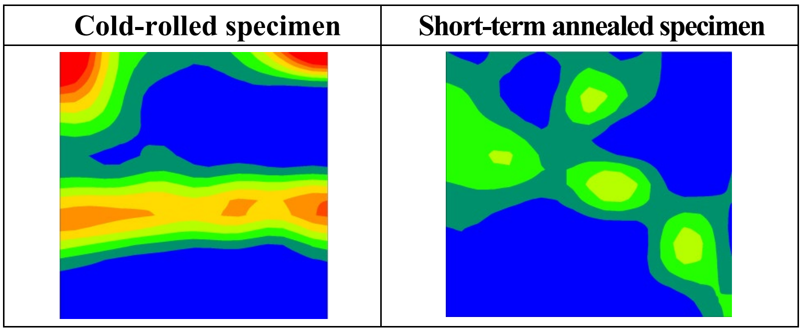

Fig. 2 Orientation determination function (ODF) maps of cold-rolled and short-term annealed specimen ($\varphi_2 = 45°$ section).

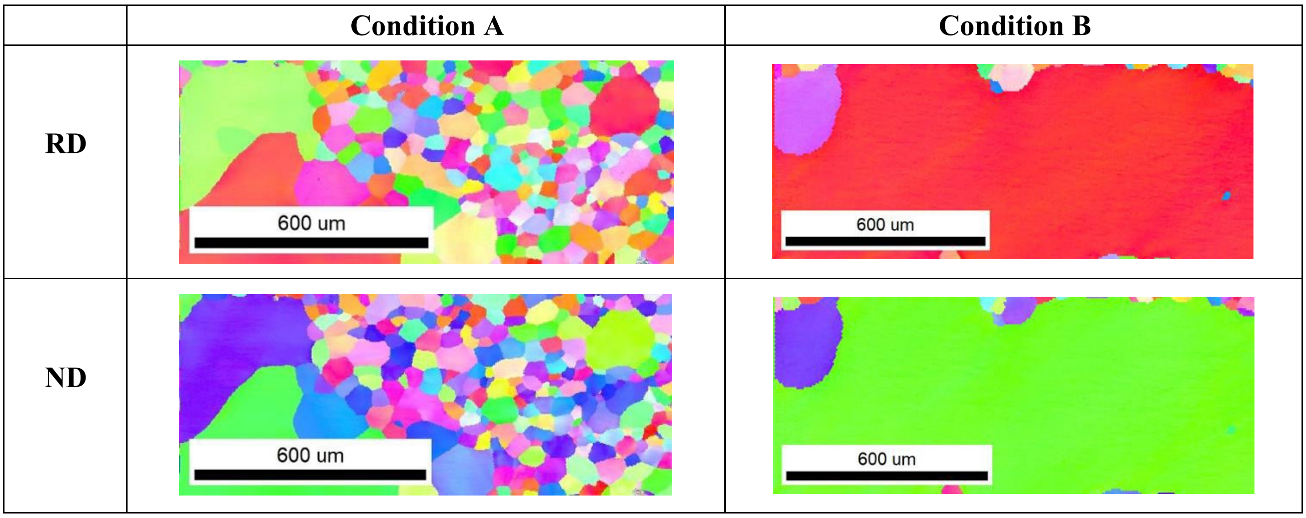

Fig. 3 Inverse pole figure (IPF) maps of long-term annealed specimens (conditions A and B).

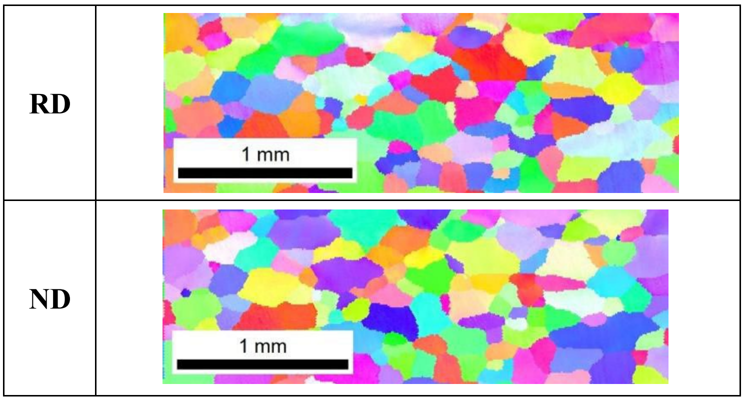

Fig. 4 Inverse pole figure (IPF) maps of the original specimen annealed for long-term.

4. Conclusions

We examined the texture of pure iron using two-way cold rolling and subsequent annealing. In the cold-rolled specimen, both α-fiber and γ-fiber were produced. Short-term annealing produced a random recrystallization texture. In addition, abnormal Goss grain growth was observed and coarse Goss grains were formed by long-term annealing.

References

1) E. Furubayashi: Recrystallization and material texture, Uchida Roukakuho, (2000), 104-107.
2)M. Tomita et al.: Development of recrystallization texture in severely cold-rolled pure iron, Tetsu-to-Hagané, 101 (2015), 204-210.

Surface hardening and nano-sized clustering during low temperature nitriding of Fe-35Ni-X (X=Cr, V, Mo, Al) alloys

Yulin Xie[1,*], Goro Miyamoto[2,3], Tadashi Furuhara[2]

[1] Graduate School of engineering, Tohoku University, Sendai, Miyagi 980-8577, Japan
[2] Institute for Materials Research, Tohoku University, Sendai, Miyagi 980-8577, Japan
[3] Research Center for Structure Materials, National Institute for Materials Science, Tsukuba, Ibaraki 305-0047, Japan.
*email: xie.yulin.r1@dc.tohoku.ac.jp

Keywords: Spinodal decomposition, short-range ordering, surface modification, nanostructure, expanded austenite.

The formation of a so-called expanded austenite (γ_N) layer on the surface of austenitic stainless steels during low temperature (~673 K) nitriding has been widely investigated since the first studies in the 1980s [1,2] showed the possibility of surface hardening without sacrificing the corrosion resistance of the material. γ_N is considered to be a hard metastable supersaturated interstitial solid solution that is produced by injecting nitrogen atoms into a face-centered cubic (fcc) alloy containing nitride-forming elements (e.g., Cr) at low temperature with no nitride precipitation [3]. At most, 37.5 at% N can be dissolved in the surface region of AISI316 stainless steel [4] due to strong Cr-N attractive interactions [5]. Studies on low-temperature nitriding of stainless steel to date have reported γ_N layers with a high hardness of up to 1500 HV [6].

However, there is a significant possibility for γ_N to be decomposed by discontinuous precipitation of CrN nitride [7]. It is also expected that nanoscale phase separation or spinodal decomposition could be induced by strong X-N attractive interactions. The subsequent formation of interstitial substitutional clusters was reported as modulated structures that produce sidebands in diffraction patterns in Fe-34Ni-0-4.4V (at%) alloys nitrided at temperatures above 873 K [8] and streaks observed by transmission electron microscope (TEM) in an Fe-29Ni-4Cr alloy nitrided at 723 K [9]. On the other hand, there is no direct evidence of X-N clustering in γ_N during the nitriding of austenitic steel at low temperatures. Research on γ_N with higher Cr and N contents mostly show the lack of a modulated structure, sidebands nor streaks under TEM and XRD observation [10,11]. On the other hand, recently we have found nanoscale Cr-N clustering with a modulated structure in γ_N in low temperature nitriding of Fe-35at%Ni-10at%Cr alloy using TEM and three-dimensional atom probe (3DAP)[12]. Therefore, the purpose of the present study is to elucidate the alloying effect of X elements (X = Al, V, Cr, Mo) with different X-N interaction on surface hardness of nitrided Fe-Ni-X alloys and nanostructures were carefully examined by TEM and 3DAP techniques,

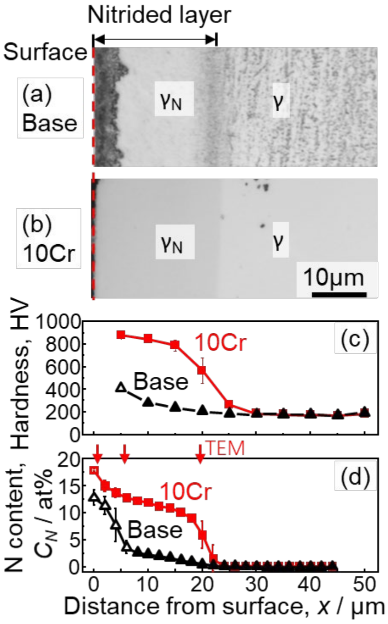

Fig. 1. (a), (b) Optical micrographs, (c) hardness, and (d) N content-depth profiles, respectively, of the Base and Fe-35Ni-10Cr alloys nitrided at 673K for 30h[12].

In the present study, Fe-35at%Ni-X (X=10at% Al, Mo, V, Cr or 30at% Cr) ternary alloys were prepared by arc or induction melting and hot working. An Fe-35Ni base alloy was prepared by continuous casting and cold rolling. The solution treated alloys were subjected to surface mechanical polishing and plasma nitriding at 673 K for 30 h, in a $N_2/H_2/Ar$ mixed atmosphere ($p(N_2):p(H_2):p(Ar)=8:4:5$) at a total pressure of 1000 Pa. Nitrided microstructure was observed using optical microscopy, FE-SEM and TEM. X-ray diffractometry (XRD, Co target, Kα line: 1.78897 Å) was employed for phase identification and lattice parameter measurement in the nitrided layer. The hardness distributions in cross-section were measured by a micro-Vickers hardness tester at a load of 10 gf. The corresponding N content was measured by FE-EPMA and standard samples of pure iron and Fe-0.98, 2.0, and 5.9 mass% N (Fe_4N) were used for calibration. 3DAP was used for evaluation of nanoscale element distribution. The measurement was conducted at 50K and the data obtained was analyzed using the IVAS ver. 3.8.8 software.

Figs. 1(a) and 1(b) show cross-sectional OM images of the Base and 10Cr alloys nitrided at 673 K for 30 h, respectively. In Fig. 1(a), a diffusion layer (γ_N) with low contrast appears beneath the dark etched layer on the surface of the Base alloy, whereas the nitrided layer in the 10Cr alloy mostly consists of γ_N with a thin dark etched layer on the surface (Fig. 1(b)). Figs. 1(c) and 1(d) show the hardness and N depth profiles for the nitrided alloys, where open symbols (□, △) near the surface represent data taken from the dark etched layer. FE-SEM and TEM analyses of the dark layer on the surface of nitrided alloys indicate that this layer is composed of a lamellar structure containing disordered γ and nitride (ordered γ'-Fe_4N for Base alloy and B1-type CrN nitride for 10Cr alloy). The γ_N layer in the 10Cr alloy shows extremely high hardness (~900HV) and high N content (~15 at%) compared with the Base alloy (~300HV for the γ_N layer, ~2.3 at% N). The N concentration and hardness gradually decrease towards the inner un-nitrided region for both alloys, with little difference in the hardness of the bulk even with the addition of 10 at% Cr. The γ_N layer is considered to be expanded austenite due to its high hardness, high N content and weakly etched contrast.

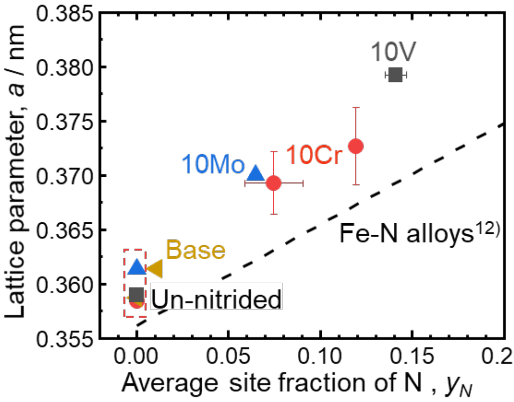

Fig. 2. The relationship between the N site fraction of γ_N layers and the lattice parameter of γ_N. The N site fraction is evaluated from N content-depth profiles as the mean value by considering X-ray penetration depth (~10μm). The lattice parameter is taken as the average value of 200, 111, 220, and 311 γ_N peaks. The black dash line plotted in is the data of unstressed retained austenite (Fe-N) taken from Ref. 13.

Similar microstructure like 10Cr alloy is observed for other ternary alloys (30Cr, 10V, 10Mo, 10Al) after nitriding at 673 K for 30 h. After plasma nitrided at 673 K for 30 hours, the addition of 10at% Al to the Fe-35Ni base alloy showed minor effect, but the N concentration increased largely by the other additives in the order of 10at% of Mo, Cr, V and 30at% Cr, consistent with the magnitude of the N-X attractive interaction in FCC. The hardness of γ_N layers is proportion to the N content, and it should be noticed that the surface hardness increased up to 1100HV in the 10V alloy and up to 1400HV in the 30Cr alloy after nitriding. Also, compared with the hardness of retained austenite in a Fe-N binary alloy, e.g. 283 HV for 8.6 at% obtained in this study, the γ_N layer in the 10Cr alloy was 600 HV harder with a similar N content. Therefore, we believe that apart from solution hardening, a large part of the high hardness observed in the γ_N layers is due to the coexistence of Cr and N (Cr-N clusters or/and Cr-N SRO).

Lattice parameters of γ_N were measured using XRD and summarized in Fig. 2 where the lattice parameters for γ and γ_N are plotted as a function of the N content in the γ_N layers. The lattice parameter for γ_N expands linearly with increasing N site fraction, which is consistent with the results of a previous study [4)]. The compositional dependence of the lattice parameter is slightly larger than that for un-strained austenite in a Fe-high N binary system [12)]. The increase in the lattice parameters with increasing N content

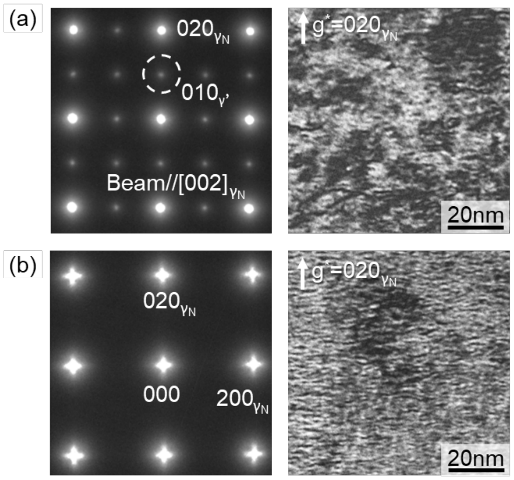

Fig. 3. Selected area diffraction patterns (SAEDs), bright field images of the 10Cr alloy nitrided at 673 K for 30 h, (a) near nitriding surface at a depth of 0.5μm and (b) 6.5μm. [12)]

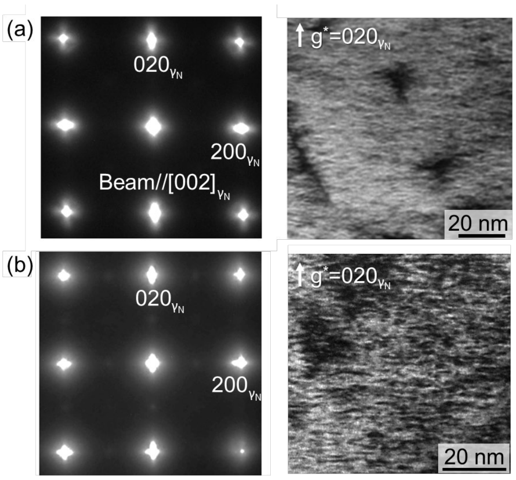

Fig. 4. Selected area diffraction patterns (SAEDs), bright field images of (a) 10V alloy and (b) 10Mo alloy nitrided at 673 K for 30 h(both at a depth of 8μm from the surface).

indicates that N atoms in the γ_N layer are present close to the solid solution state from a macroscopic perspective, which is commonly regarded as a feature of expanded austenite [3].

Fig. 3 shows selected area electron diffraction (SAED) patterns, bright field TEM images taken from γ_N in the 10Cr alloy nitrided at 673 K for 30 h at various depths from surface. At a depth of 0.5 μm (Fig. 4(a)), fcc spots with superlattice reflections indicate the presence of a Fe_4N type ordered structure in γ_N. Modulation along <010>$_\gamma$, rather than precipitation, is observed in the bright-field TEM image. At a depth of 6.5 μm (Fig. 3(b)), γ_N spots with no clear superlattice spots nor spots from any secondary phase were observed. Instead, strong streaks along the <001>$_\gamma$ direction are present, and a clear modulated structure along <010>$_\gamma$, is observed in the bright-field TEM image. Identical Fe_4N type superlattice reflections, streaks and modulations are also observed during TEM characterization of the γ_N layer formed on 10Mo and 10V alloys as shown by Fig. 4.

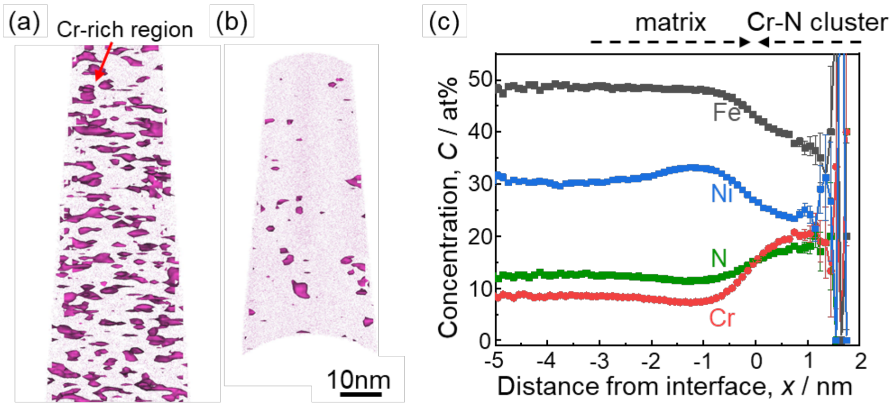

Fig. 5. 3DAP analyses of γN in 10Cr alloy nitrided at 673 K for 30 h. Cr atom map (a) at depths of 4.5 μm (γ_N layer), and (b) before-nitrided sample. (c) Proxigram revealing the concentration profile of each element across the isosurfaces of the data shown in (a). The highlighted isosurfaces in (a) and (b) represent regions where the local Cr content is 25% higher than the total Cr content[12].

3DAP analyses were conducted to gain a deeper understanding of the chemical heterogeneity in γ_N of the 10Mo, 10Cr and 10V alloys. For the 10Cr alloy, Figs. 5(a) and 5(b) show Cr atom maps, where highlighted areas represent Cr-rich regions. The number density of Cr-rich regions at a depth of 4.5 μm is clearly higher than that in the before-nitrided sample. The observed isosurfaces in Figs. 5(b) are due to the statistically higher local Cr composition in random distribution in the 3DAP data. The proxigram in Fig. 5(c) shows the concentration profile as a function of the distance from the interface shown in Fig. 5(a). Cr and N enrichment occurs simultaneously with a ratio close to 1:1, which indicates Cr-N clustering inside the γ_N layer. It should be noticed that for 10Mo and 10V alloys, similar X-N clustering is also observed.

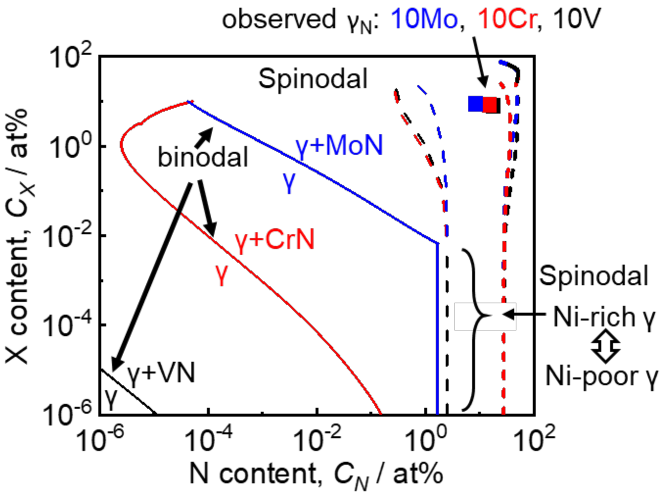

Fig. 6. Ternary diagram of (Fe-35Ni)-Cr-N system (673 K) showing binodal lines and spinodal lines in log scale. The measured N content of γ_N layer in this study is represented by the colored squares, falling inside the spinodal decomposition region.

X-N (X=Mo, Cr, V) clustering observed in this study indicates that the addition of X and N causes the free-energy surface to be upwardly convex due to the attractive X-N interactions. Therefore, it is possible for X-N clusters or nitrides to form by phase separation or spinodal decomposition in the fcc lattice. Fig. 6 shows the isothermal section of phase diagrams of the (Fe-35Ni)-X-N system with binodal and spinodal lines calculated using Thermo-Calc2021a with the TCFE9 database. Based on the calculated binodal line, X-N clusters is expected to be produced with only a small addition of X and N through phase separation into fcc (Fe-35Ni) + B1-type nitride (XN). The 10V alloy shows the widest binodal region among the three X elements, which is corresponding to the strongest attractive interaction between V and N in this study. Furthermore, the composition of γ_N for 10(Mo, Cr V) alloys in this study all falls into the spinodal region. The the formation of compositionally unstable X and N enriched fcc clusters is consistent with the lack of diffraction spots for XN nitride in the SAED patterns shown in Fig. 3-4.

In conclusion, X-N clustering in the expanded austenite layer formed during the low-temperature plasma nitriding of a Fe-

35Ni-10X alloy was directly observed. Although a N solid solution appears to be present at the macroscopic level, nanostructural characterization of the γ_N layer clearly showed the presence of X-N clusters, as evidenced by clear streaks in SAED patterns, a modulated structure in TEM images, and X/N-rich regions identified by 3DAP analyses. Thermodynamic calculations showed that the X-N clusters are formed by spinodal decomposition due to strong X-N attractive interactions. Compared with Fe-N retained austenite having a similar N content, the extremely high hardness of the expanded austenite is considered to originate from the synergetic effect of X and N.

Acknowledgement

This work was supported by Grant-in-Aid for Scientific Research on Innovative Areas (Research in a proposed research area) (18H05456, 2018-2022), JST SPRING, Grant No. JPMJSP2114, the JST "Collaborative Research Based on Industrial Demand" Grant No. JPMJSK1613, Japan and by the Tohoku University Microstructural Characterization Platform in Nanotechnology Platform Project sponsored by the Ministry of Education, Culture, Sports, Science and Technology (MEXT), Japan. T.F. and G.M. gratefully acknowledge the financial support provided by the Ministry of Education, Culture, Sports, Science and Technology through Grants-in-Aid for Grant-in-Aid for Scientific Research (A) (Nos. 17H01330, 2017-2019), Grant-in-Aid for Scientific Research (B) (Nos. 19H02473, 2019-2021), Grant-in-Aid for Challenging Research (Exploratory)(No. 21K18803, 2021-2022), and JST FOREST Program (Grant Number JPMJFR203W).

Reference

1) Z. L. Zhang and T. Bell: Surf. Eng. **1** (1985) 131-136.
2) K. Ichii, K. Fujimura and T. Takase: Technol. Rep. Kansai Univ. **27** (1986) 135-144.
3) H. Dong, Inter: Mater. Rev. **55** (2010) 65-98.
4) T. Christiansen and M. A. J. Somers: Metall. Mater. Trans. A **37** (2006) 675-682.
5)T. Nishizawa: *Thermodynamics of microstructure* (Japan Institute of Metals 2002).
6) A. Fossati, F. Borgioli, E. Galvanetto and T. Bacci: Surf. Coat. Tech. **200** (2006) 3511-3517.
7) X. Y. Li and H. Dong: Mater. Sci. Technol. **19** (2003) 1427-1434.
8) J. H. Driver, R. Sinclair, K. H. Jack: Proc. R. Soc. Lond. A **367** (1979) 99-115.
9) N. P. Babenko, A. V. Gavrilova, G. F. Kosolapov, YU. D. Tyapkin: Phys. Met. Metall. **46** (1979) 90-97.
10) M.K. Lei, X.M. Zhu: Biomaterials **22** (2001) 641-647.
11) J. C. Jiang and E. I. Meletis: J. Appl. Phys. **88** (2000) 4026-4031.
12) Y. Xie, G. Miyamoto, T. Furuhara: Scr. Mater.: **213** (2022) 114637.
13) Liu Cheng, A. Böttger, Th.H. de Keijser, E.J. Mittemeijer: Scr. Metall. Mater. **24** (1990) 509-514.

3-dimensional morphology of upper and lower bainite in the initial stage of transformation

Shotaro Jimbo[1,*], Shoichi Nambu[1]

[1] Department of Materials Engineering, The University of Tokyo, Tokyo 113-8656, Japan
*email: jimbo@metall.t.u-tokyo.ac.jp

Keywords: steel, bainite transformation, three-dimensional observation

1. Introduction

Bainite is widely used in high-strength steels such as TRIP steels, and its importance is increasing. The microstructure formation during bainitic transformation is considered to be nucleation at prior austenite grain boundaries (PAGBs) and subsequent autocatalytic growth having Kurdjumov-Sachs (K-S) orientation relationship with the austenite grain it grows1). Bainite is classified into upper bainite and lower bainite based on the precipitation site of carbide2) or the morphology of bainitic ferrite3,4). Based on the morphology of bainite, the upper bainite is a feather-like morphology or lath shape and lower bainite is like a plate shape, hereafter, upper bainite and lower bainite are defined based on morphology.

It is reported that upper bainite forms in relatively lower carbon steels and at higher transformation temperatures, the habit plane of upper bainite is close to (5 5 7)γ, and lower bainite forms in relatively higher carbon steels and at lower transformation temperatures, and its habit plane get close to (2 5 9)γ as transformation temperature decreases5). The longitudinal or the growth direction of upper bainite is close to [-1 0 1]γ that is parallel to the [1 1 1]α4). However, because of its high anisotropic shape such as lath or plate shape, the detail of the morphology such as the aspect ratio or the formation mechanism of bainite are still unclear. In addition, because the bainite typically forms from the PAGBs, the PAGB can affect the formation or the morphology of bainite. In order to understand the formation mechanism and the morphology of upper or lower bainite, it is necessary to observe microstructure of the bainite in the initial stage of transformation in 3-dimension. Therefore, the purpose of this study is to understand the formation mechanism of upper and the lower bainite through the 3-dimensional observation of the bainite in the early stage of transformation.

2. Experimental procedures:

0.4% C steel (Fe-0.39C-0.83Mn-0.97Cr-1.05Ni (in mass%)) and 0.6% C steel (Fe-0.61C-0.81Mn-1.79Si-0.027Al), were used in this study. The steels were homogenized at 1200°C for 24 h and cut into cylindrical samples, comprising 6 mm in diameter and 12 mm in height. To obtain partially transformed bainite structure, the following heat-treatment were conducted using a thermomechanical simulator (Thermomotor-Z, Fuji Electronic Industrial). The samples were austenitized at 1000°C for 10 min (0.6% C steel) or 20 min (0.4% C steel), followed by quenching to 350°C (0.6% C steel) or 450°C (0.4% C steel). They were

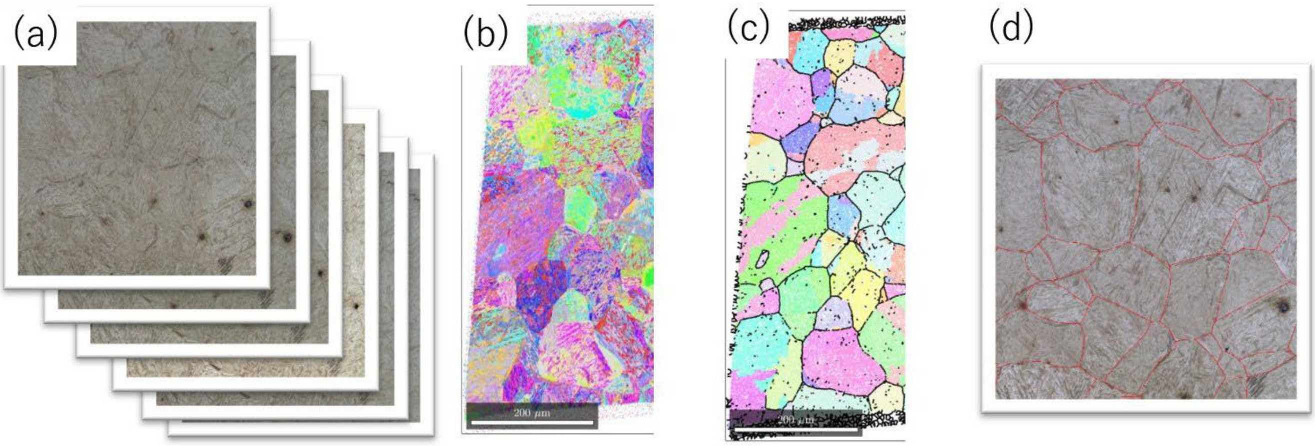

Fig. 1 Schematic of the 3-dimensional reconstruction (a) serial images by optical microscopy. (b) IPF map of bainite and martensite. (c) IPF map of the PAGBs (d) optical microscopy image with PAGBs.

then kept until 5% of the bainitic transformation proceeded. After that, they were cooled down to room temperature to stop bainite transformation by un-transformed austenite transform to martensite.

After the heat treatment, the samples were cut into a prismatic shape and surrounding area was filled with resin to efficiently align images for the construction of the 3-dimensional image. For the construction of the 3-dimensional image, optical microscopy (OM) based serial sectioning were performed with a polishing interval of about 1 μm as shown in Fig. 1(a), and crystal orientation analysis by EBSD were performed every 10 μm for the analysis of bainite and to estimate the PAG as shown in Fig. 1(b). The crystallographic orientations were analyzed using TSL-OIM software and MATLAB extensions, MTEX and PAG_GUI[6] for the reconstruction of the PAGs as shown in Fig. 1(c) and the PAGBs are drown on the OM images as shown in Fig. 1(d). Serial section images were first manually aligned, followed by automatic alignment. After adjusting the contrast of the images, 3-dimensional images were constructed by the Avizo software.

3. Result and Discussion.

3.1 3-dimensional image of upper bainite.

Figure 2(a) shows an OM image of the bainite formed at the PAGB in 0.4% C steel. Bainite can be distinguished as dark parts due to etching. Figure 2(b) shows the OM image of the same bainite in different layer. In this layer, it appears that bainite forms only one side of the PAGB, so 3-dimensional observation is necessary to correctly analyze the formation of bainite. Figure 2(c) shows the corresponding 3-dimensional image of bainite, and Fig. 2(d) shows only one bainite sheaf in Fig. 2 (c). The upper bainite forms parallel to each sheaf. The bainite formed in this condition is considered as the upper bainite based on the morphological definition.

3.2 3-dimensional image of lower bainite.

Figure 3(a) shows an OM image of the bainite formed almost parallel to the PAGB in 0.6% C steel and Fig. 3(b) is the corresponding 3-dimensional image. Unlike the case of the upper bainite, the bainite did not form in a feather-like shape, but form along the grain boundaries. Bainite growing into the austenite grains were also observed as shown in Fig. 3(c) and corresponding 3-dimensional image is shown in Fig. 3(d). In the case of the bainite in 0.6% C steel, bainite doesnot form in a feather-like shapes, which means that lower bainite forms at 0.6% C steel based on morphological definition.

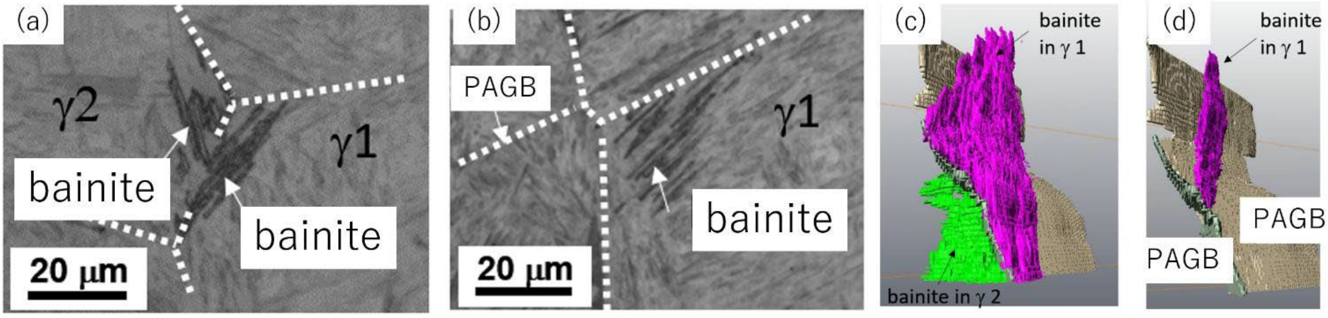

Fig. 2 (a) The OM image of bainite formed at the austenite grain boundaries. (b) The OM image of the same area but in different layer with (a). (c) 3-dimensional image corresponding to (a) and (b). (d) 3-dimensional image of single sheaf in (c).

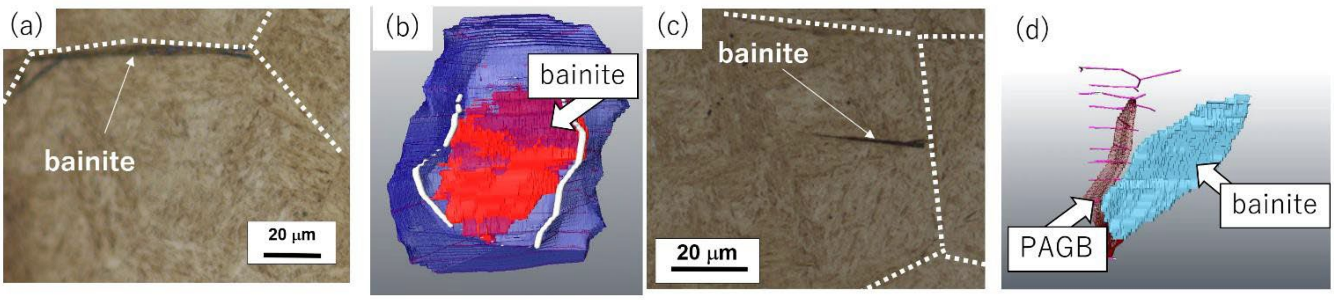

Fig. 3 (a) The OM image of lower bainite formed almost parallel to the austenite grain boundary. (b) Corresponding 3-dimensional image. (c) The OM image of lower bainite formed into the austenite grain. (d) Corresponding 3-dimensional image.

3.3 The morphology of sheaves in upper or lower bainite.

Figure 4(a) shows the length and width of the upper and lower bainite sheaves. When analyzing the sheaf length or width in the upper bainite, one sheaf was taken out and its length and width were analyzed, as shown in Fig. 2(d). When analyzing the lower bainite, the sheaf was classified into three types: bainite forms along the grain boundary, bainite forms into the austenite grain, and bainite forms from the previously formed bainite, and the length and width of each was taken. The results correspond to the upper bainite are shown as red circles, lower bainite that formed along the PAGB are shown as blue butts, lower bainite that forms into the austenite grain are shown as blue circles, and the secondary bainite are shown as blue triangles. The upper bainite formed at 0.4% C has an aspect ratio of about 5:1, while the lower bainite formed at 0.6% C has an aspect ratio of about 3:1 in the range observed in this study. The aspect ratio did not change for secondarily formed bainite, but when bainite forms along grain boundaries, the aspect ratio tended to approach 1 due to collisions with other grain boundaries.

Figure 4(b) shows the longitudinal direction of bainites and close-packed direction is also plotted. The longitudinal direction of upper bainite are plotted as red plus sign and the average direction of upper bainite is plotted with filled red rectangular. The longitudinal direction of lower bainite are plotted as blue triangle and the average direction of upper bainite is plotted with filled blue circle and the close-packed direction, that is [-1 -1 1] α, is plotted as black butts. The results show that in the case of the upper bainite, the longitudinal direction of the bainite is close to the close-packed direction, while for the lower bainite, the longitudinal direction is shifted in the direction [0 -1 1]α rather than close-packed direction.

Figure 4(c) shows the normal of the sheaf plate of bainite. In Fig. 4(c), the normal of the upper bainite sheaf is shown red plus sign and that of lower bainite is shown as blue triangles, and the normal of the habit planes calculated from the phenomenological theory of martensitic crystallography[7,8] (PTMC) is shown in black rectangular (single shear[7]) and circle (double shear[8]). The results show that the sheaf of upper bainite is close to the habit plane calculated by PTMC in double shear model, while the sheaf of lower bainite approaches to the habit plane calculated by the single shear model[7].

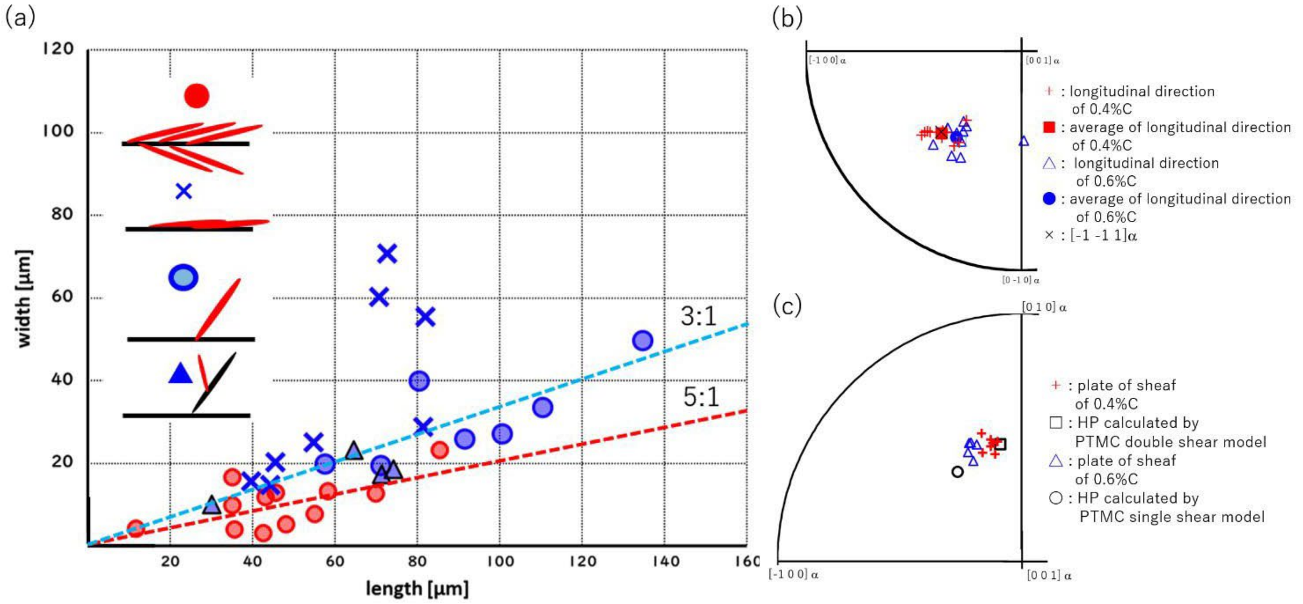

Fig. 4 (a) The length and width relationship of upper or lower bainite sheaves. (b) longitudinal direction and close-packed direction of the bainite. (c) broad plane of upper and lower bainite and calculated habit plane by PTMC.

3.4 Microstructure of upper and lower bainite.

Figure 5(a) and 5(b) show SEM images of the upper and lower bainite, respectively. It can be seen there are white contrasts in bainite sheaves. The white contrast between the bainite sheafs were retained austenite, which was confirmed by TEM observation. The trace analysis confirmed that the habit plane of the subunit is almost parallel to the close-packed plane, which is parallel to (1 1 1)γ. Comparing the upper and lower bainite, upper bainite has larger subunit than that of lower bainite, which suggests that the upper bainite sheaf grows mainly by the growth of subunits, so the plane normal and longitudinal direction of the bainite sheaf are close to the habit plane given by PTMC double shear model and [-1 -1 1]α, while the subunitof lower bainite is small comparing with that of upper bainite, which suggests that the sheaves of lower bainite do not grow by the growth of subunits but mainly by the stacking of subunits, so the plate plane and longitudinal direction of lower bainite sheaf have shifted from the habit plane of subunit and [-1 -1 1]α.

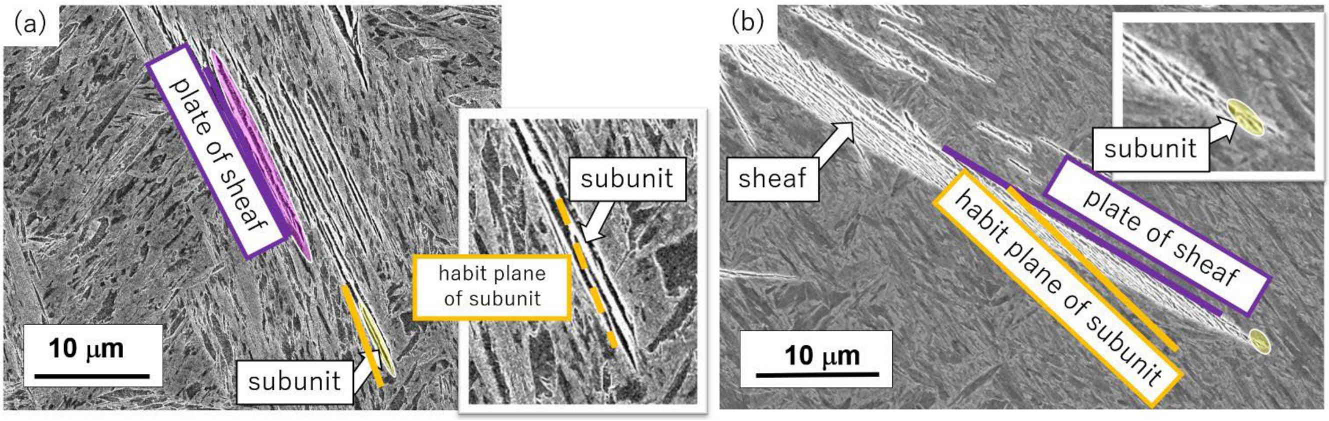

Fig. 5 (a) SEM image of upper bainite (b) SEM image of lower bainite

4. Conclusions

We conducted 3-dimensional observation of the initial stage of the upper and lower bainite transformation with OM and EBSD to understand the formation mechanism of upper and the lower bainite and following conclusions are obtained.

・The upper bainite forms on both sides the PAGB and forms feather-like shapes. On the other hand, lower bainite forms whose plate is almost parallel to the PAGB in the initial stage of bainite transformation.

・The sheaf of upper bainite in this condition has larger aspect ratio than that of lower bainite. The longitudinal direction and habit plane in upper bainite is close to [-1 -1 1]α andthe habit plane calculated by the PTMC double shear model, whilethe longitudinal direction of lower bainite is close to [-1 -1 1]α, but shifted in the direction [0 -1 1]α, and the habit plane of lower bainite is not close to the PTMC double shear model but close to the habit plane calculated by the PTMC single shear model. It is considered that the difference in the longitudinal direction and plate of bainite sheaves is owing to the microstructure in bainite sheaves.

Acknowledgement
This work was performed under the support of JSPS KAKENHI (No. 20H02475).

References

1) H. K. D. H. Bhadeshia: Bainite in Steels: Theory and Practice: 3rd ed., Maney Publishing, Leeds, UK, (2015).
2) B. L. Bramfitt and J. G. Speer: Metall. Trans., 21a (1990), 817.
3) Y. Ohmori, H. Ohtani and T. Kunitake: ISIJ Int., 11(1971), 250.
4) H. Ohtani, S. Okaguchi, Y. Fujishiro and Y. Ohmori: Metall. Trans., 21a (1990), 877.
5) M. G. Hall, H. I. Aaronson and G. W. Lorimer: Scripta Metall. 9(1975), 533.
6) T. Nyyssönen, M. Isakov, P. Peura and V. T. Kuokkala: Metall. Mater. Trans. A, 47(2016),
7) J. S. Bowles and J. K. Mackenzie: Acta Metall., 2(1954), 129.
8) P. M. Kelly: Mater. Trans. JIM, 33(1992), 235.

Spheroidization of Lamellae Cementite in Pearlitic Steel with Kinked Structure

Kazuki Okayasu *[1], Yosuke Oono[1], Rintaro Ueji[2], Daisuke Terada[1], Tadanobu Inoue[2]

[1]Chiba Institute of Technology, 2-17-1 Tsudanuma, Narashino, Chiba 275-0016, Japan
[2]National Institute for Materials Science, 1-2-1 Sengen, Tsukuba, Ibaraki 305-0047, Japan.
*email: s18a3028wn@s.chibakoudai.jp

Keywords: pearlite, cementite, ferrite, kinked structure, compression, annealing, spheroidization

Compression of the layered structure consisting of the soft and the hard phases brings kinking at which significant heterogeneous deformation occurs. Recently, it has been found that, in some types of Mg alloys with LPSO (long-periodstacking order) phase, kink band provides significant strengthening.1) Kink-like structure was also discovered in pearlitic steel2), while the strengthening by kink-kike structure is under the research. By the way, when the improvement of the strength of pearlitic steel at high temperature is considered using kink strengthening, it is necessary to clarify the thermal stability of kink-like morphology because the deformed pearlite changes its morphology by spheroidization at elevated temperature. Concerning of the spheroidization without plastic deformation, Ishida et al. 3) established the quantitative modeling based on the coarsening of precipitates. However, the study about the modeling of spheroidization with compression is not found. In this study, the change in the spheroidization behavior of pearlite by the presence or absence of kink-like structure was quantitatively clarified.

Silicon-chromium steel prepared by vacuum melting (JIS-SUP12 : Fe - 0.55C - 0.7Mn - 0.76Cr -1.48Si [wt.%]) was studied.

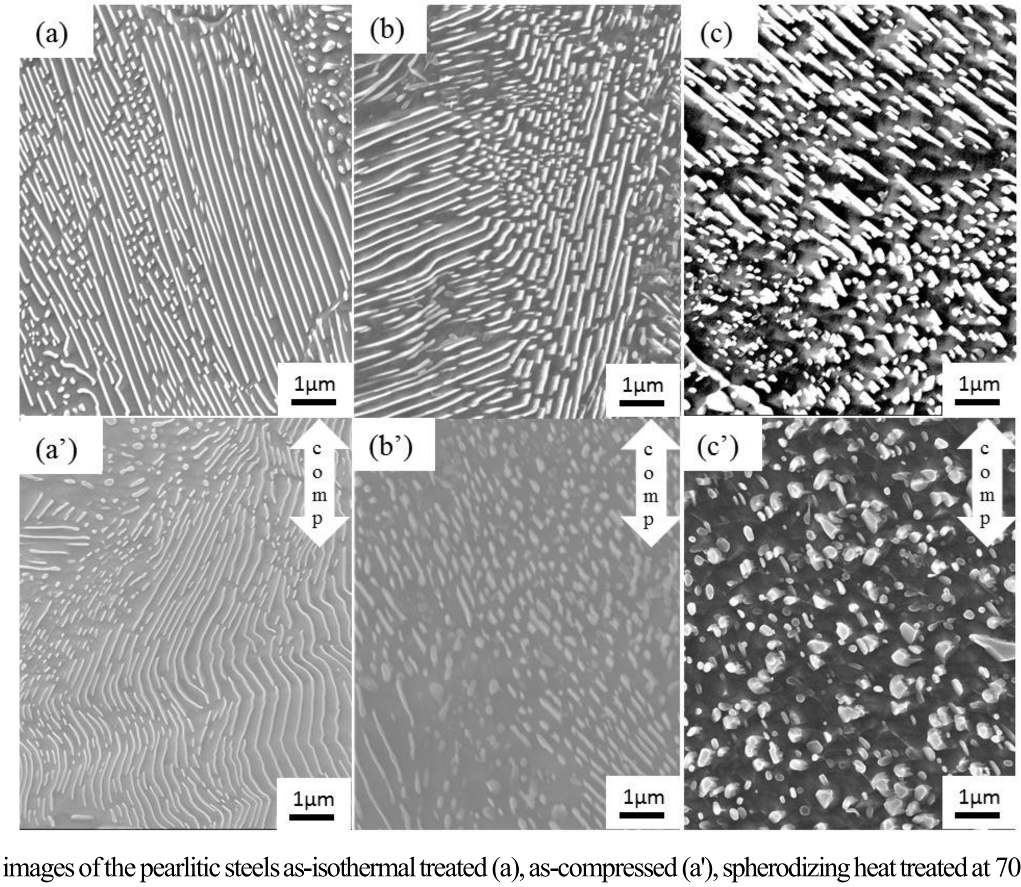

Fig.1 SEM images of the pearlitic steels as-isothermal treated (a), as-compressed (a'), spherodizing heat treated at 700 °C for 1.8ks (b, b') or 18ks (c, c'). Allow mark (comp) means the loading direction for compression.

The initial dimension of the sample is 8 mm in diameter and 12 mm in height with cylindrical morphology. The sample was austenitized at 950 °C for 180 s, followed by rapid cooling at 30 K/sec to 700 °C and then isothermal holding for 1000 s. After the isothermal heat treatment, the sample had pearlitic structure with a few % of proeutectoid ferrite. Some of the heat treated samples were compressed at room temperature at a strain rate of 10^{-3}/s to a reduction in height of 30%. The uncompressed and the compressed samples were again heated to 700 °C for the spheroidization of cementite using an electric furnace. Microstructural observation was conducted by SEM (Scanning Electron Microscope). Vickers hardness test was performed at a load of 2.0 g.

Figure 1 shows SEM microstructures of the samples as-isothermal holding (a), as-compressed (a') and heat treated at 700 °C for various conditions. (a), (b) and (c) are the microstructures of the uncompressed materials, while (a'), (b') and (c') are the images of the 30% compressed material. The black part represents ferrite while the white is cementite. The as-isothermal treated sample has pearlitic structure whose mean lamellar spacing is 150 nm, and the as-compressed sample (a′) shows the kink-like structure at which lamellar structure is sheared intensely along a plate. 35 % of the pearlitic colonies includes kink-like structure. With increasing of the holding time, lamellar structure changes to the distribution of the spherical cementite. In the samples heat treated for 1.8 ks (b, b'), some areas show the spherical cementite, meanwhile the pearlitic structure keeps remaining at the other area. When the samples heat treated at 18 ks (c, c'), only the spheroidized cementite was observed. The diameter of the cementite in the compressed samples is larger than that of the samples without compression.

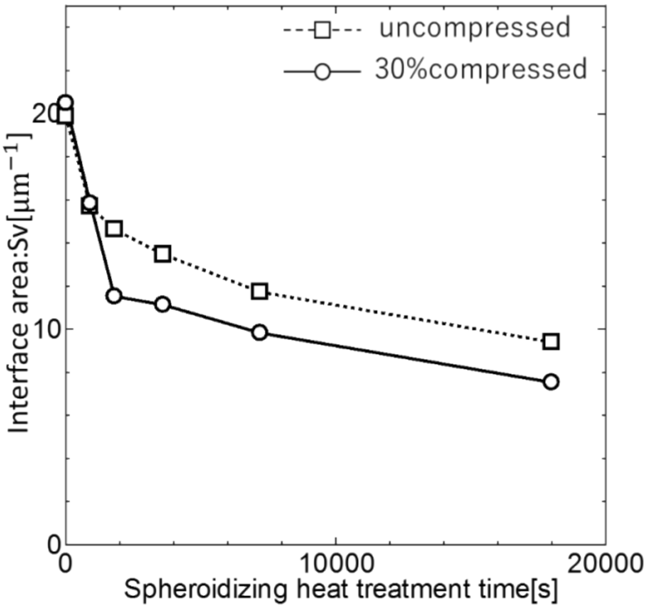

Fig.2 Relationship between the interface area per unit area and the holding time of spheroidizing heat treatment.

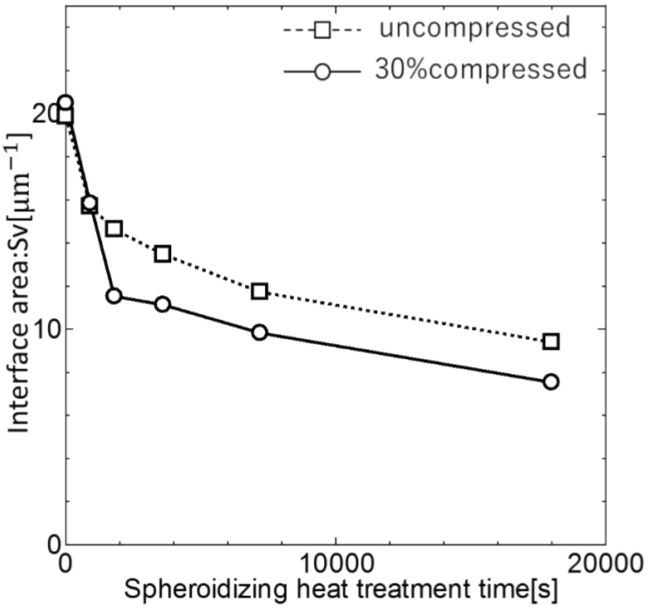

Fig.3 Spheroidization rate at various holding times for the spheroidizing heat treatment.

The ferrite/cementite interface energy provides the driving force for the spheroidization, and the area of interface decreases with the spheroidization. This means that the interface area per unit volume, S_V can be adopted as the parameter which indicates the progress of the spheroidization. Figure 2 shows the relationship between the holding time of the spheroidizing heat treatment and S_V which was measured by the counting of intercept points between the interface and randomly drawn lines on SEM images. It can be seen that the compression brings slight increase of S_V, as compared with that of the as-isothermal heat treated sample. In both the samples with or without compression, S_V decreases significantly at the initial stage of the heat treatment, and then these decrease more moderately.

In order to evaluate the progress of the spheroidization, it should be beneficial to evaluate the spheroidization rate,

$(S_V - S_0)/S_0$, which was proposed by Ishida et al. [3] S_0 means the area of the interface per unit volume at the initial conditions. Figure 3 shows the spheroidization rate of the samples with or without compression. The curves of the spheroidization rate presents the rapid increase at the initial stage and then the increasing rate becomes smaller with increasing of time. It should be noted that the spheroidization rate of the compressed sample shows larger than that of the sample without compression. This means the acceleration of the spheroidization by the compression.

Ishida et al.[3] have proposed a model for predicting the progress of spheroidization at elevated temperature. This model was developed based on the theory of Ostwald growth in which interface energy provides the driving force. The principal part of this model was presented by the following equations.

$$\left(\frac{1}{S_V}\right)^3 - \left(\frac{1}{S_0}\right)^3 = k^s t \qquad (1)$$

$$k^s = \frac{1}{(3f)^3}\frac{8\sigma V D_M}{27RT(K_M^{\theta/\alpha} - 1)X_M} \qquad (2)$$

In these equations, k^s is constant, t is time for the spheroidization heat treatment, f is the volume fraction of cementite, σ is the interface energy, V is the molar volume of cementite, D_M is diffusion coefficient of the solute, R is gas constant, T is temperature, $K_M^{\theta/\alpha}$ is solute-partitioning coefficient, and X_M is the molar fraction of the added element. These equations indicate that the change of $(1/S_V)^3$ can be estimated by the liner function of t,and this can be confirmed by the plot in Fig.4. The relationships between $(1/S_V)^3$-$(1/S_V)^3$ and t for both the samples with and without compression indicate simple linear function passing on the zero point, so that the Ishida's model is available to evaluate the spheroidization even in the deformed pearlite. It should be noted that k^s of the compressed sample is around two times larger than that of the sample without compression. This is probably because of the changes of σ and D_M due to the compression.

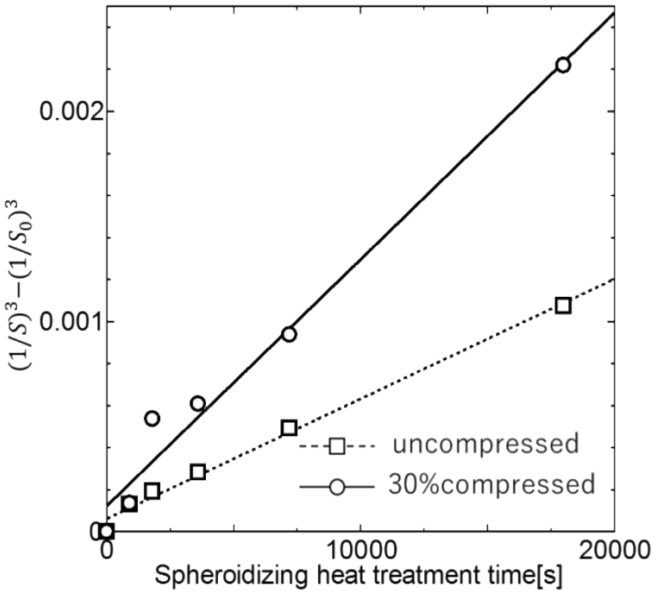

Fig.4 $(1/S_V)^3$-$(1/S_0)^3$ as a function of the holding time. The slope is corresponding to the constant, k^S, in Eq. (1).

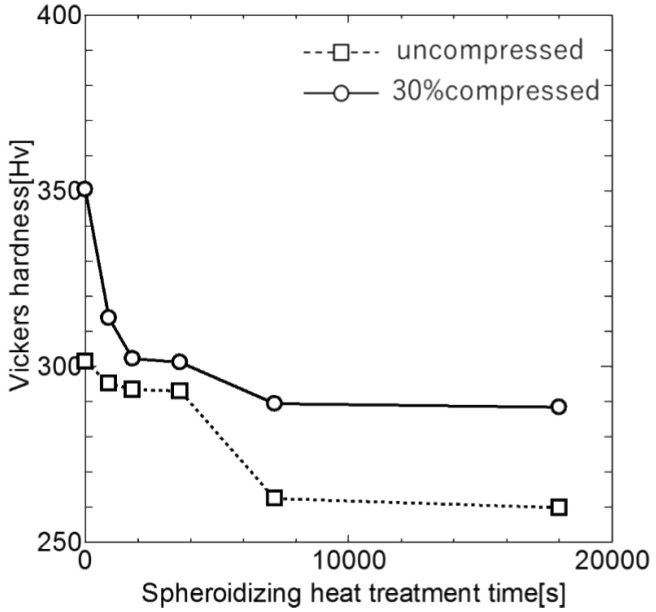

Fig.5 Change of the Vickers hardness by the spheroidizing heat treatment for various holding time.

Figure 5 shows the Vickers hardness of the heat treated samples. The hardness of as-isothermal transformed sample is around 300Hv, while that of the compressed sample exhibits around 50Hv higher. This should be because of the strengthening of dislocation and kinked structures introduced by the compression. The separation of these effects (dislocation strengthening and kink strengthening) was difficult in this study because these were evolved simultaneously during the compression. The hardness decreases with the increase of the holding time, while the hardness of the compressed sample still shows higher hardness even when the shape of cementite changes spherical completely. This means that the deformation of pearlite provides significant effect even after the sample was adequately annealed.

Acknowledgement
This work was supported by the JSPS Scientific Research on Innovative Areas “MFS Materials Science" (21H00109).

References

1) K. Hagihara and K. Higashida, Materia Japan, 54(2015) 60-64.
2) S. Tagashira, K. Sakai, T. Fukuhara, and T. Maki, ISIJ Int. 40(2000) 1149-1155.
3) K. Ishida, M. Okubo, M.Y. Wey and T. Nishizawa, J. Jpn. Soc. Met. 52(1988) 388-394.

Heterogeneous chemistry and size of retained austenite and its thermal stability in austempered Fe-2Mn-1.5Si-0.4C alloy

Miku Watanabe[1,*], Satoshi Morooka[2] , Goro Miyamoto[3] and Tadashi Furuhara[3]

[1] Department of Metallurgy, Tohoku University, Sendai, Miyagi 980-8579, Japan
[2] Materials Sciences Research Center, Japan Atomic Energy Agency, Naka-gun, Ibaraki 319-1195, Japan
[3] Institute for Materials Research, Tohoku University, Sendai, Miyagi 980-8577, Japan
*email: miku.watanabe.q3@dc.tohoku.ac.jp

Keywords: TRIP steel, bainite transformation, austenite, stability, in-situ neutron diffraction

1. Introduction

Transformation Induced Plasticity (TRIP) caused by the retained austenite (γ) is widely used to achieve high strength and good formability in low-alloyed TRIP steel for automotive applications. In TRIP steel γ is stabilized by carbon enrichment during bainite transformation, then a part of untransformed γ is retained after cooling to room temperature. The stability of γ depends on its grain size and chemistry. Although the presence of heterogeneity in the grain size and chemistry of retained γ is recognized even in the same specimen and is supposed to influence mechanical properties of TRIP steels, systematic investigations on them are scarce. Therefore, in this study, we systematically investigate the influence of carbon concentration distribution and grain-size inhomogeneity on the thermal stability of retained γ in Fe-2Mn-1.5Si-0.4C (mass%) TRIP steel by means of FE-EPMA, EBSD, as well as in-situ neutron diffraction during bainite transformation.

2. Experimental procedure

Fe-2Mn-1.5Si-0.4C (mass%) alloy was austenitized at 830 °C for 10 min, followed by austempering at 400 °C for various periods of time and subsequently quenched to room temperature. Phase identification was made by EBSD and XRD. The morphology of untransformed γ was characterized by SEM and EBSD and carbon distribution was investigated by FE-EPMA, Nano-SIMS and 3DAP. The same heat-treatment conditions were employed in in-situ neutron diffraction measurements using BL19 (TAKUMI) at J-PARC in order to measure the lattice spacing of crystals as well as the temperature- and time-dependent changes in crystal structure of TRIP steels.

3. Results and Discussion

The variation in phase fractions as a function of the isothermal holding time (a) along with the SEM micrographs of the specimens transformed for different holding time (b-d) are shown in Fig. 1. In the early stage of bainite transformation, bainite ferrite (BF) formed without carbide precipitation (Fig. 1(b)). The transformation continued till the amount of BF reaches about 75% where the amount of retained γ becomes the maximum. At longer holding time, the untransformed γ decomposed gradually through the precipitation of carbides, leading to the reduction in the amount of retained γ as seen in Figs. 1(c) and (d).

Fig. 2 shows the neutron diffraction profiles and their magnified profiles containing 111_{γ} and 001_{α} peaks during austempering at 400 °C for different holding time up to 7200 s. With the holding time, the intensities of bcc ferrite (α) peaks increase, in contrast to the decrease in the fcc γ peak intensities. The peaks obtained for 90s and 300s holding can be fitted with two distinct γ phases with small and large lattice constants as represented by blue and red curves. These two γ phases will be referred as low-C γ and high-C γ, respectively, hereafter. The intensity of the low-C γ peak decreases with time, while the intensity of the high-C γ increases up to 1800 s holding. Furthermore, the peak width of high-C γ is wider than that of low-C γ, implying that there is a wider distribution of C content and/or grain size in high-C γ than in low-C γ. Those results suggest evolution of inhomogeneity of C content in γ during bainite transformation. In the late stage of transformation (7200 s), high carbon γ decompose gradually together with the reduction in its lattice parameter, as also indicated in the SEM observation.

The carbon concentration and morphology of the untransformed γ after the 1800 s holding are evaluated. Fig. 3(a) and (b) show the SEM image and corresponding C map measured by FE-EPMA, respectively. C concentration profiles along the arrow and dashed arrow (d), respectively. In this sample, most of the γ has a blocky morphology. The blue and light regions in C map correspond to BF and carbon-enriched γ respectively. In coarse blocky-γ, C enriches in its rims while the C content in its center regions is close to that in the nominal composition. On the other hand, C is enriched uniformly about 1.3 mass% in fine blocky-γ (Fig. 3(d)).

In the poster presentation, effects of grain size and C content on individual γ stability will be discussed from a view point of Ms temperature.

Acknowledgement

This work was performed under the support of JST SPRING (JPMJSP2114).

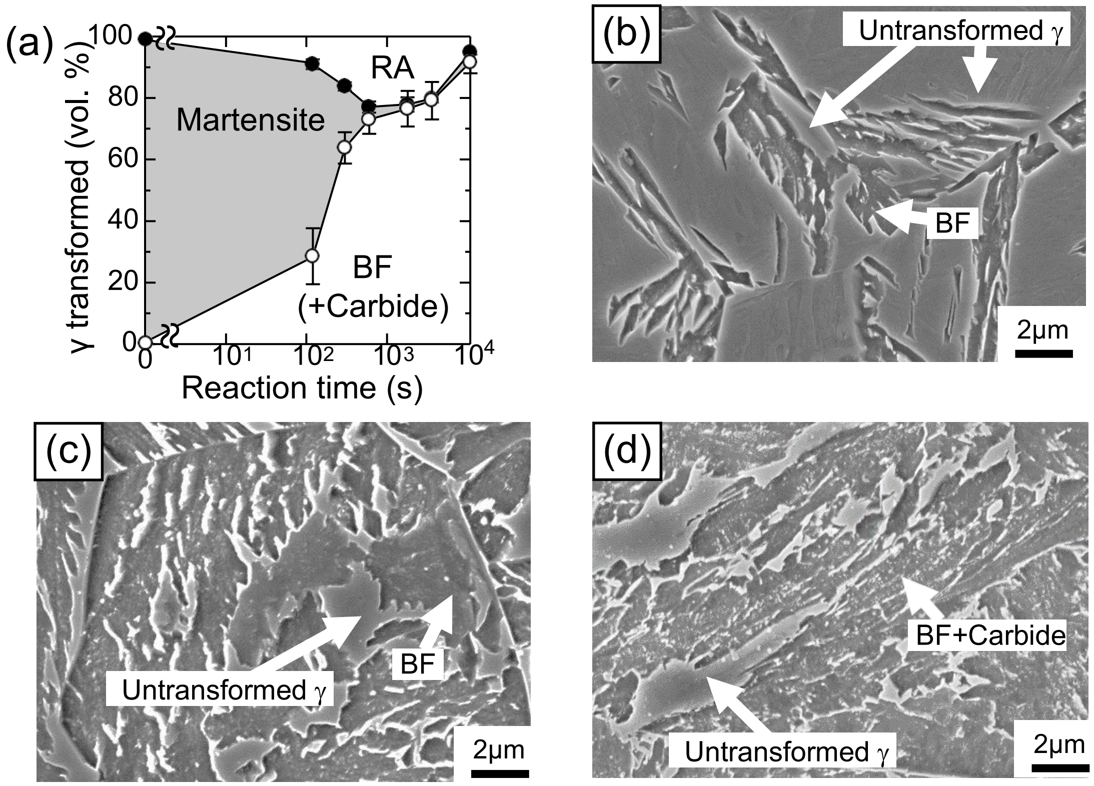

Fig. 1(a) Transformation kinetics and SEM images((b)120s，(c)1800s，(d)10800s) at holding temperature of 400°C

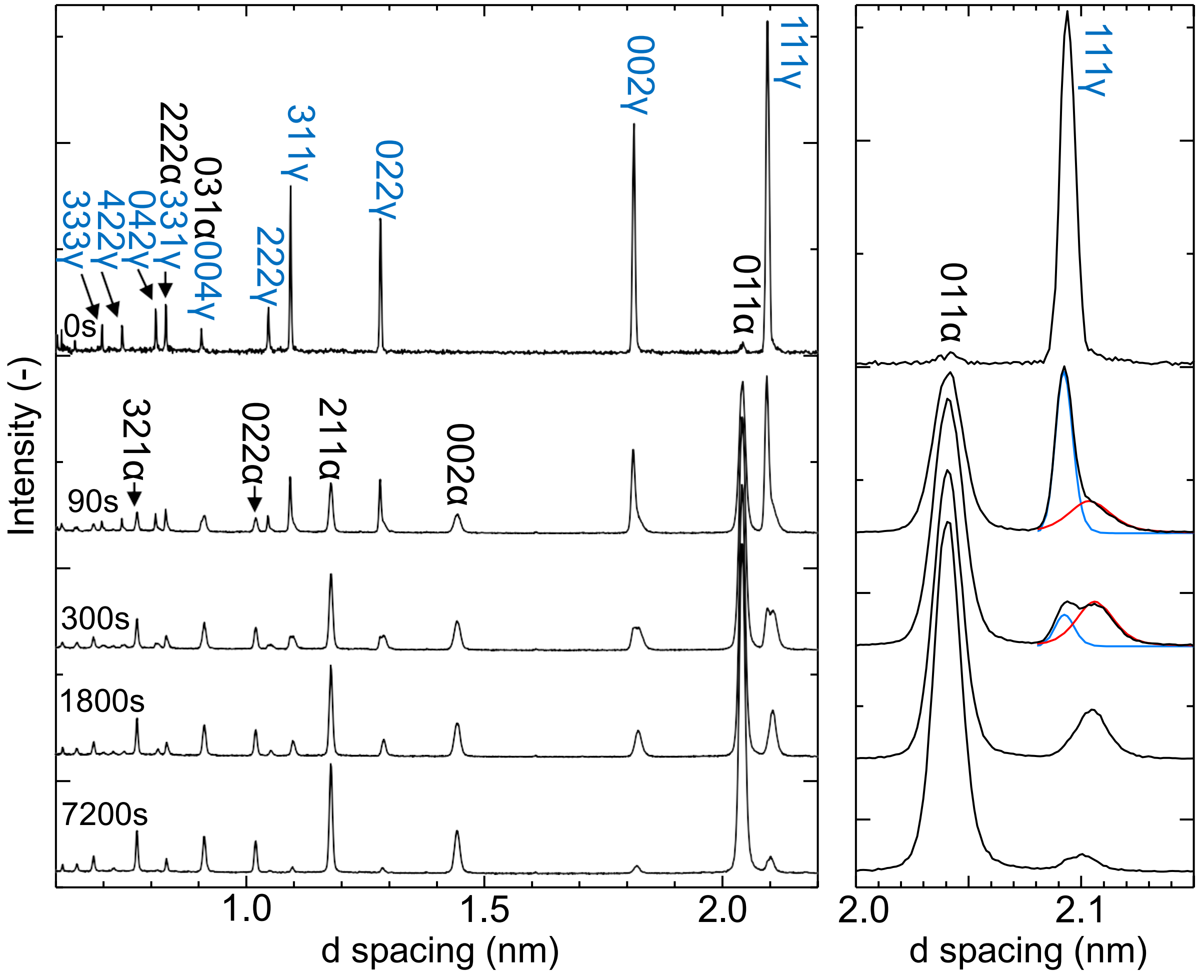

Fig. 2 Neutron diffraction profiles at 400°C and its magnified profiles (red and blue curves are results of peak fitting).

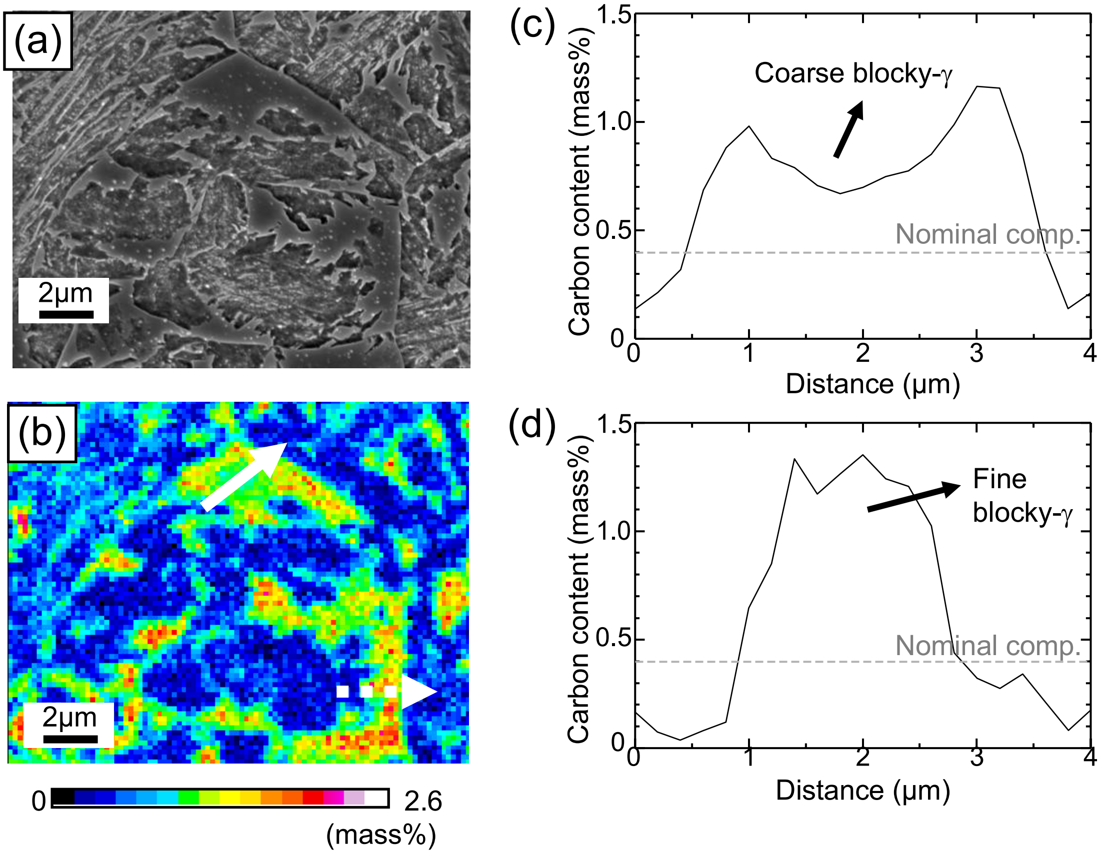

Fig. 3 (a) SEM image at 400°C for 1800s, (b) C map corresponding to (a)and Carbon concentration profiles along (c) white solid line and (d) white dashed line.

Axial tensile load fatigue testing of SCM435 steel for bolts

Chang Jiang, Zi-bo Wang, Heng-chang Lu, Xi-cheng Wei, Han Dong*
School of Materials and Science Engineering, Shanghai University, Shanghai, 200444, China
*Corresponding author: Prof. Han Dong: 13910077790@163.com

Keywords: high strength bolt steel; quenching and tempering treatment; axial tensile load fatigue; fracture analysis; banded tissue

Abstract: Axial tensile load fatigue properties of SCM435 steel were investigated in the range of 10^6 cycles by high frequency fatigue tester. The fracture morphology was analyzed by 3D macro imager and scanning electron microscope. The results show that the fatigue life decreases with the increase of stress amplitude. The fatigue strength limit of the steel is 425 MPa evaluated by the staircase method for 50 % probability of survival. Three typical fatigue fracture morphologies in the steel were observed by 3D macro imager: fatigue source region, crack propagation region and transient fracture region. The fatigue fracture morphology shows that the fatigue core originates from the surface, where only one fatigue source area existed and no obvious defects inside were observed in fatigue fracture. In addition, the crack initiation of non-metallic inclusions is excluded. Comparing the fatigue cycle times of SCM435 steel under the same stress amplitude, it is found that the cycle stress cycle difference of fatigue samples under the same stress amplitude reaches an order of magnitude. The microstructure of the fractured samples shows that the stress cycle of the fatigue sample with serious banded segregation is low, and the propagation of the secondary crack is also affected by the microstructure segregation.

Introduction

Fastener is an important part of steel products. As a connecting part, its quality is directly related to the overall safety performance [1]. The use of fasteners is affected by the mechanical performance requirements of host materials and service environment. Therefore, fastener materials have the characteristics of standardization 、 diversification and matching. SCM435 is a typical medium carbon alloy cold heading steel with high content of Cr 、 Mo and other alloy elements, so it has high hardenability. The quenched and tempered SCM435 steel has good fatigue strength and impact resistance, and good low-temperature toughness [2-3].

High-end products depend on imports, low-end products overcapacity is the development status of the domestic fastener market, especially the high-strength bolts above grade 10.9, 90 % of the sources imported. [4-5]. The fatigue performance of SCM435 steel used for domestic fasteners is unstable, which is far from that of imported fasteners. The literature shows that hydrogen embrittlement and fatigue are the two most common failure forms of high-strength fasteners. Among them, the fatigue failure stress of fasteners is often far lower than its strength limit under static load. It belongs to brittle fracture, and the fracture symptom is not obvious. It is the most harmful failure form of fastening [6].This paper mainly studies the fatigue properties of SCM435 steel and analyzes the factors affecting the instability of fatigue properties.

Experimental materials and methods

The material selected for the test is grade 10.9 high strength bolt steel (SCM435). The test steel adopts the bar with the diameter of 9.8 mm, the raw material is annealed.

The annealed SCM435 was tempered in a vacuum furnace, firstly, the steel was heated to 860 °Cand completely austenitized for 40 min, then oil quenched to room temperature. After quenching, the specimens were tempered at 530 °C and finally air cooled to room temperature. Tensile test was conducted according to the standard GB/T 228.1-2010 " Tensile test of metal materials ". The specimens were carried out on MTS C45.305 high and low temperature tensile testing machine with a tensile speed of 0.5 mm/min.The axial load tensile fatigue test is conducted according to GB/T 3075-2008 " Metal Materials Fatigue Test Axial Force Control Method " and GB/T13682-1992 " Threaded Fastener Axial Load Fatigue Specimen Method Standard ". The test is conducted in QBG-50 high frequency testing machine. The test conditions are room temperature, loading frequency f is 120 Hz, and the maximum number of cycles N is taken as 5 × 10^6 times or fracture. The fatigue test is carried out continuously under a constant average stress σm until the specimen fails or exceeds the specified number of stress cycles.

Experimental results and analysis

The microstructure of SCM435 after quenching and tempering treatment is shown in Figure 1. It is mainly tempered sorbite with grain size of 10-15 µm. After quenching and tempering treatment, the tensile strength of SCM435 reaches 1174 MPa, the yield strength reaches 1071 MPa, the reduction of area reaches 54 %, and the shrinkage after fracture reaches 13 %, all of which meet the mechanical properties requirements of 35CrMo steel after heat treatment in the national standard GB/T 6478-2015.

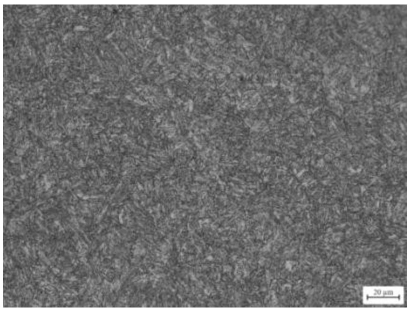

Fig. 1 Microstructure of quenched and tempered SCM435 steel

The fatigue S-N curve of SCM435 steel is shown in Figure 2. Hollow circles represent specimens with 5×10^6 cycles without fracture, solid circles represent specimens with less than 10^6 cycles and fracture. The median fatigue limit of SCM435 steel is 425 MPa and the ratio of median fatigue limit to tensile strength is obtained by calculating the average of fracture and stress amplitude of samples σ_{-1}/R_m = 0.36. In addition, in the range of 10^6 cycles, the S-N curve of SCM435 steel shows that the cycles of fatigue stress cycle decrease with the increase of fatigue cycle stress amplitude.

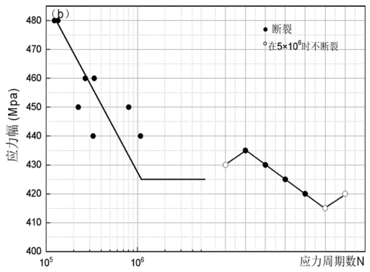

Fig. 2 S-N fatigue curve of SCM435 steel

Figure 3 shows the morphology of the fatigue source area of the fatigue fracture. It can be seen that there is only one fatigue source in the fatigue fracture of SCM435 steel, no non-metallic inclusions are found in the source area, and there are mainly small forward protruding arc fatigue striations on the fracture.

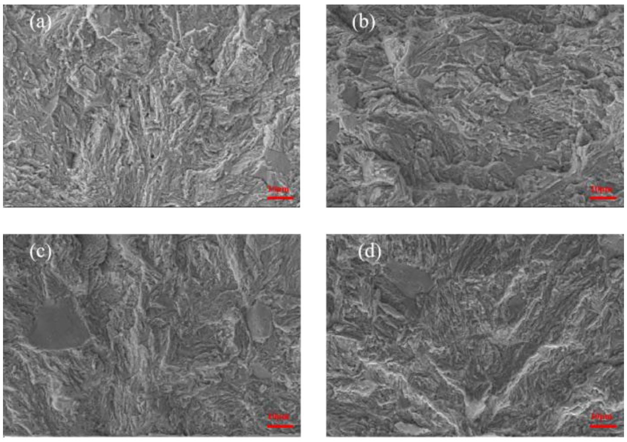

Fig. 3 Morphology of fatigue fracture source area

The inhomogeneity of the organization, such as non-metallic inclusions, sparseness, segregation and other defects, all make the fatigue resistance of metal components reduced and become an important factor of fatigue fracture[7]. In this paper, fracture analysis of fatigue fractures did not find inclusions fatigue source. The microstructure observation of the fatigue samples under the same stress amplitude is shown in Figure 4. By observing the microstructure of fatigue samples under the same stress amplitude, it is found that there is a certain relationship between the fatigue life of SCM435 steel and banded structure segregation, and there is an order of magnitude difference in the fatigue life of SCM435 steel under the same stress amplitude.

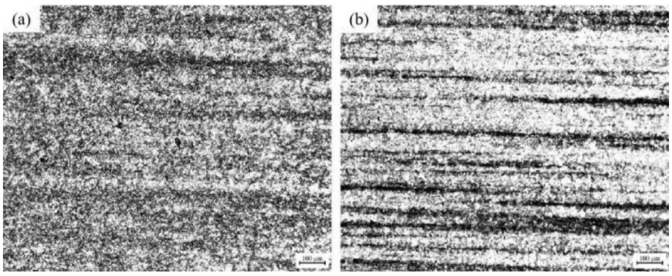

Fig. 4 Axial microstructure of fatigue fracture

Conclusions

(1) After quenching and tempering treatment, the tensile strength of annealed SCM435 steel reaches 1174 MPa, the yield strength reaches 1071 MPa, the area shrinkage reaches 54 %, and the shrinkage after fracture reaches 13 %, meeting the mechanical property requirements of the national standard GB/T 6478-2015.

(2) Constant average stress of quenched and tempered SCM435 steel. The median fatigue limit under the condition of σ_m = 430 MPa, N = 500 million times is 425 MPa, and the ratio of fatigue limit to tensile strength $\sigma_{-1/Rm}$ =0.36.

(3) In the axial tensile fatigue test, the fracture fatigue cracks of SCM435 steel originated from the surface matrix, and no inclusions were found in the sample.

(4) The poor stability of fatigue performance of SCM435 steel is related to banded structure segregation. The serious banded segregation of fatigue fracture under the same stress

amplitude is one order of magnitude.

Acknowledgement

This work is carried out with the support of Shanghai special fund for military civilian integration development (No. 2020-jmrh1-kj31).Thank Nanjing Iron and Steel Group for providing SCM435 raw materials and funding support for this experiment.

References

[1] Dong Han, Lian Xintong, Hu Chundong, et al. High Performance Steels: the Scenario of Theory and Technology[J] Journal of metals, 2020, 56(04):558-582.

[2] Guo Yingang, Jiang Chang, Lu Hengchang, et al. Essential Points of Manufacturing Key Fasteners for Automobile Enginep[J] Shanghai metal, 2020, 42(06):9-14.

[3] Xu Dong,Zheng Bing,Zhu Miaoyong,Zhao Hongyang. Evolution of Dynamically Recrystallized Grains in Steel SCM435[J]. Metallurgist,2015,59(7-8).

[4] Guo Ruohan Research on Fracture Analysis Method of Automobile Bolt Fasteners Fracture Failure[D] Dalian University of technology, 2019.

[5] Hui Weijun, Weng Yuqing, Dong Han Steel for high strength fasteners[M] Beijing: Metallurgical Industry Press, 2009.

[6] Wang Hui, Liu Haibo, Zhu Xianhua, et al Typical failure modes of fasteners[J] Shanghai metal, 2020, 42(06):20-26.

[7] D. Krewerth,T. Lippmann,A. Weidner,H. Biermann. Influence of non-metallic inclusions on fatigue life in the very high cycle fatigue regime[J]. International Journal of Fatigue,2016,84.

Elimination of orientation inheritance in a CrNiMoV steel

Chao Yang
Shanghai University

The hardenability and toughness of CrNiMoV steel large forgings largely depend on the increase of Ni content. However, the increase of Ni content easily leads to an orientation inheritance, which makes the refinement of austenite grains difficult. Herein, the phenomenon of orientation inheritance and its elimination method in a CrNiMoV large steel forging were investigated. The microstructure evolutions of samples hold at 690 °C for times ranging from 24 to 480 h were characterized by Scanning Electron Microscopy (SEM) and Electron Back-Scattered Diffraction (EBSD) techniques. The results show that the sample without holding treatment contains 7% austenite, which mainly distributes between the martensitic laths. When the holding time is increased to 96 h, the austenite is totally decomposed. With further increasing of holding time, the orientation of martensite changes from (101) to (111), which implies a gradual elimination of orientation inheritance.

The effect of □ recrystallization to B segregation and precipitation behavior after hot rolling process

Daiki Terazawa[1,*], Yusuke Shimada[1], Masaaki Fujioka[1], and Manabu Hoshino[1]

[1] Steel Research Laboratories, Nippon Steel Corporation, Futtsu, Chiba 293-8511 Japan
*email: terazawa.xc4.daiki@jp.nipponsteel.com

Keywords: steel, boron, segregation, precipitation, recrystallization,

1. Aim and Scope

Hardenability of steels is significantly increased by small amounts of boron because of the segregation of solute B at the prior austenite (γ) grain boundaries (PAGB). When B precipitates as BN and $Fe_{23}(C, B)_6$, the hardenability enhancement effect of B decreases. Therefore, optimization of the hardenability enhancement effect of B requires an understanding of the B grain segregation behavior and precipitation behavior.

When steels with added B are manufactured using an equilibrium process such as reheating, quenching, and tempering (RQ-T) after hot rolling, the hardenability enhancement effect of B is determined by the thermodynamic equilibrium state at the reheating temperature. In contrast, when steels with added B are manufactured using a non-equilibrium process such as direct quenching and tempering (DQ-T), the grain boundary segregation and precipitation behaviors of B are very different from those in the steel manufactured by RQ-T. The segregation and precipitation behaviors of B after hot rolling have been investigated using the Fission Track Etching (FTE); the results revealed that the PAGB segregation of B changes in a complicated manner because of the progress of γ recrystallization and the B precipitation 1). As the grain boundary segregation of B has a large effect on the hardenability of steel, this change in grain boundary segregation results in large variations in the strength of the steel. Therefore, clarification of the grain boundary segregation behavior of B during □ recrystallization is very important for optimizing the hardenability enhancement effect of B in DQ-T. However, until now, it has only been studied using qualitative methods, such as the FTE method described above.

Recently, the development of measurement techniques such as three-dimensional atom probe method (3DAP) enabled to quantitative measurement of the amount of segregated B at PAGBs. However, to observe and quantify the changes in the amount of segregated B because of the progress of □ recrystallization and B precipitation, it is necessary to measure the distribution of B in wide areas that include several γ grains before the transformation. Such measurements require more global methods than 3DAP.

In this study, we measured the PAGBs and □ recrystallization using electron backscatter diffraction (EBSD); we also measured the distribution of B using time-of-flight secondary ion mass spectrometry (TOF-SIMS) over large areas including several PAGBs to investigate the effect of recrystallization and B precipitation on the change of the segregated B at PAGBs.

2. Materials and Methods

The steels in this study were prepared using vacuum melting. The chemical compositions are shown in Table 1. The B steel had a composition of Fe–0.09 mass% C–1.55 mass% Mn and 10 mass ppm B. In the B steel, 50 mass ppm nitrogen was added so that BN would precipitate during hot rolling. The steels were cast into 100 kg ingots, heated at 1100 °C for 6000 s, hot rolled to a thickness of 50 mm, and water-quenched to room temperature.

Cylindrical specimens of 8 mm in diameter and 12 mm in height were taken from 1/4 thickness of the steel plate. Specimens were reheated at 1100 °C for 600 s, cooled to 850 °C at 5 °C/s, and depressed to 6.6 mm in height by one pass at a 5 /s strain velocity. After that, the specimens were held at 850 °C for 10 to 100 s and subsequently water-quenched to room temperature as shown in Fig. 1. After these thermo-mechanical treatments, we investigated the γ recrystallization state before quenching as well as the segregation and precipitation behaviors of B using EBSD and TOF-SIMS of the water-quenched specimens, respectively.

The □ recrystallization state was determined from EBSD measurements of the 300×300 □m square area around the point with a width of 1/4 and a height of 1/2 of the specimens. From the EBSD results, the crystal orientation of prior γ before the transformation was reconstructed using the automatic variant analysis program for bainite and martensite microstructures. In this analysis, the boundaries between pixels with an angular difference of 10° or more were considered PAGBs. To distinguish between recrystallized and non-recrystallized PAGs based on the differences in the strain within the PAG, grain orientation spread (GOS) analysis was performed, as shown in Fig. 2. Usually, the strain in the recrystallized grains and GOS of almost all recrystallized grains is less than 1° [2]. Therefore, the threshold of GOS analysis for recrystallization is usually set to 1°. However, in this study, grains with 6° or more GOS were defined as non-recrystallized grains because when the automatic variant analysis program reconstructs PAGs, it takes into account the deviation from the K–S relation caused by the strain induced by martensitic transformation. Therefore, the reconstructed PAGs could contain orientation differences within 5°, regardless of the actual state of PAGs. Considering the above, the threshold of GOS was set to 6° which is 1° + 5°.

Next, TOF-SIMS was performed in the same field of view as EBSD to analyze B. TOF-SIMS (TOF-SIMS5, ION-TOF GmbH, Germany) was performed, using Bi^+ as the primary ion and BO_2^- (mass-to-charge ratio $m/z = 43$) as the secondary ion. The contaminating layer on the specimen surface was removed via Cs ion beam sputtering before the measurement. The 300×300 □m square area was measured using TOF-SIMS with 2048×2048 pixels, and the obtained map data was binned to 256×256 pixels.

The "IPF (BCC)" image in Fig. 3 is the inverse polar figure of the microstructure after transformation obtained by EBSD. The "IPF(FCC)" image is an inverse polar figure of the reconstructed PAGs. The TOF-SIMS image is the BO_2^- ion map, and the brightness of the image represents the amount of B, while high-intensity lines represent segregated B. The positions of the PAGBs in the IPF(FCC) image and segregated B in the BO_2^- ion map are in good agreement, indicating the presence of solute B on the PAGBs. In addition, other grain-like points with high intensity observed on the BO_2^- ion map are considered to be BN, based on their shape and high signal intensity. In the following analysis, we assume that the signal on the high-intensity line on the PAGBs corresponds to segregated B, and the granular high-intensity signal corresponds to BN precipitation.

Table 1. Chemical composition of test steels.

	Fe	C	Si	Mn	S	Ti	B	N
B	Bal.	0.090	0.050	1.55	0.0005	0.008	0.0010	0.0050

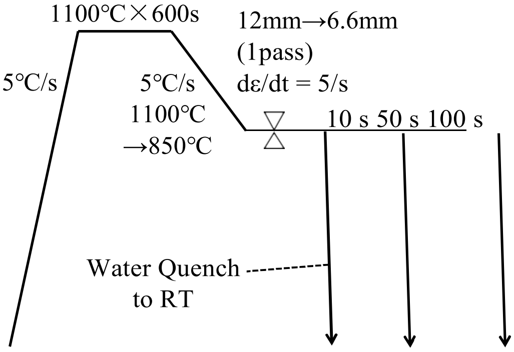

Fig. 1. Heat and press patterns of the specimens.

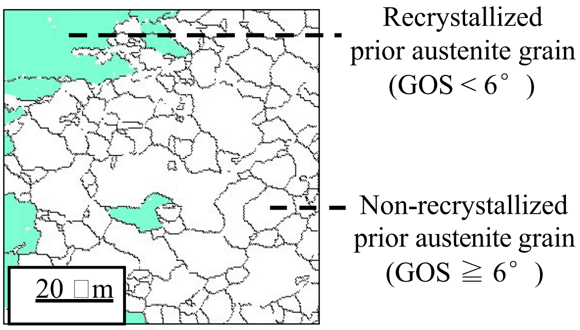

Fig. 2. EBSD GOS image map with EBSD 10° boundaries. Green hatched regions represent non-recrystallized PAGs.

3. Results and discussions

3. 1 □ recrystallization

The □ recrystallization rate was measured using GOS analysis. In this study, we defined the □ recrystallization rate as the area rate of recrystallized PAG containing less than 6° GOS. Initially, the □ recrystallization rate was 29% at 10 s after deformation. However, it increased with holding time and was 67% at 50 s after deformation. At 100 s after deformation, the recrystallization rate reached approximately 90%. As recrystallized and non-recrystallized PAGs are mixed in these specimens, especially in the specimens held for 10 or 50 s after deformation, we could extract and compare the BO_2 signal intensity from recrystallized PAGBs and that from non-recrystallized PAGBs in the same specimen using TOF-SIMS.

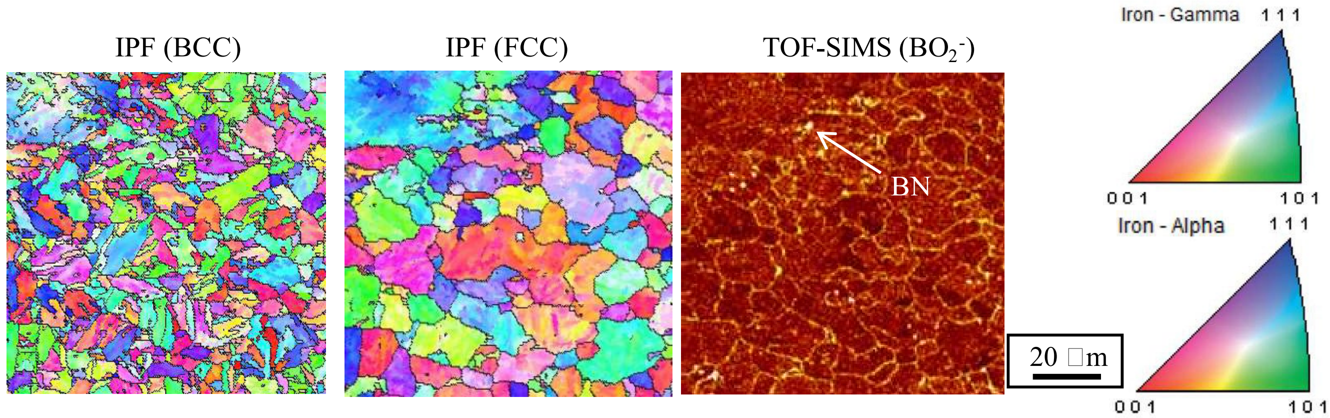

Fig. 3. EBSD (IPF: BCC, FCC) image maps and TOF-SIMS BO_2^- ion map.
IPF (FCC) map was reconstructed from IPF (BCC) map data. TOF-SIMS BO_2^- ion maps measured at the same region.

3.2 B segregation and BN precipitation

Fig. 4 shows the BO_2^- ion maps of the non-recrystallized and recrystallized grain boundaries of the specimen held for 10 s. As shown in Fig. 4, the BO_2^- signal intensity of the non-recrystallized grain boundary was lower than that of the recrystallized grain boundary. To clarify this difference quantitatively, five recrystallized and five non-recrystallized grains were selected from each specimen held for 10, 50, or 100 s. The average BO_2^- signal intensity on each PAGB was taken as the representative signal intensity of the PAGB. Fig. 5 shows the dependence of the BO_2^- signal intensity on holding time for the recrystallized and non-recrystallized PAGBs. For comparison, the average grain boundary signal intensity of the specimen, which was held at 850 °C for 10, 50, or 100 s without deformation and then water-quenched to room temperature, is shown as a black dashed line. It was confirmed that almost no B precipitated in the specimen that was water-quenched after 10 s of holding without deformation. Therefore, the amount of B at the PAGB of the specimen water-quenched after 10 s of holding without deformation was considered t the thermal equilibrium amount of B at the PAGB at 850 °C and 10 ppm B content.

After deformation, the signal intensity on the recrystallized PAGBs was about the same as that of the specimen without deformation and decreased with holding time since 50 s. In contrast, the signal intensity on the non-recrystallized PAGBs was lower than that on the recrystallized grain boundary for both 10 and 50 s after deformation. However, the SIMS signal intensity on the non-recrystallized grain boundary at 100 s after deformation could not be obtained because the recrystallization of the specimen was almost 100% complete at 100 s after deformation. These results suggest that the amount of B segregation in the recrystallized PAGB was almost the same as the amount of thermal equilibrium segregation at 850 °C, and the amount of B segregation in non-recrystallized PAGB was lower than that in the recrystallized PAGB and thermal equilibrium B segregation.

Fig. 6 shows the results of counting the number of BN precipitates in a 300×300 □m area for each recrystallization state, which is distinguished by EBSD GOS map and SIMS BO_2^- ion map. The number of BN precipitates increases with holding time. In addition, at all holding times, the majority of the precipitates were located in recrystallized PAGBs or within recrystallized PAGs. Considering the fact that recrystallized PAGBs move, this result suggests that some of the precipitates located within the recrystallized PAGs nucleated on the moving recrystallized PAGBs and left to the inside of the PAGs. As shown in Fig. 5, the amount of segregated B at PAGBs is higher in recrystallized PAGBs than in non-recrystallized PAGBs. Therefore, BN is expected to preferentially nucleate from the recrystallized grain boundary, reflecting the difference in nucleation driving force because of the differences in the B concentration at PAGBs.

4. Conclusion

The PAGB segregation behavior of B and BN precipitation behavior with □ recrystallization were investigated using TOF-SIMS and EBSD, and the following conclusions were obtained.

(1) BO_2^- ion signal intensity at recrystallized PAGBs was higher than that at non-recrystallized PAGBs, and was almost the same as that at PAGB without deformation. These results suggest that the B concentration in non-recrystallized PAGBs is lower than that at recrystallized PAGBs and at PAGBs without deformation.

(2) Most BN precipitates were located at recrystallized PAGBs or within recrystallized PAGs.

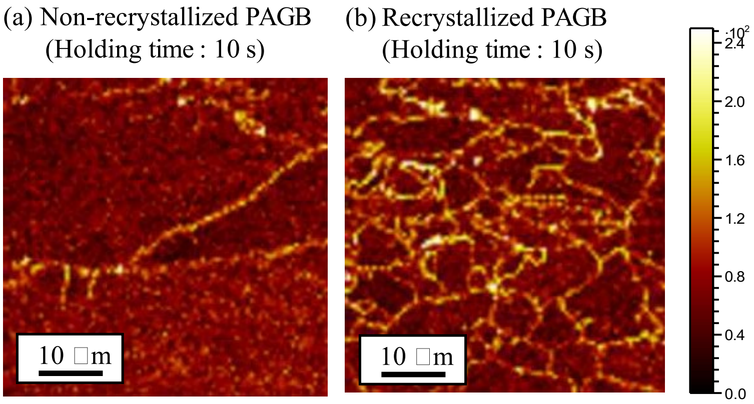

Fig. 4. TOF-SIMS BO$_2^-$ ion map in B steel held for 10 s at 850℃

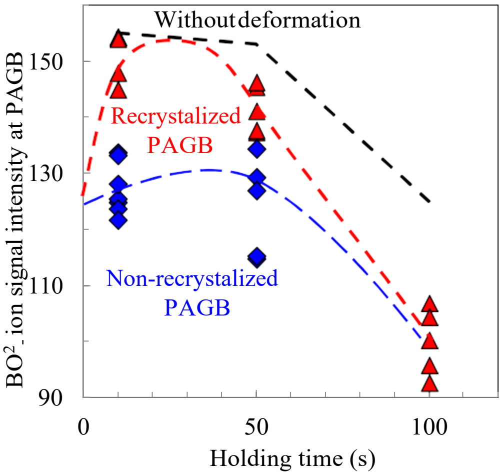

Fig. 5. Holding time dependence of BO$_2^-$ ion signal intensity at PAGBs in B steels.

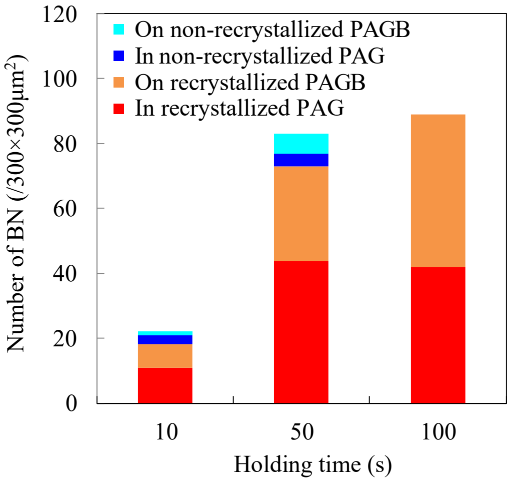

Fig. 6. Effect of holding time dependence on the number of BN precipitates.

References

1) . M Imanaka, H Terashima, C, Siga and T. Tanaka: Tetsu-to-Hagane 74 (1988) 167-174.
2) W. Polkowski, Pawel Jozwik, Zbigniew Bojar: J. Alloys Compd 624 (2014) 226-233.

Characteristics of retained austenite formed by friction stir welding of ultrahigh carbon steels

Koyo Ohga
Steel Research Laboratories,R&D Laboratories,Nippon Steel

Microalloyed ultrahigh carbon steels have a structure in which cementite is dispersed in a ferrite matrix. These steels are expected to be used structurally owing to their excellent strength–ductility balance and moderate wear resistance; however, difficulties in fusion welding have been cited as a problem. Conversely, in recent years, improved junction characteristics by friction stir welding (FSW) of ultrahigh carbon steels are required because they can be joined through FSW without melting. In general, when FSW is applied to an ultrahigh carbon steel under conditions that exceed the A1 point, martensitic structure and retained austenite are formed in the stirred zone. Here, appropriate control of the retained austenite is considered to improve joint characteristics because the retained austenite exhibits an excellent strength–ductile balance owing to the TRIP effect. Therefore, we investigated the characteristics of the retained austenite formed by FSW and attempted to explore a method to control it. Under conditions that exceeded the A1 point, FSW was performed for a material where Cr were enriched to cementite through appropriate heat treatment. Martensite and proeutectoid cementite were observed in the stirred zone. Meanwhile, the amount of undissolved cementite increased from the stirred zone to the mechanical heat-affected zone. The dispersed state of the retained austenite was investigated, and the results showed that the retained austenite was uniformly present at the center of the stirred part. However, it was also present around the region where undissolved cementite was observed. In addition, Cr-enriched regions were formed around the undissolved cementite. These results suggest that cementite enriched with Cr is partially dissolved owing to the temperature rise in FSW, Cr-enriched regions that are swept out of cementite are formed, and then, the untransformed austenite with enriched Cr is chemically stabilized in the cooling process and preferentially becomes retained austenite.

Martensitic transformation induced by electro-chemical polishing in metastable austenitic stainless steel

Hojun Gwon
Graduate Institute of Ferrous Technology, Pohang University of Science and Technology

A severe martensitic transformation in 16Cr-5Ni metastable austenitic stainless steel was observed solely by electro-chemical polishing (EP). The specimen treated by EP was sealed in a quartz tube to protect the surface from oxidation during annealing, then annealed at 1100 °C to form a single austenite phase, and again subjected to EP without additional treatment on the annealed surface. As the duration of the EP on the annealed specimen increased, the fraction of martensite also increased, and 72.2% of martensite was measured in EBSD analysis after electro-polishing for 160 s at 20 V. However, Ferritescope measurements showed that the martensite fraction of the whole specimen was < 1%; comparison of these results suggests that the martensite transformation by EP was limited to the surface. To find the mechanism of martensitic transformation during the EP treatment, COMSOL multi-physics simulation was used to calculate current density distribution and interface movement on the steel surface subjected to the EP treatment. The results of simulation successfully described the trigger of martensitic transformation due to the localized high current density at inevitable pores on the steel surface. Therefore, the results of this study show that a considerable attention is needed when quantitatively analyze the martensitic transformation of metastable austenite by EBSD or XRD after EP.

Fracture toughness prediction model for TiN-ferrite steels

Yosuke Nonaka[1,*], Tetsuya Namegawa[1], Manabu Hoshino[1] and Masaaki Fujioka[1]

[1] Steel Research Laboratories, Nippon Steel Corporation, Futtsu, Chiba 293-8511, Japan
*email: nonaka.hb6.yohsuke@jp.nipponsteel.com

Keywords: steel, toughness, cleavage fracture, inclusion, TiN, prediction model

Introduction

Increasing the strength of steel improves the design freedom of steel structures and imparts high value to our society. However, an increase in strength might reduce the toughness. This deterioration in the toughness, which could lead to the large-scale failure of steel structures, must be prevented. To develop steel materials with high strength and toughness, the relationships between the brittle fracture phenomenon and microstructures need to be understood. Particularly, various hard second-phase particles in steel, i.e. carbides and inclusions, play an important role in the cleavage fracture phenomenon as a crack initiation site.

This presentation shows a fracture toughness prediction model for TiN-ferrite steels based on microscopic fracture processes. The modeling approach proposed by Shibanuma *et al.*,[1–3)] was adopted to build the model. The model incorporates (1) microstructure information (distribution of ferrite grains and TiN particle sizes), (2) stress distribution of the toughness-testing specimen calculated by using the finite element method (FEM), and (3) fracture criteria based on microscopic cleavage fracture during crack initiation and propagation. Figure 1 shows the microscopic fracture process in this model involves the following three stages: (Stage I) crack initiation at TiN particles inside the ferrite grains; (Stage II) crack propagation into the surrounding ferrite matrix; and (Stage III) crack propagation across grain boundary. Stage I is described as a stochastic process, i.e., the cracking probability of TiN particles is approximately formulated based on experimental observations. Petch's model and Griffith's model were adopted to formulate the local fracture stress for Stages II and III, respectively.

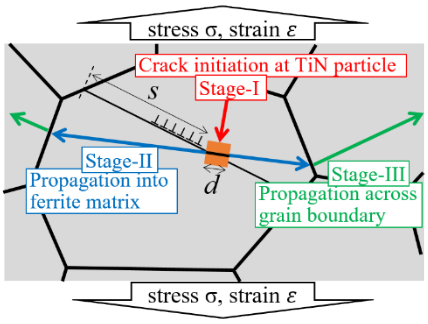

Fig. 1. Microscopic process of cleavage fracture initiation.

Preparation and basic properties of the test steels[4)]

The chemical compositions of the test steels are listed in Table 1. To change the size and number density of TiN particle, the concentration of Ti was varied as 0.03, and 0.09 mass%, and the amount of N was the stoichiometric ratio (Ti/N mass ratio of 3.4). We prepared 50 kg steel ingots with the above compositions by vacuum melting, and prepared test steels by the processes summarized in Table 2. Since the pinning effect of precipitated TiN particles varies depending on the amounts of Ti and N, we changed the heating temperature of normalizing to obtain generally the same ferrite grain size.

Table 1. Chemical compositions (mass%, *:mass ppm).

Steel	C	Si	Mn	P*	S*	Al	Ti	N*	O*
T3	0.049	0.010	1.03	<20	5	0.039	0.030	97	16
T9	0.049	0.013	1.03	<20	4	0.056	0.086	255	<10

For the test steels, we observed optical-microscope images of the mirror-polished and nital-etched test steels, performed electron backscatter diffraction (EBSD) measurements, and conducted round bar tensile and Charpy impact tests. Figure 2 shows the microstructure information obtained by the microscope observations and EBSD measurements. The parent phase of all the test steels was ferrite and pearlite. In the test steels with high Ti and N contents, we confirmed the presence of coarse TiN particles, as shown in the microstructures of the T3 and T9 steels (red arrows in the top images of Fig. 2). The equivalent circle-diameter distribution of the ferrite grains and TiN particles are shown in the middle and bottom panels, respectively. These distributions show that the test steels have almost the same ferrite-grain size and different TiN-particle size. The results of tensile and Charpy impact tests are summarized in Table 3, showing that the test steels have almost the same mechanical properties except for the toughness. From the above-mentioned characterizations, we confirmed that the difference in toughness of the test steels originates only from the TiN particles.

Table 2. Heat treatment conditions.

Steel	Hot Rolling	Normalizing		
		Heating	Holding	Cooling
T3	1250 ºC	1100 ºC	15 min.	Air
T9		1200 ºC		

Table 3. Mechanical properties.

Steel	YS (MPa)	TS (MPa)	EL (%)	vTrs (ºC)
T3	201	328	48.5	0
T9	200	338	48.6	20

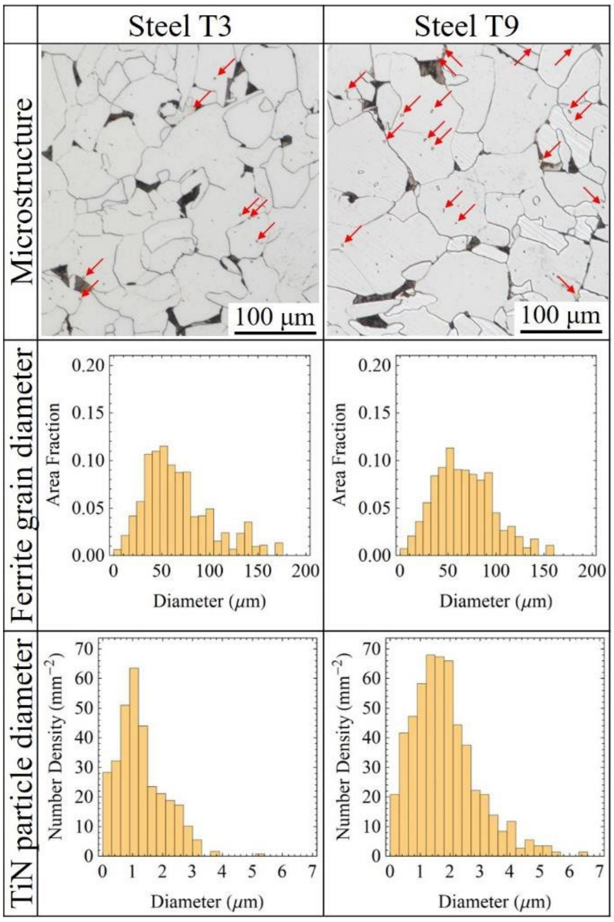

Fig. 2. Microstructures of the test steels.

Quantification of TiN crack probability[4]

To modelize the crack initiation from TiN particles (Stage I), it is necessary to clarify how the TiN particle cracks depending on macroscopic stress, strain, and particle size. Shibanuma *et al.* reported quantification of the crack probability of cementite[3,5,6]. To quantitatively observe the crack of TiN particles, we employed a similar method with some new features[4] (shown in Fig. 3): i) interrupted tensile test with notched round bar, ii) calculation of applied stress and strain by FEM, iii) observation of the TiN particles in the test specimen. Although only the average crack ratio was measured in the step iii) of previous method[3,5,6], we

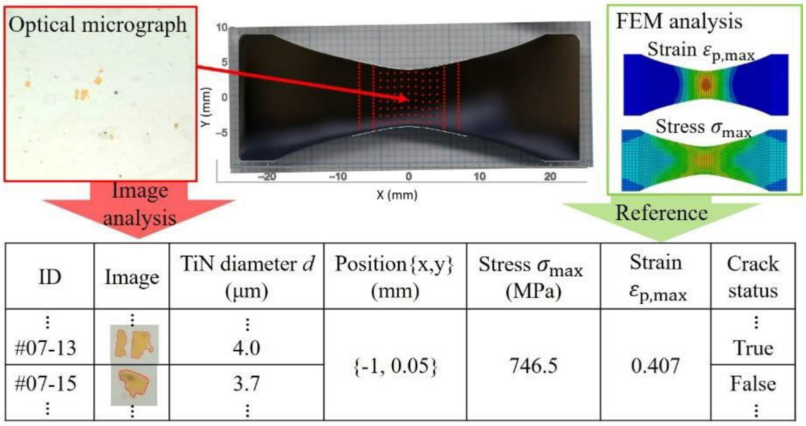

ID	Image	TiN diameter d (μm)	Position{x,y} (mm)	Stress σ_{max} (MPa)	Strain $\varepsilon_{p,max}$	Crack status
⋮	⋮	⋮				⋮
#07-13		4.0	{-1, 0.05}	746.5	0.407	True
#07-15		3.7				False
⋮	⋮	⋮				⋮

Fig. 3. Quantative observations of cracked TiN particles.

observed individual TiN particles and recorded their diameter, crack status, position, and the calculated stress and strain therein. These individual data allow us to statistically analyze how the recorded values affect crack probability.

Figure 4 shows the result of the statistical analysis (details were reported elsewhere[4)] and will be presented in poster). We experimentally formulated the TiN crack probability as follows:

$$p = 6.23 \times 10^{-5} \times \varepsilon_{p,\max}\sigma_{\max}d^2 + 2.12 \times 10^{-2}$$

where p, $\varepsilon_{p,\max}$, $\sigma_{\max}$, and d represent the crack probability, the maximum principal plastic strain, the maximum principal stress (MPa), and the equivalent circle diameter of TiN particle (μm), respectively.

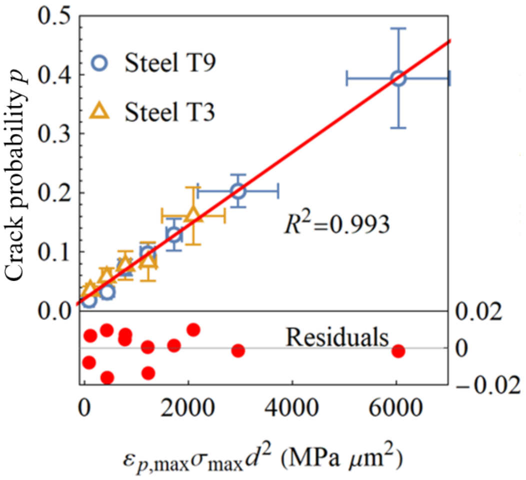

Fig. 4. Statistically analyzed crack probability of TiN particle

Evaluation of effective surface energy between TiN particle and ferrite matrix

To formulate the crack propagation phenomenon from a TiN particle to surrounding ferrite matrix (Stage II), Petch's model[7)] are adopted by substituting the TiN-particle size for the cementite thickness. According to Petch's model, fracture stress $\sigma_{FTiN\alpha}$ is expressed as

$$\sigma_{FTiN\alpha} = \sqrt{\frac{4E\gamma_{TiN\alpha}}{\pi(1-\nu^2)d} - \frac{{k_y}^2 s}{8\pi^2 d^2}} - \frac{k_y\sqrt{s}}{2\sqrt{2}\pi d},$$

where ν, k_y, E, s, and $\gamma_{TiN\alpha}$ represent the Poisson's ratio, the locking parameter in the Hall-Petch relationship, Young's modulus, length of slip plane (see Fig. 1), and effective surface energy when a crack propagate from TiN particle into ferrite, respectively. Note that this equation was simplified by ignoring the case for much smaller TiN particles. By solving this equation about $\gamma_{TiN\alpha}$, we obtain following relationship:

$$\gamma_{TiN\alpha} = \frac{\pi(1-\nu^2)d}{4E}\left(\frac{{k_y}^2 s}{8\pi^2 d^2} + \left(\sigma_{FTiN\alpha} + \frac{k_y\sqrt{s}}{2\sqrt{2}\pi d}\right)^2\right).$$

As shown in Fig.5, we estimated s, d, and $\sigma_{FTiN\alpha}$ from fractography and FEM analysis of 9 fractured specimens. By substituting these estimated values in the above equation, we obtained experimental values of $\gamma_{TiN\alpha}$ scattered around 70 J/m^2 as shown in Fig. 6.

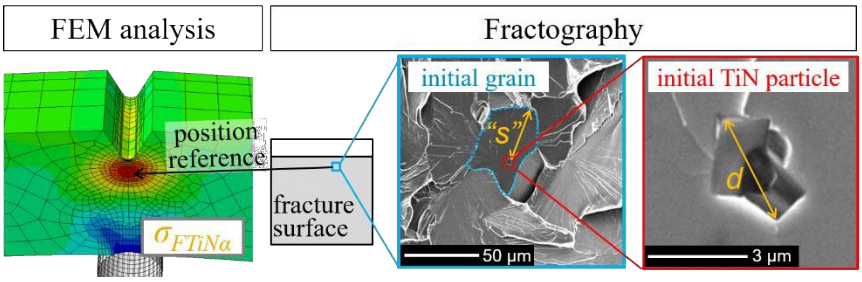

Fig. 5. Estimation and measurement of the variables.

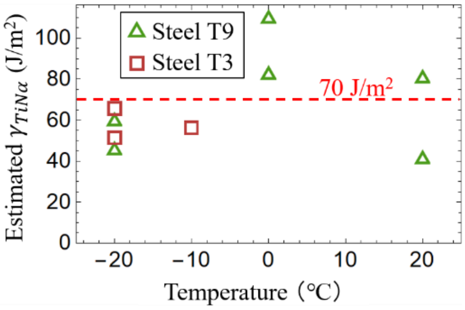

Fig. 6. Estimated $\gamma_{TiN\alpha}$

Model calculation of Charpy impact test

So far, the stage I and II of the toughness prediction model were quantitatively formulated. Since the stage III (crack propagation across ferrite grain boundary) is the same as that of previous report on cementite-ferrite steel, we can build the model of TiN-ferrite steels based on the microscopic process shown in Fig. 1. Details of numerical methods to calculate toughness is almost the same as previous reports[1–3] (will be presented in poster). Note that $\gamma_{TiN\alpha}$ was assumed to be 70 J/m^2 (mean of the scattered experimental vales).

Figure 7 shows the comparison between experimental and calculated absorbed energy of Charpy impact test. This comparison shows that prediction model reproduce the experimental results.

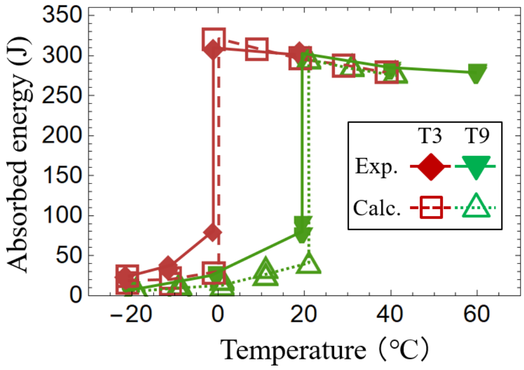

Fig. 7. Comparison between the experimental and caluculated results of Charpy impact test.

References

1) K. Shibanuma, S. Aihara, and K. Suzuki: *Engineering Fracture Mechanics*, 151 (2016), 161, https://doi.org/10.1016/j.engfracmech.2015.03.048.

2) K. Shibanuma, S. Aihara, and K. Suzuki: *Engineering Fracture Mechanics*, 151 (2016), 181, https://doi.org/10.1016/j.engfracmech.2015.03.049.

3) K. Shibanuma, S. Aihara, M. Matsubara, H. Shirahata, and T. Handa: *Tetsu-to-Hagane*, 99 (2013), 40 (in Japanese), https://doi.org/10.2355/tetsutohagane.99.40.

4) Y. Nonaka, T. Namegawa, M. Hoshino, and M. Fujioka: *Tetsu-to-Hagane*, 108 (2022), 199 (in Japanese), https://doi.org/10.2355/tetsutohagane.TETSU-2021-091.

5) K. Shibanuma, S. Aihara, and S. Ohtsuka: *Tetsu-to-Hagane*, 99 (2013), 582 (in Japanese), https://doi.org/10.2355/tetsutohagane.99.582.

6) K. Shibanuma, S. Aihara, and S. Ohtsuka: *ISIJ International*, 54 (2014), 1719, https://doi.org/10.2355/isijinternational.54.1719.

7) N.J. Petch: *Acta Metallurgica*, 34 (1986), 1387, https://doi.org/10.1016/0001-6160 (86)90026-X.

Abnormal grain growth in martensitic steel

Delphic Chen
Steel Product Development Section, Iron & Steel Research & Development Department,
China Steel Corp

Instability of low temperature Charpy absorption energy was found in martensitic steel. Single-side cleavage fracture was observed the appearance of the Charpy specimen while the other side remain nearly shear fracture. The microstructure examination of the specimen shows the existence of extraordinary pancake-shaped grains which can be seen by naked eyes in the “cleavage” side of the Charpy specimen. EBSD analyses revealed that the density of high angle grain boundary in the cleavage side is relatively low in comparison with the shear side of the specimen. The low density of HAGBs cause the deleterious effect in Charpy absorption energy. The further examination of the cleavage area shows the microstructure is composed of pancake-shaped coarse martensite grains and fine equiaxed fine martensite grains. The size of the pancaked-shaped coarse grain could be several millimeters in length and 1-2mm in width while the diameter of the fine equiaxed grain is only about 20-30μm. Laboratory microstructure simulation was carried out to trace the cause of the phenomenon. The simulations showed the abnormal grain growth occurred beneath the surface during the reheating stage prior to rolling. Some grains can grow abnormally to 10-20mm in length. According to other studies, that the grain size itself limit the occurrence of the static recrystallization during rolling. The abnormal coarse grain would stops recrystallizing at higher temperature while the other fine grain keeps recrystallizing during rolling. Therefore, the microstructure would become a mixture of pancake-shaped coarse grain and equiaxed fine grain after rolling and quenching. Further simulations and analyses showed the abnormal grain nucleated from the grain boundary ferrites. The size/shape of the precipitates and the morphology of the grain boundary ferrite both plays important roles in the abnormal grain growth.

The effect of precipitate size on magnetic properties of non-oriented electrical steels

Po-Yu Chen[1,*], Lin Hsu[1]

[1] Iron and Steel Research & Development Department, China Steel Corporation, Kaohsiung City, 81233, Taiwan (R.O.C)

*email: 205211@mail.csc.com.tw

Keywords: non-oriented electrical steel, precipitation, permeability, iron loss, texture

Aim and scope

In recent years, the strong demands for reducing energy consumption drive the development of highly efficient silicon steels. A lower iron loss and higher permeability grade of non-oriented electrical steel can be one of the ideal solutions for improving energy efficiency of electrical motors. It is well-known that the production of low-loss grades of electrical steels is mainly achieved by increasing alloy contents, such as silicon and aluminum. However, this would also lead to another negative effect on the saturation magnetization. The magnetic flux density and permeability at high induction are accordingly decreased due to the reduction of ferromagnetic iron atoms. Thus, it is a challenge to obtain low core loss and high permeability simultaneously in non-oriented electrical steel manufacturing.

The key factors to achieve this target are supposed to be adequate crystallographic texture and precipitation control. By promoting the development of η-fibre ([001]||RD) and Goss texture ({011}<100>) and reducing γ-fibre ([111]||ND), both iron loss and magnetic flux density can be effectively improved[1,2)]. The most common method to improve the texture after final annealing is obtaining coarse grains prior to cold rolling[3-6)]. On the other hand, the precipitation is closely related to the magnetization behavior. It was reported that the movement of domain wall during magnetization would be affected by precipitates in the matrix[7)]. However, comparing with the discussion of texture control, little attention has been devoted on the influence of precipitation.

In view of the above facts, the present study aims at investigating the detailed relationship between precipitation and magnetic properties. The effect of precipitation size prior to cold rolling on texture evolution and grain growth was examined, which may help to develop the low-loss and high-permeability non-oriented silicon steel.

Materials and methods

The starting materials were 2mm-thick hot bands (Si+Al=1.9wt.%). In order to obtain different precipitation size, one hot band was annealed with a long but low temperature heat treatment which expected to maintain the initial grain size. The original hot band and annealed hot band were cold rolled to 0.5mm thickness, and then fully recrystallized by specified annealing treatments. Additionally, the fully recrystallized specimens were subjected to the stress relief annealing (SRA, 750°C 120min) for obtaining the exact performance of magnetic properties.

Microstructural examination was conducted on the cross-sectional area parallel to the transverse direction (TD) by using optical microscopy. In order to characterize the morphology of precipitates, transmission electron microscopy (TEM, JEOL JEM-2100Plus) observations with energy dispersive spectrometer (EDS, Oxford Xmax^{80T}) were performed on carbon extraction replicas.

Macrotexture was measured at polished surface of recrystallized specimen by using X-ray texture goniometer (Bruker D8 DISCOVER). The $\varphi_2 = 45°$ section of the Euler space in orientation distribution function (ODF) is selected to show relevant orientations and fibres of each sample. The magnetic measurements for the presented study were conducted with single sheet tester (SST) in Brockhaus measurement system MPG200D. Magnetic flux density at 5000A/m (B_{50}), the iron loss $W_{15/50}$ and permeability $\mu_{15/50}$ were determined at induction of 1.5T and 50Hz. These measurements were done in both RD and TD, and the data were averaged to provide a representative value.

Results

Figure 1 shows the microstructure of original hot band and annealed hot band. Recrystallized and equiaxed grains are found in both specimens, and the annealed hot band shows a little larger grain size (180μm) relative to initial state (160μm). The morphology of precipitates distributed in each specimen is shown in Figure 2. It was observed that the precipitates (MnS as the major precipitation) in annealed hot band are obviously larger than those in initial hot band. The precipitate size significantly increased from about 50nm to more than 150nm after the low-temperature annealing treatment.

The effect of these coarsened precipitates on magnetic properties is indicated in Table 1. Before the SRA treatment, the iron loss $W_{15/50}$ of each specimen is close, but the flux density B_{50} and permeability $\mu_{15/50}$ of the specimen with coarse precipitates have better value. An obvious discrepancy in magnetic properties occurred after SRA treatment. For the specimen with coarse precipitates, the iron loss decreased remarkably from 3.80W/kg to 2.99W/kg, and the increment in permeability is about double (2247->4107). On the other hand, the specimen with fine precipitates only showed iron loss of 3.49W/kg and permeability of 3408 after SRA.

Through iron loss separation, this obvious decrease in iron loss can be verified as the contribution of decreasing hysteresis loss. It was also found that the grain size of the specimen with coarse precipitates grain increased after SRA, while the other one was not (as shown in Figure 3). That is to say, these precipitates with a large size can effectively promote grain growth, even work at as low temperature as SRA. In addition, a similar mechanism brough by these precipitates also worked on the domain wall movement during magnetization. The permeability was thus improved by the ease of magnetization. In contrast, the small precipitates would result in strong pinning effect on both grain boundary and domain wall.

Since the similar grain size of the hot band specimens, the effect of coarse grain prior to cold rolling for improving the following texture was supposed to be alike. However, the results of magnetic flux density B_{50} implied that the precipitates may also have some positive influence on the texture evolution. Figure 4 displays the ODF of the recrystallized specimens, which annealed at various temperatures to observe the orientation changes during grain growth. It was discovered that the fine precipitates may result in the intensity of γ-fibre raising significantly and the other components such as Goss dramatically dropped after grain growth. On the other hand, the orientations in the specimen with coarse precipitates showed only slight shifts in each texture components. Most of ideal textures can be conserved. Generally, the γ-fibre is the preferred orientation during growth and depends on the nucleation mechanism. In other words, coarse precipitates can effectively reduce the heterogeneous nucleation sites, and consequently suppress the growing of γ-fibre, and ideal textures can be conserved.

Table 1 Magnetic properties of two kinds of hot-band specimens

Specimen	**Before SRA**					**After SRA**				
	$W_{15/50}$ (W/kg)			**B_{50} (T)**	**$\mu_{15/50}$**	**$W_{15/50}$(W/kg)**			**B_{50} (T)**	**$\mu_{15/50}$**
	W_s	**W_e**	**W_h**			**W_s**	**W_e**	**W_h**		
Fine precipitates	3.82	1.20	2.62	1.76	2129	3.49	1.10	2.39	1.76	3408
Coarse precipitates	3.80	1.29	2.50	1.78	2247	2.99	1.21	1.77	1.77	4107

*W_s: total loss, W_e: eddy current loss, W_h: hysteresis loss

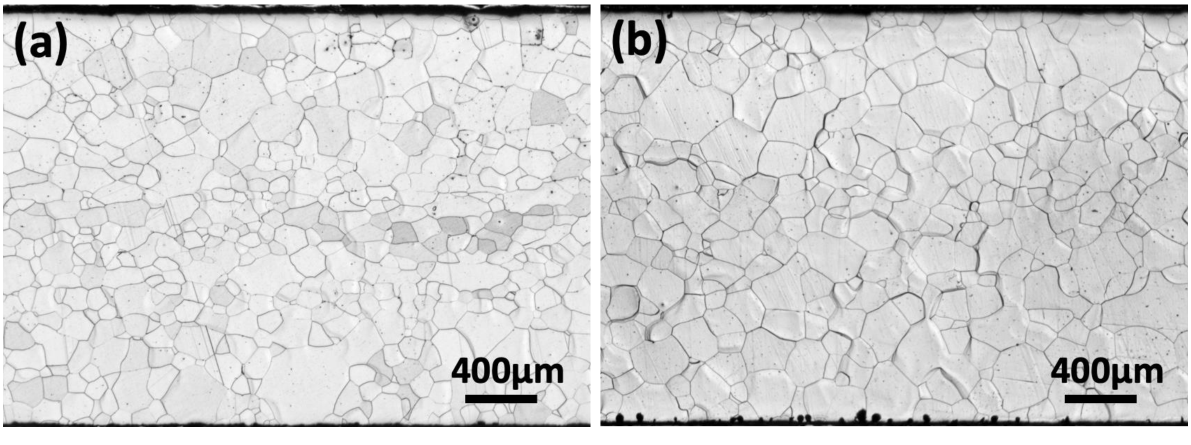

Figure 1 Optical microstructure of (a) original hot band and (b) annealed hot band.

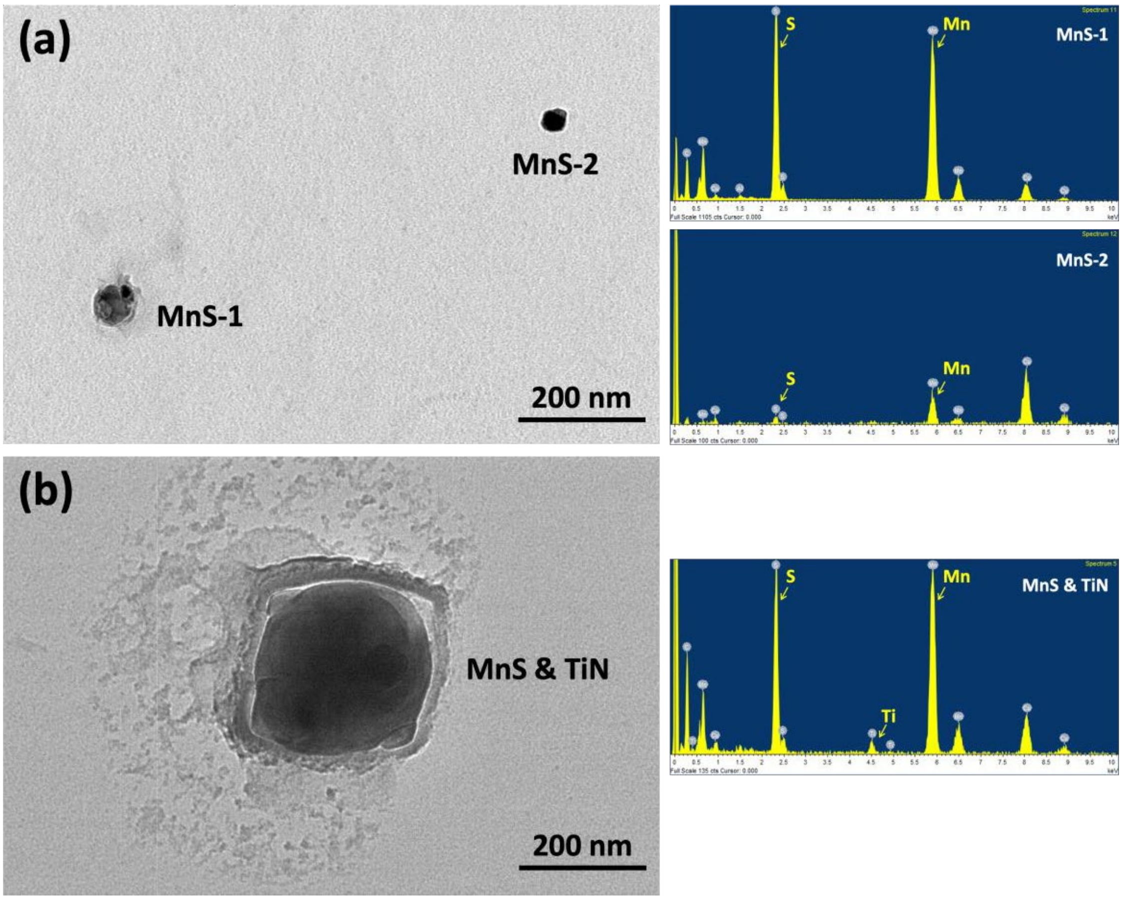

Figure 2 Morphology of precipitates and energy spectrum in (a) original hot band and (b) annealed hot band

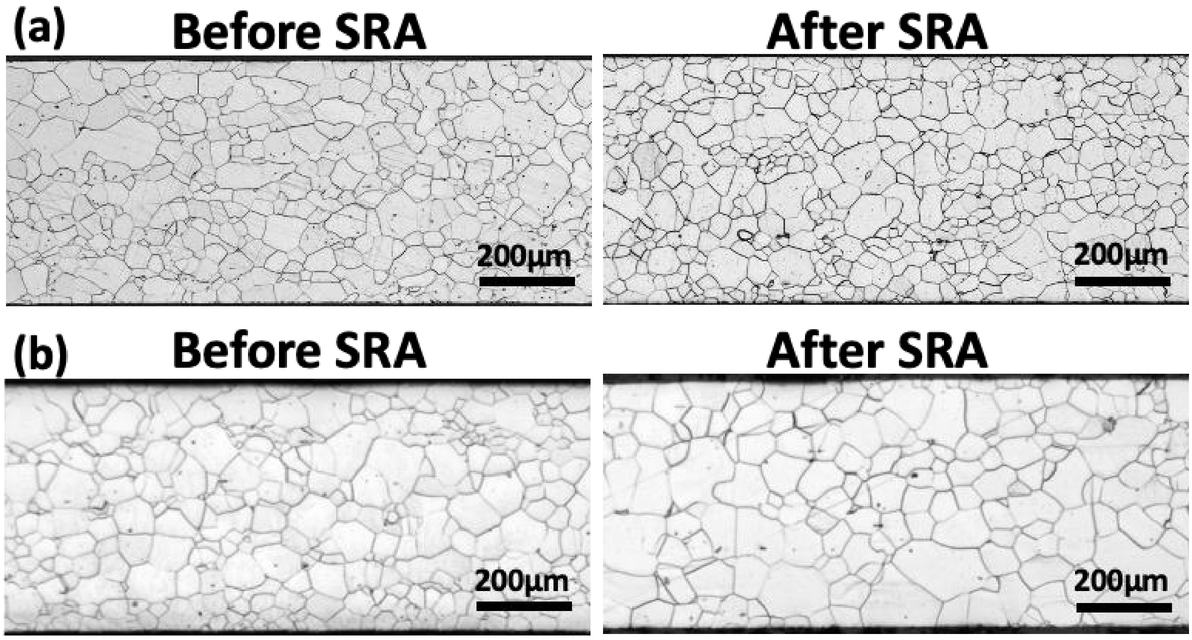

Figure 3 Optical microstructure before/ after SRA: (a) specimen with fine precipitates and (b) specimen with coarse precipitates.

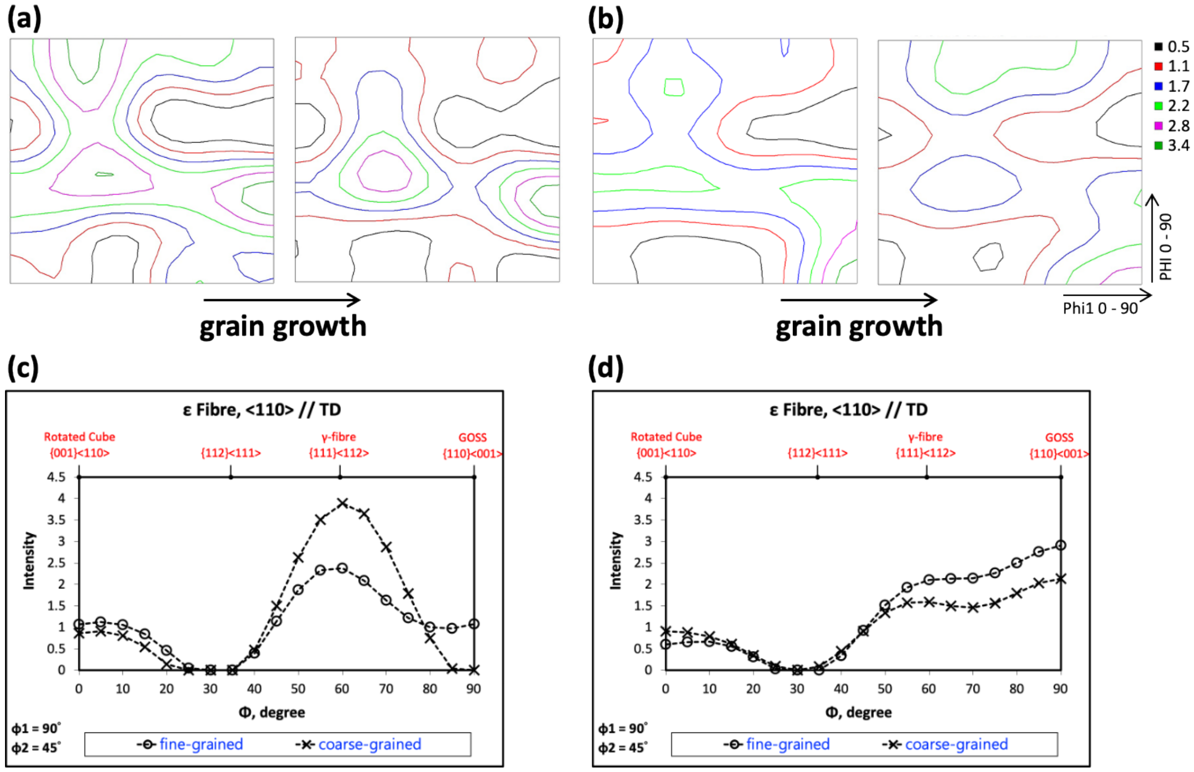

Figure 4 φ_2=45° section of ODF in recrystallized specimens and the intensity of ε-fibre ([110]||TD): (a) and (c) fine precipitates; (b) and (d) coarse precipitates.

Conclusion

In this work, the effect of precipitate size on magnetic properties was comprehensively investigated. It is shown that the permeability increased significantly with increasing precipitate size, which means that the coarse precipitate effectively reduced the impedance of domain wall motion during the magnetization process. The coarse precipitate also enhanced the grain growth after stress relief annealing, and the iron loss accordingly can further decrease with increasing grain size. In addition, the texture analysis indicated that the coarse precipitate may improve the development of {100}<uvw> texture in the coarse-grained microstructure after high-temperature final annealing. It was achieved by the inhibition of γ-fibre and more fraction of Goss component can be left after grain growth. These results imply that the appropriate precipitate control can strongly improve the magnetic properties of non-oriented electrical steels.

References

1) S. C. Paolinelli and M. A. da Cunha: Journal of Magnetism and Magnetic Materials, 2006, vol. 304(2), pp. e596-e598
2) M. A. Da Cunha and S. Da Costa Paolinelli: Materials Science Forum, 2004, vol. 467-470, pp. 869-874
3) M. F. Campos: Methods for texture improvement in electrical steels. Vol. 1. 2019, pp. 7-11
4) J. l. Qiao, L. Liu, F. h. Guo, et al.: Ironmaking & Steelmaking, 2020. Vol. 47(1), pp. 22-30
5) M. F. d. Campos, F. J. G. Landgraf, R. Takanohashi, et al.: ISIJ International, 2004, vol. 44(3), pp. 591-597
6) J. T. Park and J. A. Szpunar: ISIJ International, 2005, vol. 45(5), pp. 743-749
7) S. Tumanski: Handbook of magnetic measurements, 2011, CRC Press, pp. 13-17

The influence of pre-plating on the LME phenomenon of advanced high strength steel

Xue Bai
Shougang Research Institute of Technology

The usage of the advanced high-strength steels (AHSS) is to meet the requirement for lightweight, safety and crashworthiness. The galvanized steel plate is developed to protect the car from air-pollution or corrosion. During the resistance spot-welding process, since the melting temperature of the zinc coating is about 440-460ºC, the liquid metal embrittlement phenomenon occurs because of the low melting temperature, then the melted Zn or Zn intermetallic compounds would get penetrated into austenite grain boundaries, causing the intergranular crack formation under high temperature and complex stress called liquid metal embrittlement (LME). The LME cracks mostly distributed around the pressed zone edge, which shows as the peak of temperature and stress according to the SORPAS simulation. It degrades the mechanical properties of the high strength steel. The vibrations of the automobiles promote the growth of these micro-cracks, affecting the reliability and mechanical performance of welds. The results of electron probe micro-analyzer (EPMA) show that Zn penetrates along grain boundaries. The pre-plating technology has been used to improve the LME resistance property of the galvanized steel in our study. The high-temperature three-point bending tests have been employed to evaluate the crack propagation path. The tests under 600°C and 1mm/min parameters would be the prime ones for the experimental simulation to produce intergranular LME cracks. The columnar Ni grains of the pre-plating layer provide more channels for liquid Zn to diffusing, forming the high-melting-point Γ1-Ni_5Zn_{21} intermetallic phase. It could be found from the microstructure analysis and gleeble tests that the pre-plating technology could improve LME resistance. The pre-plating layer in technique-A sample is thicker and denser with more Zn-Ni intermetallics comparing with technique-B, thus technique-A sample could still get well elongation.

First-principles study on the P-induced embrittlement and de-embrittling effect of B and C in ferritic steels

Jingliang Wang
University of Science and Technology Beiing

First-principles calculations of the Σ5(310) grain boundary in Fe with B, C and P were performed to reveal the mechanism of P-caused embrittlement and de-embrittling effect of B and C. Independent and/or joint effect of B, C and P on the grain boundary energetics and cohesion were determined as a function of concentration. It is found that interstitial segregation sites are more favorable than substitutional sites for all the three elements, and only substitutional P aggravates the grain boundary cohesion, which explains the experimental observation that P only embrittles the grain boundary beyond a critical content. The energetic preference of interstitial B and C makes interstitial P at a disadvantage during the site competition, whereas the de-embrittling cannot be simply explained by the intrinsic strengthening effect of B and C. The influence of these elements on the grain boundary cohesion is further interpreted as a net result of mechanical contribution and chemical contribution, which proved to play the dominant role in the embrittling/strengthening effect of substitutional P and interstitial segregants respectively. It turns out that replacing part of P atoms by B and C can mitigate the strong mechanical distortion, and thus alleviate the P-caused embrittlement. In the spirit of Rice-Wang model, we propose a possible method to quantify the variation in chemical bonding upon fracture based on the concept of integral of crystal orbital Hamilton populations (ICOHP). A close relationship was found between the change in total ICOHP of bonds across the grain boundary and the calculated chemical contribution.

Effect of Nb and Mo on the morphology of martensite

Yuzo Kawamoto[1,*], Manabu Hoshino[1] and Masaaki Fujioka[1]

[1] Nippon Steel Corporation, 20-1 Shintomi, Futtsu, Chiba 293-8511, Japan
*email: kawamoto.fa4.yuuzoh@jp.nipponsteel.com

Keywords: martensite, morphology, crystallography, grain refinement

Introduction

Recently, high strength steel's demands are increasing due to construction's increasing in size, weight reduction, life prolongation. Martensite is one of the most important structure because its strength is over 1GPa even in low carbon steel. For expanding range of using martensite, suppression of brittle fracture and toughening by grain refinement is required.

Martensite structure has hierarchical structure consisted of packet, block, lath. It is efficient to refinement of packet and block by refining prior austenite grain for improving toughness of steel [1, 2)]. But as prior austenite grain size becomes smaller, course block tends to occupyprior austenite grain [3)]. For more grain refinement, packet and block refinement in one prior austenite grain is required.

There are many results that C is an efficient elements that is efficient for packet and block refinement [4-8)]. One hypothesis is that strain accommodation in prior austenite grain is inhibited by austenite strengthening and block pair which has high angle boundary increases. However, C deteriorate steel's toughness and which is not proper way to grain refinement and toughening steel. This research aims to clarify the mechanism of martensite refinement by prior austenite strengthening by other than C.

Experimental procedure

Table 1 shows chemical component of steel used in this study. 0.05%C-10.5%Ni was selected as the base steel which is easily obtain martensite structure and has course packet and block. Nb and Mo was selected of strengthening element. Maximum addition of elements was 0.2%Nb and 8.8Mo, respectively. 0.02%C-4.52%Mn and 0.3%C-4.52%Mn was evaluated for a comparison.

Austenite strength was measured by compression test. After austenitized at 1223K for 300s, cylindrical specimen, which size was $8\mathrm{mm}\phi \times 12\mathrm{mmH}$, was compressed at 1123K～973K with $\dot{\varepsilon} = 0.1$, $\varepsilon = 0.3$. $\sigma_{0.1}$ (compressed stress at $\varepsilon = 0.1$) at Ms (martensitic transformation start temperature) was evaluated by extrapolation of $\sigma_{0.1}$ at each temperature.

Specimens were also austenitized at 1223K for 300s and quenched by He gases for obtain full martensite structure. Each sample was observed by optical microscopy, scanning electron microscopy, transmission electron microscopy.

Table.1 Chemical composition of tested steel (mass percent, *:ppm) and Ms Temperature(℃)

mark	C	Si	Mn	P*	S*	Ni	Mo	Nb	Al	N*	O*	Ms
N1	0.05	<0.003	<0.003	<20	<3	10.5	0	0	0.012	<5	17	328
N2	0.05	0.003	<0.002	<20	<3	10.3	4.9	-	0.013	6	21	269
N3	0.05	0.004	<0.002	<20	<3	10.4	8.8	-	0.010	7	30	261
N4	0.05	<0.003	<0.003	<20	<3	10.5	-	0.11	0.014	<5	14	325
N5	0.05	<0.003	<0.003	<20	<3	10.5	-	0.21	0.013	<5	19	334
C1	0.02	0.069	4.52	20	4	-	-	-	0.004	14	13	395
C2	0.05	0.053	4.46	20	<3	-	-	-	0.005	16	10	356
C3	0.17	0.071	4.53	20	5	-	-	-	0.002	14	10	284
C4	0.30	0.071	4.52	20	5	-	-	-	0.003	12	10	233

Result

Fig. 1 shows the relationship between Ms and $\sigma_{0.1}$ at Ms. $\sigma_{0.1}$ increased as C or Mo added. On the other hand, as Nb addition increased, Ms wasn't varied and $\sigma_{0.1}$ was increased. It was considered that strengthening mechanism of N4, N5 were NbC precipitation strengthening and those of C1 ~ C4 were solute strengthening and Ms lowering. N2, N3 was strengthened by Mo solute strengthening, Mo_2C precipitation strengthening, and the effect of Ms.

Figure 1 The relationship between Ms temperature and austenite strength.

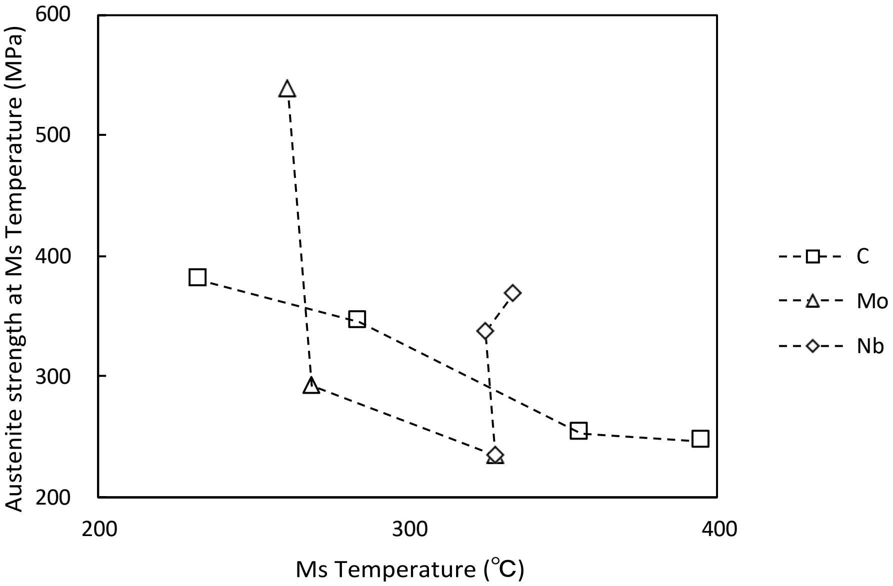

Fig. 2 shows TEM observation result of N3, N5 which aimed to clarify whether precipitation strengthening was occurred. At each sample, precipitation which size were about 10 nm were observed. It was concluded that strengthening mechanism of N4, N5 were mainly precipitation strengthening and those of N2, and N3 were both precipitation strengthening and solute strengthening.

Figure 2 Result of observation of precipitates by TEM (a) N3 (b) N5
Each precipitates is highlighted by the result of EDS mapping.

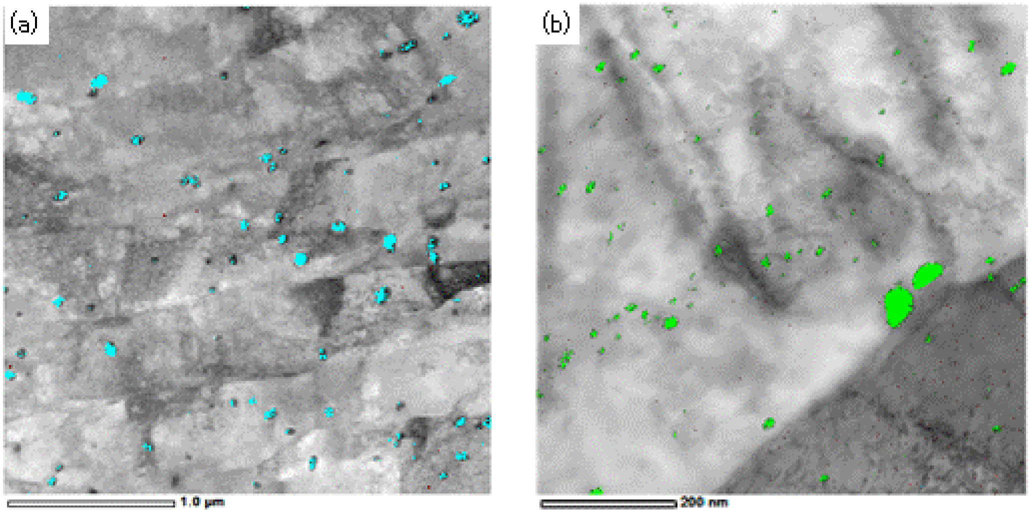

Fig. 3 shows crystal orientation map obtained by EBSD analysis. As previous reports, C was effective elements for martensite refinement. It was notable that refined packet and block was observed in N2～N5 sample even those C concentration was 0.05%. To clarify the difference of hierarchical structure of martensite in each sample, each block in same austenite grain was classified to variant group. Hereafter, V1~V24 was based on the notation used in Morito's paper[4)]. As amount of Nb or Mo increased, the number of packet and block was increased, which was a same tendency with C.

Figure 4 Inverse pole figure map of martensite cropped by prior austenite grain.
(a) N1 (b) N3 (c) N5 (d) C1 (e) C3

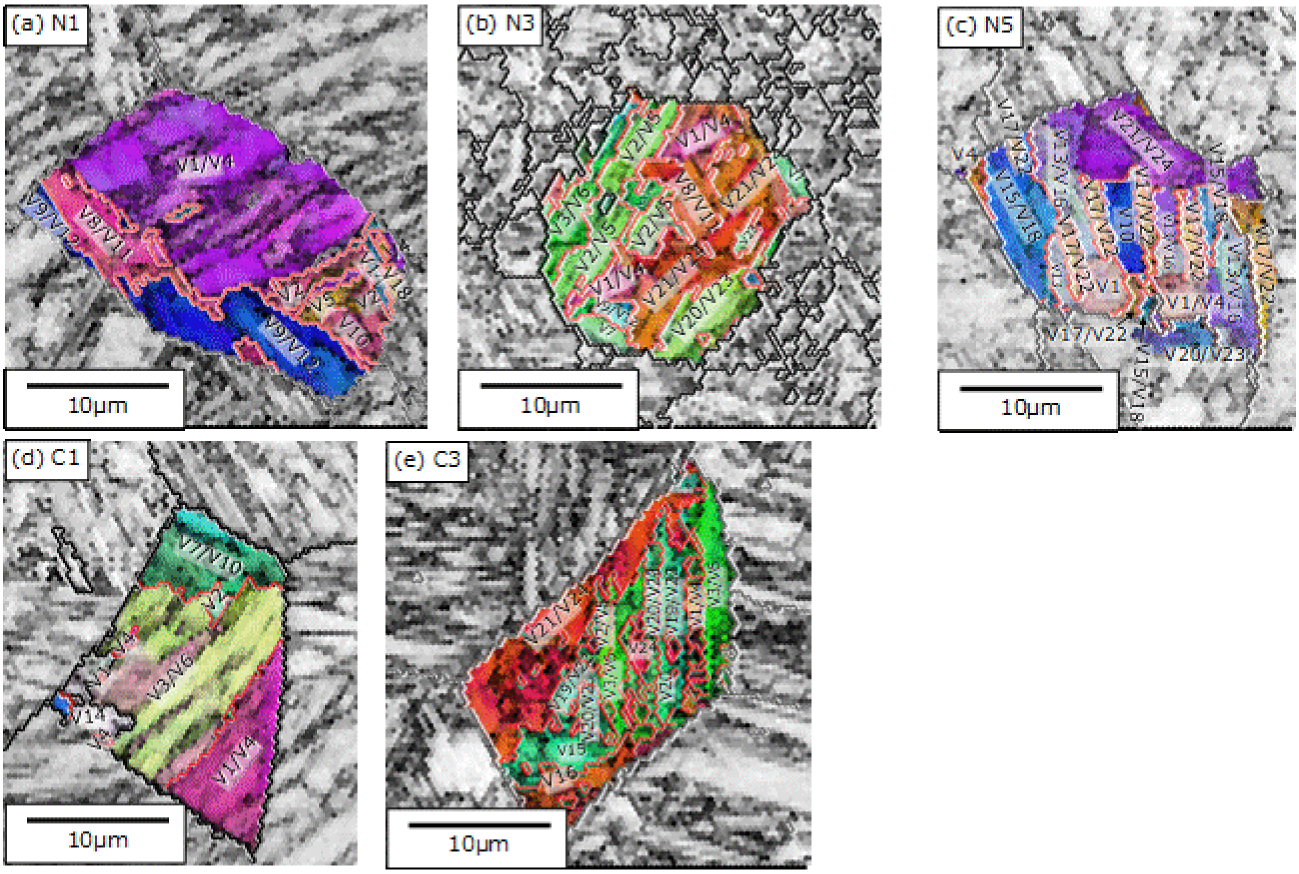

To confirm the relationship between prior austenite strength and block size, $\sigma_{0.1}$ was compared with area fraction of the largest block size in prior austenite grain. As Fig. 5 shown, block size related to prior austenite strength clearly, regardless of strengthening mechanism. This results suggests that martensitic transformation is affected by strain accommodation in prior austenite and elastic strain energy caused by volume dilation.

From the observation of microstructure, it was considered that not only morphology but also variant selection was varied as austenite strength increasing. Fig. 5 shows the comparison of variant selection between each sample. As Nb or Mo added, low angle boundary (V1/V4) was decreased, which trend was same with C. To focus on the high angle boundary, V1/V2 was increased in C1~|C4. But other variant pair like V1/V15 or V1/V23 was increased in N1~N5. The former pair is block boundary and the latter is packet boundary. This result suggests that C, Nb and Mo are the effective elements to refine lath martensite through prior austenite strengthening, but there is the different mechanism of refinement of martensite.

Conclusion

In order to clarify the effect of prior austenite strength to the morphology of lath martensite, steels containing 0.2%Nb or 8.8%Mo was tested. Through the observation, it was clear that block was refined as austenite strength increasing regardless of strengthening mechanism. The change of variant selection suggests that solute strengthening and precipitation strengthening affect differently on the elementary process of martensitic transformation.

Figure 5 Variant selection of each sample.

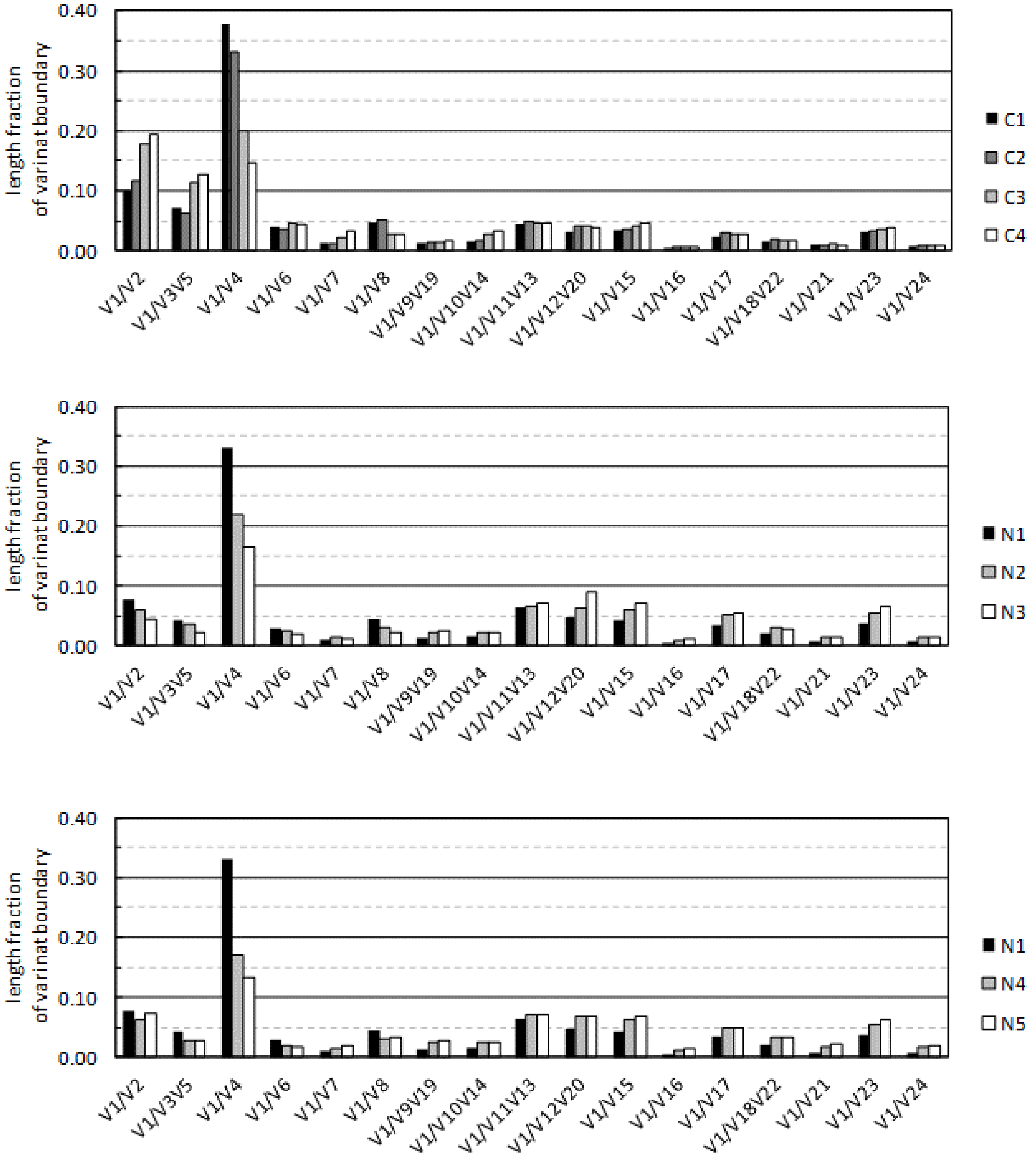

References

1) S. Matsuda, T. Inoue, M. Ogasawara, Trans. JIM, 9 (1968) 343-348.
2) S. Morito, H. Yoshida, T. Maki, X. Huang, Materials Science and Engineering A, 438-440 (2006) 237-240.
3) S. Morito, H. Saito, T. Ogawa, T. Furuhara , T. Maki, ISIJ Int., 45 (2005) 91-94.
4) S. Morito, H. Tanaka, R. Konishi, T. Furuhara , T. Maki, Acta Materialia, 51 (2003) 1789-1799.
5) S. Morito, X. Huang, T. Furuhara, T. Maki , N. Hansen, Acta Materialia, 54 (2006) 5323-5331.
6) A. Stormvinter, G. Miyamoto, T. Furuhara, P. Hedström , A. Borgenstam, Acta Mater., 60 (2012) 7265-7274.
7) S. Morito, Y. Edamatsu, K. Ichinotani, T. Ohba, T. Hayashi, Y. Adachi, T. Furuhara, G. Miyamoto , N. Takayama, Journal of Alloys and Compounds, 577S (2013) S587-S592.
8) B. Hutchinson, J. Hagström, O. Karlsson, D. Lindell, M. Tornberg, F. Lindberg, M. Thuvander, Acta Meterialia, 59 (2011) 5845-5858.

A comparative study on intrinsic mobility of incoherent and semicoherent interfaces during the austenite to ferrite transformation

Haokai Dong[1, 2*], Yongjie Zhang[3], Goro Miyamoto[3], Hao Chen[1], Zhigang Yang[1], Tadashi Furuhara[3]

[1] School of Materials Science and Engineering, Tsinghua University, Beijing 100084, China
[2] School of Mechanical and Automotive Engineering, South China University of Technology, Guangzhou 510640, China
[3] Institute for Materials Research, Tohoku University, Aoba-ku, Sendai 980-8577, Japan
*email: dong-hk16@tsinghua.org.cn; donghk@scut.edu.cn

Keywords: Interface migration, Ferrite transformation, Interface character, Intrinsic mobility, Energy dissipation

1. Introduction

Interface intrinsic mobility (M_{int}) is a key parameter to connect the thermodynamics with the kinetics of austenite (γ) to ferrite (α) transformation in steels. Although substantial efforts have been made on the evaluation of M_{int}, its value remains quite scattering especially for the pre-exponential constant. Moreover, compared to the incoherent interface, the information about M_{int} for the migrating semicoherent interface is still absent, which is indeed very important for understanding the mechanism of displacive transformation such as for the Widmanstätten α (WF) and bainite α (BF) formations. According to the mixed-mode model, the interface velocity (v) can be expressed as the product of M_{int} and net driving force (ΔG_m), i.e. $v = M_{int} \cdot \Delta G_m = M_{int} \cdot (\Delta G_t - \Delta G_e)$, where ΔG_t is the total driving force that equals to the total energy dissipation, ΔG_e is the extrinsic energy dissipation such as solute drag effect and transformation strain. Unlike the traditional method by fitting experimentally determined growth kinetics with specific models, a straightforward approach via direct measurements of interfacial C content in γ (C^{γ}) and v is employed to quantify M_{int} and ΔG_e in this study.

2. Experimental procedure

A high purity Fe-0.071C (mass%) alloys were prepared. Specimens were austenitized at 1200°C for 10min, and then quenched into salt bath to perform isothermal treatment at 750°C~825°C for various holding time. The microstructures of the specimens were observed by optical microscopy. The interface character and C^{γ} were measured by EBSD and high-accuracy FE-EPMA, respectively.

3. Results

Fig. 1(a) compares the measured C^{γ} of Allotriomorphic ferrite (AF) and Widmanstätten ferrite (WF) with γ/(α+γ) phase boundary. The dashed lines represent Ae3 line calculated by including various undercoolings, which correspond to the energy dissiaption. For AF at 825°C and 800°C, the C^{γ} deviates from the equilibrium composition at quite early stage (5s) but reach the equilibrium soon (15s). By decreasing the temperature to 750°C, the deviation becomes larger. Compared to AF, the Cγ of WF is much lower at the same condition. Its deviation is larger at lower temperature or shorter holding time. Fig. 1(b) summarizes time evolution in energy dissipation estimated from Cγ. Regardless of AF and WF, the energy dissipation decreases with increasing holding time at all the temperatures, or with raising the transformation temperature. Quantitatively speaking, the energy dissipation for WF is much larger than that for AF at the same reaction condition.

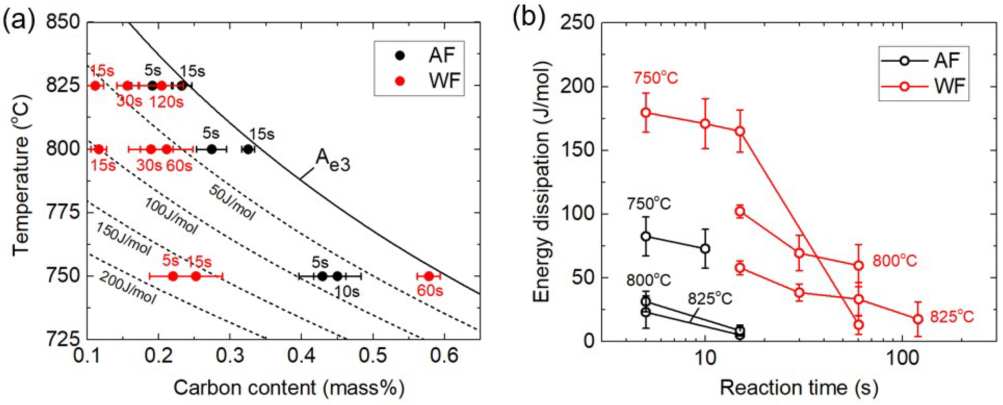

Fig. 1 (a) Comparison between the measured interfacial C content and Ae3 line with consideration of different undercoolings; (b) Variations in energy dissipation evaluated from interfacial C content with transformation time.

Fig. 2(a) plots the interface velocity of the migrating AF/γ and WF/γ interfaces with their energy dissipation at various temperatures. For reconstructive transformation, as the volumetric misfit strain between α and γ can be effectively relaxed by the diffusive transport of vacancies towards interface at elevated temperatures, the energy dissipation due to transformation strain (ΔG_s) is usually negligible. Therefore, the M_{int} of the incoherent AF/γ interfaces can be estimated by linear fitting of experimental data from the origin point. The amount of M_{int} is the slope of fitting lines. In contrast, the transformation strain during WF formation should be relatively large, because the shear strain component emanated from displacive transformation can be hardly accommodated. To quantify the ΔG_s, the amount of shear strain is assumed to be constant against transformation time. Thus, the dissipation due to transformation strain can be obtained by the intercept of linear fitting lines. Interestingly, the ΔG_s on WF formation are estimated to be ~20J/mol irrespective of reaction temperatures, which are smaller than the stored energy (~50J/mol) on the tip of WF suggested by Bhadeshia et al. [1]. In addition, the M_{int} of both AF/γ and WF/γ interfaces are found to decrease by lowering the transformation temperature.

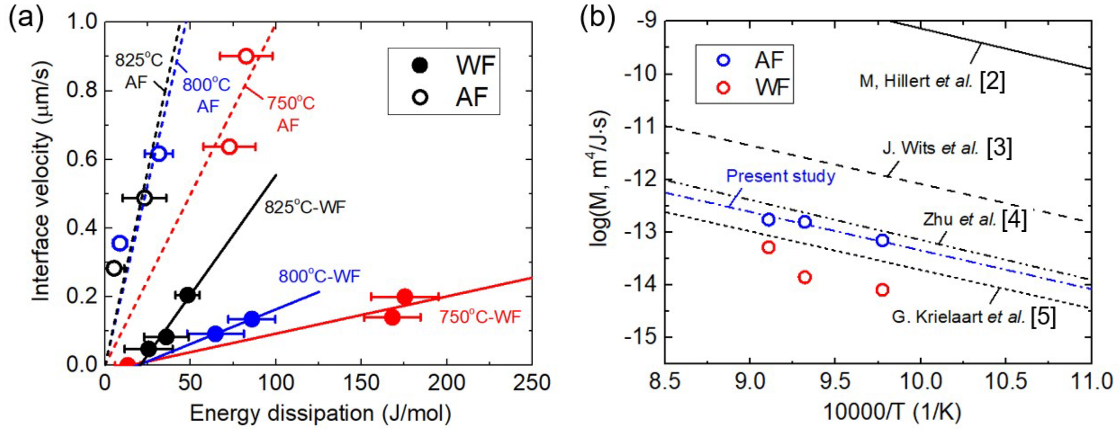

Fig. 2 (a) interface velocity of the migrating AF/γ and WF/γ interfaces with their energy dissipation at various temperatures; (b) Estimated intrinsic mobility of the migrating AF/γ and WF/γ interfaces and comparison with the reported data.

Fig. 2(b) shows the estimated M_{int} as a function of temperature and compares with the reported data [2-5]. Clearly, the M_{int} of the AF/γ interface are located between the values reported by Zhu et al. [4] and Krielaart et al. [5], and the logarithm of M_{int} follows an approximate linear function with 1/T, which is consistent with Arrhenius relationship assumed for the intrinsic mobility. Supposing the activation energy (*Q*) is the same as the previous works [3, 5], an alternative M_{int} formula for the migrating incoherent interface can be evaluated as $M_{int} = 9.4\times10^{-7}\exp(-140000/R/T)$ $m^4/J\cdot s$ in the current study. The value of M_{int} is close to the lower boundary of those estimated based on cyclic phase transformation approaches in the Fe-C alloys [6]. Compared to the AF/γ interface, the M_{int} of the semicoherent WF/γ interface is rather smaller. The explanation for such discrepancy may be concerned with the difference in activation energy that is intimately related to the interface migration mechanisms. This part will be discussed in the poster presentation. The readers can also refer to our published paper [7] if they are interested.

Acknowledgement

This work was performed under the support of National Natural Science Foundation of China (Grant 51771100), and the Ministry of Education, Culture, Sports, Science and Technology through a Grant Grant-in-Aid for Scientific Research (B) No.19H02473.

References

1) A. Ali, H. K. D. H. Bhadeshia, Mater. Sci. Technol. 6 (1990) 781-784.
2) M. Hillert, L. Höglund, Scr. Mater. 54 (2006) 1259-1263.
3) J.J. Wits, T.A. Kop, Y. van Leeuwen, J. Sietsma, S. van der Zwaag, Acta Mater. 54 (2000) 1431-1440.
4) J. Zhu, H. Luo, Z. Yang, C. Zhang, S. van der Zwaag, H. Chen, Acta Mater. 133 (2017) 258-268.
5) G.P. Krielaart, S. van der Zwaag, Mater. Sci. Technol. 14 (1998) 10-18.
6) E. Gamsjäger, M. Wiessner, S. Schider, H. Chen, S. van der Zwaag, Philos. Mag. 95 (2015) 1-19.
7) H. K. Dong, Y. J. Zhang, G. Miyamoto, H. Chen, Z. G. Yang, T. Furuhara. Scr. Mater, 188 (2020) 59-63.

Molecular Dynamics Approaches for Migrating Boundary Induced Plasticity of Iron

Simoon Sung[1], Jaehoon Jang[2], Yanghoo Kim[3] and Heung Nam Han[1,*]

[1] Department of Materials Science and Engineering & Research Institute of Advanced Materials, Seoul National University, Seoul 08826, Republic of Korea
[2] Steel Department, Korea Institute of Materials Science, Changwon, 51508, Republic of Korea
[3] Gangwon Division, Korea Institute of Industrial Technology, Gangneung, 25440, Republic of Korea
*corresponding author: hnhan@snu.ac.kr

Keywords: molecular dynamics; transformation plasticity; migrating boundary induced plasticity; grain growth

It has been observed that a permanent deformation occurs during solid-solid phase transformation of ferrous or other alloys, even when subjected to stress much lower than the yield stress [1-3]. It is known that this phenomenon, which is known as transformation plasticity or transformation induced plasticity, can cause many serious engineering problems originating from the residual strain during various metallurgical processes. Interestingly, similar phenomena were observed, not only during phase transformation but also during recrystallization and grain growth [4-5]. Through these observations, a migrating boundary induced plasticity (MIP) model was proposed that the permanent deformation can be caused by the diffusion flow of vacancy occurring at the migrating boundary. [5]

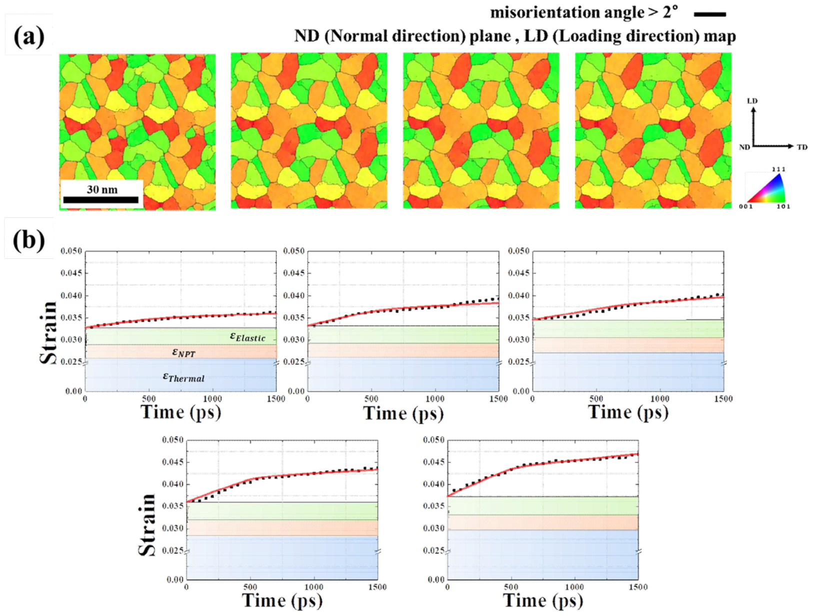

Fig. 1. Simulation results; (a) Snapshot of microstructure during molecular dynamics simulation under 1100K, 0.3GPa conditions, (b) comparison of plastic strain (black symbol) and calculation results with migrating boundary induced plasticity model (red line) under applied stress of 500MPa.

In this study, we propose a technique for predicting permanent deformation due to external stress during grain growth using molecular dynamics simulation.

This study was conducted as follows. First, to quantify the grain growth of the polycrystalline shape that was made, crystallographic information of atoms was obtained, and using this, the grain growth was verified from the change in the fraction of the region defined as the grain boundary. At the same time, the strain was measured by changing the size of the cell in the direction of the applied stress, and it was confirmed that a significant amount of strain occurred despite the application of the stress of several hundred MPa, which is lower than the yield stress during grain growth. Among these significant amounts of strain, the amount of permanent strain was quantified. As for elastic strain, we first calculate the elastic constant of a single crystal through MD simulation at a finite temperature using the stress fluctuation method[6]. After that, we derive the elastic modulus of a polycrystalline cell using the elastic-self consistent method[7]. In addition to this, factors that can cause permanent deformation, such as thermal expansion and dislocation, are taken into account.

It was found that the permanent deformation phenomenon is a thermal activation process from the relationship between the amount of permanent deformation and temperature. In addition, the activation energy value was very similar to the vacancy formation energy value at the migrating grain boundary, which is consistent with MIP. Based on these results, a newly modified phenomenological MIP model was proposed, and this modified MIP model was able to explain the permanent deformation obtained by MD results.

Acknowledgement

This work was supported by the National Research Foundation of Korea (NRF) grant funded by the Korea government Ministry of Science and ICT (MSIT) (No. NRF-2020R1A5A6017701, No. NRF-2021R1A2C3005096, and No. NRF- 2019M3D1A1079215)

References

1) G.W. Greenwood, R. Johnson: Proc. R. Soc. A: Math. Phys. Eng. Sci. **283** (1965) pp.403-422.
2) C.L. Magee, H.W. Paxton: CARNEGIE INST OF TECH PITTSBURGH PA. (1966)
3) Han. H.N, Suh. D.W: Acta. Mater. **51 (16)** (2003) pp. 4907-4917.
4) Han. H. N, Lee. J. K, Kim. S. J: Mater. Lett. **59** (2005) pp. 158-161
5) Han. H. N, Kim. S. J, Kim. M, Kim. G, Suh. D. W, and Kim. S. J: Philos. Mag. **88.12** (2008) pp.1811-1824.
6) Clavier. G. Desbiens, N. Bourasseau, E. Lachet, V. Brusselle-Dupend. N, and Rousseau. B: Mol. Simul. **43.17** (2017) pp.1413-1422.
7) Kim. Y, Kim. Y. M, Koh. J. Y, Lee. T. H, Woo. W. C, and Han. H. N: Scr. Mater. **119**, (2016) pp.1-4.

Computational approach for predicting anisotropy and formability of thermo-mechanically processed steel sheet in terms of texture control

Kyung Mun Min, Hyukjae Lee, Myoung-Gyu Lee, and Heung Nam Han*

Department of Materials Science and Engineering & RIAM, Seoul National University, Seoul 08827, Republic of Korea
*email: hnhan@snu.ac.kr

Keywords: crystal plasticity, phase field, anisotropy, formability

The manufacturing of steel sheets is commonly composed of a thermo-mechanical process, which includes a series of hot rolling, cold rolling, and heat treatments. The microstructure which evolves in this process has a direct effect on the mechanical properties of the final product. Therefore, a better understanding of the relationship between process, microstructure, and property is the crux of materials design and process optimization.

In this work, as a complementary scheme to the conventional experiment-based approach, a virtual identification scheme for predicting the formability of thermo-mechanically processed steel sheets is presented by integrating the crystal plasticity and phase field model. This integrated numerical approach aims to understand the effect of microstructural characteristics on the mechanical performance of the final product.

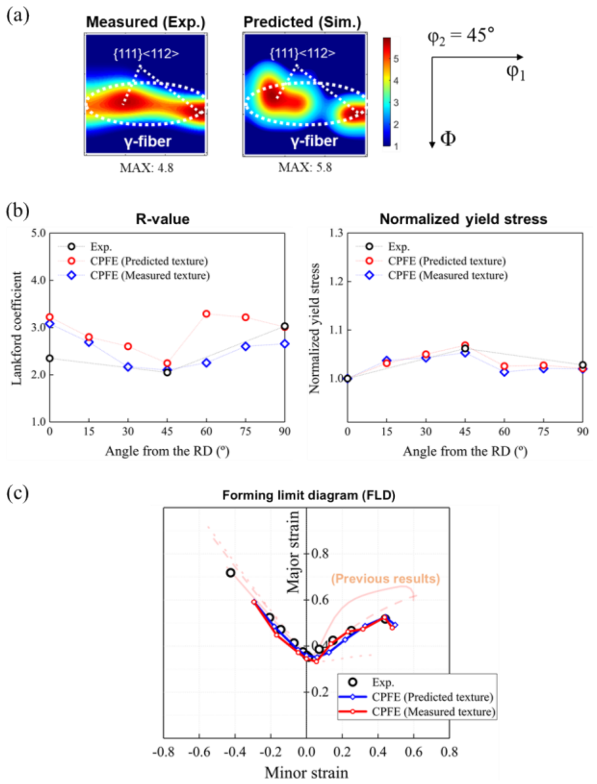

Fig. 1. Comparison of predicted results of low carbon steel with experiment; (a) Recrystallization texture, (b) R-value and normalized yield stress, and (c) forming limit diagram (FLD)

For this purpose, cold rolling followed by an annealing process is simulated, based on the mechanical properties and microstructural data of hot rolled low carbon steel. Local inhomogeneities during cold rolling such as rolling texture and shear band formation are predicted by the crystal plasticity finite element model (CPFEM), while microstructure evolution during annealing is analyzed by phase field model (PFM). Here, recrystallization texture is calculated by generalized strain energy release maximization (GSERM) model, based on the results of CP analysis. [1]

After simulating the sheet manufacturing process of steel, the representative volume elements (RVEs) which include deformation history and recrystallized microstructural data are generated for evaluating the anisotropy and formability. Virtual mechanical tests along different angles from RD are performed numerically. R-values and normalized yield stresses are calculated and compared to experiments for validation.

Not only the conventional approach using the phenomenological anisotropic yield function based on anisotropic mechanical properties, but also the crystal plasticity-based approach to consider the texture evolution during the deformation in real-time is discussed and quantitatively compared [2]. The predicted anisotropy and formability are experimentally validated to confirm the accuracy of the proposed approach.

Acknowledgement
This work was performed under the support of Hyundai Motor Company (HMC), which is greatly appreciated.

References

1) K. M. Min, W. Jeong, S. H. Hong, C. A. Lee, P. R. Cha, H. N. Han, and M. G. Lee: Int. J. Plast. **127** (2020) 102644
2) H. J. Bong, J. Lee, X. Hu, X. Sun, and M. G. Lee: Int. J. Plast. **126** (2020) 102630

Bake hardening behavior accompanying yield point phenomenon in low carbon steel

Woojin Cho
Department of Materials Science and Engineering and Research Institute of Advanced Materials,
Seoul

Baking treatment (BT) is usually subjected to pre-formed automobile body parts to increase the yield strength without reduction of thickness. So far, composition, pre-straining, and baking condition have been considered as the factors affecting bake hardening (BH). However, for the materials with yield point phenomenon which accompanies Lüders band (LB) formation, the effect of BT under the inhomogeneous pre-strains caused by the LB formation has not studied. In this research, comprehensive uniaxial tensile behavior containing BH response and yield point phenomenon was analyzed. The two types of microstructure in a low carbon steel (C<0.07 wt%) accompanying yield point phenomenon were designed: the annealed polygonal ferrite with little mobile dislocation (denoted as PF) and the acicular ferrite with enough mobile dislocations (denoted as AF). The pre-strain conditions for observing the BH behavior were 25, 50, 75, and 100% of the strain at which the LB was completely propagated to the gauge length. After all pre-strains, the specimens were heat-treated with the same BT condition of 20 mins at 170 oC and were subsequently reloaded. To visualize the propagation of the LB and the strain distribution in the gauge length, the digital image correlation (DIC) technique was utilized. The BH behavior after the BT showed completely different trend depending on whether the LB was fully propagated in the gauge length on both specimens. These BH behaviors also influenced the subsequent plastic deformation behavior. To elucidate the BH and uniaxial tensile behavior, macro and nanoindentation tests were performed. Especially, the newly created clusters in the baking-treated specimens were detected using small-angle neutron scattering (SANS), and through this, the origin of the increase in the yield and tensile strength was understood.

Computer-aided Estimation of Plastic Properties using Instrumented Indentation Tests

Ta-Te Chen[1, 2, *] and Ikumu Watanabe[1, 2]

[1] Research Center for Structural Materials, National Institute for Materials Science, Tsukuba, Ibaraki 305-0047, Japan
[2] Graduate School of Pure and Applied Science, University of Tsukuba, Tsukuba, Ibaraki 305-8573, Japan
*email: CHEN.TaTe@nims.go.jp

Keywords: instrumented indentation test, finite element method, inverse analysis, response surface, material database

Nowadays, structure materials with high strength, ductility, and good strength-to-weight ratio are required for industries. A highly efficient method to characterize the mechanical properties is necessary for material design and development. Instrumented indentation test provides high throughput and non-destructive ways to characterize the mechanical properties of alloys. However, it is hard to directly get the stress-strain relationship corresponding to the tensile test from the load-depth curves due to the complex stress state beneath the indenter. Various estimation approaches for the plastic properties have been proposed based on instrumented indentation test1,2). In our previous study3), the interaction effect between two neighboring indentations was utilized to determine the two material constants of a simple constitutive model of plasticity. The proposed approach was validated for application to aluminum alloys and stainless steel. The estimated stress-strain curves agree with the experimental results in aluminum alloys. Still, the high-work-hardening behavior in stainless steel cannot be followed due to the limitation of the power-law hardening constitutive model.

In this study, a new data-driven approach to estimate the plastic properties of alloys using instrumented indentation test was proposed with a modified constitutive model to represent the high-work-hardening behavior of alloys. The response surfaces of the indentation parameters were used as a material database to determine a set of material constants for the modified plastic constitutive model, which was prepared by the finite element simulation of instrumented indentation test. The material constants were estimated by load-depth curves and pile-up topography of indentation impression from instrumented indentation tests. The proposed approach was applied to high-work-hardening steel for validation. The estimated plastic properties show good agreement compared with the experimental tensile test.

Acknowledgment

The authors wish to acknowledge Ms. Y. Yamamoto, Dr. S. Taniguchi, Ms. E. Nakagawa, Mr. D. Araki, and Prof. H. Murakami of the National Institute of Materials Science for their technical support.

This research was financially supported by JSPS KAKENHI [grant number 21H01220].

References

1) K. Goto, I. Watanabe, and T. Ohmura: Int. J. Plast. **116** (2019) 81-90.
2) K. Goto, I. Watanabe, and T. Ohmura: Mater. Des. **194** (2020) 108925.
3) T. Chen, I. Watanabe, D. Liu, and K. Goto: Sci. Technol. Adv. Mater. Methods **1** (2021) 143-151.

Relationship Between Hall-Petch Coefficient and Grain Boundary Segregation of Carbon and Nitrogen in Ferritic Steel

Y. X. Zhou[1], *, T. Masumura[2, 3], T. Tsuchiyama[2, 3, 4]
1. Graduate School of Engineering, Kyushu University, 744, Moto-oka, Nishi-ku, Fukuoka 819-0395, Japan
2. Department of Materials Science and Engineering, Graduate School of Engineering, Kyushu University, 744, Moto-oka, Nishi-ku, Fukuoka 819-0395, Japan
3. International Institute for Carbon-Neutral Energy Research (WPI-I2CNER), Kyushu University, 744, Moto-oka, Nishi-ku, Fukuoka 819-0395, Japan
4. Research Center for Steel, 744, Moto-oka, Nishi-ku, Fukuoka 819-0395, Japan
* Corresponding author. E-mail address: zhou.yuxiong.408@s.kyushu-u.ac.jp

Keywords: Hall-Petch relation, grain boundary segregation, thermodynamic calculation.

Abstract

To figure out the correlation between the enhancement of the Hall-Petch coefficient (K_y) and the grain boundary (GB) segregation, the concentrations of Carbon and Nitrogen segregated at the GB in Fe-C, Fe-N binary alloys and Fe-C-N ternary alloys were calculated using the McLean and the Hillert-Ohtani theoretical thermodynamic models. Comparison of the calculated results with experimental values obtained by three-dimensional atom probe tomography revealed that the experimental values were roughly explained by the Hillert-Ohtani model and the McLean model shown an excessive evaluation. Furthermore, it is supposed that Carbon not only has a notable effect on the K_y, but also tends to displace N when they segregated at the GB simultaneously, even though there is very little Carbon impurity. Based on these results, the K_y of Fe-C and Fe-N alloys, determined from tensile tests, has a direct proportion with the predicted concentrations of segregated C, which can be described by a typical mathematical formula. It is indicated that the K_y can be predicted from the content of C and heat treatment temperature via thermodynamic calculations.

1. Introduction

The yield strength of polycrystalline metals linearly increases as a function of the inverse of square root of grain size, which is referred to as Hall-Petch relationship [1], as follows:

$$\sigma = \sigma_0 + K_y \cdot d^{-\frac{1}{2}}$$

σ, σ_0, K_y and d are the yield strength, the friction stress, Hall-Petch coefficient and the grain size, respectively. Hall-Petch relationship plays a very important role among grain refinement strengthening in polycrystalline iron and steel materials. However, it becomes much more difficult when machining grain size to an ultra-small area, and we determined to focus on the slope of the relation, K_y. The enhancement of K_y can perform a higher yield strength without reducing the grain size. It is found that the addition of Carbon and Nitrogen improved the K_y of ferritic steels [2]. Based on the dislocation pile-up theory among deformation process [3], it is supposed that segregated atoms at the grain boundary (GB) lead to the increasement of the K_y. Although the concentration of segregated atoms at the GB is hard to obtain experimentally, it can be calculated by thermodynamic models. In the present study, the concentrations of C and N segregated at the GB were calculated in Fe-C, Fe-N, Fe-C-N alloys and compared with the experimental results obtained by three-dimensional atom probe tomography (3DAP). Then, the calculated GB segregation results were plotted with K_y and summarized by mathematical formula.

2. Methodology

2. 1. Thermodynamic models

Two different thermodynamic models were used to get an accurate result. The McLean model and the Hillert-Ohtani model. These two models are all restricted in an equilibrium situation, which is thought can be closely achieved under a 90% cold roll.

The McLean model assumed the GB as a free surface and typically describe the change of Gibbs free energy on a free surface when atoms move into or out of it [4]. Generally, in a binary system, the McLean model can be written as:

$$\frac{X_{gb}}{1-X_{gb}}=\frac{X_i}{1-X_i}\exp\left(\frac{\Delta G}{RT}\right) \qquad (1)$$

where X_i, X_{gb}, ΔG, T and R are the bulk concentration of solute atoms, the concentration of segregated atoms at the GB, the Gibbs free energy of segregated elements, temperature and gas constant, respectively.

The Hillert-Ohtani model is based on two persons` theory. Hillert supposed the GB as a separate phase different from the bulk grain [5]. Based on the equality of components` chemical potentials, he gave an expression of the GB segregation concentration as:

$$\frac{dG^{gb}}{dX^{gb}}=\frac{dG^{ma}}{dX^{ma}} \qquad (2)$$

G^{gb} , G^{ma} X^{gb} and X^{ma} are the Gibbs free energies of the GB and the bulk, the atomic fraction at the GB and the bulk, respectively. Once the Gibbs free energies of the GB (G^{gb}) is known, it can easily reach the calculation result of the segregation concentration at the GB (X^{gb}). However, the thermodynamic information of the GB is almost unclear by now, it is hard to obtain the available X^{gb}.

As a solution, Ohtani reported an assumption that the Gibbs free energies of the GB can be thermodynamically equivalent to the Gibbs free energies of the liquid phase [6]:

$$G^{gb} = G^{liq} \qquad (3)$$

Then, combining Eq. 2 with Eq. 3 and a feasible formula will be obtained:

$$\frac{dG^{liq}}{dX^{gb}}=\frac{dG^{ma}}{dX^{ma}} \qquad (4)$$

That is the Hillert-Ohtani model.

2. 2. Tensile tests

To gain the K_y of ferritic steels with different amount of carbon and nitrogen, we used the data from Takaki [2]. The chemical compositions of specimens with various carbon and nitrogen additions are summarized in **Table 1**. Tensile tests were carried out on standard specimens according to JIS13B with strain rate of 1.0×10^{-3} s^{-1}.

Table 1 Chemical compositions of polycrystalline ferritic steels used for calculation in this study.

	C	N	Si	Mn	P	S	Ti	Fe
Base	5	9	<30	<30	<20	<3	<20	Bal.
C30	28	11	<30	<30	<20	<3	-	Bal.
C60	56	11	<30	<30	<20	<3	-	Bal.
N30	11	24	<30	370	<20	<3	-	Bal.

N60	5	54	<30	830	<20	<3	-	Bal.
C30N60	35	26	<30	380	<20	<3	-	Bal.
IF-steel	4	10	<30	<30	<20	<3	240	Bal.

3. Results and Discussion

3.1. The verification of two thermodynamic models

A situation was assumed that 100 mass ppm carbon was added in IF steel and used two models to simulate the GB segregation. For the calculation of the McLean model, the Gibbs free energy of segregated C and N were relied on the literature, which are 78 kJ/mol and 58 kJ/mol at 973K, respectively [7]. For the Hillert-Ohtani model, calculation was performed by = 973K, 10k Pa, and the SSOL7 database was used. Fig. 1 shows the relationship between C, N segregation concentrations at the GB calculated by two models at 973 K. The black line shows the results by the McLean model, and the red line shows the Hillert-Ohtani`s. The results measured by 3DAP were plotted with quadrilateral marks. Obviously, the experimental values are closer to the predicted ones in both C-added and N-added alloys when using Hillert-Ohtani model. It is indicated that the Hillert-Ohtani model has more accurate results when predicting the GB segregation in binary alloys.

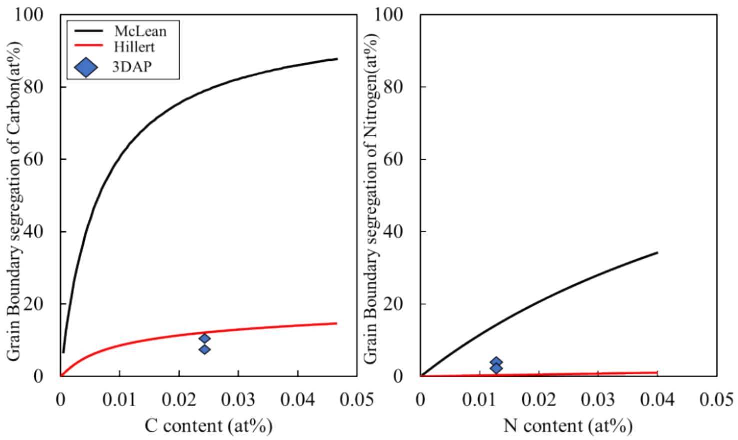

Fig. 1 Calculated results and experiment results in Fe-C and Fe-N binary systems.

3.2. The interaction of Carbon and Nitrogen in segregation concentration at the GB

When various amount of C and N were added in steels, the change of the K_y displayed a different tendency [2]. It is appeared that N almost gave no effect on the K_y. However, Araki reported that the enhancement of the K_y in C added steels is similar to it in N added steels under aging treatment [8]. The results indicated that N has a notable effect on the K_y though it is lower than C. Thus, the results in Fig. 2 might be relevant to the concentration of GB segregation.

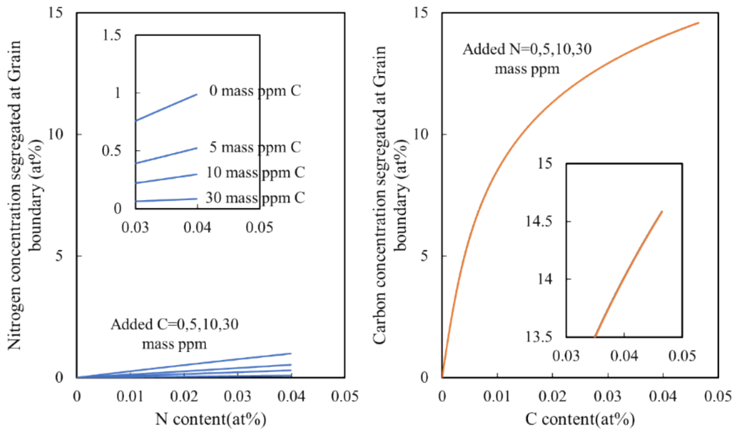

(a) Added C in Fe-N alloys (b) Added N in Fe-C alloys

Fig. 3 Calculated results in Fe-C-N ternary systems.

The chemical composition in Table 1 shows that there is little C and N impurity mixed in each of the specimens. To figure out if there is any interaction between C and N, the Fe-C-N theory systems had been simulated by the Hillert-Ohtani model. Two kinds of ternary systems were simulated, steels with 100 mass ppm N mixed with C and 100 mass ppm C mixed with N. Data of the binary systems are also contained to give a comparation. The results are shown by Fig. 2 (a) and (b). Fig. 2(a) shows the changes in the segregated N as a function of the N content with the addition of C at 0.005at%, 0.01at% and 0.03at%. Fig. 3(b) shows the segregated C as a function of the C content with the addition of N at 0.005at%, 0.01at% and 0.03at%. Fig. 2(a) exhibited an obvious reduction on the amount of segregated N along with an increase in the coexisting C. On the other hand, there is little change on the segregated C when N was coexistent in steel. It is indicated that the tendency of C atoms to segregate at the GB is much stronger than that of N, which makes segregated C dominate the K_y.

3.3. The Relationship Between K_y and GB Segregation

Due to the strong segregation tendency of C, the effect of segregated elements on K_y in Fe-C alloys and Fe-N alloys will be measured only by C. The calculated results of segregated C at the GB in previous research were adopted as horizontal axis [2], and K_y obtained by tensile tests as vertical axis to investigate the relationship. Fig. 3 exhibited the graphic that shows the relationship between the C segregation at the GB calculated by the Hillert-Ohtani model and the experimental K_y. It is revealed that the K_y can be predicted from the content of C in Fe-C-N ferritic steels.

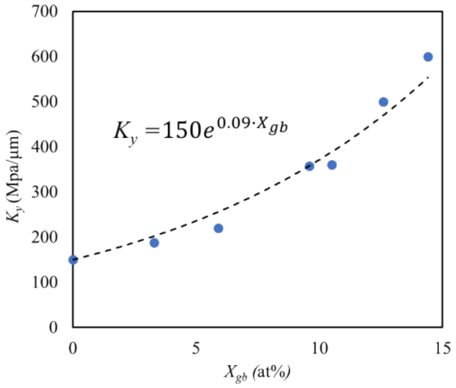

Fig. 3 Relationship between K_y and GB segregation concentration.

4. Conclusions

In the present study, thermodynamic calculation was used to simulate the concentration of atom segregation at the GB and the Hillert-Ohtani model provided a reasonable prediction in Fe-C and Fe-N binary systems. The K_y enlarged along with the increasing concentration of segregated atoms at GB and the relation can be summarized as a formula, which can help to predict the mechanical properties of Fe-C-N ferritic steels.

Acknowledgements: This work was supported by JST SPRING, Grant Number JPMJSP2136.

Reference:

[1] E. O. Hall: Società Lond. B **64** (1951) 747.

[2] K. Takeda, N. Nakada, T. Tsuchiyama, S. Takaki: *ISIJ Int.*, **48** (2008), 1122.

[3] A.H. Cottrell: Dislocations and Plastic Flow in Crystals, Oxford (1953)

[4] D. Mclean: Grain Boundaries in Metals, Clarendon Press, Oxford (1957) 116.

[5] M. Hillert H.I. Aaronson ed.: Lectures on the Theory of Phase Transformations, AIME, New York, 1975.

[6] H. Ohtani, M. Enoki: Proceedings of the 5th ISSS, (2017) 50.

[7] H. J. Grabke: Steel Res., **57** (1986), 178.

[8] S. Araki, K. Fujii, D. Akama, T. Tsuchiyama, S. Takaki, T. Ohmura, J. Takahashi: *ISIJ Int.*, **58** (2018), 1920.

Numerical study on the effect of interfacial energy on the interfacial strength and toughness of bcc-Fe tilt interfaces

Sien Liu[1] and Shoichi Nambu[1,*]

[1] Department of Materials Engineering, The University of Tokyo, Bunkyoku, Tokyo 113-8656, Japan
*email: nambu@metall.t.u-tokyo.ac.jp

Keywords: Molecular dynamics; interfacial energy; tilt interface; solid-state bonding; uniaxial tensile loading

Abstract

Interfaces have been found to play a significant role in improving mechanical properties in layered metallic materials. Many studies indicated that interfacial energy as a dominant factor influence the interface characteristics and hence, mechanical properties. To investigate the effects of interfacial energy on interfacial atomic configuration and tensile behaviour, we conducted molecular dynamics (MD) simulations of solid-state compressive bonding between two single crystals of bcc iron, and uniaxial tensile separation test. 54 symmetric tilt interfaces about <100> and <110> axis were generated to obtain models with various interfacial energies. It was found that interfacial energy is significantly dominated by the coherency of interfacial atomic configuration which is influenced by tilt angle and Σ value. From tensile separation results, an approximate linear relationship between interfacial strength and interfacial energy shows that interfacial energy is the dominant influencing factor. However, both interfacial energy and atomic structure essentially influences the interfacial work of adhesion. In addition, twinning deformation and interfacial dislocations were observed in low-energy coherent interface and high-energy disordered interfaces respectively. This relates to the observation that lower-energy interfaces generally have desired tensile separation performance.

Introduction

Solid-state compressive bonding has been widely investigated due to its unique advantages, such as the ability of jointing dissimilar metals, ease of precision control, and the absence of hazardous heat-affected zone. Previous hypotheses [1-3] suggested that recrystallization, oxide films, and potential energy may contribute to the mechanism of interface which plays a dominant role in mechanical property evolution. Previous studies had proved that strong interface helps to achieve excellent strength-ductility combination, while relatively weak interface is preferred to improve interfacial toughness. Hence, it is important to clarify the dominated factors of interface[4].

MD simulation method has been applied in the past decade to investigate atomic-scale interfacial behaviour in bicrystal systems. Nagano and Enomoto [5] and Shibuta et al. [6] calculated the interfacial energy between tilted bcc and fcc iron and showed the presence of interfacial energy cusps at specific orientations. Pongmorakot et al. [7] studied the intrinsic strength mechanism of dissimilar iron-nickel interface. It revealed that the decrease of interfacial disordered atoms with respect to isothermal holding improves intrinsic strength by energy dissipation in nanoscale. Many previous works indicated that interfacial energy plays a significant role in interfacial mechanical behaviour.

Recently, tilt-crystal grain boundary and interface attracted considerable attention as an effective method to achieve various interfacial energies [8,9]. However, the intrinsic influencing factors of interfacial behaviour and their mechanisms are still not clarified. Hence, the numerous MD observations are hard to be connected to look for relevance between properties and deformation behaviour. Moreover, investigation on the effects of interfacial energy becomes the pivotal factor for further evolution on interfacial mechanical property.

The main objectives of this study are to investigate the relationship between interfacial energy, atomic configuration, and the evolution of interfacial mechanical behaviour, and to clarify the intrinsic mechanism of different interfacial behaviour under tensile loadings. In addition, it is aimed to elucidate the principle of dislocation and other possible deformations in different tensile response, including the behaviour of interfacial strength and work of adhesion.

Simulation Methodology

MD-based simulations were performed in parallel LAMMPS to investigate the symmetric tilting interfaces between single-crystal bcc Fe. The embedded atom method (EAM) potential proposed by Zhou et al. [10] was utilized to calculate the interatomic interaction Fe atoms, where the potential is well defined for material properties including elastic constants, bulk moduli, lattice constants and dislocations line energies.

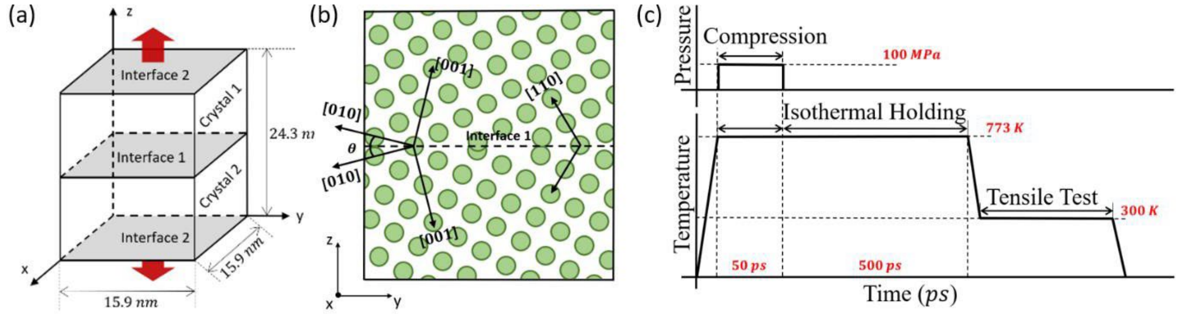

Fig. 1. (a) Schematic of the bicrystal simulation cell; (b) 2D atomic configuration on y-z plane; (c) thermo-mechanical process used in the MD simulation.

Figures 1 (a) and (b) show the schematic of simulation cell and the atomic configuration on y-z plane, respectively. The total atom number is approximately 500,000. Each sample contains two symmetric Fe crystals and two interfaces. In this work, a symmetric interface (hkl) is defined as the connected plane of two rotated single crystals in opposite directions along the same tilt axis <abc>. In all samples, the rotational axis was fixed as x axis, and the interfacial planes are always perpendicular to z axis. Shibuta et al. 5) [5] demonstrated the relationship between Miller index, tilt angle θ and rotational angle ϕ with respect to the tilt axis as

$$\theta = 2\phi = 2\cos^{-1}\left(\frac{|bh - ak|}{\sqrt{(a^2 + b^2)(h^2 + k^2 + l^2)}}\right)$$

To achieve various interfacial energies, 54 models tilted along <100> and <110> axis were investigated. The interfacial energy σ_{int} was calculated as the potential energy difference between the bi-crystal system, E_{bi}, and the two separated single crystals before compression, E_1 and E_2,

$$\sigma_{int} = \frac{E_{bi} - E_1 - E_2}{2A}$$

where A is the interfacial area. The interfaces are classified by Coincidence Site Lattice (CSL) sigma value Σ which indicates the periodicity of interfacial atomic configuration.

Figure 1 (c) illustrates the thermo-mechanical processing curve used for all samples. Two single crystals were firstly prepared at 0 K, and then heated to 773 K within 10 ps. Subsequently, uniaxial compressive loads of 100 MPa were applied at 773 K along z axis and held for 50 ps. An isothermal-isobaric ensemble (NPT) was employed, where temperature and pressure were controlled using Nose-Hoover thermostat and barostat. To relax the whole system, the as-compressed samples are followed by 500-ps isothermal holding without pressure.

After the relaxation, uniaxial tensile deformation with a constant true strain rate of $2 \times 10^3\ ps^{-1}$ along z-axis direction was applied to all bi-crystal systems until fracture. Boundary conditions were employed in top and bottom layers with 10 Å thickness. During the tensile loading, the isothermal-isobaric ensemble (NPT) was used to maintain the temperature at 300 K and zero pressure in x- and y-axis direction. The visualization software Ovito was used to illustrate the bi-crystal models. The Common Neighbour Analysis technique helps to identify the evolution of structural defects and interfacial disordered atoms during tensile deformation, and the Dislocation Extraction Algorithm (DXA) was used to calculate the Burger vectors of interfacial and propagated dislocations.

Simulation Results

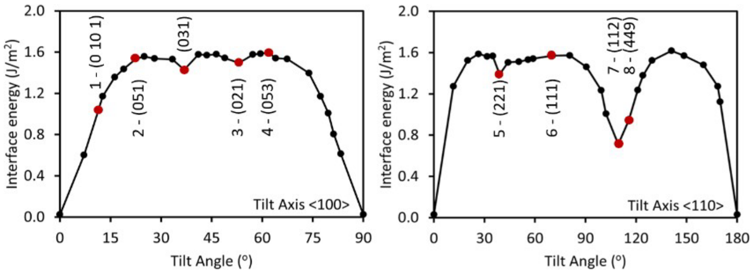

Fig. 2. Interfacial energies of <100> group (left) and <110> group (right).

Figure 2 shows the change of interfacial energy as functions of tilt angle along <100> and <110> axis respectively. In the case of <100> axis, two interfacial energy cusps were observed on the curve for (031)Σ5($\theta = 36.87°$) and (021)Σ5($\theta = 53.13°$) interfacial planes which have lowest Σ values. Although samples with 15°-75° maintain within a stable interfacial energy range, the high- and low-angle samples show decreased interfacial energies with approaching 0° or 90°. On the other hand, the <110> tilt samples show a deep interfacial energy cusp at $(112)\Sigma 3$ ($\theta = 109.47°$), and a small cusp was also observed at $(221)\Sigma 9$ ($\theta = 38.94°$). Interestingly, another interfacial plane $(111)\Sigma 3$ (70.53°) did not show local interfacial energy drop. Hence, it is inferred that low-Σ interfacial plane is not a necessary condition to form low-energy interface. The interfacial energy simulation results generally agree to the previous study by Shibuta et al.$^{5)}$.

Fig. 3. Atomic configuration of interfaces with various interfacial energies.

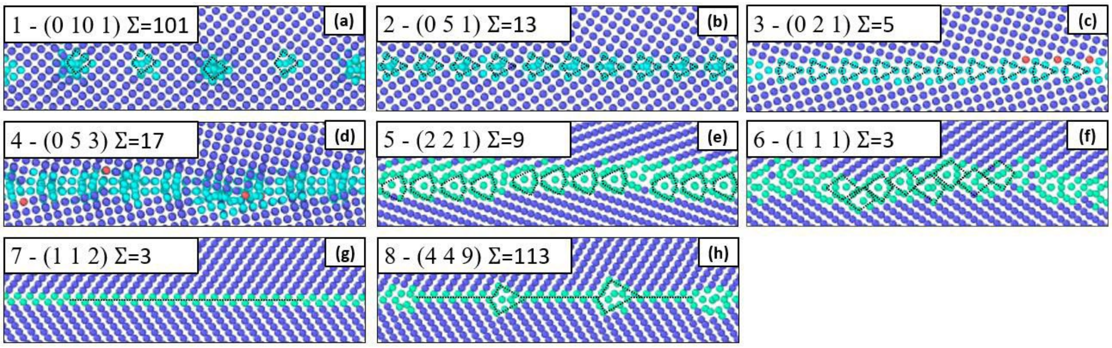

Figure 3 illustrates the atomic configuration of interfaces 1-8 as coloured in Fig. 2. It can be observed that most models have periodic configuration of interfacial atomic layer, and the periodicity is decided by the Σ values. Interface (a) $(0\ \ 10\ \ 1)\Sigma 101$ with high Σ value show repeating coherent part and disordered atom clusters within a single periodic range. This explains the drop of interfacial energy curves at low and high tilt angles. Interfaces (c) $(021)\Sigma 5$ and (g) $(112)\Sigma 3$ show the most uniform and coherent interfacial configuration in <100> and <110> cases respectively, which correlates to the local interfacial energy cusps. Generally, high-energy interfaces such as (d) $(053)\Sigma 17$ and (f) $(111)\Sigma 3$ show more disordered configuration with gathered clusters and oblique interfaces. However, interfaces (b) $(051)\Sigma 13$ and (e) $(221)\Sigma 9$ with lower energy show clear periodic configurations in ordered kite-shaped structure. In addition, the semi-coherent interface (h) $(449)\Sigma 113$ interface indicates that low interfacial energy is possible to achieve at high-Σ interfaces.

Figure 4 shows the relationship of interfacial strength and work of adhesion changing with interfacial energy. It indicates that both <100> and <110> models show approximately linear relationship between interfacial strength and energy, that low-energy interfaces with more ordered and coherent interfaces are more likely to have higher interfacial strength. Work of adhesion versus interfacial energy relationship shows a similar decreasing tendency. Nevertheless, the much higher variation of data point indicates that it is hard to build an accurate linear relationship with satisfied adaption. It is inferred that interfacial energy is the dominant influencing factor of interfacial strength, but there may exist other factors which decide work of adhesion behaviour.

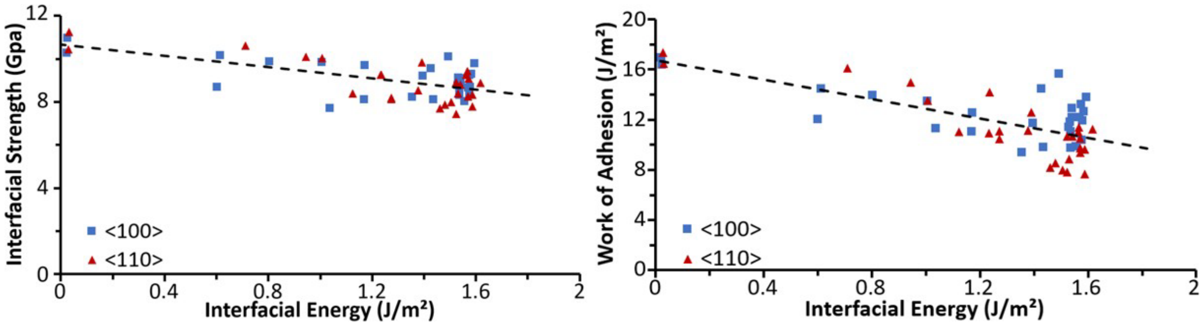

Fig. 4. Interfacial strength (left) and work of adhesion (right) versus interfacial energy relationship.

To further clarify the mechanism of work of adhesion, the interfacial deformation behaviour under tensile loading is investigated. Figure 5 shows two different interfacial deformation behaviour, twinning planes and interfacial dislocations, and their corresponding work of adhesion distribution. Twinning deformation mainly occurs in low-energy coherent interfaces, while dislocations were observed in high-energy disordered interfaces. Growth of interfacial deformations under tensile separation with coloured by atomic strain indicates different atomic movement behaviour. Twinning planes generate from interfacial periodic patterns along $(0\bar{1}1)$ planes, which generally results in higher work of adhesion. On the other hand, interfacial dislocations nucleate relatively randomly from interface, and forms dislocation networks to withstand separation.

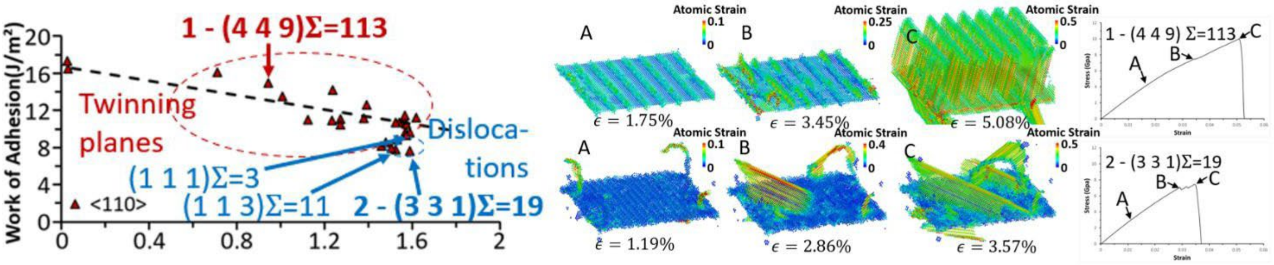

Fig. 5. Work of adhesion of the <110> group and interfacial disordered atoms for (4 4 9) and (3 3 1) interfaces.

Discussion

The main factors which decide deformation pattern are interfacial energy and atomic configuration. Fig. 5 indicates that many low-Σ interfaces with relatively higher interfacial energies show dislocation deformations. This is because highly atomic-concentrated spots due to high periodicity are likely to form local disordered clusters, which provides potential location for nucleation of interfacial dislocations. In the <100> group, no interfacial dislocation was observed, which relates to the observation that most low-Σ interfaces have locally decreased interfacial energy. It is inferred that high interfacial energy and local disordered atomic clusters promote the nucleation of interfacial dislocations.

Many studies have proved that low Σ value is not a necessary condition to form low-energy interface. For example, interface 8 - (449)Σ113 in Fig. 3 shows a coherent interface with low interfacial periodicity. It is hard to conclude the relationship between Σ values and mechanical property although partial consistency was previous reported. The current interfacial deformation analysis suggests that by influencing the interfacial atomic configuration, Σ value can affect the interfacial deformation behaviour under tensile loadings, as well as the deformation density along the interface. So, Σ value becomes an indirect influencing factor of work of adhesion.

Twinning deformation generally shows higher work of adhesion. This attributes to interfacial atomic strain which determines the overall separation behaviour. Twinning planes provides local atomic movement evenly among the interface to withstand separation. This explains why high elongation are mainly observed in low-Σ interfaces which have high twinning density. However, dislocation network hinders local atomic movement to enhance strength. As a result, high atomic strain is local concentrated, where potential weak spots for separation fracture nucleates. As an evidence, Fig. 5 shows that the overall strain to reach 0.5 maximum local atomic strain are highly different. This becomes a main reason of the work of adhesion difference between the deformations.

Conclusion

In this study, MD based simulations were carried out to study the relationship between interfacial energy, interfacial atomic structure and tensile behaviour mechanisms at bcc-Fe tilt interface. Local interfacial energy cusps were observed at $(031)\Sigma5(\theta = 53.13°)$ and $(112)\Sigma3\ (\theta = 109.47°)$. Low-energy interfaces show coherent and periodic atomic configuration, while high-energy interfaces have disordered interfacial structure. A linear relationship between interfacial energy and interfacial strength indicates that interfacial energy is the dominant influencing factor. But work of adhesion is influenced by both interfacial energy and deformation behaviour which includes twinning and dislocations.

References

1) B. Derby and E.R. Wallach: J. Mater. Sci. **19** (1984) pp. 3140-3148.
2) Y. Takahashi and K. Inoue: Mater. Sci Technol. **8.11** (1992) pp. 953-964.
3) K. Pongmorakot, S. Nambu and T. Koseki: Sci. Technol. Weld. Join. 23.4 (2017) pp. 344-350.
4) S. Nambu, M. Michiuchi, J. Inoue and T. Koseki: Compos. Sci. Technol. **69.11-12** (2009) pp. 1936-1941.
5) T. Nagano and M. Enomoto: Metall. Mater. Trans. **37.3** (2006) pp. 929-937.
6) Y. Shibuta, S. Takamoto and T. Suzuki: ISIJ Int. **48.11** (2008) pp. 1582-1591.
7) K. Pongmorakot, S. Nambu and T. Koseki: Mater, Trans. **59.4** (2018) pp. 568-574.
8) X. W. Zhou, R. A. Johnson and H. N. G. Wadley: Phys. Rev. B **69.14** (2004) 114113.
9) C. Cui, Q. Yu, W. Wang, W. Xu and L. Chen: Vacuum **184** (2021) 109874.
10) D. Singh, A. Parashar, A. Kedharnath. R. Kapoor and A. Sarkar: J. Mater. Sci. **54.4** (2019) pp. 3082-3095.

NanomechanicalAnalysis of SUS304LStainless Steel with Bimodal Distribution in Grain Size

Viola Paul[1,2], Yanxu Wang[2], Kei Ameyama[3], Mie Ota-Kawabata[3], Takahito Ohmura[1,2,*]

[1]Department of Materials Science and Engineering, Kyushu University, 774 Motooka, Nishi-ku, Fukuoka 819-0395, Japan
[2] Research Center for Structural Materials, National Institute for Materials Science, Tsukuba, Ibaraki 305-0047, Japan
[3]Department of Mechanical Engineering, Ritsumeikan University, 1-1-1 Nojihigashi, Kusatsu, Shiga, 525-8577, Japan
*email: ohmura.takahito@nims.go.jp

Keywords: Nanoindentation, stainless steel, bimodal grained microstructure, mechanical property, plastic deformation

An improved combination of strength and ductility is generally a trade-off relationship, and it remains a major research topic in the field of structural materials. A SUS304L steel with bimodal grained microstructure called "harmonic structure" consisting of a coarse-grained region "core" and a surrounding fine-grained region "shell," exhibits a good balance between strength and ductility[1)]. Therefore, the exact reason for the strengthening mechanism needs to be investigated. In the present study, we conducted nanomechanical characterization to evaluate the individual strengthening factors, including matrix strength (σ_0), and grain boundary effect (*k*), in the Hall–Petch model for each region of the core and shell to clarify the strengthening mechanism in the bimodal grained microstructure. The nanoindentation technique was applied locally in the "grain interior" to evaluate σ_0, and "on grain boundary" and "near grain boundary" to assess the grain boundary effect associated with the *k* value. The grain interior nanohardness was found to be higher in the core region than that in the shell, which is explained by the higher pre-existing dislocation density in the core region. The nanomechanical characterization of the "on grain boundary" and the "near grain boundary" regions show a higher barrier effect due to the grain boundary in the shell than that in the core, which is presumably dominated by the higher internal strain at the shell grain boundary. Furthermore, a Hall–Petch plot was constructed using nanohardness, Vickers hardness, and grain size to estimate the *k* value. The plot showed a higher *k* value in the shell, which is consistent with the higher strengthening effect of the shell grain boundary that is evaluated independently in the local region. Therefore, the macroscopic strength of the shell region is significantly affected by both grain boundary effect as well as fine grain size.

References

1) Z. Zhang, S.K. Vajpal, D. Orlov and K. Ameyama: Mater. Sci. Eng. A **598** (2014) (106•113)

Grain refinement strengthening in Si-C combined added ferritic steel

Tianze Ma[1,*], Yuxiong Zhou[1], Takuro Masumura[2], Toshihiro Tsuchiyama[2]

[1] Department of Materials, Graduate school of Engineering, Kyushu University, Ni-shi ku, Fukuoka 819-0373, Japan
[2] Department of Materials, Kyushu University, Ni-shi ku, Fukuoka 819-0373, Japan
Email: ma.tianze.220@s.kyushu-u.ac.jp

Keywords: grain boundary segregation, interstitial element, Hall-Petch coefficient, grain refinement strengthening

Introduction

The yield stress of polycrystalline metals increases with grain refining, and the relationship between yield stress (σ_y) and grain size (d) is known as Hall-Petch relationship $\sigma_y = \sigma_0 + k_y d^{-1/2}$, where σ_0 and k_y represent friction stress and Hall-Petch coefficient, respectively (1). The k_y represents the hardening effect of grain refinement strengthening and is an important parameter to evaluate the yield stress of polycrystalline metals. With a higher value of k_y, a higher yield stress can be predicted even without a grain refinement. One of the yielding mechanisms is described as Pile-up model: those dislocations, which are created by the external force, move from Frank-Read resource to the grain boundary and pile up at the grain boundary, which causes a stress concentration to the grain boundary. When the stress concentration reaches the critical grain boundary shear stress (τ_{cr}), the material yielding is occurred (2)(3). It has been reported that the k_y is improved with grain boundary segregation of alloying elements, such as carbon and nitrogen, through the increment of τ_{cr}(4). However, because only the single addition effect of the alloying element has been investigated, the influence of the combined addition of alloying is necessarily to be discussed to enhance the k_y more effectively

Aim and scope

In this study, we will discuss the change of k_y in the Si-C combined addition ferritic steels which contains different amount of Si and same amount of C. And then, the effect of Si on k_y is compared between the Si single addition alloys (5)and Si-C combined addition alloys.

Materials & experimental procedure

The combined addition ferritic steels containing (1, 2, 3 mass%) Si with 60 mass ppm C were prepared. The chemical compositions of the alloys are listed in **Table 1**. The ingots of 1.5 kg were produced by vacuum melting. These ingots were homogenized at 1273 K for 3.6 ks and then hot-rolled to 10 mm thickness. The hot-rolled plates were subjected to 90% cold rolling. In order to change the ferrite grain size, the specimens cut from cold-rolled plates were annealed in a ferrite single-phase region at 973 K for 20 s to 10.8 ks, followed by water quenching. Above heat treatment diagram is shown in **Fig. 1**. Tensile testing was performed at an initial strain rate of 10^{-3} s^{-1} for plate test pieces standardized by JIS13B at room temperature to measure the yield strength. The equilibrium concentrations of Si and C segregated at grain boundary were calculated by Hillert-Ohtani theory (6)(7).

Table 1 Chemical compositions of alloys (mass%)

	Si	C	Mn	P	S	Fe
1Si-C	0.92	0.006 (60ppm)	<0.01	<0.002	<0.001	Bal.
2Si-C	1.93	0.006 (60ppm)	<0.01	<0.002	<0.001	Bal.
3Si-C	2.92	0.006 (60ppm)	<0.01	<0.002	<0.001	Bal.

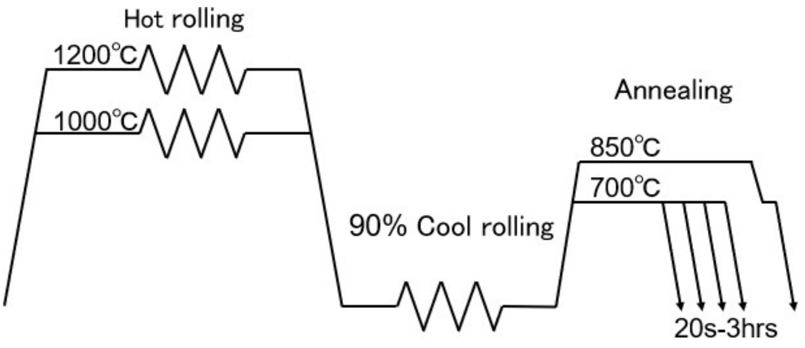

Fig. 1 Heat treatment diagram.

Experimental results & discussion

Fig. 2 shows the Hall-Petch relationship of 1, 2, 3% Si-C combined specimens. The yield strength of each specimen increases with the grain refinement and the amount of Si. The k_y, which is calculated with the least-square method, is 753, 761, 769 MPa·$\mu m^{-1/2}$,respectively.

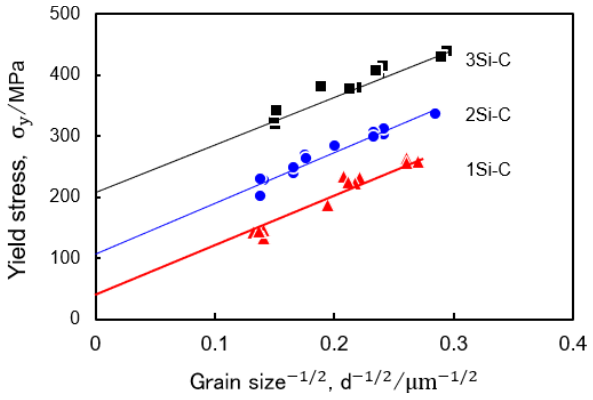

Fig.2 Hall-Petch relations of 1Si-C, 2Si-C, 3Si-C with various grain size.

Fig. 3 shows the k_y of Si single addition and Si-C combined addition alloys. In Si single addition specimens $^{(5)}$, the k_y monotonically increases with increasing the Si content. On the other hand, in the Si-C combined addition specimens, the k_y significantly increases by the addition of 1%Si, but the change in k_y by further addition of Si was small. The k_y of Si-C combined addition specimens is significantly larger than the sum of k_y of 3%Si and 60ppm C single addition specimens, which indicates the Si-C combined addition is more efficient than combined addition in grain boundary segregation strengthening.

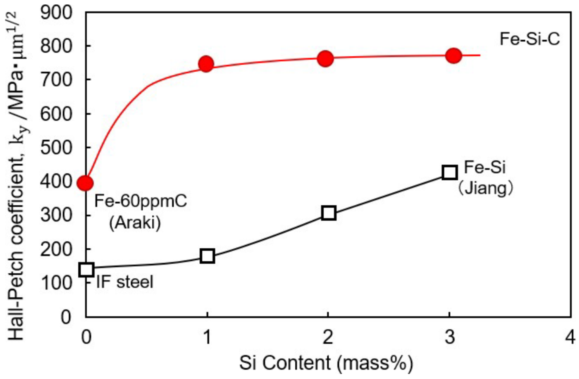

Fig. 3 Comparison of Hall-Petch coefficient between Fe-Si-C and Fe-Si with varied Si contents.

To clarify the effect of grain boundary segregation of alloying elements, the equilibrium grain boundary segregation concentrations of Si (Si^{GB}) and C (C^{GB}) were calculated by Thermodynamics method using the Hillert-Ohtani model (6)(7). **Fig. 4** shows the equilibrium grain boundary segregation concentration of Si and C in single and combined addition specimens. In combined addition specimens, the C^{GB} slightly increases with increasing Si content, while the Si^{GB} is less than that in single addition specimens, which would be due to the repulsive interaction of Si and C in Fe (8). Therefore, the high k_y of Si-C combined specimens cannot be explained in the terms of the grain boundary segregation concentration. However, because the Si^{GB} might not reach at the equilibrium condition in the specimens used in this study, the direct observation of Si and C at grain boundary by 3DAP is necessary.

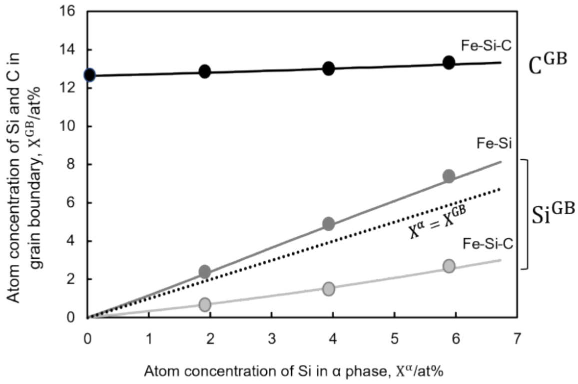

Fig. 4 The equilibrium grain boundary segregation concentration of Si and C calculated by Hillert-Ohtani model in Fe-Si single addition specimens and Fe-Si-C combined addition specimens.

References

1) M.Etou, et al.: ISIJ International, Vol.48 (2008), No.8, pp.1142-1147.
2) R.W.Armstrong, C.S.Coffey and W.L.Elban: Acta Metall., Vol.30 (1982), p.2111.
3) J.D.Eshelby, F.C.Frank and F.R.N.Nabarro: Philos Mag., Vol.42 (1951), p.351.
4) S.Araki, K.Fujii, D.Akama, T.Tsuchiyama, S.Takaki, T.Ohmura, J.Takahashi: Tetsu-to-Hagané, Vol.103(2017), pp.491-497.
5) F.L.Jiang, T.Masumura, T.Tuschiyama, S.Takaki: ISIJ International, Vol. 59 (2019), No. 10, pp. 1929–1931.
6) M. Hillert: Lectures on the theory of phase Transformations, ed. by H. I. Aaronson, Metallurgical Society of AIME, New York, (1975), 36.
7) H. ohtani and M. Enoki: Proc. 5th ISSS, The Iron and steel Institute of Japan, Tokyo, (2017), 65.
8) K.Tagashira, N.Sumita and H.Hayakawa: Mater. Trans.JIM, Vol.30 (1989), p.10.

Microstructure and Mechanical Properties of Resistance Spot Welding Joints Between Two Hot Stamping Boron Steels and DP1180 steel

Chao Lin[a]; Hao Sun[a]; Chengjie Liu[a,b]; Xicheng Wei[a]*

[a] School of Materials Science and Engineering, Shanghai University, Shanghai, 200444, China
[b] Baosteel Research Institute, Baoshan Iron & Steel Co., Ltd., Shanghai 201900, China
*email: wxc1028@shu.edu.cn

Keywords: Hot stamping steel; B1800HS; Resistance spot welding; Mechanical properties

1. Introduction

Vehicle lightweight is an important solution to reduce fuel consumption and CO_2 emissions. The application of high strength hot stamping boron steel is one of the effective methods to realize automobile lightweight without damaging the safety performance[1, 2]. It has been widely used for anti-collision structural parts of car body-in-white (BIW), such as A-pillar, B-pillar and bumper[3, 4, 5]. In the process of automobile manufacturing, resistance spot welding (RSW) is one most prevailing joining techniques for the assembly of sheet metal components because of its low cost and good performance. In this paper, the effect of strength of hot stamping boron steel on the microstructure and mechanical properties of RSWJ composed of dissimilar steel sheet were studied.The influence of mechanical properties and carbon content of different grades steels on the strength and failure behavior of resistance spot welding joints (RSWJ) were compared.

2. Materials and Methods

The applied materials were hot stamping steels B1800HS, B1500HS with 1.6 mm thickness and DP1180 cold-rolled dual-phase steel sheet with 1.4 mm thickness provided by Baosteel. The chemical composition and carbon equivalent(C_{eq}) were shown in Table 1.

Table 1 Chemical composition of the steel sheet (wt%)

Steels	C	Si	Mn	Cr	Al	Ni	Ti	P	B	Cu	C_{eq}
B1800HS	0.346	0.227	1.469	0.209	0.043	0.011	0.017	0.005	0.003	0.011	0.634
B1500HS	0.282	0.226	1.162	0.152	0.070	0.004	0.024	0.004	0.002	0.007	0.506
DP1180	0.119	0.442	2.631	0.018	0.031	0.005	0.019	0.008	0.001	0.007	0.562

The hot stamping test was carried out on THP01-500A four-column single-acting high-speed hot pressing hydraulic press with hot pressure plate quenching die and cooling system. The steels were heat treated in HT-1800M high temperature furnace. Steels were heated to 930 °C and quenched after 4 min temperature preservation. The mechanical properties of the three quenched steels are listed in Table 2.

Table 2 Mechanical properties of B1800HS and B1500HS and DP1180

Steels	Tensile strength (MPa)	Yield strength (MPa)	Elongation (%)
B1800HS	1850	1260	6.5
B1500HS	1542	1142	5.3
DP1180	1201	815	12.1

The resistance spot welding test was carried out on the Meida DM150 power frequency AC spot welding test machine, which electrode is CrCu alloy with tip diameter of 6 mm. The main experimental parameters in this paper are as follows: welding current 7.5 KA, welding time 20 cycles, electrode pressure 3.6 KN.

ZEISS SIGMA300 thermal field emission scanning electron microscope (SEM) was utilized to analyze the microstructure and composition. The microhardness measurement was carried out on MH-3 microhardness tester along the diagonal direction of nugget with 300 g load and 5s holding time. Test point spacing in the fusion zone and heat affected zone is 0.20 mm and 0.10 mm, respectively.

The tensile-shear (TS) test of RSWJs was carried out on the MTS C45-305 tensile testing machine. The Instron machine was utilized to conduct cross tensile (CT) test with a loading speed of 10mm/min. Both shape and dimension of TS and CT specimens were designed according to the GWS-5A standard of General Motors.

3. Results and discussion

Fig. 1 shows the overall microstructure of the HAZ, in which the upper side is the HAZ of B1800HS and the lower side is the HAZ of DP1180. The martensite lath at the FZ boundary is coarse and radially oriented. As the distance increases away from the edge of the nugget zone, the peak temperature and the heat input decreases, the grain gradually becomes finer, finally approaching the grain size of the matrix. There is obvious microstructural change at the junction between the HAZ and base material, as shown in the red dotted line in the Fig. 1. According to the peak temperature and microstructure evolution in the HAZ, the HAZ can be divided into four parts: coarse grain heat affected zone (CGHAZ), fine grain heat affected zone (FGHAZ), intercritical heat affected zone (ICHAZ) and subcritical heat affected zone (SCHAZ).

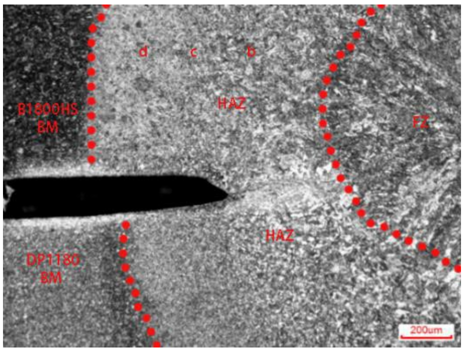

Fig. 1 HAZ macro and microstructures of B1800HS side joint (a) overall; (b) CGHAZ; (c) FGHAZ; (d)ICHAZ

Fig. 2 shows the microhardness distribution of the RSWJs of B1800HS and B1500HS with DP1180 respectively. The hardness of FZ decreases slightly from B1800HS side to DP1180 side in the B1800HS/DP1180 RSWJ as the carbon equivalent and strength of B1800HS matrix is higher than that of DP1180. The hardness of the FZ on the B1800HS side is about 510 HV0.3, and that on the DP1180 side fluctuates between 480 and 500 HV0.3. The hardness of the transition zone between CGHAZ and FZ decreased slightly, while the hardness on the DP1180 side dropped to 419.9 HV0.3. Lu[6] believed that a large amount of Al element in hot-formed boron steel formed ferrite at the FZ boundary, leading to a slight decrease in hardness here.

Sherepenko[7] found that the effect carbon segregation can account for the softening of fusion boundary. High-temperature δ ferrite is formed in fusion boundary during the heating process, which originates from the liquid or γ phase. It may restrain carbon redistribution during the subsequent rapid cooling process. Coarse lath martensite is formed in the CGHAZ of both sides which leads to a slight increase in hardness. The maximum HAZ hardness of B1800HS side is 596HV0.3, while the maximum hardness of DP1180 side is 464 HV0.3. Since the carbon equivalent of B1800HS is higher than that of DP1180, it means that the martensite transformed accordingly has higher carbon equivalent, so the HAZ hardness of B1800HS side is higher than that of DP1180 side.

In the softening zone, that is, the SCHAZ, the hardness decreased greatly. The supersaturation of martensite decreases and the precipitation of a small amount of carbides is not enough to compensate for the hardness loss caused by tempering.The hardness drops sharply in ICHAZ due to its narrow temperature range. The hardness drops to a minimum in SCHAZ adjacent to Ac1 line as the peak temperature is slightly lower than Ac1 and the microstructure undergoes a violent tempering transition. As the distance increases, the degree of tempering decreases and the hardness continues to increase, which corresponds to the microstructure gradient of SCHAZ.

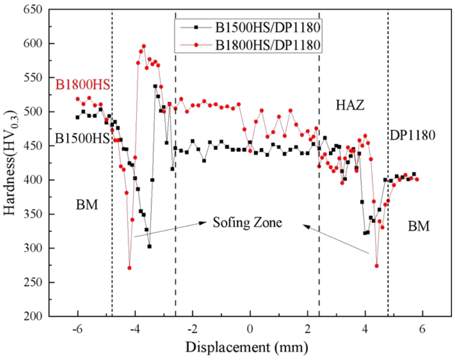

Fig. 2 Microhardness distribution of B1800HS/DP1180 and B1500HS/DP1180 RSWJs.

The lowest hardness of the softening zone on the B1800HS side is 271.1 HV$_{0.3}$, and its H$_{loss}$ value is 0.47 compared with the matrix, while lowest hardness of the softening zone on the DP1180 side is 274.1 HV$_{0.3}$ with a loss of 32%. Therefore, the softening degree of B1800HS side was higher than that of DP1180 side.

For B1500HS/DP1180 RSWJ, the hardness of the softening zone at the B1500HS side is the minimum of 302.4 HV$_{0.3}$, and its H$_{loss}$ value is 0.38 compared with the matrix. The hardness loss is smaller than that of B1800HS, which reflects the greater hardness loss of hot formed steel with higher strength and carbon equivalent.

Stöhr[8] found that the degree of martensite tempering is more sensitive to temperature than time. During the tempering process, the carbide precipitated and coarsened, and the microstructure in this region is seriously softened. The microhardness distribution of B1800HS/DP1180 joint is similar to that of B1500HS/DP1180 joint. The microhardness of the FZ and CGHAZ on the B1800HS side is slightly higher than that on the B1500HS side, and the softening degree of B1800HS SCHAZ is more serious. Rezayat[9] found that the softening degree is closely related to the tempering temperature and increases with the increase of the volume fraction of martensite in the base metal.

4. Conclusions

This paper investigated the microstructure evolution, softening mechanism of HAZ and mechanical properties of hot forming boron steel spot welded joints with different strength grades. The following conclusions can be drawn from this work:

(1) The nugget of the RSWJ is asymmetric. The subcritical HAZ experiences drastic tempering and martensitic lath decomposed especially the region adjacent to ICHAZ. Carbides precipitate along the prior austenite grain boundary, block boundary, interlath and intralath.

(2) Hot formed steel with high strength and carbon equivalent has serious softening and hardness loss during welding process.

(3) In the TS and CT tests, both TS and CT strength of the B1500HS/DP1180 RSW joint is high than that of B1800HS/DP1180 RSWJ. It can be attributed to the low carbon equivalent and slight softening ratio of B1500HS compare to that of B1800HS. It may no longer maintain a positive relationship between the RSW joint strength and matrix strength for 1500MPa grade and above hot formed boron steels.

Acknowledge

The support from Shanghai Automotive Industry Foundation [grant No. 1827].

References

[1] Mori K, Bariani PF, Behrens B-A, Brosius A, Bruschi S, Maeno T, Merklein M, Yanagimoto J. Hot stamping of ultra-high strength steel parts. CIRP Annals - Manufacturing Technology. 2017; 66(2):755-777.

[2] Li Y, Cui X, Luo Z, Ao S. Microstructure and Tensile-Shear Properties of Resistance Spot Welded 22MnMoB Hot-Stamping Annealed Steel. Journal of Materials Engineering and Performance. 2017; 26: 424–430.

[3] Zhang H, Qiu X, Bai Y, Xing F, Yu H, & Shi Y. Resistance spot welding macro characteristics of the dissimilar thickness dual phase steels. Materials & Design. 2014; 63: 151-158.

[4] Liang W, Liu Y, Zhu B, Zhou M, & Zhang Y. Conduction heating of boron alloyed steel in application for hot stamping. International Journal of Precision Engineering and Manufacturing. 2015; 16(9), 1983-1992.

[5] Karbasian H, & Tekkaya AE. A review on hot stamping. Journal of Materials Processing Technology. 2010; 210(15); 2103-2118.

[6] Lu, Y., Peer, A., Abke, T., Kimchi, M., & Zhang, W. (2018). Subcritical heat affected zone softening in hot-stamped boron steel during resistance spot welding. Materials & Design, 155, 170-184.

[7] Sherepenko O, Kazemi O, Rosemann P, et al. Transient Softening at the Fusion Boundary of Resistance Spot Welds: A Phase Field Simulation and Experimental Investigations for Al–Si-coated 22MnB5[J]. Metals, 2020, 10(1): 10.

[8] Stöhr T, Lechler J, Merklein M. Investigations on different strategies for influencing the microstructural properties with respect to partial hot stamping[C]//2nd International Conference on Hot Sheet Metal Forming of High Performance Steels, Luleå, Sweden, June. 2009: 15-17

[9] Rezayat H, Ghassemi-Armaki H, Babu S S. Effects of Heat Affected Zone Softening Extent on the strength of Advanced High Strength Steels Resistance Spot Weld[EB/OL]. OSF(2018-09-08). doi:10.17605/OSF.IO/DH53G.

Deformation behaviors and fracture mechanism in medium Mn forged steels

Tinghui Man*, Tengshi Liu, Yihao Zhou, Weijun Wang, Hongshan Zhao, Han Dong*

School of Materials and Science Engineering, Shanghai University, Shanghai 200444, China
*Email: Corresponding author: Tinghui Man: mantinghuilove@163.com
Han Dong: 13910077790@163.com

Keywords: medium Mn forged steels, deformation behaviors, fracture mechanism, dislocations

1. Aim and scope

Medium Mn steels as a representative of the third-generation advanced high strength steels have received an increasing emphasis on lightweight automobile application, exhibiting attractive product of ultimate tensile strength and total elongation associated by transformation induced plasticity (TRIP) effect [1-6]. The key to achieve such excellent product of ultimate tensile strength and total elongation for the steels is to ultimate austenite reverted transformation during intercritical annealing that generates desired austenite volume fraction and mechanical stability which can be tuned by the parameters of intercritical annealing temperature and duration [7-10]. Therefore, in the past decades, most of researches were focused on development of combined characteristics regarding both ultra-high strength and high ductility. In our recent studies, we found that an extraordinary tensiled fractography in the medium Mn forged steels after annealing treatments. However, little literatures discussed the damage initiation and fracture behavior in medium Mn steels. This study aims to reveal the relationship between microstructures and deformation behaviors during annealing treatments, and demonstrate the fracture mechanism in medium Mn forged steels.

2. Materials and methods

The Fe-0.2C-7Mn forged steel was used in this study, and the chemical composition was listed in Tab. 1. The ingot was homogenized at 1200 °C, forged between 1150 °C and 850 °C into bars with a diameter of φ30 mm, then cooled to 550 °C with holding time of 8 h, and finally cooled to ambient temperature in air. The samples for tensile tests were cut into a dimension of φ16 × 150 mm from the bars. The samples were heated at 880 °C for 0.5 h followed by air-cooled to ambient temperature, then austenitized at 850 °C for 1 h followed by water-quenched to ambient temperature. Subsequently, the samples were respectively annealed at 450, 500, 550, 600 °C for 4 h followed by air-cooled to ambient temperature, hereafter noted as M450, M500, M550, M600.

Table 1 The chemical composition of Fe-0.2C-7Mn forged steel

C	Mn	Si	P	S	Cr	Al	Fe
0.19	7.64	0.15	0.0084	<0.0005	0.012	0.024	Bal.

Uniaxial tensile tests were performed on MTS C45 machine at ambient temperature using dog-bone shaped samples of different annealing conditions with a gauge length of 50 mm and a diameter of 10 mm at a strain rate of 10^{-3} s^{-1}. All the reported tensile properties were taken as the average of two or more repeated tests. The fractured surfaces of the samples M500 and M600 were observed by Bright MAS 600 optical microscope (OM) and ZEISS Sigma 300 scanning electron microscope (SEM) after cleaned in acetone for several minutes.

The microstructures for the cross-sectional surfaces of the samples M500 and M600 were characterized through a combination of SEM, X-ray diffraction (XRD), and electron backscattered diffraction (EBSD) measurements. The samples were mechanically polished for XRD measurements, subsequently etched in a solution of 4 % nitric acid for SEM observations, and electro-polished in a solution of 10 % perchloric acid and 90 % ethanol under a voltage of 25 V for EBSD mapping. XRD measurements were performed on D/MAX2500V analyzer using Cu Kα radiation, where the patterns were taken in the 2θ range from 40 ° to 100 ° with a scanning speed of 1 °/min. The integrated intensities of $(200)_\alpha$, $(211)_\alpha$, $(200)_\gamma$, $(220)_\gamma$ and $(311)_\gamma$ diffraction peaks were calculated to obtain the volume fraction of retained austenite by the following equation [11]:

$$V_\gamma = \frac{1.4 I_\gamma}{I_\alpha + 1.4 I_r}$$

where V_γ is the volume fraction of retained austenite, I_γ is the integrated intensity of the austenite peaks, and I_α is the integrated intensity of the ferrite peaks. EBSD mapping was performed on ZEISS Sigma 300 SEM equipped with C-Nano detector which was operated at an accelerating voltage of 20 kV with a tilt angle of 70° and a scanning step size of 0.03 μm, and the analyses were post-processed by using AZtecCrystal software.

The microstructures at the center of necking and ruptured regions were observed using transmission electron microscope (TEM). The surface was protected by carbon deposition to avoid damage during focused ion beam milling performed on JEOL JEM-4000. After lift-out the sliced samples, the samples were respectively fixed to a nano mesh in such a way to view the cross-section of the microstructures. The TEM samples were then thinned from both sides to give a thickness of ~100 nm, which guaranteed its transparency to the electron beam for imaging. A final beam current of 10 pA was employed with an accelerating voltage of 5 kV. TEM observations were performed using a JEOL JEM-2100F operated at 200 kV.

3. Results

From the true stress *vs.* true strain curves of the samples M450 to M600 in Fig. 1(a), it shows that increasing annealing temperature decreases the ultimate tensile strength and yield strength owing to the increased grain size, whereas keeps the total elongation constant at about 20 % from 450 ℃ to 550 ℃ and subsequently increased to 33 % at 600 ℃. Additionally, work hardening behaviors of all the samples exhibit two stages including sharp decrease and slow decline. Moreover, the stage II continues until the greater fracture strain at 600 ℃, which suggests that a more sustainable TRIP effect contributes to best mechanical properties. Interestingly, the fracture morphology for the sample M500 show butterfly-like that necking occurs to a certain extent but ruptures not at the center as shown in Fig. 1(b), in which this situation exhibits as well as in the samples M450 and M550.

The extraordinary tensiled fractography and the fracture mechanism will be analysed and discussed on Poster Session of ICAS2022.

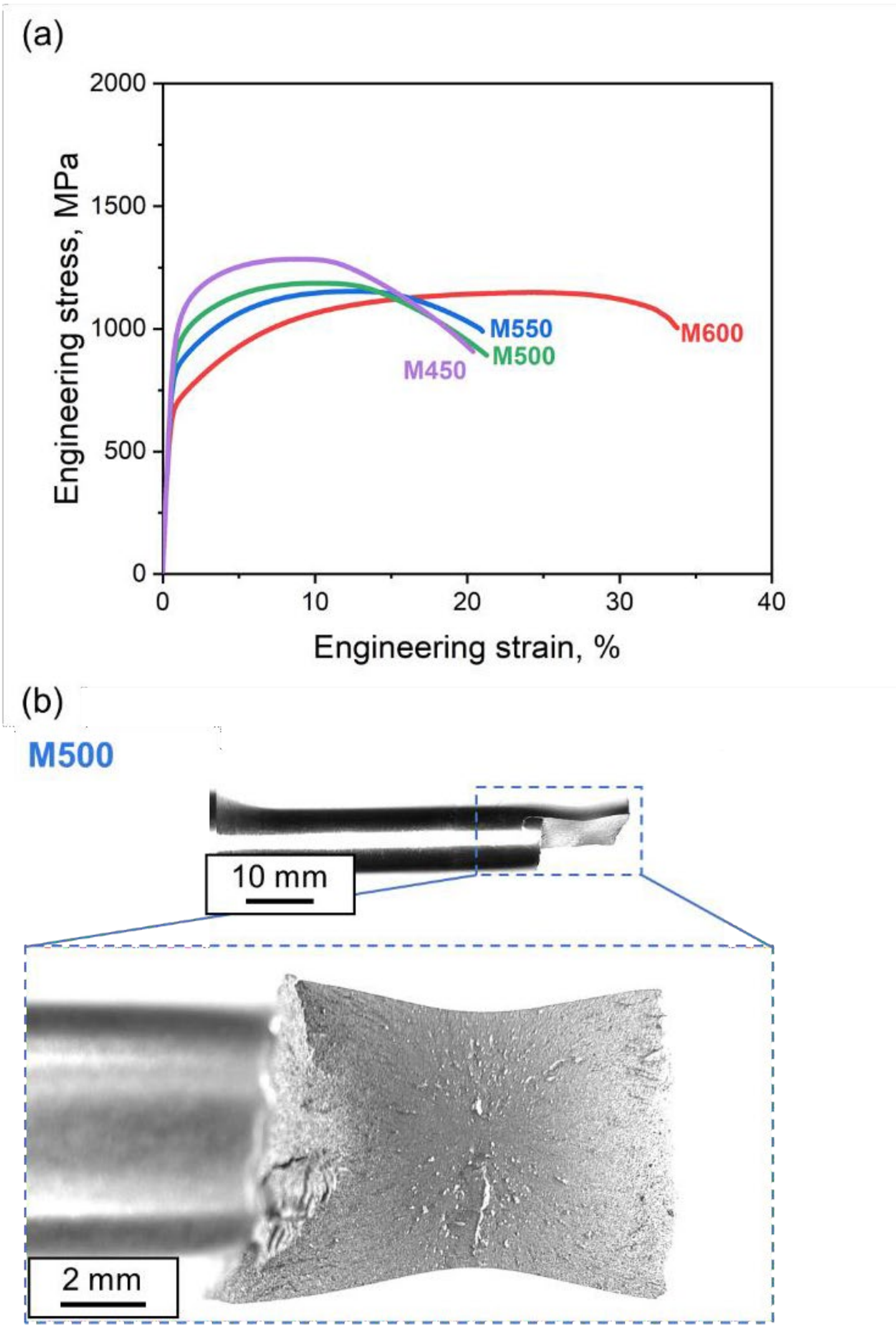

Figure 1 (a) The true stress *vs.* true strain curves of the samples M450 to M600, (b) the fracture morphology for the sample M500

4. Conclusion

The Fe-0.2C-7Mn forged steel exhibits lower total elongation and the extraordinary tensiled fractography showing butterfly-like at the annealing temperatures of 450 to 550 °C. This is presumably attributed to the reduction in volume fraction of reverted austenite and Mn partitioning, which leads to the TRIP effect occurred insufficiently during deformation.

Acknowledgement

This work was supported by National Natural Science Foundation of China (No. 52031004).

We thank Mr. Jincai Gu and Zhangjiagang Guangda Special Material Group for supplying the medium Mn forged steels.

References

1) R.L. Miller, Metall. Trans. 3 (1972) 905-912.
2) M.J. Merwin, Mater. Sci. Forum 539-543 (2007) 4327-4332.
3) J. Shi, X. Sun, M. Wang, W. Hui, H. Dong, W. Cao, Scripta Mater. 63 (2010) 815-818.
4) E. De Moor, P. J. Gibbs, J. G. Speer, D. K. Matlock, J. G. Schroth, AIST Trans. 7 (2010) 133-144.
5) L. Liu, B. He, M. Huang, Adv. Eng. Mater. 20 (2018) 1701083.
6) S. Li, P. Wen, S. Li, W. Song, Y. Wang, H. Luo, Acta Mater. 205 (2021) 116567.
7) W.Q. Cao, C. Wang, J. Shi, M.Q. Wang, W.J. Hui, H. Dong, Mater. Sci. Eng. A 528 (2011) 6661-6666.
8) P.J. Gibbs, E. De Moor, M.J. Merwin, B. Clausen, J.G. Speer, D.K. Matlock, Metall. Mater. Trans. A 42 (2011) 3691-3702.
9) S. Lee, B.C. De Cooman, Metall. Mater. Trans. A 44A(2013) 5018-5024.
10) J. Hu, L.X. Du, G.S. Sun, H. Xie, R.D.K. Misra, Scripta Mater. 104 (2015) 87-90.
11) Z. Li, D. Wu, ISIJ Int. 46 (1) (2006) 121-128.

Mechanical behavior of Si-alloyed interstitial free steels investigated by pop-in analysis during nanoindentation

Ryota Hamana
Toyohashi University ofTechnology

Nanoindentation technique is one of the powerful methods to probe the nanoscale mechanical response of a sample. The mechanical response of a material in a nanoindentation test is generally recorded as a load-displacement (p-h) curve. Under a reversible elastic deformation, mechanical response of a material in a p-h curve takes a continuous form and can be described by the Hertzian theory. The occurrence of irreversible plastic deformation such as dislocation nucleation, dislocation source activation, phase transformation and mechanical twinning can be observed as deviations from Hertz theory. With the onset of plastic deformation, a rapid excursion of displacement, which is referred to as a pop-in, is frequently observed during the test. Activation parameters for the onset of plasticity such as activation volume can be analyzed by measuring the cumulative probability of pop-in shear stress. In this work, the deformation behavior of Si-alloyed interstitial free (IF) steels during the first pop-in event is systematically investigated. The effect of solute Si in IF steel on the dislocation nucleation mechanism was discussed from the perspective of statistical analysis of the pop-in shear stress. As a means of investigating the deformation behavior in a pop-in event, the plastic deformation initiation shear stress is calculated based on the load at the time of the first pop-in The activation volume remained constant regardless of the Si content. It has been suggested that solute Si atoms act as dislocation nucleation site and possess the ability to increase activation energy for dislocation nucleation.

Effect of aging temperature on microstructure and mechanical properties of microalloyed steel for cold heading bolt

Zi-bo WANG, Heng-chang LU, Ting-hui MAN, Hong-shan ZHAO, Han DONG*
(School of Materials and Science Engineering, Shanghai University, Shanghai, 200444,China)
*Corresponding author: Prof. Han Dong: 13910077790@163.com

Abstract：The effect of aging temperature on the microstructure and mechanical properties of microalloyed steel for cold heading bolt with a cold-drawing area reduction of 47.9% was investigated by tensile tests, scanning electronic microscope (SEM). The results showed that there was a yield plateau existed at aging temperature of 350 °C, while it continued to yield at 250 °C. The yield strength increased from 748 MPa to 942 MPa and 927 MPa, meanwhile, the tensile strength increased from 960 MPa to 1022 MPa and 1009 MPa as the aging temperature increased to 250 °C and 350 °C, respectively. Interestingly, the total elongation increased from 7 % to 11 % and 16 %. SEM images showed that the microstructure consisted of proeutectoid ferrite and pearlite, which were elongated along the drawing direction after cold-drawing. After aging at 250 °C and 350 °C, the microstructure did not change obviously. The change in mechanical properties at different aging temperatures should be caused by interaction between dislocations, precipitation of fine nano-size carbides and interstitial atoms. The dislocation density would be increased after cold-drawing. As the aging temperature increases, the recovery of dislocations and the formation of sub-grain reduce the dislocation density, leading to a decrement of strength, meanwhile, the nano-sized carbides and the activated interstitial atoms would hinder the movement of dislocations, thus the strength increase. The total elongation increased for the residual stress caused by cold-drawing would be relieved after aging treatment.

Keywords: microalloyed steel; cold heading bolt; aging; microstructure; mechanical properties

Introduction

Bolts are used in a large amount and a wide range in the field of engineering and machinery. The process of cold heading bolt is: hot-rolled wire rod → pickling → cold drawing → cold heading → edge trimming → wire rolling → aging treatment → surface treatment → finished product[1]. The high-strength bolts made of deformation-strengthened microalloyed steel can omit the quenching and tempering process. It not only greatly reduces the processing cost, but also avoids a series of quality problems caused by heat treatment, especially to ensure the straightness of the slender, so that cold heading bolt with microalloyed steel has broad application prospects[2]. However, in practice, it is found that there are still many problems in the application of microalloyed steel for cold heading bolt, such as mold wear, matching relationship between cold drawing process and product quality stability. Therefore, it is still necessary to increase investment in research. In the process of cold drawing, there are high-density movable dislocations and other defects in the microstructure of the wire rod, and its microstructure and performance are unstable, which makes the bolt prone to excessive plastic deformation during service[3-5]. Therefore, it is necessary to age the wire rod before cold heading. Aging not only eliminates the residual stress caused by cold working, but also further increases the strength of the bolt.

Material and processing

The raw material used in this study is the microalloyed steel hot-rolled wire rod with a surface reduction rate of about 47.9% after drawing, and its chemical composition (mass fraction, %) is: 0.20 C, 0.20 Si, 1.50 Mn, 0.018 P, 0.007 S, 0.015 Al, 0.04 Nb, and Fe balance. Aged samples were cut from cold drawn wire, about 150 mm in length and were aged in a box-type resistance furnace. The aging process parameters were: 250 ℃ × 1 h and 350 ℃ × 1 h. Scanning electron microscope (SEM) was used to observe the microstructure of the samples in different states, and tensile tests were performed on cold drawn materials and aged samples on a universal testing machine.

Results

Figure 1 shows the SEM images of the microstructure of the test steel in different states. Before cold drawing,the matrix structure of the test steel is ferrite + fragmented pearlite, and the structure is elongated along the drawing direction after cold drawing, as shown in Fig. 1(a)(b). Microalloying technology is used to add trace alloying element Nb to test steel. Nb dissolved in austenite improves the stability of supercooled austenite, reduces the temperature of pearlite transformation, and the size of transformed pearlite clusters, so that the pearlite lamella is fragmented. The microstructures before and after aging treatment are all deformed ferrite and pearlite, and the grain size does not change significantly. After aging at 250 ℃, the microstructure did not change significantly, however, arter aging at temperature of 350 ℃, it can be seen that there is a certain amount of substructures in the ferrite grains.

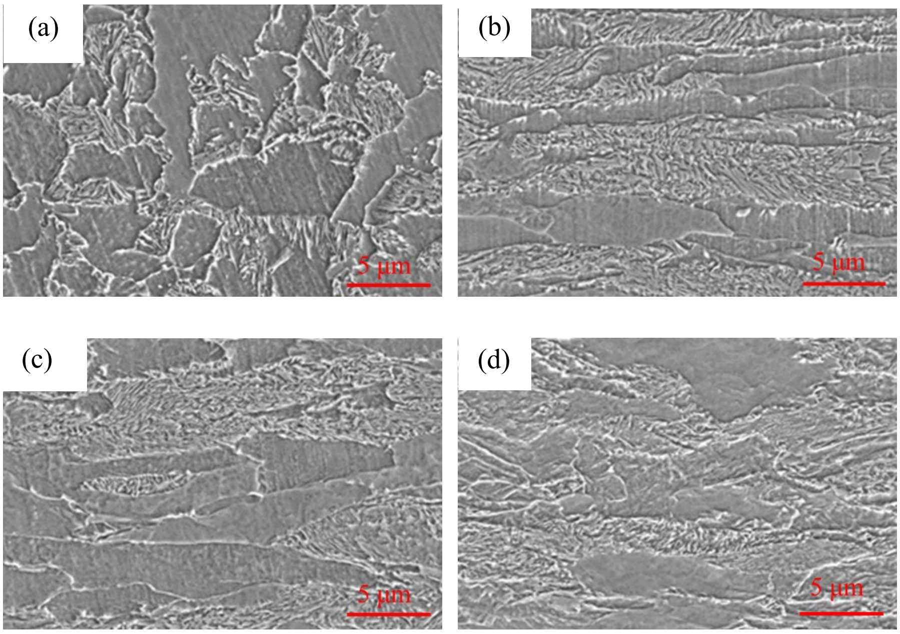

Fig. 1 The microstructures in microalloyed steel for cold heading bolt
(a) Before cold-drawing; (b) After cold-drawing; (c) Aging at 250 ℃; (d) Aging at 350 ℃

Figure 2 shows the tensile properties of the test steel in different states. The results show that there is a yield plateau when the aging temperature is 350 °C, and continuous yielding occurs at 250 °C. As the aging temperature increased to 250 °C and 350 °C, respectively, the yield strength increased from 748 MPa to 942 MPa and 927 MPa, while the tensile strength increased from 960 MPa to 1022 MPa and 1009 MPa. Interestingly, the total elongation increased from 7 % increased to 11% and 16%.

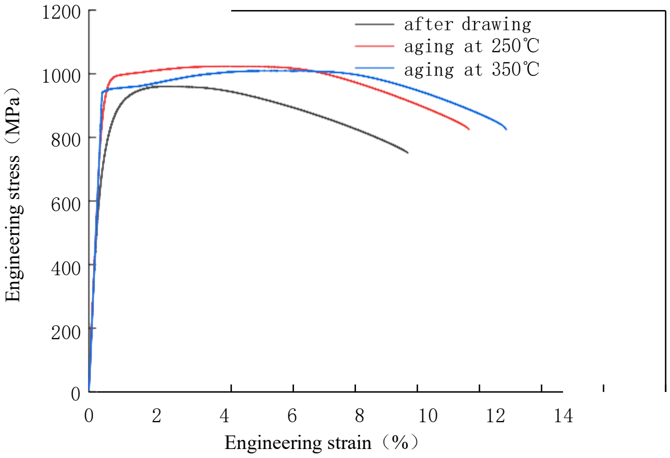

Fig. 2 Tensile properties of test steel in different states

Conclusions

For the microalloyed steel wire with a cold deformation reduction rate of 47.9 %, under the aging process of 250 and 350 °C × 1h, the yield strength and tensile strength first increase and then decrease, and the elongation continues to increase. After aging at 250 °C, the microstructure did not change significantly compared with that before aging. At the aging temperature of 350 °C, it can be seen that there are obvious substructures in the ferrite grains, and the tensile plasticity has the highest value at this time.

Acknowledgements

This work was performed under the support of Nanjing Iron & Steel Co., Ltd and Pan-Asia Automotive Technology Center Co., Ltd.

References

[1] Luo Zhijun, Li Shujia, Sun Qisong, et al. Deformation behavior of non heat-treated steel high strength bolts under static load [J].Journal of Materials HeatTreatment,2016,37(11).

[2] Dong Han, Lian Xintong, Hu Chundong, et al. High Performance Steels: the Scenario of Theory and Technology[J] Journal of metals, 2020, 56(04):558-582.

[3] Wang Lijun, Ruan Shipeng, Wang Ningtao, et al. Development and application on non-quenched and tempered steel for high strength fasteners [J].Steel,2018,53(11).

[4] X.Y. Mao et al. Effect of ageing on mechanical and impact properties of non-quenched and tempered steel wire strengthened by cold forming[J]. Philosophical Magazine Letters, 2014, 94(3) : 135-140.

[5] Hao Bin, Zhang Xiaojuan, Yuan Shaoqiang. Dissolving and precipitation behavior of Nb-Ti carbonitrides in microalloyed steels[J]. Metal Heat Treatment, 2014, 39(08): 1-4.

Deformation behaviour of two different types of medium carbon bainitic steel designed by Sparse Mixed Regression Model (SMRM)

Elango Chandiran[1,*], Rintaro Ueji [1], Hidetoshi Somekawa[1], Yukiko Ogawa[1], Kenta Nagata[2] and Masahiko Demura [2]
[1] Research Center for Structural Materials, National Institute for Materials Science, Tsukuba, Ibaraki 305-0047, Japan
[2] Research and Services Division of Materials Data and Integrated System, National Institute for Materials Science, Namiki 1-1, Tsukuba, Ibaraki, 305-0044, Japan
*email: CHANDIRAN.elango@nims.go.jp

Keywords: medium carbon steel, retained austenite, bainitic ferrite, transformation induced plasticity, sparse mixed regression model

To meet the increasing demand for weight reduction of automobiles and passenger safety, high strength steel with adequate ductility is required 1). Medium carbon bainitic steels are known to meet such requirements 2-4). The microstructure of medium carbon bainitic steels is mainly composed of carbide-free bainitic ferrite with retained austenite 4). There are several variables such as chemical composition, heat treatment conditions that can directly affect the microstructure and, in turn, the mechanical properties 3-5). Therefore, developing medium carbon bainitic steels with excellent properties requires a labour-intensive process of experimental trial and error method.

In recent years, machine learning techniques provide a new tool for the development of materials with a superior combination of mechanical properties 6-9). Brun et al.6) used a neural network model to design high creep resistant ferritic steels. Datta et al.8) used neural networks and multi-objective genetic algorithms to design high strength multi-phase steels with improved strength–ductility balance. Reddy et al. 9) demonstrated an artificial neural network can be employed for the estimation and analysis of mechanical properties as a function of chemical composition and/or heat treatment conditions for low alloy steels.

More recently, Ueji et al.10), proposed a series of medium carbon bainitic steels designed by Sparse Mixed Regression Modelling (SMRM), a Bayesian statistics-based model11), and they successfully obtained high strength and adequate elongation through optimization of the heat treatment conditions. However, the detailed deformation mechanism involved in such proposed steels is not investigated. In bainitic steels, the retained austenite plays an important role in the overall deformation behaviour. Therefore, the purpose of the present study was to provide an experimental elaboration of the novel medium carbon bainitic steels designed based on the SMRM and to clarify the role of retained austenite in the overall deformation behaviour in these steels.

Two medium-carbon Si-bearing steel, Fe-0.53C-1.55Si-0.48Mn-0.59Cr-0.05Ni (wt%, low-alloyed steel) and Fe-0.64C-1.74Si-2.11Mn-0.2Cr-0.15Ni (high-alloyed steel) used in this study. These compositions were designed by SMRM 10). The Mn content of high-alloyed steel is basically similar to conventional TRIP (transformation-induced plasticity)-aided steels reported in the previous studies12,13). The characteristics of the low -alloyed steel is the smaller amount of manganese. From the hot-calibre rolled bar, cylindrical samples of 8 mm in diameter and 40 mm in height were cut for the heat treatment purpose. The heat-treatment was carried out using a thermomechanical simulator equipped with a vacuum chamber and induction heating coils (Fuji Electronic Industrial). To obtain bainitic structures with different retained austenite fraction and morphology, the low-alloyed steel was austenitized at 980 °C for 180 s followed by austempering at 325 °C for 1.8 ks and then gas quenched. In the case of the high-alloyed steel, austenitization was done at 770 °C for 180 s, followed by austempering at 300 °C for 10.8 ks and then gas quenched. The SMRM was applied to determine these heat treatment conditions as well 10).

The microstructures were characterized by scanning electron microscopy (SEM) with electron backscattered diffraction (EBSD) techniques (TEM). The mechanical properties are characterized by a uniaxial tensile test at room temperature with an initial strain rate of 10^{-3} s^{-1}. In addition, to clarify the deformation behaviour, the heat-treated samples were strained to 4% and 10% reduction in height by uniaxial compression at room temperature using cylindrical samples (diameter 8mm and height 12 mm), at an initial strain rate of 10^{-3} s^{-1}.

Figure 1 shows the phase distributions of the heat-treated samples. The prior austenite grain size (d_{PAG}) is 35 μm and 6 μm, in the low-alloyed steel and the high-alloyed steel, respectively. The retained austenite mostly exists in the thin-film form and its fraction is 0. 06 in the low alloyed steel (Fig.1a), whereas the retained austenite is either a blocky or thin-film form and its fraction is 0.36 in the high-alloyed steel (Fig.1b). The blocky austenite is often observed in the vicinity of the prior austenite grain boundary(white lines) and its area fraction is 0.25. The larger prior austenite grain size of the low-alloyed steel is because of its higher austenitization temperature, while the higher retained austenite fraction of the high-alloyed steel can be attributed to its higher concentration of strong austenite stabilizers such as Mn and Ni [4,5]. It should be mentioned here that the X-rays diffraction peak profile analysis confirmed the microstructure is free from large carbides.

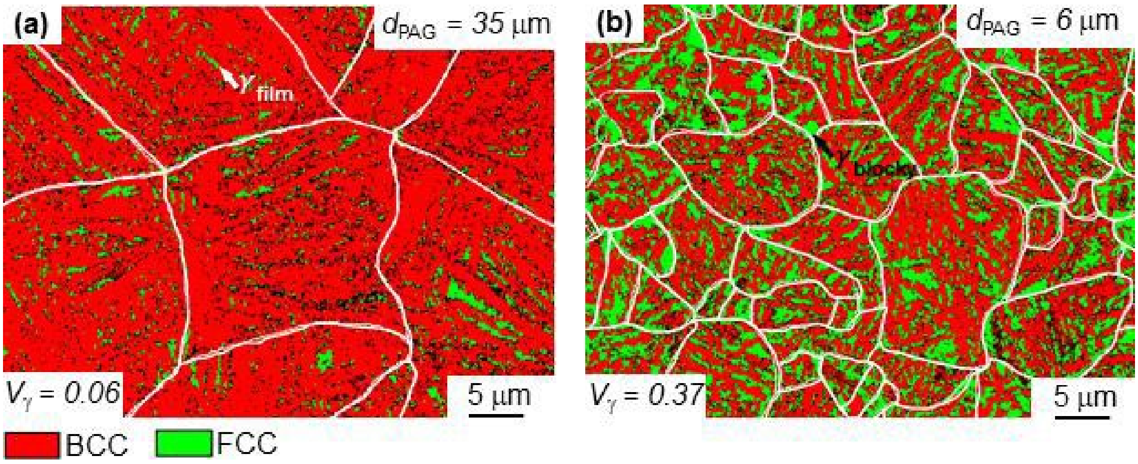

Figure 1. Phase distribution maps of the (a) low-alloyed steel and (b) high-alloyed steel. The γ_{film} and γ_{blocky} indicates the thin-film form and blocky form retained austenite, respectively.

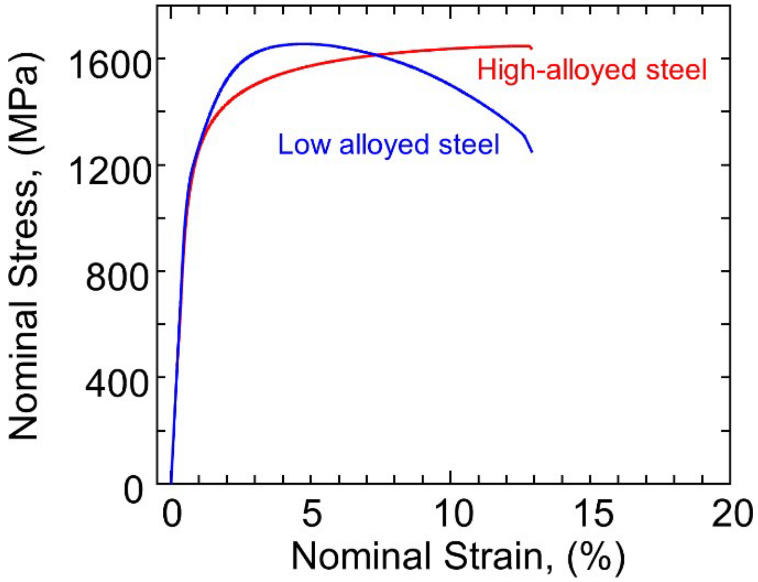

Figure 2. Nominal stress-strain curves of the low-alloyed and high-alloyed steels.

The nominal stress-strain curve of the studied samples is shown in Fig.2. It can be seen that the yield strength of the low-alloyed steel is higher than the high-alloyed steel, while both the samples showed high tensile strength (> 1.6 GPa) and large total elongation (> 12%). The tensile strength-elongation balance is over 20 GPa •% in both samples. It should be noted that the low-alloyed steel shows large post-uniform elongation (9%) and smaller uniform elongation (3%). On contrary, the high-alloyed steel shows large uniform elongation (12%) and smaller post-uniform elongation. The work-hardening rate of the high-alloyed steel is significantly larger than the low-alloyed steel.

Figure 3 shows the fracture surfaces after the tensile test, as observed by SEM. The reduction in area of the low-alloyed steel is 44%, which is higher compared to the high-alloyed steel (22%). This is in good agreement with the observed large post-uniform elongation. The fracture surface of these samples is distinctly different. In the low-alloyed steel, shear lips are observed near the surface while dimples of various sizes are found in the centre region (Fig.3a-b). In the high-alloyed steel, the shear lips are observed but only in a smaller region compared to the low-alloyed steel and the centre region is comprised of flat surfaces with negligible dimple features (Fig.3c). The higher magnification observation from the center region reveals that the surface comprises cleavage facets with river markings and some isolated micro-sized dimples (Fig.3d). The fracture surface features indicate that failure in the low-alloyed steel occurred by ductile failure mechanism and in high-alloyed steel predominately through brittle failure mechanism.

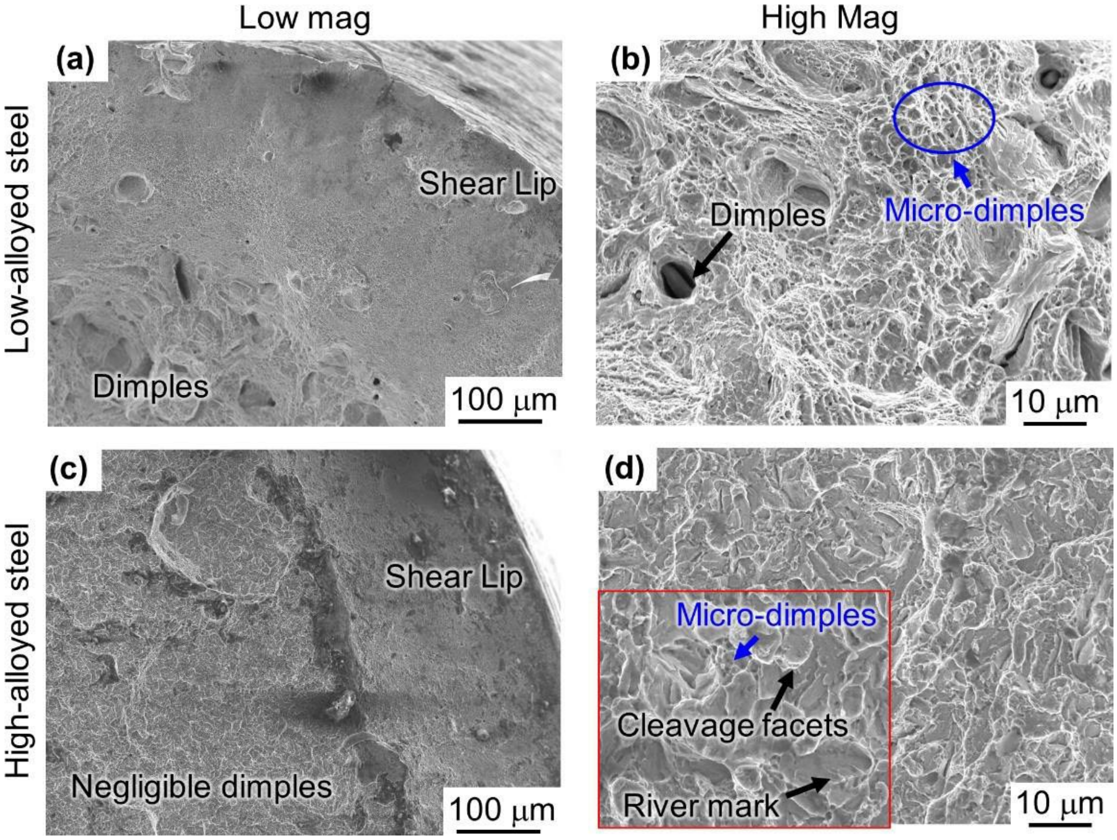

Figure 3. The fracture surface of the (a,b) low-alloyed steel and (c,d) high-alloyed steel.

To clarify the role of retained austenite in the deformation behaviour, the interrupted deformation was conducted and the subsequent changes in the retained austenite fraction are evaluated. The interrupted deformation was performed in the compression mode. The applied compressive strain was 10% at a maximum, with no cracking and significantly bulging. The maximum achievable uniform strains in tension mode are limited to relatively small strain, especially in the low-alloyed steel, so that interrupted deformation was carried out in compression mode.

In the low-alloyed steel, with the increase in strain, the retained austenite fraction shows no significant change (Fig.4a). But, in the high-alloyed steel, the retained austenite fraction decreases with the increase in strain. The phase distribution map shows that after deformation, the blocky form retained austenite is lesser than undeformed condition, qualitatively (Fig.4b and 4c). This indicates that blocky form retained austenite is more likely transformed into martensite through deformation. It was emphasized that blocky form retained austenite is less stable than thin-film, so it transforms into martensite by deformation with ease 4,14). It was also reported that the carbon content of the blocky form retained austenite is often lesser than thin-film, which can lower its stability 15).

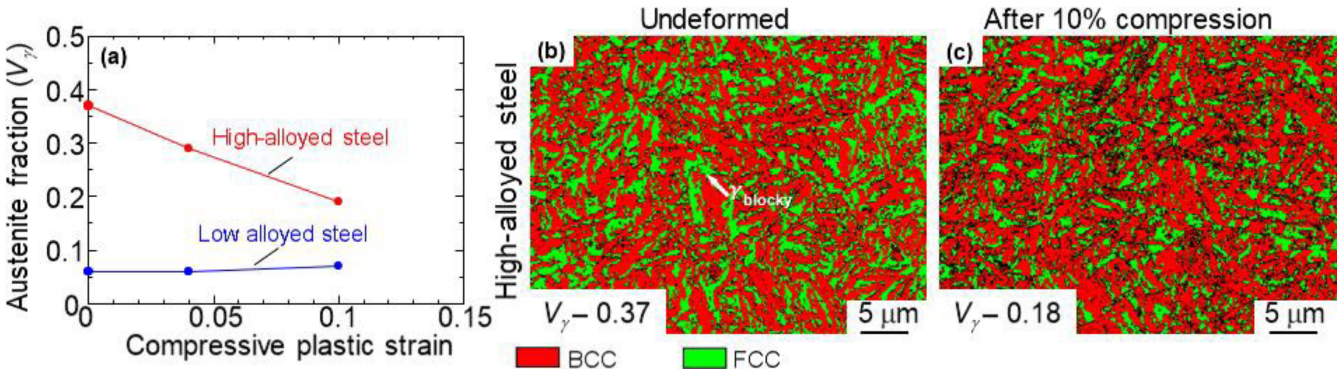

Figure 4. (a)Variation of the retained austenite fraction as a function of applied plastic strain, phase distribution map of high-alloyed steel (b) in undeformed condition and (c) after 10% compression.

These results demonstrate that deformation-induced martensitic transformation (DIMT) occurs in the high-alloyed steel but not significantly in the low-alloyed. Therefore, in the high-alloyed steel, the transformation induced plasticity effect caused by DIMT leads to a higher work hardening rate and delays the onset of plastic instability, thereby contributing to higher uniform elongation. The presence of a smaller fraction of the second phase in alloys consisting of two ductile phase is known to increase the strain to fracture 16-18), especially the post-uniform elongation is increased, because more strain partitioning is required for void initiation between the two phases 18). The low-alloyed steel has a small fraction of the retained austenite, and it is inherently ductile 4), these combinations would have promoted the ductile fracture mechanism (Fig.4a-b), leading to observed higher post-uniform elongation. The observation of the stable retained austenite in the low alloyed steel indicates that the refinement of austenite grains is more important that the acceleration of DIMT if the post-uniformelongation is desired. In addition, small amount of manganese also contributes the maintenance of ductility due to the restriction of segregation. The obtained results suggest that producing a low-alloyed bainitic structure with small stable retained austenite with limited content of manganese is a promising strategy for accomplishing high strength with excellent ductility, especially large post-uniform elongation in medium carbon steels.

In the present study, the experimental examination for the novel medium carbon bainitic steels designed by the sparse mixed regression model (SMRM) and the role of the retained austenite in the deformation behaviour is investigated. The low-alloyed steel designed by SMRM showed high post-uniform elongation than uniform elongation due to stable retained austenite and a small amount of retained austenite.

References

1) M. Takahashi:Nippon Steel Techn. Rep., 88 (2003) 2.
2) O. Matsumura, Y. Sakuma, Y. Ishii and J. Zhao: ISIJ Int., 32 (1992) 1110-1116.
3) K. Sugimoto, T. Iida, J. Sakaguchi and T. Kashima: ISIJ Int., 40 (2000) 902-915.
4) B.C. De Cooman: Curr. Opin. Solid State Mater. Sci., 8 (2004) 285-303.
5) H.K.D.H. Bhadeshia and D.V. Edmonds: Metal Sci., 17 (1983) 411-419.
6) F. Brun, T. Yoshida, J.D. Robson, V. Narayan, H.K.D.H. Bhadeshia and D.J.C. MacKay: Mater. Sci. Tech., 15 (1999) 547-554.
7) H.K.D.H. Bhadeshia : ISIJ Int., 39 (1999) 966-979.
8) T. Dutta, S. Dey, S. Datta and D. Das: Comput Mater Sci, 157 (2019) 6-16.
9) N.S. Reddy, J. Krishnaiah, S.G. Hong and J. S. Lee: Mater Sci Eng, A, 508 (2009) 93-105.
10) R Ueji, K.Nagata, H.Somekawa and M.Demura: Submitted to Scr. Mater.
11) S.Tokuda, K.Nagata and M.Okada: J. Phys. Soc. Jpn 86 (2017) 024001-9.
12) Y. Sakuma, O. Matsumura and H. Takechi: Metall Trans A, 22 (1991) 489-498.
13) H. K. D. H. Bhadeshia: ISIJ International, 42 (2002) 1059-1060
14) N. Tsuchida, T. Tanaka, and Y. Toji, , ISIJ Int., 60 (2020) 1349-1357.
15) F.G. Caballero, C. Garcia-Mateo, M.J. Santofimia, M.K. Miller and G.D. Andres: Acta Mater., 57 (2009) 8-17.
16) Z. Fan and A.P. Miodownik: Acta metall, mater. 41 (1993) 2415-2423.
17) S. Ankem and H. Margolin, Metall. Trans., 17A (1986) 2209-2226.
18) T. Inoue and S. Kinoshita: Trans. ISIJ., 17 (1977) 245-251.

Hydrogen Absorption Behavior and Absorbed Hydrogen Trapping Sites in Rolling Contact Fatigue

Miyuri Kameya[1,*], Toshiyuki Manabe[1], Naoki Matsui[1], Shingo Yamasaki[2] and Tomohiko Omura[1]

[1] Steel Research Laboratories, Nippon Steel Corporation, 20-1 Shintomi, Futtsu-Shi, Chiba, 293-8511, Japan
[2] Advanced Technology Research Laboratories, Nippon Steel Corporation, 20-1 Shintomi, Futtsu-Shi, Chiba, 293-8511, Japan
*email: kameya.rr7.miyuri@jp.nipponsteel.com

Keywords: martensitic steel, retained austenite, hydrogen embrittlement, rolling contact fatigue, thermal desorption analysis

1 Introduction

Bearings are used as important component parts in a wide variety of applications. Particularly in recent years, demand has risen for higher-strength steels for bearings used in the undercarriages and drive units of automobiles to satisfy requirements for smaller and lighter vehicles. Bearings have a problem of crack initiation and short life flaking caused by white etching area (WEA) alteration, a microstructural change that occurs during rolling contact fatigue[1-2)]. WEA is regarded as a microstructure generated due to dislocation rearrangement and dislocation cell formation during cyclic stressing under rolling contact fatigue[3)]. Because the WEA is simulated in a rolling contact fatigue test with hydrogen-charged steel[4)], it is considered as a phenomenon related to hydrogen in steel. To improve the rolling contact fatigue life of bearings, it is important to understand the behavior of hydrogen absorption into steels and the trapping sites of absorbed hydrogen during rolling contact fatigue.

In this study, the transitions during fatigue test in hydrogen absorption behavior and microstructure before the formation of WEA were investigated by using a two-roller rolling contact fatigue tester. To investigate the possibility of retained austenite being the trapping sites for absorbed hydrogen, specimens with different volume fraction of retained austenite were prepared, and the effect of the volume fraction of retained austenite on hydrogen absorption behavior was investigated.

2 Experimental Method

2. 1 Material

The test steel is JIS SCr420 (0.21C-0.25Si-0.74Mn-0.002P-0.001S-1.05Cr, mass %) which is the low-alloyed steel for machine structural use. The steel was vacuum melted, casted, and hot forged into φ35 mm round bars. From the φ35 mm round bars, φ26 mm roller specimens were prepared for the two-roller rolling contact fatigue test. The specimens were vacuum carburized at 1,203 K and quenched in a 353 K oil tank. The specimen A was tempered at 453 K after carburizing. The specimen B was subzero treated after carburizing to reduce the volume fraction of retained austenite and then tempered at 473 K. Because the volume fraction of retained austenite which is softer than martensite was lower in the specimen B than the specimen A, the specimen B was tempered at a higher temperature than the specimen A to achieve the same hardness as the specimen A.

2. 2 Rolling Contact Fatigue Test

The rolling contact fatigue test was conducted using a two-roller rolling contact fatigue tester. The small φ26 mm roller is the test roller and the large φ130 mm roller is the loading roller. The loading roller was made of JIS SUJ2 high-carbon chromium-bearing steel. The two-roller rolling contact fatigue test was conducted with a Hertzian maximum contact stress of 2.7GPa and slip rate of -40%. The contact width between the small and large rollers was about 6 mm. The number of cycles was varied between 5×10^5 and 2×10^7, and the test was finished before flaking occurred. After the test, the small-roller specimens were subjected to microstructural analysis and hydrogen analysis. The specimens for hydrogen analysis were removed from the tester immediately after the test and were stored in liquid nitrogen to prevent desorption of the hydrogen until the hydrogen analysis.

2. 3 Microstructural Analysis

The small-roller specimens before and after the tests were investigated for their microstructure, dislocation density, and volume fraction of retained austenite. The microstructures were observed with a transmission electron microscope (TEM).

The dislocation density was calculated by using the modified Warren-Averbach method from the average contrast factor. The TEM observations, and x-ray diffraction for the dislocation density calculation were conducted at a depth of 200 μm from the surface of carburized layer in which near the depth of maximum shear stress under the test conditions. The volume fraction of retained austenite was measured by X-ray diffractometry. The x-ray diffraction measurements were conducted at 0, 0.1, 0.2, 0.3, and 0.5 mm from the surface of carburized layer. The five-point average values were taken as the retained austenite volume fraction of the specimens.

2. 4 Hydrogen Analysis

The hydrogen analysis was conducted with the thermal desorption analysis (TDA) method, using a gas chromatograph as the detection system. From the small rollers after the test, φ26 × 5 mm L semicylindrical specimens containing the contact area with the large roller were cut out. These specimens were heated at a constant rate of 100 K・h^{-1} from room temperature to 873 K, and analyzed for hydrogen once per 5 min.

3 Results

Figure 1 shows the volume fraction of retained austenite before and after the rolling contact fatigue test. The volume fraction of retained austenite decreased with increasing number of cycles, probably because the martensite transformation of the retained austenite proceeded under rolling contact stress. Figure 2 shows dislocation substructure of the specimen A before the test and after 2 × 10^7 test cycles. The dislocations before the test were high in density and uniformly distributed. After 2 × 10^7 test cycles, on the other hand, there were regions where the dislocations were distributed at high density as before the test and regions where dislocation cell structures were formed. The specimen B showed the same microstructural changes as the specimens A. The dislocation density was 1.7 × 10^{16} m^{-2} and 9 × 10^{15} m^{-2} for the specimen A before the test and after 2 × 10^7 test cycles, respectively, and was 1.5 × 10^{16} m^{-2} and 7 × 10^{15} m^{-2} for the specimen B before the test and after 2 × 10^7 test cycles, respectively. This clarified that the dislocation densities decreased during contact fatigue test in both specimens A and B, and that the dislocation densities before and after the test were almost the same in both specimens A and B.

Figure 3 shows the hydrogen evolution-rate curves by TDA of the specimens A and B before the rolling contact fatigue test and 2 ×10^7 test cycles. The desorption of hydrogen was confirmed to have occurred between 300 and 450 K and between 623 to 873 K before the test. After 2 × 10^7 test cycles, the desorption of hydrogen was confirmed to have occurred between 300 and 423 K and between 623 and 873 K, and also between 423 and 623 K. These hydrogen desorption peaks are respectively called the first, second, and third peaks in ascending order of hydrogen desorption temperature. It was confirmed that only the second peak increased with an increasing number of cycles in both specimens A and B. Figure 4 shows the relationship between the hydrogen concentration at the second peaks of the specimens A and B and the number of cycles in the rolling contact fatigue test. It was confirmed that the increment of the second-peak hydrogen concentration during the rolling contact fatigue test was higher in the specimen A which is contained higher amount of retained austenite than the specimen B before the fatigue test.

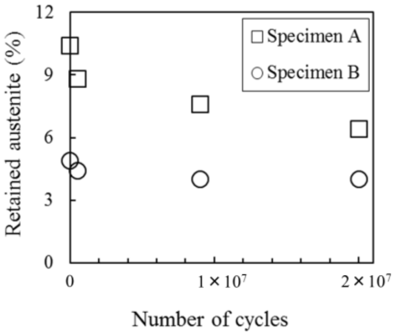

Fig. 1. Change in volume fraction of retained austenite before and after the rolling contact fatigue test[5].

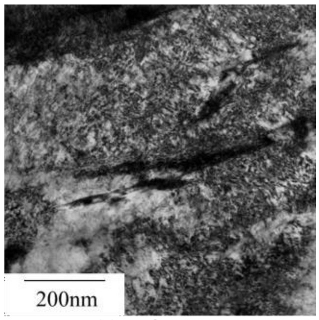

(a) Before test

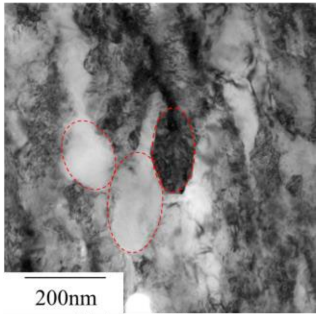

(b) After 2x10^7 cycles

Fig. 2. TEM micrographs of dislocation substructure in specimen A before the rolling contact fatigue test and after 2x10^7 test cycles. Circles represent the regions where dislocation cells formed.

To investigate the depth from the surface of specimen to which absorbed hydrogen exists, the test rollers of the specimen A (φ 26 mm) were thinned to φ 24.64 mm (0.68 mm reduction in radius) and to φ 23.0 mm (1.5 mm reduction in radius) after 9 × 10^6 cycles of the test. The normalized hydrogen concentration decreased as the thickness reduction in radius increased. Low levels of hydrogen were present in the specimen thinned by 1.5 mm in radius. This clarified that absorbed hydrogen was trapped to 1.5 mm depth beneath the rolling-contact surface under the rolling-contact fatigue test conditions of the present study. Figure 5 shows the hydrogen evolution rate curves of the specimen A preserved at room temperature for 30 days after the fatigue test to investigate the stability of the second-peak hydrogen. The first-peak hydrogen disappeared during 30 days after the fatigue test. On the other hand, it was confirmed that the height of the second-peak hydrogen did not change significantly from the value taken immediately after the test.

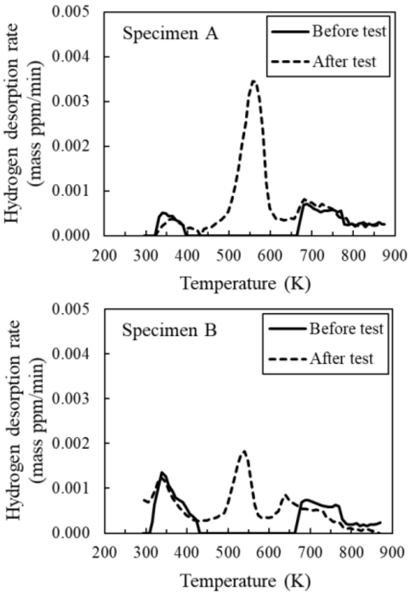

Fig. 3. TDA profiles of hydrogen before and after the rolling contact fatigue test.

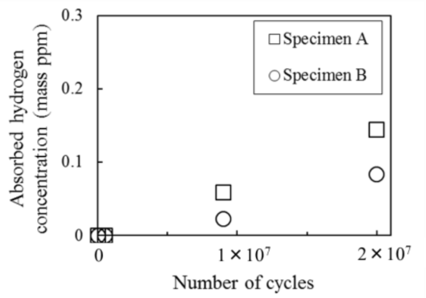

Fig. 4. Relationship between the absorbed hydrogen concentration at the second peaks and the number of cycles[5].

4 Discussion

4. 1 Microstructural Changes with Rolling Contact Fatigue

From both results of TEM observations and dislocation density measurements, it is considered that cyclic stressing under rolling contact fatigue caused the rearrangement of dislocations and the formation of dislocation cells[6], resulting in a decrease of the dislocation density. The reduction in the volume fraction of retained austenite was greater in the specimen A, which contained the higher volume fraction of retained austenite before the fatigue test. This mechanism is considered to be as follows: The specimen A contains larger volume fraction of thermally unstable austenite than the specimen B because the subzero treatment transformed the thermally unstable austenite to martensite in the specimen B. Assuming the similarity between thermal stability and stability against plastic deformation of retained austenite, thermally unstable retained austenite is easily transformed to martensite by plastic deformation associated with rolling contact fatigue[7].

4.2 Hydrogen Trapping Sites in Rolling Contact Fatigue

It has been reported that dislocation cores[8] and retained austenite[9] can be considered as trapping sites for the hydrogen desorbed at temperature around 423 to 623 K in TDA. The binding energy between the dislocation cores and hydrogen is 42 kJ·mol^{-1} [10], and the binding energy between the dislocation cores and carbon is 63.6 kJ·mol^{-1} [11]. Therefore, it has been reported that the hydrogen trapped by dislocation cores decreased during 7 days preservation of specimens at room temperature, because of the site competition with carbon atoms of which binding energy with dislocation is higher than that of hydrogen atoms[8]. In the present study, it was expected that if the trapping sites of the second-peak hydrogen were dislocation cores, the hydrogen in the dislocation cores would be replaced by carbon due to the site competition effect and would desorb from the specimens as the specimens were preserved at room temperature. However, the results in Figure 5 confirmed that the absorbed hydrogen concentration at the second peak did not change significantly when the rolling contact fatigue test specimens were preserved at room temperature for 30 days.

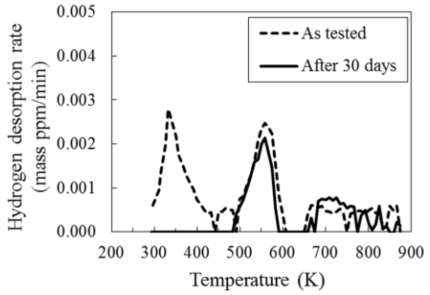

Fig. 5. TDA profiles of hydrogen of specimen A preserved at room temperature for 30 days after the rolling contact fatigue test[5].

The second-peak hydrogen concentration depended on the volume fraction of retained austenite before the fatigue test, and it was considered that the dislocation cores would not work as the main trapping sites for the second-peak hydrogen. From these results, it is considered that the main trapping sites of hydrogen absorbed during the fatigue test were related to retained austenite. The hydrogen trapping sites related to retained austenite are considered to be the bulk of retained austenite or the interface between martensite and retained austenite. The reason why the absorbed hydrogen concentration increases despite the decrease in the volume fraction of retained austenite with an increasing number of fatigue cycles is possibly due to the extremely high hydrogen solubility in FCC metals than that in BCC metals[12]. The absorbed hydrogen detected as the second-peak in the TDA profiles is not sufficient in the trapping sites originating from retained austenite at the early stage of fatigue cycles, and increases with an increasing number of cycles. Although the volume fraction of retained austenite decreases as the number of fatigue cycles increases, it is considered that stable retained austenite that has not transformed in rolling contact fatigue contributed as hydrogen trapping sites.

4. 2. 3 Activation Energy of Hydrogen Trap

To clarify the trapping sites for the second-peak hydrogen from the activation energy of hydrogen desorption Ea, Ea was calculated from the heating rate dependence of the hydrogen desorption peak temperature in TDA profiles by the Choo-Lee method[13]. The specimens of 2×10^7 fatigue test cycles were adopted and the heating rate was varied 0.014 to 0.056 $K \cdot s^{-1}$.

The Ea after the rolling contact fatigue test was 51 $kJ \cdot mol^{-1}$ for the specimen A and 56$kJ \cdot mol^{-1}$ for the specimen B. These Ea values of the specimens A and B are higher than 30 to 46 $kJ \cdot mol^{-1}$ reported by Sekine et al.[14] for a dual-phase steel composed of martensite and 10% retained austenite and 46 $kJ \cdot mol^{-1}$ reported by Takai et al.[12] for Inconel 625, an FCC metal. If the hydrogen trapping sites of the specimens A and B are austenite retained without transforming, the reason why the Ea is higher for the specimen B is considered to be the difference in hydrogen trapping energy between the bulk of retained austenite and the ferrite/austenite interface, or the difference in the size of the retained austenite. The hydrogen trapping energy by the dislocation cores is reported to be 42 $kJ \cdot mol^{-1}$ [10] and is lower than the Ea of the specimens A and B after the test. It was therefore considered that the dislocation cores are not considered to be the main trapping sites for the absorbed hydrogen.

In this study, it was presumed that the absorbed hydrogen is trapped in retained austenite. However, the Ea values after the rolling contact fatigue test were higher than the reported ones due to austenite. These results suggest that the absorbed hydrogen during the rolling contact fatigue would be trapped in more stable trapping sites relating to the retained austenite, which were formed under cyclic stressing by contact fatigue.

5 Conclusions

The hydrogen absorption behavior and microstructural changes in the rolling contact fatigue process were investigated by using the carburized SCr420 steel with the different volume fractions of retained austenite controlled by the subzero treatment. Following findings are obtained from the results:

(1) Hydrogen analysis using the TDA method confirmed hydrogen desorption at the second peak between 423 and 623 K only after the rolling contact fatigue test. The second-peak hydrogen concentration increased with an increasing number of cycles in the test. Absorbed hydrogen concentration was lower in the specimen, which reduced the initial volume fraction of retained austenite by subzero treatment.

(2) The second-peak hydrogen concentration depended on the volume fraction of retained austenite before the rolling contact fatigue test. The trapping sites for the hydrogen absorbed during the rolling contact fatigue test are mainly thought to have caused by retained austenite.

(3) The activation energy of hydrogen desorption after the rolling contact fatigue was 51～56 $kJ \cdot mol^{-1}$. It was higher than the reported ones due to austenite. This suggests that cyclic stressing formed more stable hydrogen trapping sites than no stressing, and that hydrogen was trapped at these sites.

References

1) H. Harada, T. Mikami, M. Shibata, D. Sokai, A. Yamamoto and H. Tsubakino: ISIJ International, **45** (2005), 1897.
2) Y. J. Li, M. Herbig, S. Goto and D. Raabe: Materials Characterization, **123** (2017), 349.
3) H. Harada, N. Oguma, A. Yamamoto and H. Tsubakino: *Tetsu-to-Hagané*, **89** (2003), 789 (in Japanese).
4) H. Uyama, H.Yamada, H. Hidaka and N.Mitamura: Tribology Online, **6**(2011), 123.
5) M. Kameya, T.Manabe, N. Matsui, S. Yamasaki and T. Omura: ISIJ International, **61** (2021), 1264.
6) E. Sakurada, S. Hiwatashi and K. Ushioda: J. Japan Inst. Metals, **80**(2016), 655 (in Japanese).
7) R. C. Dommarco, K. J. Kozaczek, P. C. Bastias, G. T. Hahn and C. A. Rubin: *Wear*, **257**(2004), 1081.
8) D. Hirakami, S. Yamasaki, T. Tarui and K. Ushioda: *Tetsu-to-Hagané*, **100** (2014), 1322 (in Japanese).
9) T. Nagase, T. Ito, Y. Nishimura, H. Suzuki and K. Takai: *Tetsu-to-Hagané*, **102** (2016), 534 (in Japanese).
10) S.Taketomi, R.Matsumoto and N.Miyazaki: *Acta Mater.*, **56**(2008), 3761.
11) E.Clouet, S.Garruchet, H.Nguyen, M.Perez and C.S.Becqart: *Acta Mater.*, **56**(2008), 3450.
12) K. Takai, K. Murakami, N. Yabe, H. Suzuki and Y. Hagihara: J. Japan Inst. Metals, **72** (2008), 448 (in Japanese).
13) W. Y. Choo and J. Y. Lee: METALLURGICAL TRANSACTIONS A., **13**(1982), 135.
14) D. Sekine, K. Takai, Y. Sakiyama and T. Omura: *CAMP-ISIJ*, **31**(2018), 798, CD-ROM (in Japanese).

Exploration of optimal microstructure for improving strength and ductility of dual-phase steels

Takayuki Shiraiwa
The University of Tokyo

In recent years, with the increasing demand for weight reduction of automobile bodies to save energy and reduce environmental impact, research and developments of advanced high strength steels (AHSS) that achieve both higher strength and workability are actively conducted. However, increasing the tensile strength (TS) generally tends to decrease the elongation at failure (EL), which is well known as a “strength-ductility trade-off.” In this study, to overcome the trade-off relationships between TS and EL, we examined three types of exploration methods for optimizing the microstructure of dual-phase (DP) steels. The strategy of this study is to create a large number of synthetic microstructures with a wide range of morphology in advance and then search within the microstructural database with crystal plasticity finite element analysis (CPFEA) with ductile damage model. Initially, 100 random searches (RS) with CPFEA were conducted to obtain initial values of TS and EL, and random forest regression was performed on the results of RS to extract important microstructural descriptors. The volume fraction of martensite, the principal component of the persistent homology representing the connectivity of martensite grains, and the principal component of the two-point spatial correlation function representing the band structure were selected as the important microstructural descriptors. The selected microstructural descriptors were used for each exploration. The first exploration method is Bayesian optimization using Gaussian process regression, the second method is BLOX (BoundLess Objective-free eXploration), and the third is a one-class support vector machine (OCSVM). The results of three types of exploration methods will be discussed in the presentation.

Atomistic calculations of the interaction between screw dislocations and symmetric tilt grain boundaries in iron

Chiharu Kura[1,*], Masato Wakeda[2], Kazushi Hayashi[1] and Takahito Ohmura[2]

[1] Applied Physics Research Laboratory, Kobe Steel, Ltd., 1-5-5 Takatsukadai, Nishi-ku, Kobe 651-2271, Japan
[2] Research Center for Structural Materials, National Institute for Materials Science, 1-2-1 Sengen, Tsukuba, Ibaraki 305-0047, Japan
*email: kura.chiharu@kobelco.com

Keywords: screw dislocation, grain boundary, iron, molecular static simulation

1. Introduction

It is still important to develop steel with higher strength and longer life for weight reduction and the safety of transportation equipment and social infrastructures. The yield strength and fracture strength of steel depend on the lattice defects such as dislocations and grain boundaries (GBs). However, the effects of lattice defects on the fracture of steel are still unclear. Even in brittle fractures at the GB, dislocation-based plastic deformation occurs near the GB before the final fracture. Therefore, revealing the dislocation-GB interaction should provide a useful understanding of the GB related to deformation and fracture. In this study, we report the interaction between screw dislocations and symmetric tilt grain boundaries (STGB) in bcc-Fe based on molecular static (MS) simulation.

2. Experimental

The interaction energy between the screw dislocation and <111> STGB [Σ7(123), Σ37(347)] was evaluated by MS simulation at 0 K. The model size was 800 nm × 0.75 nm × 600 nm, and the number of atoms was about 26 million. Periodic boundary conditions were applied only in the y-axis direction ($[1\,1\,\bar{1}]$). Then, a screw dislocation, in which both the Burgers vector and line direction are parallel to the $[1\,1\,\bar{1}]$ y-axis, was introduced in the models.

3. Results

The interaction energies between the GB and the screw dislocation ($E_{disl\text{-}GB}$) were evaluated in terms of the dislocation-GB distance along the x-axis. $E_{disl\text{-}GB}$ was defined as follows:

$$E_{disl\text{-}GB}(d) = E(d) - E_0 \qquad (1)$$

where $E(d)$ gives the potential energy of the models with the distance d after relaxation, and E_0 is the potential energy of the model with the largest d after relaxation. As a result, Σ7 GB shows a large attractive interaction energy ($E_{disl\text{-}GB}$ = -19.0 eV /Å), in contrast to Σ37 GB has a negligibly small interaction energy.

Furthermore, as a result of stress distribution investigation, when the spiral dislocation reached Σ7GB, the screw dislocation was dissociated into two partial dislocations along the GB, and the GB was twisted and shifted in the y direction. On the other hand, in Σ37GB, no significant change was observed in the stress field regardless of the dislocation position.

4. Conclusion

We investigated the interaction energy between screw dislocations and the STGB in BCC-Fe by using large-scale models for the MS simulations. We found that the interaction between screw dislocations and the STGB and the atomic shifts depends on the stability of the GB structure. Furthermore, it is thought that these differences can be discussed from an energy landscape perspective.

Acknowledgement

This work was performed under the support of the National Institute for Materials Science (NIMS).

Effect of hardenability on anisotropic deformation of steel cylinder in carburized quenching process

Haruka Yoshida[1,*], Yusuke Kawaragi[1], Yusuke Usui[2],
Hideki Imataka[3], Masayuki Horimoto[4] and Kazuo Okamura[4]

[1] Research & Development, Nippon Steel Corporation, Amagasaki, Hyogo 660-0891, Japan
[2] Osaka Office, Nippon Steel Corporation, Osaka City, Osaka Pref. 541-0041, Japan
[3] Kyushu Works, Yawata Area, Nippon Steel Corporation, Kitakyushu, Fukuoka 804-8501, Japan
[4] Research & Development, Nippon Steel Corporation, Futtsu, Chiba. 293-8511, Japan
*email: yoshida.4st.haruka@jp.nipponsteel.com

Keywords: steel, quenching, hardenability, quench distortion

1. Introduction

Heat treatment is used to impart desirable properties to steel. To improve the strength of steel alloys, quenching that produces martensitic structures is used. During the quenching process, hardenability is an important indicator that represents the ability of steel to form martensite. If the hardenability of steel is high, the product has a martensitic structure up to the inner part. Quenching often causes deformation and it can become a challenge in manufacturing. To suppress deformation with quenching, it is important to clarify the effects of hardenability on deformation.

In this study, the effects of hardenability on deformation in the carburizing-quenching process in the case of a steel cylinder specimen are investigated. The study includes the quenching process and numerical analysis which simulates the experiment and attempt to clarify mechanisms of deformation.

2. Experimental and Simulation Procedures

2.1 Experimental procedure

Heat treatment experiments, which includes carburization, quenching and tempering step, were carried out with cylindrical test pieces of steel. The diameter and length of the test pieces were 27 mm and 200 mm, respectively. Three types of steel were used. The experiment was done at two temperatures of quenching oil, 60°C and 80°C. The changes in diameter after heat treatment were investigated using the laser displacement sensor. The changes in length after heat treatment were investigated using the depth gauge. The hardenability of steel alloys was also evaluated by measuring the hardness at the center of the cylinder.

2.2 Simulation procedure

Numerical analysis which simulates the experimental quenching process was carried out to calculate deformation, stress and volume fraction of phases through the quenching process. It was carried out using finite element program ABAQUS1) with the developed user subroutine2). The reaction kinetics model proposed by Li et al. was adopted3) to consider diffusional transformation.

Common conditions used for simulations were as follows, material properties of various structural steel alloys with specified hardenability bands were used. The model used in the simulation was 1mm in length, which was part of the φ27mm cylinder test piece as shown in Fig. 1 (a). To simplify the procedure, the axisymmetric model shown in Fig. 1 (b) was used. The heat treatment process of the experiment shown in Fig. 2 was considered in the simulation. The temperature of quenching oil was set at 60°C before the austenite grain size was set at 6.0.

Various conditions of hardenability and transformation plasticity coefficient were used for the simulation to investigate their effects on deformation with quenching. To consider hardenability, the chemical composition of steel was varied within the range of structural steel alloys with specified hardenability bands. It is possible to change incubation time until diffusional transformation starts. Transformation plasticity coefficients were given as the values of cases 1-4, as shown in Table 1. K_B and K_M are coefficients for bainite transformation plasticity and martensite transformation plasticity, respectively.

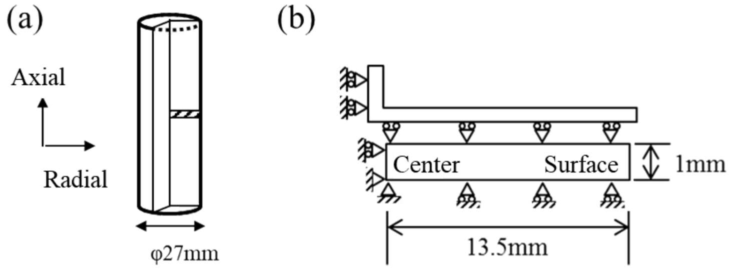

Fig. 1 Model used for the simulation

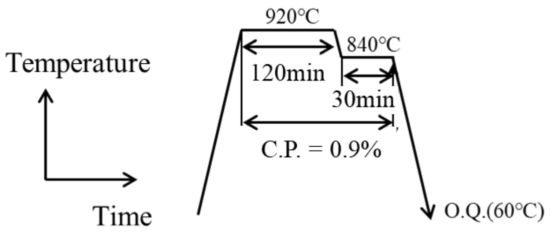

Fig. 2 Heat treatment process

Table 1 Conditions of transformation plasticity coefficient

Case	K_B ($\times 10^{-5}$ [MPa^{-1}])	K_M ($\times 10^{-5}$ [MPa^{-1}])
1	10.0	7.64
2	10.0	0.0
3	0.0	7.64
4	0.0	0.0

3. Results

Fig. 3 shows the relationships between measured (a) diameter and (b) length change rate as a function of hardness at the center of the specimen. Fig. 3 (a) shows that the measured change rate in diameter increases as hardenability increases. This coincides with a general relationship that the whole volume expands as the volume fraction of martensite increases. Conversely, the length change rate increase under 30 HRC hardness and decrease over 30 HRC hardness as hardenability increases, as shown in Fig. 3 (b). Therefore, the measured change in length does not agree with the relationship mentioned above.

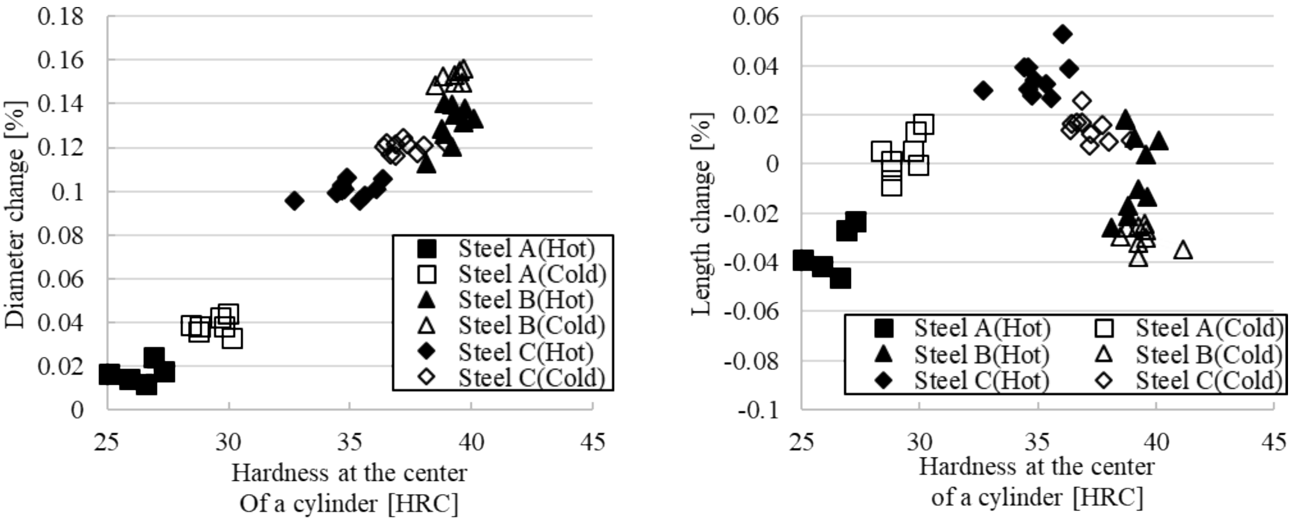

(a) Diameter change

(b) Length change

Fig. 3 Relationship between measured deformation and hardness in carburized quenching process.

Fig. 4 (a) and (b) show the relationship between calculated deformation and hardness in the carburized quenching process. The conditions of cases 1-4 are shown in Table 1. In case 1, the simulated results show the same trend as shown in Fig. 3. In case 4, both diameter and length change rates increase with the increase of hardness. However, in cases 1 and 2, the slope of length change rate decreases as the hardenability increase.

Moreover, differences in diameter change and length change between case 1 and case 4 are shown in Fig. 5 (a). It was concluded that the values indicate the effect of transformation plasticity. The differences of diameter change are positive values in the range of 0.048 to 0.076, as shown in Fig. 5 (a). The results depict a convex upward curve. However, the differences of length change resulted in a convex downward curve with negative values in the range of -0.15 to -0.098. Fig. 5 (b) shows the replots the values in Fig. 5 (a) using twice the diameter changes and the negative values of length change. These values are approximately the same, see Fig. 5 (b).

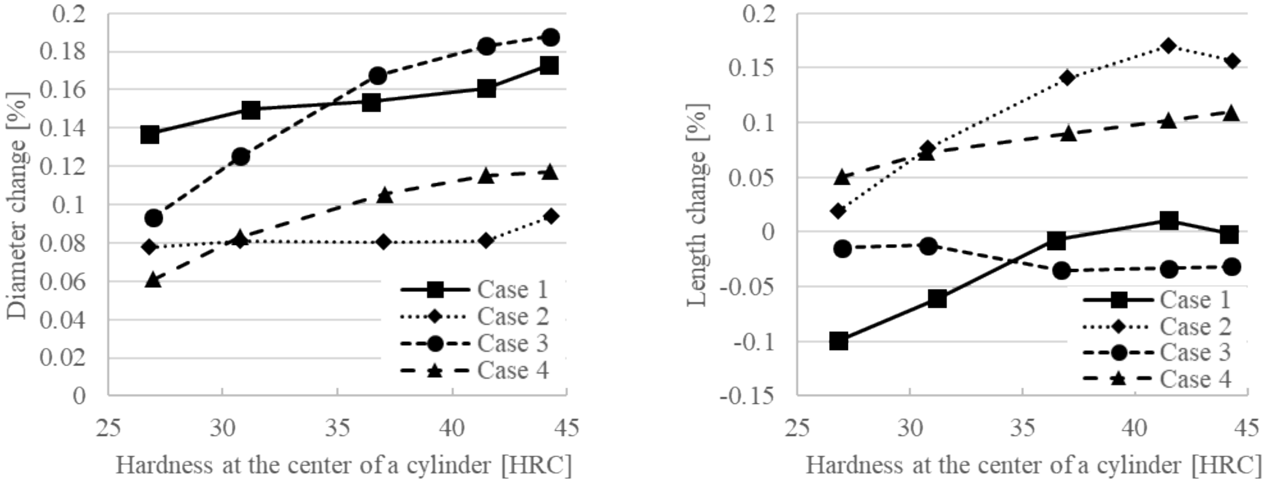

(a) Diameter change (b) Length change

Fig. 4 Relationship between calculated deformation and hardness in carburized quenching process.

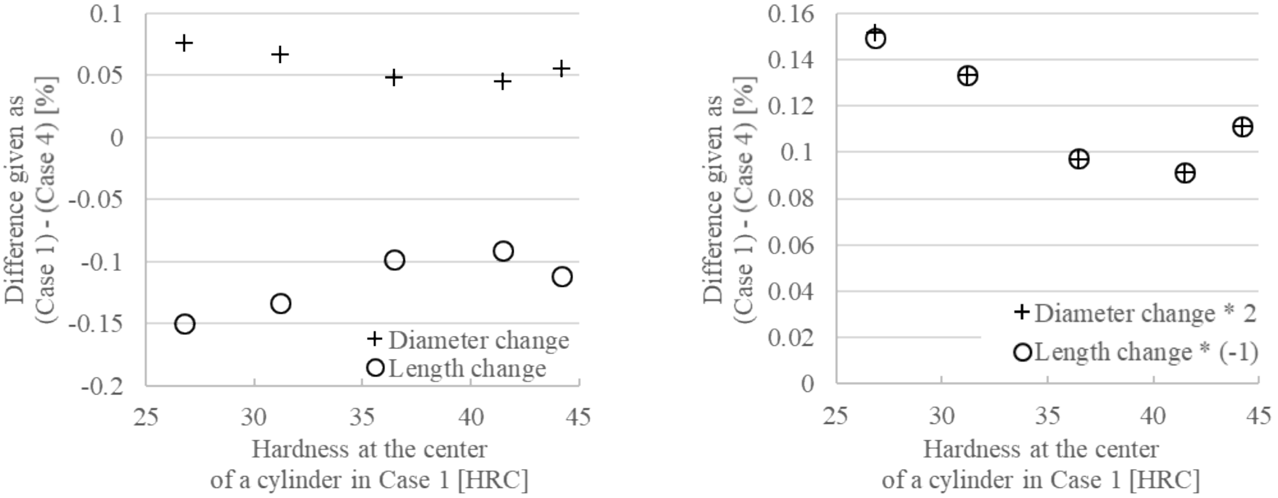

(a) Values of differences (b) Differences multiplied by coefficients

Fig. 5 Differences in diameter change and length change between case 1 and case 4.

4. Discussion

The calculated results shown in Fig. 4 (a) and (b), for cases 1 and 2, show the same trend as the experimental results in which the slope of length change rate decreases as hardenability increases. Case 1 and 2 includes transformation plasticity with bainite transformation. Therefore, numerical analysis indicates that bainite transformation plasticity affects the change in length.

Although the volume expansion on phase transformation was said to be isotropic, the ratio of transformation plasticity strain in a radial to axial direction was -1:2. It is shown as the ratio of changes in diameter and length change between case 1 and case 4, see Fig. 5 (b). This is explained by the axisymmetric model which has increments of transformation plasticity strain proportional to deviation stress. Therefore, transformation plasticity results in a smaller strain in the radial direction and a larger strain in the axial direction. Consequently, in the radial direction, monotone increases because phase transformation is the dominant factor of strain in quenching deformation. However, in the axial direction, transformation plasticity is the dominant factor of strain. Therefore, the characteristic trend that the change in length changes from increasing to decreasing is shown, and it was derived from bainite transformation plasticity. This is indicative of different behavior of quenching deformation in both radial and axial directions.

The main factors determining transformation plasticity are stress and volume fraction of the new phase. Fig. 6 shows the two factors 25 s after quenching. Fig. 6 (a) shows the volume fraction of bainite (solid lines) and the volume fraction of martensite (dashed lines) of the cylindrical specimen at the center to its surface. Within 5mm from the center axis, only bainite transformation takes place. However, over 5 mm away from the center axis, martensite transformation takes place. As hardenability increases, bainite volume fraction decreases and martensite volume fraction increases. The distribution of axial stress through the model of the cylindrical specimen from the center to its surface is shown in Fig. 6 (b). The results show more change in stress for the inner part compared to the outer part as hardenability increases. In low hardenability, compressive stress occurs in the inner part, however, for medium and high hardenability, tensile stress occurs in the inner part. Accordingly, as the hardenability increases, the axial stress during bainite transformation increases and the volume fraction of bainite decreases. Thus, the transformation plasticity with bainite transformation results in shrinkable strain for low hardenability, larger expansion strain for medium hardenability, and smaller expansion strain for high hardenability. This is also indicative of the maximum value shown at medium hardenability for the change in length.

In quenching, bainite transformation occurs in the inner part, and martensite transformation occurs in the outer part at the same time. The volume expansion with martensite transformation is greater than that with bainite transformation. However, displacement in axial direction is constrained. This is indicative of occurrence axial tensile stress in the inner part.

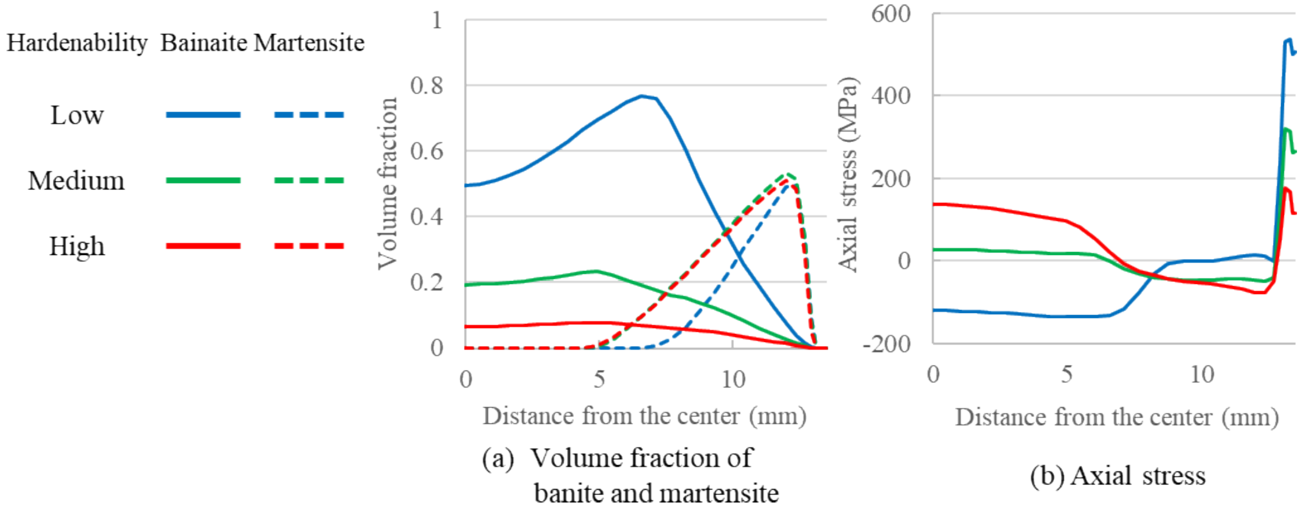

(a) Volume fraction of banite and martensite

(b) Axial stress

Fig. 6 Volume fraction and axial stress after 25 s from start of quenching in calculation.

5. Conclusion

The effects of hardenability on deformation in the carburized quenching process in the case of steel cylinder specimens were investigated. The experiment was performed with the quenching process and numerical analysis which simulates the experiment and attempt to clarify the mechanism of deformation.

The results show that upon quenching, diameter change increases as the hardenability increase. However, length change decreases as hardenability increases in high hardenability steel alloys. This is due to the difference of the dominant factor on the strain. The dominant factor in diameter change was the volume expansion, however, in length change was transformation plasticity. As hardenability increases, axial stress during bainite transformation increase with the decrease in volume fraction of bainite. This is shown as the maximum value of change in length at medium hardenability.

References

1) ABAQUS/Standard User's Manual for version 6.14, Dassault Systèmes(2014).

2) Fukumoto M., Yoshizaki M., Imataka H., Okamura K. and Yamamoto K., J. Soc. Mat. Sci., Japan, Vol.50, No.6, pp.598-605(2001).

3) M.Victor Li, David V.Niebuhr, Lemmy L.Meekisho, and David G.Atteridge, Metallurgical and materials transactions B, Vol.29B, pp.661-672(1998).

Micromechanical investigation of ductile void nucleation in dual-phase steels with varying microstructure

Fabien Briffod[1,*], Kyohei Murayama[1], Takayuki Shiraiwa[1] and Manabu Enoki[1]

[1] Department of Materials Engineering, The University of Tokyo, 7-3-1 Hongo, Bunkyo-ku, Tokyo 113-8656, Japan
*email: briffod@rme.mm.t.u-tokyo.ac.jp

Keywords: Dual-phase steel, finite element method, damage initiation stress triaxiality, Lode angle

1. Introduction

Dual-phase (DP) steels, composed of a mixture of soft and ductile ferrite grains and harder and more brittle martensite islands are among the most widely used materials in structural application due to their simple alloying composition, good formability, and cost-effective thermomechanical treatments[1)]. To overcome the so-called strength-ductility trade-off, it is desired to develop damage-resistant DP steels through microstructural optimization. Microstructure-oriented design strategy based on the virtual exploration of microstructural instances using especially the finite element method (FEM) has become an attractive strategy to accelerate such exploration, thus circumventing lengthy and costly experiment-based trial-and-error approaches. However, reliable predictions require both an accurate representation of microstructural features and a physically based constitutive model of its deformation and damage mechanisms at the relevant scale.

In this study, an integrated experimental-numerical procedure is therefore proposed for the calibration of the ductile void nucleation locus in DP steels at the microstructural scale. To this end, interrupted tensile tests were performed on different DP steels with varying microstructure to track the location and nucleation sequences of voids with applied strain. The microstructures were numerically reproduced in a FE software and subjected to the same loading conditions. The local stress-strain paths at observed void sites were extracted and used for the calibration of a phenomenological Hosford-Coulomb (HC) ductile damage model considering the effect of the local plastic strain, the stress triaxiality and the Lode angle[2)].

2. Materials and Method

2.1. Materials and experimental procedures

The materials investigated in this work are DP steels produced from the same commercial low-carbon (Fe-0.15C-1.5Mn) ferrite-pearlite hot-rolled steel with different thermal treatments as depicted in Fig. 1. The obtained microstructures are referred to as DP800, DP900 and DP1000 as their tensile strength were about 800, 900 and 1000 MPa, respectively. The martensite volume fraction was 35%, 57% and 79% for the DP800, DP900 and DP1000 steel.

Double-dogbone micro-tensile specimens with a gage length of 2 mm, a width of 1.5 mm and a thickness of 1.4 mm were machined from the heat-treated materials. They were subjected to uniaxial tensile test, interrupted at different strain level. At each interruption, the complete specimen surface was recorded by laser microscope for digital image correlation (DIC) analysis and by scanning electron microscope for void tracking. DIC analysis was performed using the open-source software Ncorr for Matlab[3)].

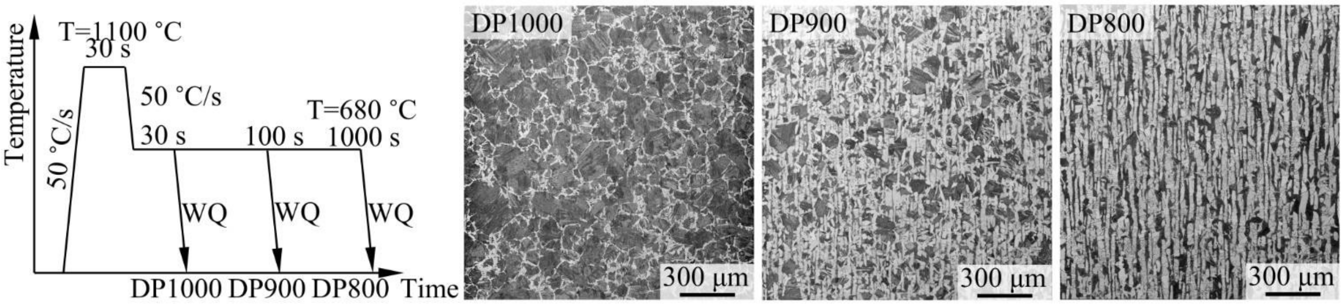

Fig. 1 Schematic diagram of the thermal treatment and optical micrographs of the different dual-phase steels.

2.2. Numerical procedure

Phase maps were extracted from the segmentation and binarization of optical micrographs of the specimens surfaces and exported into a FE software. They were subjected to the same loading condition as in the experiment following a sub-modeling approach proposed by Matsuno et al.[4]. The mechanical response of each phase was modeled by isotropic elasticity and isotropic hardening based on the Voce law using a von Mises yield surface. The constitutive parameters were calibrated using 3D representative volume element (RVE) of the different steels. The mechanical response of the ferritic phase was kept constant for the three materials, while that of the martensitic phase was adjusted notably to account for the difference in carbon content in this phase due to a variation of volume fraction for the three materials. To validate the procedure the equivalent plastic strain fields predicted by numerical simulations and estimated by DIC were compared for each material.

The local stress-strain paths at void sites, described in terms of equivalent plastic strain ε_p, stress triaxiality η and Lode angle parameter θ were extracted for each microstructure and used for the calibration of the phenomenological HC model[2] where the strain to failure is defined as:

$$\varepsilon_f(\eta,\bar{\theta}) = b(1+c)^{1/n}\left\{\left[\frac{1}{2}\left((f_1-f_2)^a+(f_2-f_3)^a+(f_1-f_3)^a\right)\right]^{1/a} + c(2\eta+f_1+f_3)\right\}^{-1/n}, \qquad (1)$$

where a, b, c, n are fitting parameters and

$$f_1(\bar{\theta}) = \frac{2}{3}\cos\left[\frac{\pi}{6}(1-\bar{\theta})\right],\ f_2(\bar{\theta}) = \frac{2}{3}\cos\left[\frac{\pi}{6}(3+\bar{\theta})\right],\ f_3(\bar{\theta}) = -\frac{2}{3}\cos\left[\frac{\pi}{6}(1+\bar{\theta})\right], \qquad (2)$$

three trigonometric function dependent on the Lode angle parameter. The procedure for the calibration is described in our recent work[5].

3. Results and Discussion

3.1. Stress-strain curve and void distribution

Fig. 2 depicts the stress-strain curve of the DP800 and DP1000 steels as well as the number of voids observed on the surface at the different interrupted strains, distinguishing between ferrite/martensite (**F/M**) decohesion and martensite/martensite (**M/M**) cracking. First voids were observed to nucleate at relatively low macroscopic strain, between 1.4 to 2.4% strain for the two materials. The number of voids continuously increased until failure of the specimen at about 10% strain. Both **F/M** and **M/M** were observed in relatively equivalent proportion for the DP1000 steel while most voids in the DP800 material originated from **M/M** cracking. The fracture surface of the DP800 specimen formed a clear 45° angle with the loading direction while the path it was more serrated for the DP1000 with the main crack mostly propagating within ferritic phase.

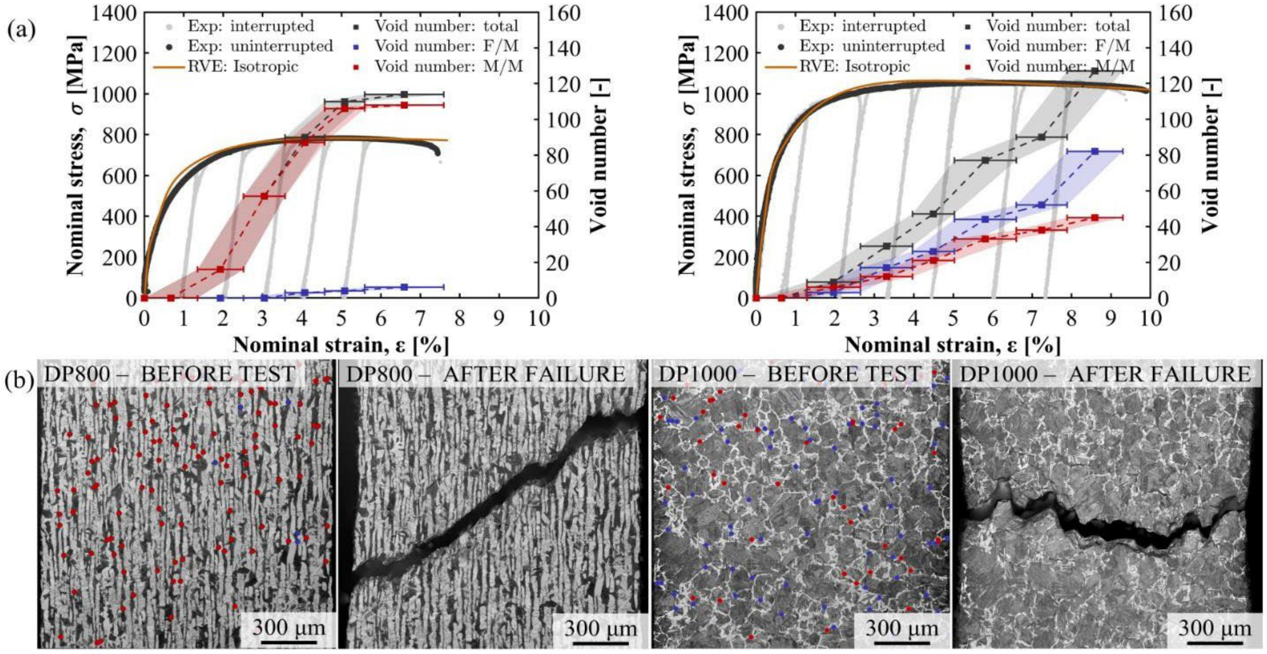

Fig. 2 (a) Stress-strain curve of the DP800 and DP1000 steels with void numbers per strain increment and (b) optical micrographs of the specimen before test and after failure. Locations of void sites are reported in the micrograph before test.

3.2. Comparison of plastic strain distributions

To validate the modeling approach and clarify the effect of microstructure morphology on strain partitioning, the equivalent plastic strain field estimated by DIC and FE analysis were compared. Fig. 3 reports the equivalent plastic strain fields at a macroscopic strain of about 2.5% of the experiments and simulations for the DP800 and DP1000 specimens. Significant plastic strain accumulation was observed at **F/M** interfaces for the two materials. In addition, the plastic activity in the martensitic phase of the DP1000 was higher than that of the DP800. Overall, the numerical simulation correctly predicted the spatial distribution of the plastic activity but slightly overestimated local intensity especially in region with high strain concentration.

The results suggests that the strain partitioning in ferritic phase is mainly affected by the spatial distribution and phase contrast between the two phases. In addition, the modeling approach correctly reproduced the higher plastic activity in the martensite phase of the DP1000 which can be attributed to larger block size due to coarser prior austenite grains as the block size in lath martensite is generally proportional to the prior austenite grain size[6].

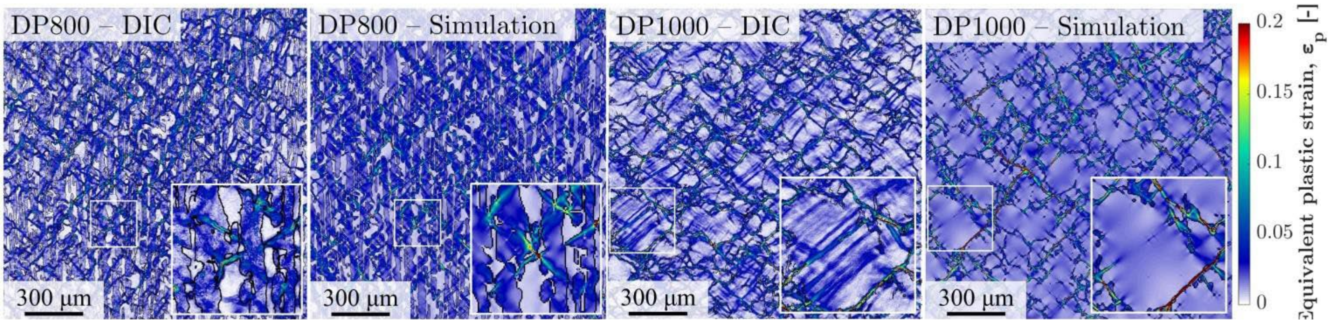

Fig. 3 Comparison between the equivalent plastic strain fields at a macroscopic strain of about 2.5% estimated by DIC and FE analysis for the DP800 and DP1000 steel.

3.3. Stress-strain path of void sites and damage initiation locus

The stress-strain phat of surface void nucleation sites were extracted from the results of the simulations and reported in the mixed stress-strain (η, θ, ε_p) in Fig. 4. Only voids observed after the third interruption were reported. At the beginning of the tensile load, within the macroscopic elastic domain, paths were located close to the (η=1/3, θ=1) corresponding to the plane-stress uniaxial tension condition. While **M/M** void paths showed a smooth evolution and remained confined to a limited region close to the initial point, the **F/M** voids were more erratic and revealed significant path changes before any significant plastic deformation occurred. These results suggested that the loading type conditioned the initial local stress-state, but other intrinsic factors related to microstructural features (phase distribution and strength discrepancies) highly affect the paths upon straining, especially for the ferrite phase near void sites.

The different stress-strain paths were used to calibrate the ductile damage initiation HC model through the introduction of a strain-based damage variable D:

$$D(\varepsilon) = \int_0^{\varepsilon} \frac{d\varepsilon_p}{\varepsilon_f(\eta,\bar{\theta})} \tag{3}$$

where a void is assumed to nucleate once D=1. Prior to reaching 1, the local microstructure is considered damage-free. The HC model defined in Eq. 1 was thus calibrated so that the damage variable for each loading path reached 1 within the interruption interval where void was observed to nucleate. The damage initiation loci of the best fit for the HC model are thus reported in Fig. 4 together with the evolution of the damage variable.

Considering **M/M** voids, the damage initiation loci for the two materials were predicted to be the same and nearly independent on the stress triaxiality and Lode angle. Consequently, **M/M** damage initiation may only depend on the equivalent plastic strain which was found to be close to 4% for the materials. This result is consistent with common modeling hypothesis for martensite failure where stress-based criterion based for instance on the maximum principal stress component are often used[7].

On the other hand, for **F/M** void sites, the result of the fitting suggests a strong dependence on the stress triaxiality but limited to no effect of the Lode angle. The strain to failure at void sites appeared to decrease with the increase in stress triaxiality which is consistent with other investigations[8].

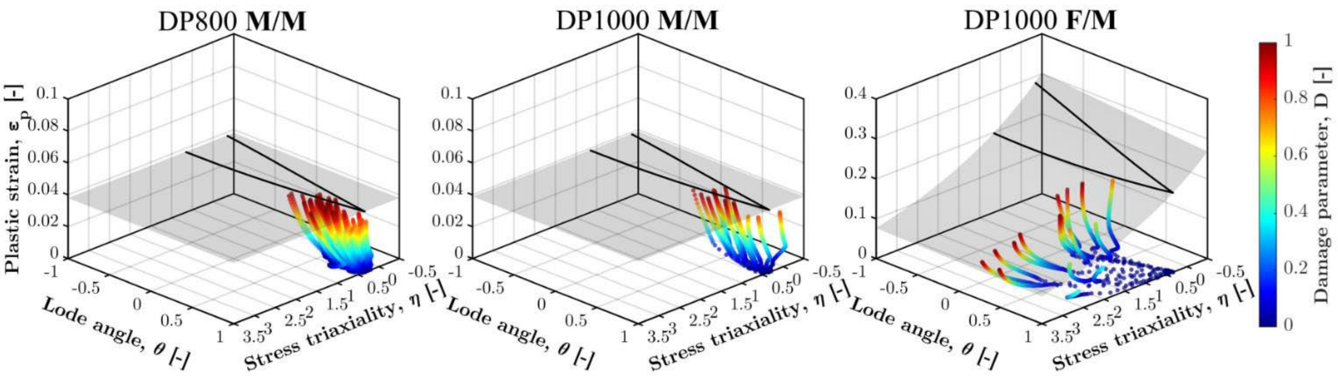

Fig. 4 Local stress-strain path at void sites for the DP800 and DP1000 steels and estimated Hosford-Coulomb damage initiation locus.

Conclusions

In the present study, an integrated experimental-numerical analysis was presented for the investigation of local stress-strain path at void sites in DP steels and the precise calibration of a phenomenological damage initiation model. The following conclusions can be drawn:

1- The comparison of plastic activity observed experimentally and predicted numerically suggest that the phase distribution and strength discrepancy are critical parameters controlling the local stress-strain paths at void sites.

2- The calibration of the HC model for **M/M** voids suggested an independence of damage nucleation on both the stress triaxiality and Lode angle.

3- Damage initiation at **F/M** interface was observed to be dependent on the stress triaxiality but not the Lode angle parameter, with a decrease in strain to failure with the increase in stress triaxiality.

Acknowledgement

This work was partially supported by Council for Science, Technology and Innovation (CSTI), Japan, Cross-ministerial Strategic Innovation Promotion Program (SIP), Japan, "Materials Integration", for Revolutionary Design System of Structural Materials (Funding agency: JST) and by the JSPS KAKENHI for Early-Career Scientists (Grant No. 20K14604).

References

1) C.C. Tasan, M. Diehl, D. Yan, M. Bechtold, F. Roters, L. Schemmann, C. Zheng, N. Peranio, D. Ponge, M. Koyama, K. Tsuzaki and D. Raabe: Annu. Rev. Mater. Res. **45** (2014) 391-431.
2) D. Mohr and S.J. Marcadet: Int. J. Solids Struct. **67-68** (2015) 40-55.
3) J. Blaber, B. Adair and A. Antoniou: Exp. Mech **55** (2015) 1105-1122.
4) T. Matsuno, C. Teodosiu, D. Maeda and A. Uenishi: Int. J. Plast. **74** (2015) 17-34.
5) F. Briffod, T. Shiraiwa and M. Enoki: Mater. Sci. Eng. A **826** (2021) 141933.
6) S. Morito, H. Yoshida, T. Maki and X. Huang: Mater. Sci. Eng. A **438-440** (2006) 237-240.
7) A. Ramazani, A. Schwedt, A. Aretz, U. Prahl and W. Bleck: Comput. Mater. Sci. **75** (2015) 459-474.
8) N. Vajragupta, V. Uthaisangsuk, B. Schmaling, S. Münstermann, A. Hartmaier and W. Bleck: Comput. Mater. Sci. **54** (2012) 271-279.

Evaluation of residual stress at circular punched end-face and its validity

Yuji Sakiyama[1*], Tomohiko Omura[1], Takashi Yasutomi[2], Takayuki Harano[3], Kengo Noami[4]

[1] Steel Research Lab., Nippon Steel Corporation, Futtsu, Chiba, 293-8511, Japan
[2] Nagoya Research Lab., Nippon Steel Corporation, Tokai, Aichi, 476-8686, Japan
[3]Advanced technology research Lab., Nippon Steel Corporation, Futtsu, Chiba, 293-8511, Japan
[4]Nippon Steel Technology Co., Ltd., Futtsu, Chiba, 293-0011, Japan
*email: sakiyama.76d.yuuji@jp.nipponsteel.com

Keywords: Residual stress, Shearing, Hydrogen embrittlement

Abstract: The deformation and shearing that occur in the manufacturing of steel products depend on various factors. However, these phenomena often deteriorate the mechanical and other properties of the products. For example, it is known that the sheared edge is degraded by residual stresses. In this study, we investigated the residual stresses at a circular punched endface in tempered martensitic high-strength steel sheets. The residual stresses were measured using the $\sin^2\psi$ method of X-ray diffraction (XRD), which can only evaluate stress along one direction. To evaluate the shear residual stress on the plane (x-y), it is necessary to perform XRD measurements in three directions, i.e., along the thickness (x-axis), circumference (y-axis), and diagonal. The maximum principal stress of the residual stress was calculated using the Jacobi method based on the assumption that there were no residual stresses in the depth direction (z-axis). The 1/4t, 1/2t, and 3/4t parts of the punched end face in 2 mm-thick sheetswere evaluated. The maximum principal stress at 1/2t was almost consistent with its tensile strength. However, the maximum principal stress at the 1/4t part was lower than that at other parts. This is because the normal stress along the thickness direction was significantly lower than that for the other parts. To confirm the accuracy of the residual stress values, hydrogen cracks were formed on the punched end face in the same specimen by cathodic hydrogen charging. The direction of the cracks showed good agreement with the angle of the maximum principal stress.

1. INTRODUCTION

In recent years, efforts to reduce the weight of automobiles have led to remarkably improved fuel efficiency. Therefore, it is necessary to increase the strength of steel to further reduce the weight of automobiles. However, hydrogen embrittlement poses as a serious problem as the strength of steel increases. Therefore, the number of studies on the hydrogen embrittlement of steel sheets for automobiles is increasing. The effect of hydrogen embrittlement on the cut surface (end face by shearing) is very important to consider. Hydrogen embrittlement is caused by three factors: material type, amount of hydrogen in materials, and degree of stress in materials. As stress factors in hydrogen embrittlement at sheared end faces, it is necessary to consider both, the load stress and residual stress. This further complicates studies because it is difficult to investigate the residual stress on the end face. Previous studies have reported measurements of residual stress at the shear end face[1-3)]. The normal stresses in only two directions, width and thickness, were measured in these studies. However, hydrogen embrittlement occurs because of the maximum principal stress. In other words, it is not sufficient to measure only two normal stresses to accurately understand the criteria for hydrogen embrittlement; it is also necessary to measure the shear stresses and estimate the maximum principal stress.

In this study, the plane stress and maximum principal stress were evaluated by measurements in three directions using the $\sin^2\psi$ method. Furthermore, the relationship between the maximum principal stress and hydrogen cracking was verified to confirm the accuracy of the residual stress values.

2. EXPERIMENTAL

2.1. Materials

A low-alloy steel, Japanese Industries Standard (JIS)-SCM435, with the chemical composition listed in Table 1, was used. The steel was melted in a vacuum induction furnace and cast into an ingot. The ingot was hot-rolled into a 3.5 mm-thick plate. The plate was cold-rolled into a 2.0 mm sheet. The sheet was kept at 1153 K for 4 min, die-quenched, then tempered at 673 K for 20 min. The obtained steel sample had a tempered martensitic structure with a tensile strength of 1501 MPa. The Vickers hardness was 468 Hv.

Table 1. Chemical composition of the steel used (mass%).

C	Si	Mn	P	S	Al	Cr	Mo	N
0.36	0.30	0.77	0.016	0.014	0.03	1.03	0.17	0.003

2.2. Circular punching

50 × 50 mm sheets cut from a 2.0 mm-thick tempered steel sheet were sheared with a 10 mm circular punch. The clearance was 11.6 %. The punching speed was set to 100 mm/s.

2.3. Residual stress measurement

The residual stress at the sheared end face was measured using the $\sin^2\psi$ method. However, this method can only evaluate one-directional normal stress. Therefore, in the following discussion, the plane stress condition was assumed. Three normal stresses were measured. Fig. 1 shows the X-ray measurement method and positions. Ten incident X-ray angles were set between 0° and 45°. The *x*- and *y*-axes represent the thickness and circumferential directions, respectively. The incident X-ray directions were 180°, 225°, and 270°. The measurement positions were 1/4t, 1/2t, and 3/4t. Cr K α radiation was employed, and the X-ray-irradiated area was 0.3 mmϕ.

The normal stress σ_{xx} in the thickness direction was determined from measurements in the ϕ=180° direction. The normal stress σ_{yy} in the circumferential direction was determined from measurements in the ϕ=270° direction. The shear stress σ_{xy} on the *x-y* plane was calculated using Eq. 1(θ= 45°). The normal and shear stresses in the depth direction (*z*-axis) were set to zero. The maximum principal stress and its angle in the *x-y* plane were calculated using the unique formula of the stress tensor and the Jacobi method.

$$\sigma_{[\varphi=225^\circ]} = \frac{\sigma_{xx}+\sigma_{yy}}{2} + \frac{\sigma_{xx}-\sigma_{yy}}{2}\cos 2\theta + \sigma_{xy}\sin 2\theta \qquad \text{Eq. 1}$$

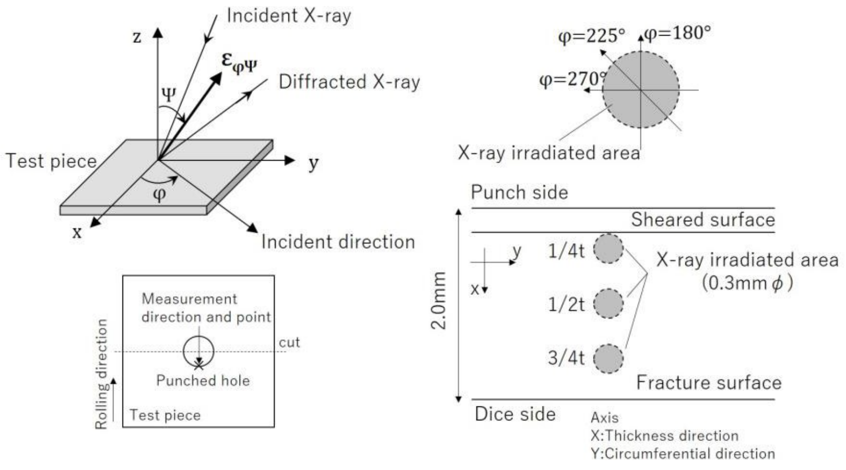

Fig. 1. Setup for XRD measurements and positions of the specimen.

2.4. Relationship between the maximum principal stress and hydrogen embrittlement

The relationship between the direction of the maximum principal stress and the hydrogen cracks was verified. Hydrogen cracks occurred on the punched end face in the same specimen after cathodic hydrogen charging for 1 h. The solution consisted of 3% NaCl and 3 g/L NH_4SCN. The cathode current density was 1.0 mA/cm^2. Hydrogen cracks were observed using an optical microscope (200 × magnification).

3. RESULTS

3.1. 2θ-sin2 ψ diagram

Fig. 2 shows 2θ-$\sin^2\psi$ diagrams against three measurement directions at the 1/4t position. Ψ splits were confirmed in the 180° and 225° directions at each position, indicating the occurrence of shear stress. The 1/2t and 3/4t positions exhibited the same tendency, so they are omitted from the discussion here.

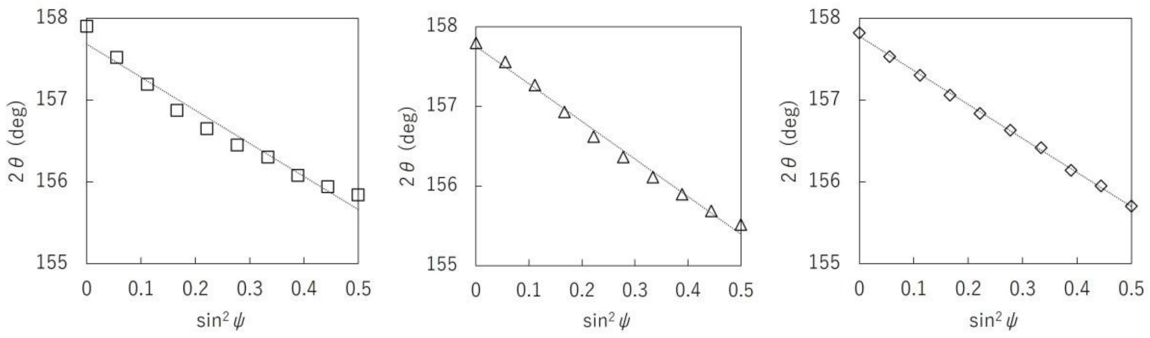

(a) ϕ=180° (b) ϕ=225° (c) ϕ=270°

Fig. 2. 2θ-$\sin^2\psi$ diagrams at the 1/2t position.

3.2. Residual stress

Fig. 3 shows the normal stresses measured at positions 1/4t, 1/2t, and 3/4t. The σ_{yy} in each position changed slightly compared with σ_{xx}. By contrast, only σ_{xx} at 1/4t was significantly lower than σ_{xx} at the 1/2t and 3/4t positions. Fig. 4 shows the shear stresses estimated at each position. There was little difference between σ_{xy} at each position, and these values were much lower than the normal stresses. Fig. 5 shows the maximum principal stresses at each position. The σ_1 values at 1/2t and 3/4t were almost consistent with its tensile strength. On the other hand, σ_1 at the 1/4t position was slightly lower than σ_1 at 1/2t and 3/4t. This is because σ_{xx} was significantly lower than σ_{xx} at the other positions.

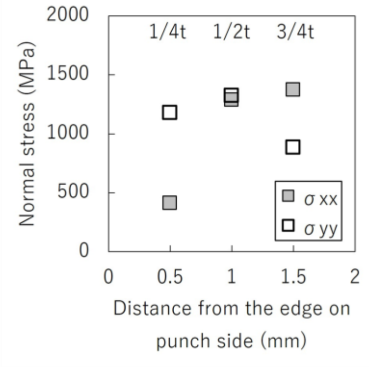

Fig. 3. Normal stresses.

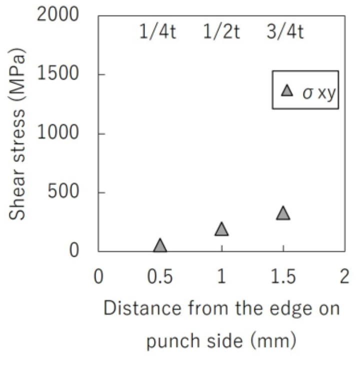

Fig. 4. Shear stresses.

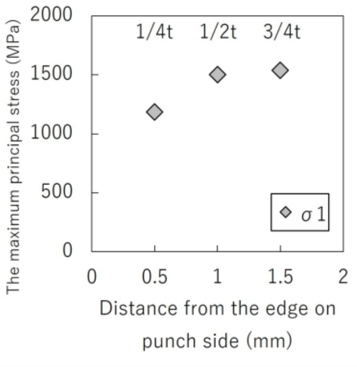

Fig. 5. Maximum principal stresses.

3.3. Hydrogen crack

Fig. 6 shows an optical micrograph of the punched end face after cathodic hydrogen charging. The red dashed lines indicate hydrogen cracks, and the X-ray-irradiated areas are shown. Hydrogen cracks did not occur in the X-ray-irradiated area at the 1/4t and 1/2t positions. However, the crack extended in the thickness direction on the right side of the X-ray-irradiated area at the 1/4t and 1/2t positions. At the 3/4t position, multiple cracks were observed in the X-ray-irradiated area.

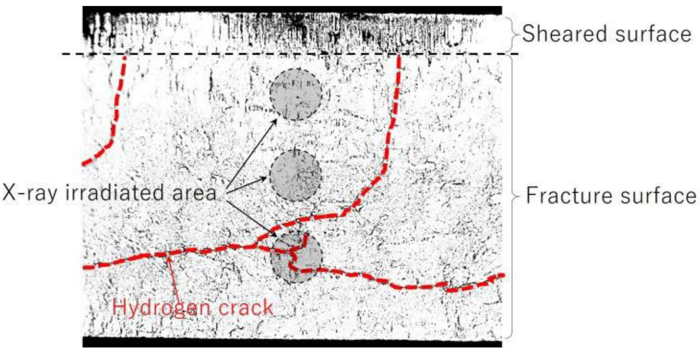

Fig. 6. Hydrogen cracks on the punched end face.

4. DISCUSSION

Hydrogen embrittlement occurs because of the maximum principal stress. Therefore, the relationship between the maximum principal stress and hydrogen cracks was investigated. The cracks were considered to have occurred perpendicular to the angle of σ_1. Fig. 7 shows the hydrogen cracks estimated from the calculated angle of σ_1. The estimated crack angle was closer to vertical on the punch side and closer to horizontal on the dice side. This result indicates that the direction of the cracks was in good agreement with the angle of the maximum principal stress. Therefore, the estimated residual stresses in this study were considered to be accurate.

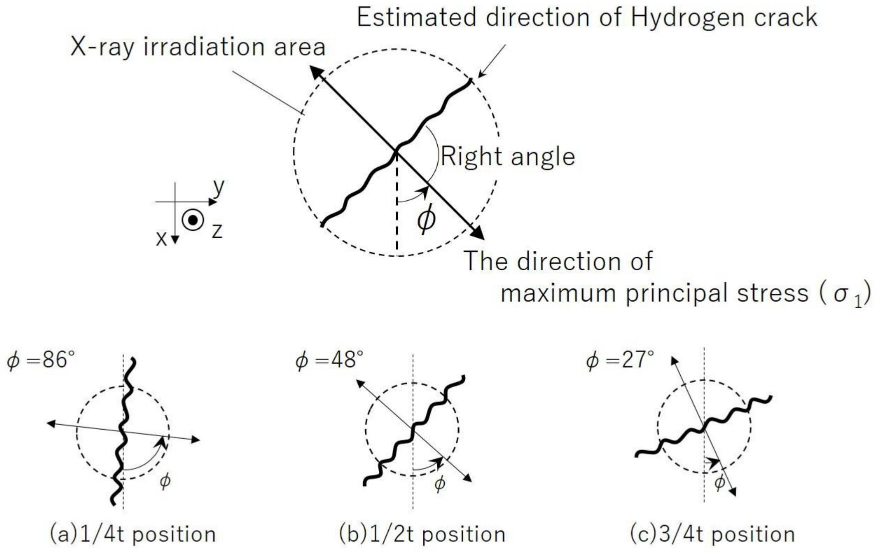

(a)1/4t position (b)1/2t position (c)3/4t position

Fig. 7. Angle of hydrogen crack estimated from the calculated angle of the maximum principal stress.

CONCLUSION

The residual stresses at the circular punched end face were measured using the $\sin^2\psi$ method. The maximum principal stress and the relationship between the maximum principal stress and hydrogen embrittlement were estimated for these stresses. The following results were obtained:

1) Ψ splits were confirmed in the 180° and 225° directions at each position. This result indicated that shear stress occurred.

2) The maximum principal stress at 1/2t was almost consistent with its tensile strength. However, the maximum principal stress at 1/4t was lower than that at other parts. This is because the normal stress along the thickness direction was significantly lower than that for the other parts.

3) The direction of the hydrogen cracks was estimated based on the angle of the maximum principal stress, and was in good agreement with it.

References

1) K. Mori, N. Nakamura, Y. Abe and Y. Uehara: *J Manuf Process*., 68(2021), 435-444.
2) T. Matsuno, Y. Sekito, E. Skurada, T. Suzuki, K. Kawasaki and M. Suehiro: *Testu-to-Hagané*, 100(2014), 29-35.
3) T. Yasutomi, S. Yonemura, T. Yoshida, M. Mizumura: *Sosei-to-Kako,* 60(2019), 301-306.

The work-hardening behavior of pearlite under strain path changes

Kohei Nakada[1,*], Takeshi Toyoda[2], Shigeru Yonemura[2], Akihiro Uenishi[2]

[1] Nagoya Works, NIPPON STEELCORPORATION,Tokai, Nagoya 476-8686, Japan
[2] Reserch and Development, NIPPON STEEL CORPORATION, Futtsu, Chiba 293-8511, Japan
*email: nakada.ha8.kohhei@jp.nipponsteel.com

Keywords: steel, work-hardening, Bauschinger effect, pearlite

The mechanical behavior of pearlite steel has been investigated mainly focusing on its high work hardening rate. It is said that the high work hardening rate of pearlite steel is contributed from the elastic backstress emerging on ferrite/cementite surface, so Bauschinger effect in pearlite steel is presumed to be large. In this study, we focused on the relationship between the morphology of cementite and Bauschinger effect in pearlite steel, which isn't well clarified. In order to evaluate the effect of lamellar spacing of cementite, we conducted simple-shear tests, in which we changed the strain path to the opposite direction from the direction of pre-strain in order to evaluate Bauschinger effects. The samples were prepared to have several lamellar spacing of cementite by varying the phase transformation temperature, chemical composition of chromium, and annealing time. Generally, the work hardening behavior can be divided to the isotropic hardening deriving from intersections of dislocations and the kinetic hardening deriving from elastic back stress by depositions of moving dislocations. To divide the work hardening behavior to isotropic hardening component and kinetic hardening component, we used Lemaitre-Chaboche model to evaluate them by parameters Rsat and Xsat, which represent the saturation stress of isotropic hardening and kinetic hardening respectively. Compared to ferrite steel, the rate of Xsat to initial yield stress was larger in pearlite steel. This means that the flow stress of the work hardened pearlite steel mainly consists of the elastic back stress emerging at cementite interface at least in initial stage of deformation. Also, kinetic hardening component of pearlite steel increased as the lamellar spacing decreased. This result indicates that the emerging elastic back stress in pearlite may increase in mean free path of dislocations decreases.

1. Introduction

Pearlite steel can be one of the highest tensile strength steels because of its outstanding high work-hardening rate. It is an important issue to elucidate the work-hardening mechanism of pearlite steel in order to increase the strength of steel. There are several studies in which pearlite steels are deformed in one direction, for example, the wire drawing deformation. However, in order to reveal the mechanisms of the work-hardening behavior around the yielding points, it is rather effective to analyze the work-hardening behavior by changing strain paths . When the direction of deformation changes, unique phenomena such as the Bauschinger effect[1)] or the cross effect[2)] occur. By these phenomena, the stress-strain curve changes from that of one direction deformation, which gives us the information of dislocation substructure related to work-hardening. Generally, the work hardening behavior can be divided into isotropic hardening deriving from intersections of dislocations and the kinetic hardening deriving from elastic back stress by depositions of moving dislocations. To divide them, it is effective to use Lemaitre-Chaboche model[1)], which describes the yield function by the isotropic hardening components and the kinetic hardening components. In this study, we focused on the influence of lamellar spacing of cementites on Bauschinger effects in pearlite steel. We performed the simple-shear-to-simple-shear tests to several pearlite steels which have different lamellar spacing in cementites and investigated the relationship between the morphology of cementites and the work-hardening behavior by using Lemaitre-Chaboche model.

2. Experimental procedures and data analysis

Steel ingots having the chemical components shown in Table 1 were casted. Ingots were hot-rolled to the thickness of 3.0 mm and inserted into a furnace at the temperature (T_1=660℃, 620℃, 580℃) shown in Figure 1 for 30 minutes to obtain fully pearlite steels with different lamellar spacing (P1, P2, P3 steel). We also prepared ferrite-pearlite steel with pearlite fraction of 8% as the purpose of comparison (F steel). After the hot-rolling or the following annealing, we grinded the surface of the sheet steels to the thickness of 2.0 mm and cut off the simple-shear tests samples shown in Figure 4.

Table 1. Chemical composition of the steels (mass%)

	C	Si	Mn	P	S	Al	Cr	Ti
P1	0.70	0.20	0.99	0.009	0.002	0.017	-	-
P2	0.69	0.19	0.98	0.008	0.002	0.018	0.40	-
P3	0.69	0.19	0.99	0.008	0.002	0.018	0.70	-
F	0.09	0.02	0.74	0.008	0.001	0.020	-	0.06

Figure 2 shows the examples of SEM imaging of samples. By changing Chromium contents and transition temperatures, fully pearlite steels were obtained with different lamellar spacing.

Figure 4 shows the schematic illustration of simple-shear-to-simple-shear tests. In this tests, we applied simple-shear stress at the illustrated section in Figure 4, and measured the angle θ to convert into the shear strain. After the shear plastic strain reaching 0.05, 0.1, 0.15, we changed the shear stress to oppsite direction. From the shear stress τ and the shear strain γ, we calculaterd the stress–strain curves and fitted it by Lemaitre-Chaboche model3) shown bellow.

$$
\begin{gathered}
\mathrm{J}(\sigma - X) - R - Y = 0 \\
\mathrm{dR} = C_R(R_{sat} - R)d\,\epsilon \\
dX\ = C_X(X_{sat}d\epsilon_p/d\epsilon_p - X)d\epsilon_p
\end{gathered}
$$

In these formula, Y represents initial yielding stress, Rsat represents saturation stress of isotropic hardening, and Xsat represents saturation stress of kinetic hardening. Xsat and Rsat can be affected by the dislocation behavior: the former is related to the immobilization of dislocations and the latter is related to the elastic back stress in the material emerging from piling up of dislocations around precipitates or harder second phases.

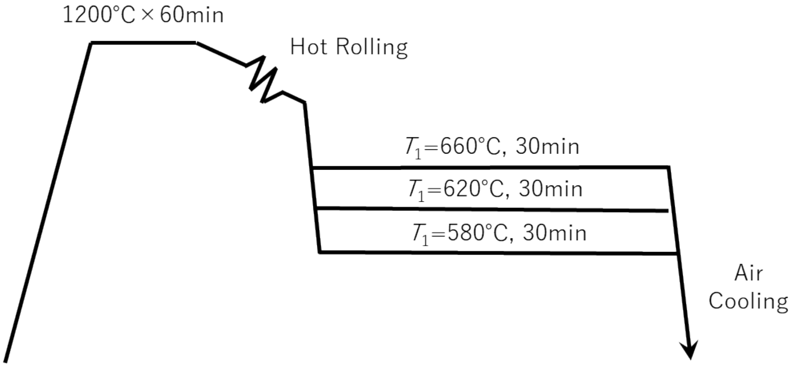

Figure 1. Condition of hot-rolling and annealing

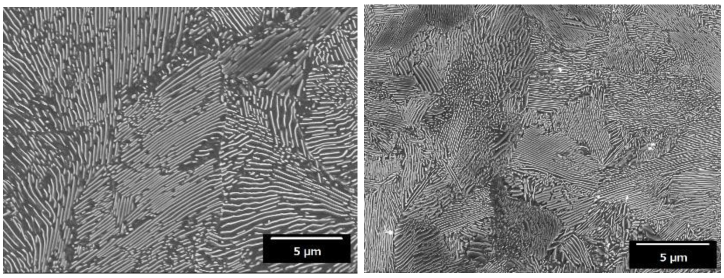

Figure 2. SEM image of samples
[left: P1(T_1=620℃), right: P3(T_1=580℃)]

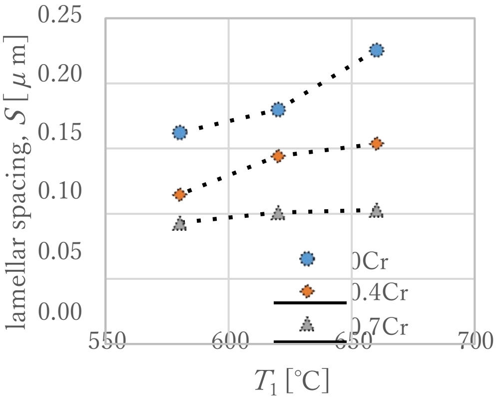

Figure 3. lamellar spacing of samples

3. Results and Disscussions

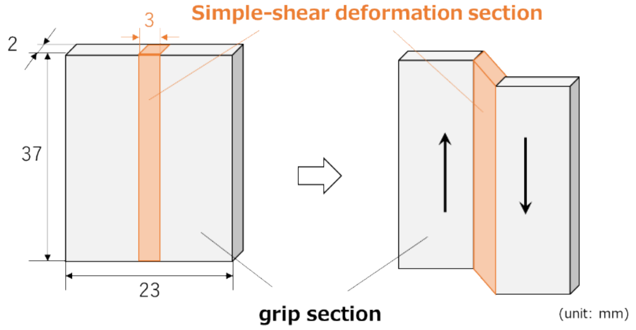

Figure 4. Simple-shear tests

Figure 5 shows the shear-stress-shear-strain curves of P1 steel with T_1=620℃ and F steel. When the pre-strain of 0.15 (shear strain) is applied, flow stress (shear stress) P1(T_1=620℃) and F are 587 MPa and 296 MPa respectively. When the pre-strain of 0.15 is applied, 0.2% proof shear stress of P1(T_1=620℃) and F are 58 MPa and 254 MPa. Therefore, the reductions of yielding stress by Bauchinger effect of P1(T_1=620℃) and F are 529 MPa and 4 MPa respectively, which means that the Bauchinger effect of pearlite significantly appears compared to that of ferrite.

Table 2 shows the value of fitting parameter of Lemaitre-Chaboche model. To exclude the difference of strength among samples, we will discuss Xsat/Y and Rsat /Y. Compared to ferrite steel, Xsat/Y of pearlite steel was large. Also, Rsat /Y. of pearlite was small compared to ferrite steel. Since Xsat/Y is much larger than Rsat /Y in pearlite, it is thought that the work-hardening behavior in pearlite is mainly dominated by the elastic back stress emerging from piling up of dislocations around cementite. This tendency became prominent when the lamellar spacing of pearlite was small.

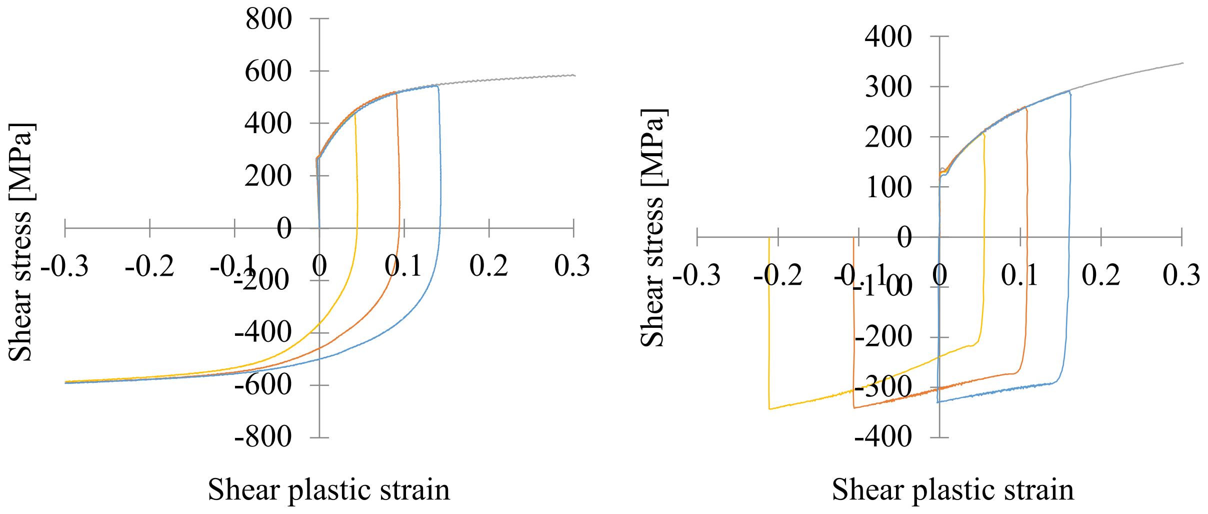

Figure 5. Stress-Strain curve in simple-shear-to-simple-shear tests [left: P1(T_1=620℃), right: F]

Table 2. Fitting parameter of Lemaitre-Chaboche model

sample	P1(T_1=660℃)	P1(T_1=620℃)	P1(T_1=580℃)	P2(T_1=660℃)	P2(T_1=620℃)	P2(T_1=580℃)	P3(T_1=660℃)	P3(T_1=620℃)	P3(T_1=580℃)	F
lamellar spacing [µm]	0.225	0.180	0.162	0.153	0.144	0.114	0.120	0.110	0.093	-
C_r	2.93	2.93	2.93	2.93	2.93	2.93	2.93	2.93	2.93	6.24
C_x	30.2	26.5	31.6	29.0	26.6	25.3	30.5	33.4	34.5	142
R_{sat}	247	182	155	193	129	38	194	126	37	246
X_{sat}	428	487	535	504	554	609	527	598	660	52
Y	548	577	596	594	616	666	635	660	694	81
X_{sat}/R_{sat}	1.7	2.7	3.4	2.6	4.3	16.0	2.7	4.7	17.7	0.21
R_{sat}/Y	0.5	0.3	0.3	0.3	0.2	0.1	0.3	0.2	0.1	3.05
X_{sat}/Y	0.781	0.844	0.897	0.848	0.899	0.914	0.830	0.906	0.951	0.64

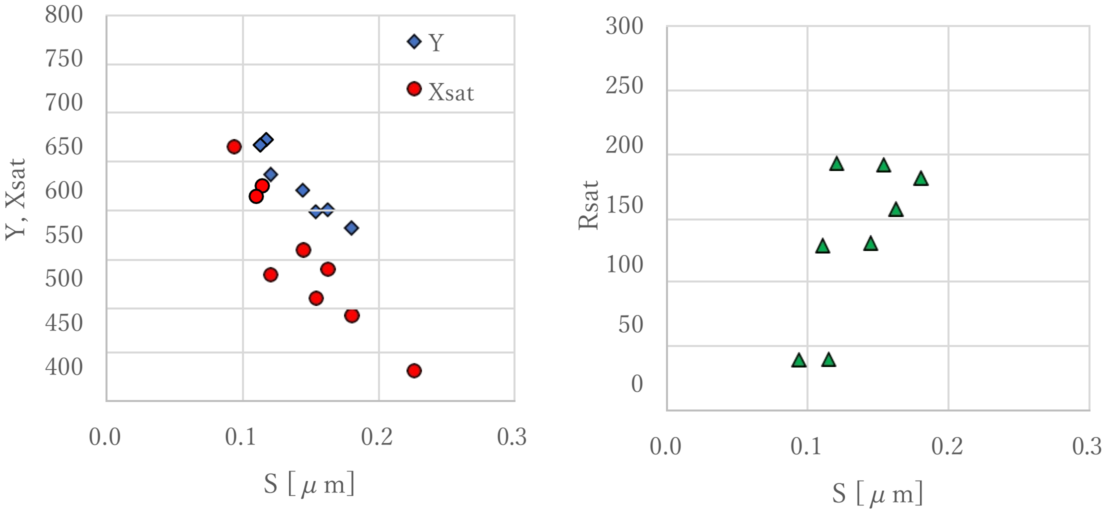

Figure 6. relationship between lamellar spacing and Y, Xsat, Rsat

Figure 6 shows the relationship between lamellar spacing in pearlite and parameters of Lemaitre-Chaboche model. As lamellar spacing become small, initial yielding stress Y and the saturation stress of kinetic hardening Xsat become large but the saturation stress of isotropic hardening become small. This can be thought as shown in Figure 7, which illustrates piling up dislocations around cementites in pearlite. When the lamellar spacing become small, the number of locations in which dislocations are pile up increased. Also, the chance of immobilization of mobile dislocations can decrease. As a result, when lamellar spacing of pearlite decreases, Xsat can increase and Rsat can decrease.

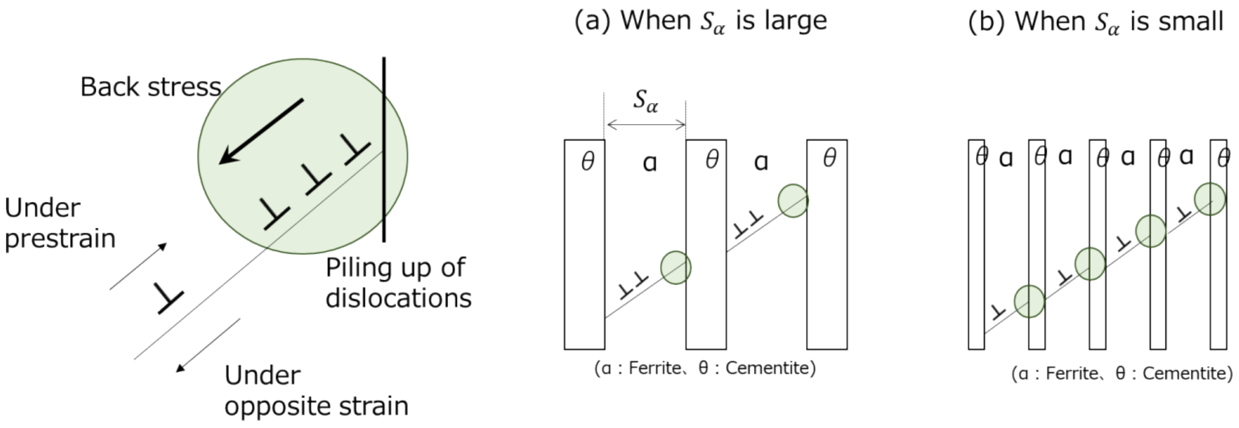

Figure 7. shematic illustration of mechanism of Baushinger effect in pearlite

4. Conclusions

(1) Work-hardening behavior of pearlite steel is mainly dominated by the elastic back stress compared to that of ferrite steel.

(2) When the lamellar spacing of pearlite become small, the saturation stress of isotropic hardening Rsat become small and the saturation stress of kinetic hardening Xsat become large. This means that the chance of immobilization of dislocations can decrease and the elastic back stress around cementites can increase with decreasing of lamellar soacing.

References

1) J. Lemaitre and J. –L. Chaboche: Mechanics of Solid Maaterials, Cambridge University Press
2) E. V. Nesterova, B. Bacroix, C. Teodosiu: Metal. And Mater. Trans. A. **32A** (2001) 2527-2538

Characterization of the Portevin-Le Chatelier Effect in Austenitic Stainless Steel using High-Temperature Digital Image Correlation Analysis

Seung-Yong Lee[1,*], Nobuo Nakada[1], Chikako Takushima[2], and Jun-ichi Hamada[2]

[1] Department of Materials Science and Engineering, Tokyo Institute of Technology, Yokohama, Kanagawa 226-8503, Japan
[2] Research & Development Center, NIPPON STEEL Stainless Steel Corporation, Hikari , Yamaguchi 743-8550, Japan
*email: lee.s.aw@m.titech.ac.jp

Keywords: Austenitic stainless steel, Dynamic strain aging, Portevin-Le Chatelier (PLC) effect, Digital image correlation (DIC), Local strain distribution

1. Introduction

Austenitic stainless steel (γ-STS) has been widely used for various applications in a wide temperature range. At an elevated temperature, the stress-strain curves of γ-STSs shows serrated flow. It has been reported that the serrated flow in γ-STSs is closely related to dynamic strain aging (DSA), which is the dynamic strengthening effect that results from the interaction between diffusive solute atoms and moving dislocations. DSA is also accompanied with a strain localization, which is known as the Portevin-Le Chatelier (PLC) effect. Because of the PLC effect, the deformation of the gauge part of a tensile specimen is highly localized in a bad shape, thus, the PLC band develops. Meanwhile, there have been few studies on high-temperature PLC band characteristics in γ-STS, even though mechanical properties are significantly affected by the DSA associated with the PLC effect 1). To further understand the PLC effect and better control the mechanical properties of γ-STSs, it is necessary to investigate the PLC band characteristics at high temperature where DSAoccurs. In this study, the propagation behavior of A-type PLC band in γ-STS was investigated by high-temperature digital image correlation (DIC) analysis.

2. Experimental procedure

The stable γ-STS, Fe–19Cr–13Ni–0.2C in mass%, was used in this study. High-temperature tensile testing supported with DIC system was carried out at temperatures from 723 K to 823 K under varying applied strain rates from 10^{-4} s^{-1} to 10^{-2} s^{-1}. The strains were globally and locally measured as ε^{DIC-G} and ε^{DIC-L}, respectively. ε^{DIC-G} indicates the macroscopic average strain throughout the gauge part of a tensile test piece, while ε^{DIC-L} is the microscopic strain calculated from a subset, such as to evaluate the strain in a PLC band. The detailed testing method is in Ref. 2.

3. Results and discussion

The stress-strain curves at various temperatures are shown in Fig. 1(a). A serrated flow associated with plastic instability was observed in all stress strain curves. Fig. 1(b) indicates the series of DIC images taken at 773 K/10^{-4} s^{-1}. Clearly, a typical A-type PLC band was developed; a PLC band nucleated at an edge of the gauge part and then propagated toward the opposite edge. It was found that the overall deformation of the gauge part proceeds with the propagation of the PLC band; the overall strain is restricted to a PLC band.

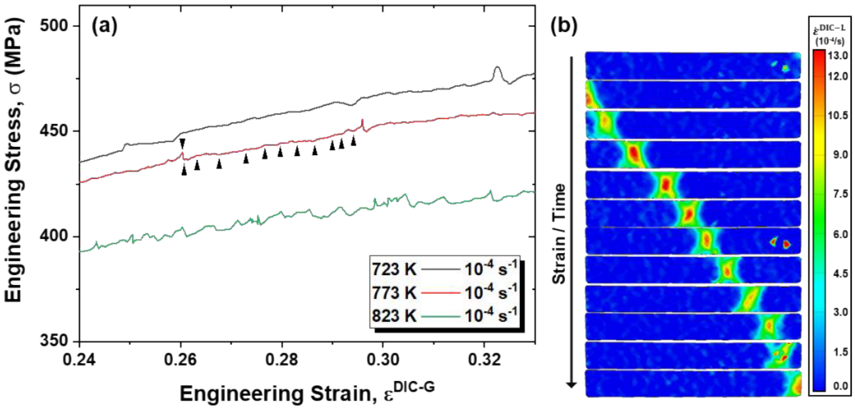

Figure 1 (a) Engineering stress vs, strain curves of specimens tested at temperatures from 723 K to 823 K under a strain rate of 10^{-4} s^{-1}. (b) Strain rate distribution map showing A-type PLC band propagation in the gauge part of a test piece deformed at 723 K/10^{-4} s^{-1}. Each imagewas acquired at the strain represented by the black triangles in the stress vs. strain curve in (a).

Fig. 2(a) schematically shows the local strain development by the A-type PLC band where the *i*-th PLC band is propagating. When the (n+1)-th PLC band propagates, the deformation of the gauge part is highly localized at the PLC band with a steep gradient of $\varepsilon^{\text{DIC–L}}$, and the gradient gradually increases with increasing number of PLC bands. This figure reveals that the local strain rate, $\dot{\varepsilon}^{\text{DIC–L}}$, is maximized at the PLC band, suggesting that DSA should be considered under the local condition. Therefore, the change in the mean $\dot{\varepsilon}^{\text{DIC–L}}$ of the PLC band was measured under 773 K/10^{-4} s^{-1} and displayed as a function of $\varepsilon^{\text{DIC–G}}$ in Fig. 2(b). $\dot{\varepsilon}^{\text{DIC–L}}$ is consistently much higher than the applied strain rate (10^{-4} s^{-1}) and gradually increases from 2.0×10^{-4} to 1.4×10^{-3} s^{-1} before the necking deformation. It suggests that the initiation of necking deformation through the development of the A-type PLC band is closely associated with the increase in $\dot{\varepsilon}^{\text{DIC–L}}$ at the PLC bands.

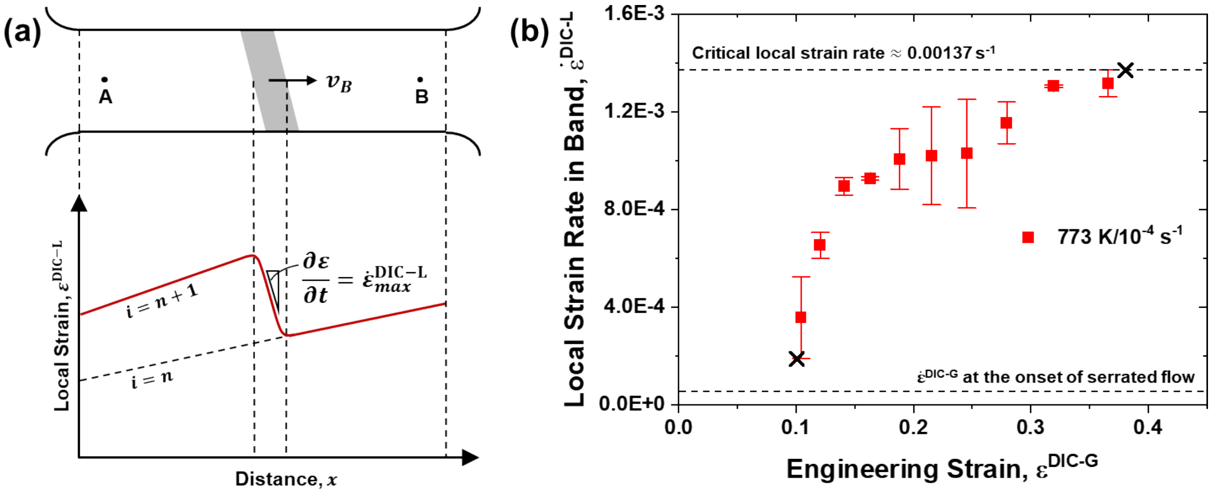

Figure 2 (a) Schematic illustration showing the local strain distribution in the gauge part where the *i*-th PLC band propagates; (b) Change in local strain rate $\dot{\boldsymbol{\varepsilon}}^{\text{DIC–L}}$ in each band as a function of the global strain $\boldsymbol{\varepsilon}^{\text{DIC–G}}$ at 773K/10^{-4} s^{-1}.

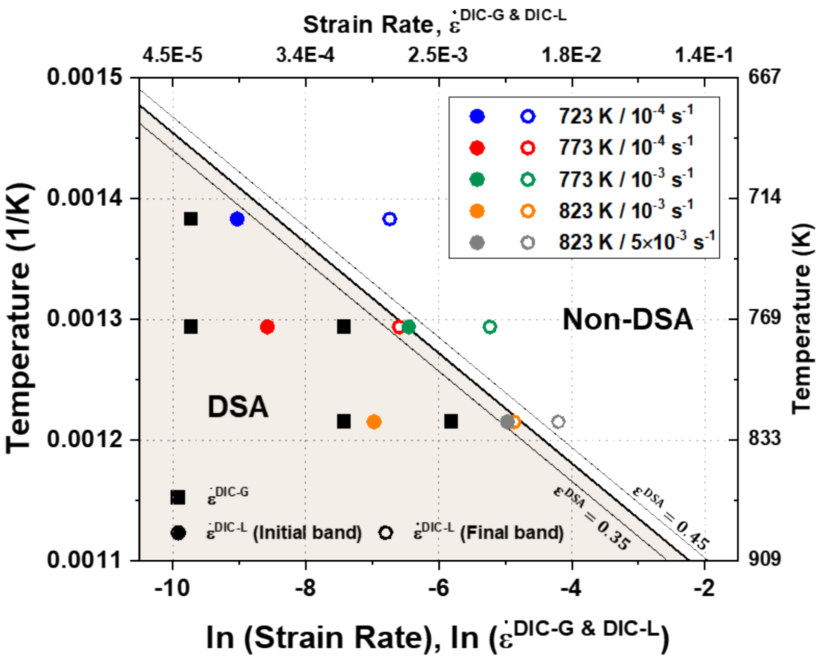

Figure 3 Map of ln $\dot{\varepsilon}$ and ***1/T***, indicating the critical condition of the A-type PLC effect. The global strain rate $\dot{\boldsymbol{\varepsilon}}^{\text{DIC–G}}$ at the onset of serrated flow in the tensile curves is represented by a black solid square, whereas the local strain rate $\dot{\boldsymbol{\varepsilon}}^{\text{DIC–L}}$ at the initial and final PLC bands are indicated with colored solid and open circles, respectively.

Under the tensile deformation condition at a higher temperature and lower strain rate than the transition boundary (lower left region in the graph), the A-type PLC effect should occur before reaching the strain for necking deformation. It shows that the initial $\dot{\varepsilon}^{\mathrm{DIC-L}}$ tends to be in the DSA region, whereas the final $\dot{\varepsilon}^{\mathrm{DIC-L}}$ is in the non-DSA region under all deformation conditions. This result suggests that the local condition in PLC bands transited from DSA to non-DSA regions during tensile deformation. The transition causes softening due to the weakening DSAeffect, because of which the PLC band propagation stops, and necking deformation occurs within the PLC band. Thus, the necking process with the A-type PLC band is activated when the local strain rate inside the PLC band reaches the critical value, at which the diffusion of solute atoms can no longer restrict the movement of dislocations.

Acknowledgement

This research did not receive any specific grant from funding agencies in the public, commercial, or not-for-profit sectors.

References

1) Y. Zhang, J.P. Liu, S.Y. Chen, X. Xie, P.K. Liaw, K.A. Dahmen, J.W. Qiao and Y.L. Wang: Prog. Mater. Sci. 90 (2017) 358.
2) S.Y. Lee, C. Takushima, J. Hamada and N. Nakada: Acta Mater. 205 (2021) 116560.

Creep Properties of High Chromium Steel Weld Metals

H. Oyamada[1,*], H. Takauchi[1], H. Nako[2], T. Miyamura[2] and S. Nanba[2]

[1] Welding Business, KOBE STEEL, LTD., Fujisawa, Kanagawa 251-8551, Japan
[2] Materials Research Laboratory, KOBE STEEL, LTD., Kobe, Hyogo 651-2271, Japan
*email: oyamada.hiromi@kobelco.com

Keywords: high Cr steel weld metals, creep properties, boron, Monkman-Grant relation

Introduction

High Chromium steels such as ASME Gr. 91 (9Cr-1Mo-V-Nb steel) and Gr. 92 (9Cr-1.8W-0.5Mo-V-Nb steel) are widely used in Ultra Super Critical (USC) boilers with steam temperature over 600ºC. Additionally, Gr. 93 steel (9Cr-3W-3Co-Nd-B steel) was technologically developed in order to further improve efficiency1). The coal fired power generation is considered to be reduced to achieve carbon neutrality in recent years. On the other hand, from the viewpoint of stable power supply, it is important to develop materials with excellent high temperature performance in order to improve the efficiency of thermal power generation and extend the life of power plants.

Boron is added to Gr. 92 and Gr. 93 steels to improve creep strength. Although boron addition has been reported to suppress the growth of $M_{23}C_6$ particles during the creep2, 3), it is not sufficiently understood how boron affects the particle growth suppression. In this study, the influence of boron addition to weld metals on creep rupture time was investigated for Gr. 92 / 93 steel weld metals. In addition, the relationship between creep rupture time and minimum strain rate of Gr. 91, 92, and 93 weld metals is discussed.

Materials and Methods

Samples

The weld metals were produced using covered electrode with 4.0 mm core rode. The welding conditions were described as follows, polarity: DCEP, welding current: 150 A, arc voltage: 24~25 V, heat input: 2.5~3.0 kJ/mm, preheat-interpass temperature: 200~300ºC. The groove configuration and pass sequences are shown in Fig. 1. Chemical composition and Post Weld Heat Treatment (PWHT) conditions of the weld metals are shown in Table 1 and 2 respectively.

Table 1 Test materials of Gr. 92 weld metals.

Specimen mark	Chemical composition of weld metals (mass%, B in ppm)											PWHT condition	Creep rupture test condition
	C	Si	Mn	Ni	Cr	Mo	W	V	Nb	N	**B**		
(2A)	0.1	0.4	1.0	0.5	9.6	0.2	1.7	0.4	0.03	0.05	**Free**	750ºC-5 h	650ºC-100 MPa
(2B)	0.1	0.4	1.0	0.6	9.8	0.2	1.7	0.4	0.03	0.05	**12**		
(2C)	0.1	0.4	1.0	0.5	9.6	0.2	1.6	0.4	0.04	0.05	**28**		

Table 2 Test materials of Gr. 93 weld metals.

Specimen mark	Chemical composition of weld metals (mass%, B in ppm)									PWHT condition	Creep rupture test condition
	C	Si	Mn	Cr	Co	W	V	Nb	**B**		
(3A)	0.1	0.3	0.6	8.4	3	3	0.2	0.05	**Free**	760ºC-4 h	650ºC-140 MPa
(3B)	0.1	0.3	0.7	8.7	3	3	0.2	0.05	**59**		
(3C)	0.1	0.3	0.7	8.8	3	3	0.2	0.06	**95**		

Creep Rupture Test

The all-weld-metal creep specimens were machined from the center of weld metals in the longitudinal direction after PWHT conducted. The round bar specimens have nominal diameter of 6.0 mm, and the nominal gauge length of 30 mm. The test condition is shown in Table 1 and 2.

Metallographic Observation

In order to evaluate the precipitations and the microstructure before and after creep rupture test, replica and film observation were carried out by means of Transmission Electron Microscope (TEM) for some samples.

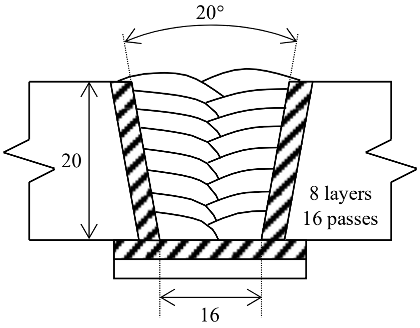

Fig. 1 Groove configuration. (mm)

3-Dimensional Atom Probe

It is observed where boron atoms existed, by means of 3-Dimensional Atom Probe (3DAP) tomography. The specimens containing Prior Austenite Grain Boundaries (PAGB), $M_{23}C_6$ particles and the matrix were prepared by a focused ion beam device. 3DAP analysis with 15 % pulse fraction was conducted at -233°C.

Extraction Residue

In order to investigate the amount of precipitates in the Gr. 93 weld metals, electrolytic extraction of precipitates and X-ray Diffraction (XRD) analysis of the residues were carried out. 10% acetylacetone + 1% tetramethylammonium chloride + methanol was used as the extraction liquid, the residues were collected by the polycarbonate filter. In the obtained X-ray diffraction pattern, the semi-quantitative analysis by Reference Intensity Ratio (RIR) method of analysis software (JADE) was carried out from the integrated intensity of crystal plane of each precipitated phases.

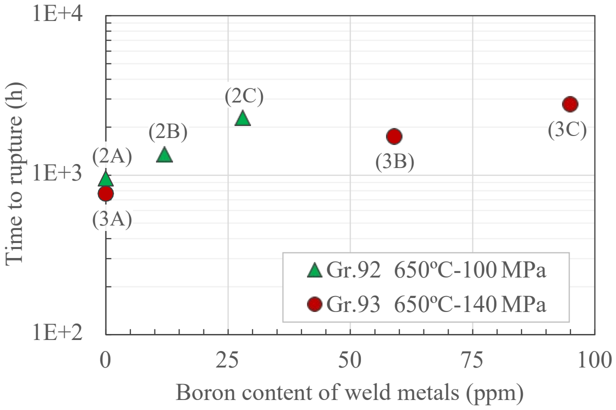

Fig. 2 Influence of boron content of weld metals on creep rupture time.

Results and Discussions

Effects of Boron

Fig. 2 shows relationship between creep rupture time of Gr. 92 / 93 weld metals and boron content. The addition of boron significantly prolonged creep rupture time both Gr. 92 and Gr. 93 weld metals. This is the same tendency as the effect of boron in 9%Cr base metals[2)].

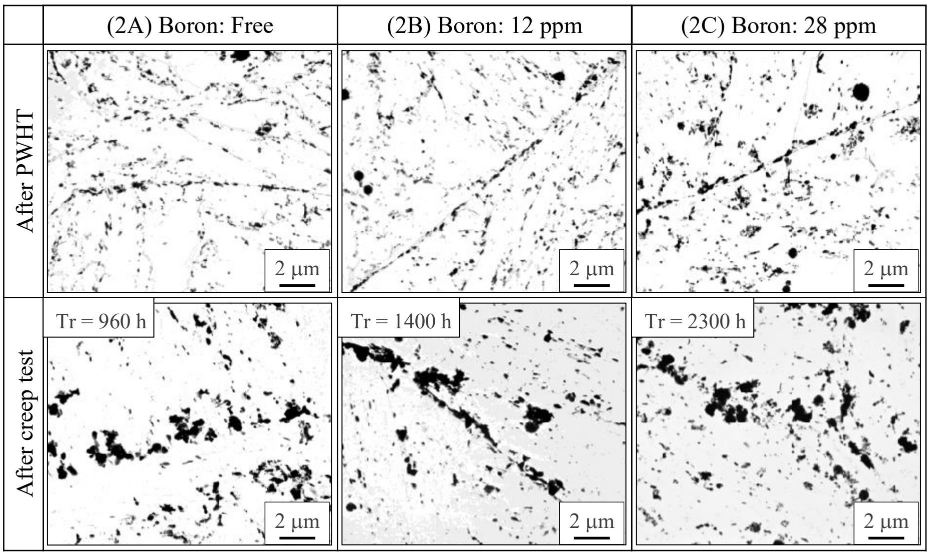

Fig. 3 Replica TEM images of Gr. 92 weld metals.
(Tr = Time to rupture)

Fig. 3 shows replica TEM images of Gr. 92 weld metals: (2A), (2B), and (2C) after PWHT and after creep rupture test. According to TEM observation and thermodynamic calculation using Thermo-Calc software, the species of precipitates were identified as $M_{23}C_6$ (Cr-rich) and MC (V, Nb-rich) after PWHT, and in addition to them Laves phases (Fe_2Mo) were observed after creep rupture test. Focusing on (2A), the

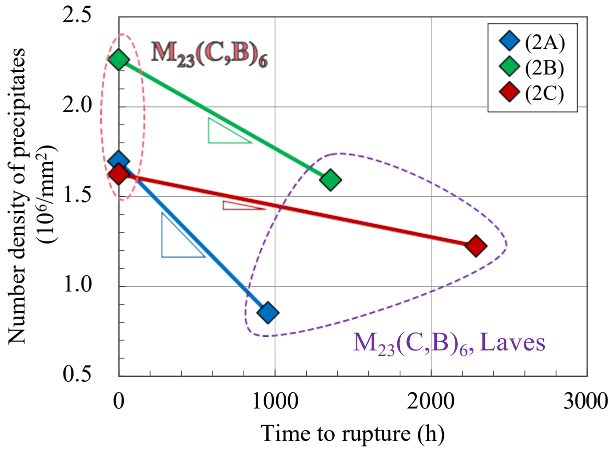

Fig.4 Change in number density of precipitates before and after creep test.

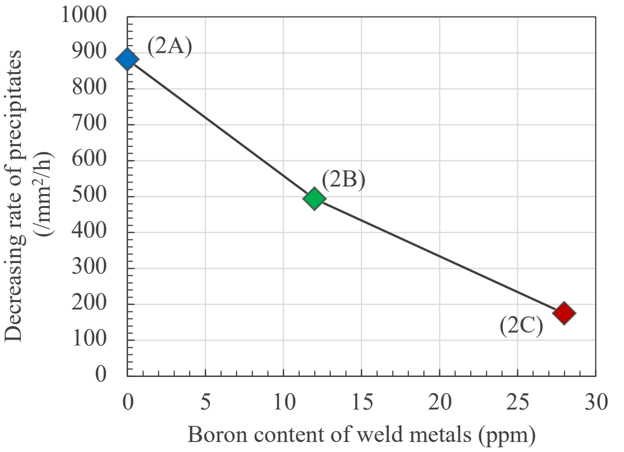

Fig.5 Relationship between decreasing rate of precipitates and boron content of weld metals.

(Tr = Time to rupture)

precipitates were coarsened and the number density was enormously decreased after creep rupture test compared with that of after PWHT. But in (2B) and (2C) which contain boron, fine precipitates remained after creep rupture test. Fig. 4 shows the change in the number density of precipitates before and after creep rupture test. The number density of precipitates was the highest in (2B) with boron content of 12 ppm, both before and after creep rupture test. On the other hand, focusing on the decreasing rate of the number density of precipitates during the creep rupture test, which is represented by the gradient in Fig. 4, the decreasing rate became lower as boron content increases (Fig. 5). From the relationship between creep rupture time and boron content of weld metals shown in Fig. 4, it is considered that the creep rupture time was prolonged by lowering the decreasing rate of the number of precipitates during creep rupture test.

Fig. 6 shows 3-DAP of carbon, chromium, phosphorus and boron of (2B) with boron content of 12 ppm after PWHT. Each dot in the figure represents an atom. The size of each dot is not related to the actual sizes of the atoms but drawn with visibility. The region where both chromium and carbon atoms are highly concentrated was $M_{23}C_6$ particle. In the $M_{23}C_6$ region, boron atom concentration was also observed. Boron atom was hardly detected in the matrix. There were some PAGBs in the other 3-DAP analysis volume. According to them, boron segregation was detected neither at PAGB nor at the matrix / $M_{23}C_6$ particle interface. And the same tendency was seen after creep rupture test. From these results, it was found that the large parts of added boron have dissolved in the $M_{23}C_6$ particles.

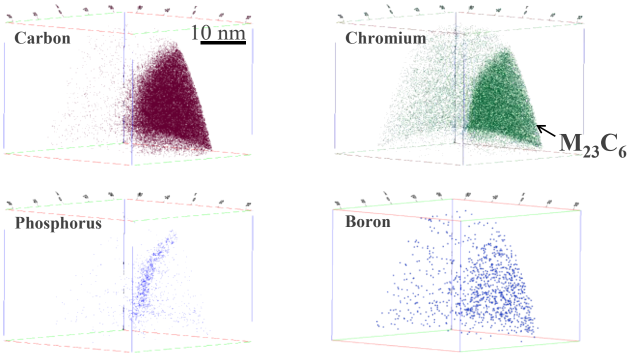

Fig. 6 3-dimensional atom maps of (2B) after PWHT.
(*Size of dot does not correspond to size of atom.)

Table 3 Relationship between boron content of weld metals and amount of precipitates after PWHT (760ºC-4 h).

	Boron content of weld metals (ppm)	Amount of precipitates (mass%)	
		$M_{23}C_6$	Fe_2W
(3A)	Free	2.09	0.07
(3B)	59	2.07	0.17
(3C)	95	2.11	0.24

The creep strength of Gr. 93 weld metals is superior to that of Gr. 92 weld metals. In Gr. 93 weld metals, suppressing of the rate of decrease in the number density of $M_{23}C_6$ particles by boron addition is also effective similar to Gr. 92 weld metals. Additionally, the large precipitation of W-rich Laves phase (Fe_2W) also contributes to the improvement of creep strength. Table 3 shows the amount of precipitates such as $M_{23}C_6$ and Laves phase which obtained from electrolytic extraction and XRD after PWHT of Gr. 93 weld metals. The amount of Laves phase increased by adding of boron. It is reported that Laves phase nucleates and grows on grain boundary segregating of silicon ejected from $M_{23}C_6$ 4). Although the reference paper only mentioned to Mo-rich Laves phase, this results suggest that the similar mechanism also occurs in W-rich Laves phase. Therefore, it is assumed that boron affects amount of W-rich Laves phase through influence $M_{23}C_6$ in Gr. 93 weld metals. For all of the above, influences of boron addition on creep property of Gr. 93 weld metals is suppression of recovery of martensitic structure by suppression of coarsening of $M_{23}C_6$ and increasing the amount of W-rich Laves phase.

Prediction of Creep Rupture Time

Fig. 7 shows the relationship between rupture time of Gr. 91 / 92 / 93 weld metals and the minimum strain rate. As a formula for predicting the rupture time from minimum strain rate, the Monkman-Grant relation is generally known5). According to Fig. 7, it was found that the relationship between the minimum strain rate and rupture time of Gr. 91 / 92 / 93 weld metals is colinear, and can be applied the common prediction expression if rupture time is less than 10,000 h. Additionally, "×" means predicted rupture time using Gr. 91 weld metal's Monkman-Grant relation. Predicted values of rupture time showed good correction. On the other hand, it its generally known that the creep curve of Gr. 91 steels fold down to short time rupture in long time, and the verification is necessary whether the same prediction expression can be applied to the data exceeding 10,000 h for Gr. 91 / 92 / 93 weld metals.

Fig. 8 compares the relationship between the minimum strain rate and rupture time of weld metals and base metals of 9%Cr steels. The base metal's data is referred to NIMS creep data sheet. (Gr. 91: MGA, MGB, MGC, Gr. 92: MJT, MJU) Though each inclination is the same level, rupture time of the weld metals become a little shorter even at the same minimum strain rate, and it is proven that there is a risk of estimating the rupture time longer, when the prediction expression of base metals is applied to weld metals. Therefore, it is necessary to use the regression expression obtained only from weld metals data to predict rupture time of weld metals.

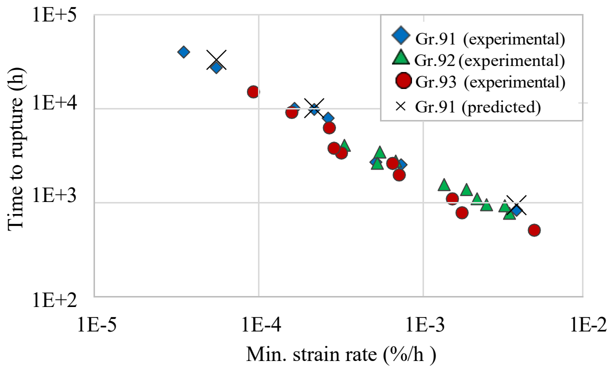

Fig.7 Relationship between creep rupture time and minimum strain rate of Gr. 91/92/93 weld metals.

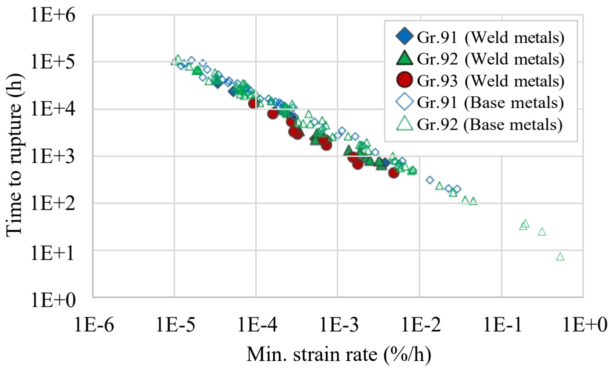

Fig.8 Comparison of relationship between creep rupture time and minimum strain rate of weld metals and base metals of 9%Cr steels.

Conclusions

1 The creep rupture time of Gr. 92 weld metals was prolonged by boron addition through the lowering of the decreasing rate of the number density of precipitates during creep rupture test.

2 According to 3-dimensional atom maps, the large parts of boron in Gr. 92 weld metals have dissolved in the $M_{23}C_6$ particles. Boron segregation was detected neither at PAGB nor at the matrix / $M_{23}C_6$ particle interface.

3 It is considered influences of boron addition on creep property of Gr. 93 weld metals is suppression of recovery of martensitic structure by suppression of coarsening of $M_{23}C_6$ and increasing the amount of W-rich Laves phase.

4 The relationship between the minimum strain rate and rupture time of Gr. 91 / 92 / 93 weld metals is colinear, can be applied the common prediction expression if rupture time is less than 10,000 h. The rupture time of the weld metals become a little shorter even at the same minimum strain rate, and it is proven that there is a risk of estimating the rupture time too long, when the prediction expression of base metals is applied to that of weld metals.

References

1) T. Hamaguchi: Journal of the Japan Welding Society **90** (2021) pp.436-440.
2) F. Abe: Science and Technology of Advanced Materials **9** (2008) 013002.
3) M. Arai, K. Asakura, H. Doi, H. Kawanaka, T. Koseki and T. Horiuchi: Tetsu-to-Hagané **96** (2010) pp.620-628.
4) M. I. Isik, A. Kostka, G. Eggeler: Acta Materialia **81** (2014) pp.230-240.
5) K. Maruyama: Tetsu-to-Hagané **105** (2019) pp.767-777.

Elastic limit of Martensitic Steel Sheet Containing Retained Austenite

Junya Tobata[1*], Hidekazu Minami[1], Yuki Toji[1] and Shinjiro Kaneko[1]

[1] Steel Research Laboratory, JFE Steel Corporation, 1, Kawasaki-cho, Chuo-ku, Chiba 260-0835, Japan
*email: j-tobata@jfe-steel.co.jp

Keywords: yield strength; martensite; retained austenite; stress-induced transformation.

1. Introduction

Martensitic steel sheets have been applied to a variety of automobile parts. High yield strength is required for automobile body parts in order to secure the anti-collision performance. The yield strength of martensitic steel sheets can be influenced by retained austenite[1,2]. However, the detailed mechanism is not clear. Therefore, it is necessary to clarify the yielding mechanism of steel sheets which consists of martensite and retained austenite in order to realize the stable yield strength. The objective of this study is to clarify the mechanism of yielding of martensitic steel sheet containing retained austenite.

2. Experimental procedure

The chemical composition of the steel used was 0.18%C-1.5%Si-3.0%Mn (mass%). In order to vary carbon content in the retained austenite, the steel sheet was austenitized at 870°C, then quenched to 200 °C followed by tempering at 250-400 °C. X-ray diffractometry was used to measure the volume fraction of retained austenite and the carbon concentration in the retained austenite of the samples. The tensile properties of the samples were evaluated by tensile tests using JIS No.5 tensile test piece (GL: 50 mm, GW 25 mm) at the cross head speed of 10 mm/min.

3. Results and Discussion

Fig. 1 shows the retained austenite volume fraction and the carbon concentration as a function of tempering temperature. Although the volume fraction of retained austenite did not change with increasing tempering temperature, the carbon concentration of retained austenite increased. **Fig. 2** shows the nominal stress-strain curves of the samples with different tempering temperature. The elastic limit of the steel sheets increased with increasing tempering temperature, i.e. increasing carbon content in the retained austenite. It was found that the yielding in low carbon martensitic steel sheets containing retained austenite was strongly influenced by the stress-induced martensite transformation of the retained austenite, because the required stress to induce the transformation was lower than the yield strength of martensite or retained austenite.

4. Summary

The yield strength of the samples increased with increasing the carbon concentration of retained austenite, which indicates the yielding of martensitic steel sheets containing retained austenite can be controlled by the stability of the retained austenite.

References

1) B. C. De Cooman, P. Gibbs, S. Lee and D. K. Matlock: *Met. and Mat. Trans. A*, **44A** (2013), pp2563-2572. 2)
G.N. Haidemenopoulos, M. Grujicic, G. B. Olson and M. Cohen, Acta metall, **37**(1989), pp1677-1682.

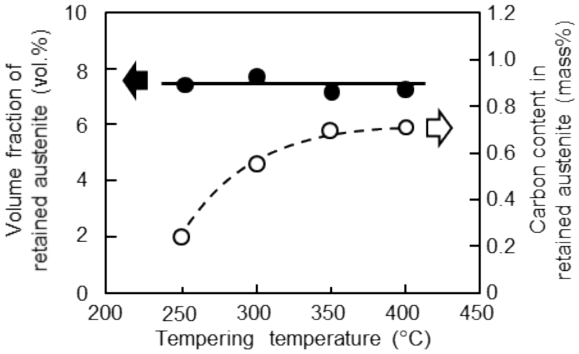

Fig.1 Retained austenite volume fraction and carbon concentration in the austenite as a function of tempering temperature.

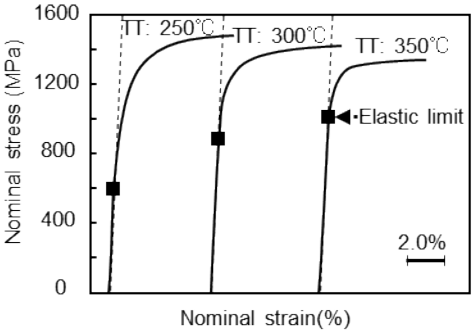

Fig.2 Nominal stress-strain curves of the samples with different tempering temperature(TT).

Effects of Tensile Testing Temperature on Mechanical Properties and Deformation Behavior in Medium Mn Steels

Yoshiyasu Kawasaki[1,*], Yuki Toji[2], Tatsuya Nakagaito[1] and Shinjiro Kaneko[2]

[1] JFE Steel Corporation, 1 Kokan-cho, Fukuyama, Hiroshima, 721-8510, Japan
[2] JFE Steel Corporation, 1 Kawasaki-cho, Chuo-ku, Chiba, 260-0835, Japan
*email: yosh-kawasaki@jfe-steel.co.jp

Keywords: medium Mn steel, deformation temperature, tensile deformation behavior, stability of retained austenite

The effects of volume fraction and stability of retained austenite on the tensile deformation behavior at various temperatures has been studied in medium Mn steels[1-3]. In this poster, to clarify the condition for achieving excellent strength-elongation balance by controlling the stability of retained austenite optimizing tensile deformation temperatures in the medium Mn steel, the tensile deformation behavior at various temperatures were investigated in detail.

A medium Mn steel with a thickness 1.4 mm with chemical composition of 0.15C-0.5Si-5Mn (mass %) was annealed at 660 °C for 2 h using an alumina fluidized furnace. In the tensile test, JIS No. 5 specimens (GL: 50 mm, GW: 25 mm) were taken along the direction parallel to the rolling direction, and the cross head speed was 10 mm/min. The tensile test was conducted by changing the tensile testing temperature in accordance with JIS G 0567. After the tensile test specimens were reached at temperatures of -40, 20 and 200 °C, the specimens were held for 10 min at the specified temperature, subjected to tensile deformation to fracture, and then air-cooled. The volume fraction of retained austenite ($V\gamma$) were measured by the integrated intensity for the (200)α, (211)α, (210)α, (200)γ, and (220)γ peaks by an X-ray diffraction technique with Co-Kα.

Fig. 1 shows nominal stress-strain curves obtained from tensile tests at various temperatures. All the t nominal stress-strain curves showed an upper yield point and yield elongation of about 6 %. The work hardening rate decreased significantly in the high strain region after yield elongation with increasing the tensile testing temperature. Medium Mn steels often exhibit a upper yield point followed by Lüders band behavior and then work hardening characterized by serrations and Portevin–Le Châtelier (PLC) bands[4]. The serrated flow behavior may be indicative of dynamic strain aging (DSA) potentially due to C-Mn point defect complexes interacting with stacking faults in the retained austenite[4], although in some cases, serrated flow has been attributed to the martensite transformation from autenite[5]. Table 1 shows $V\gamma$ after tensile tests until fracture at various temperatures. $V\gamma$ before tensile tests was 29 %. In the tensile tests at -40 and 20 °C, most of the retained austenite was transformed to martensite. On the other hand, in the tensile test at 200 °C, about 7% of $V\gamma$ was transformed to martensite. In other words, about 22% of $V\gamma$ remained.

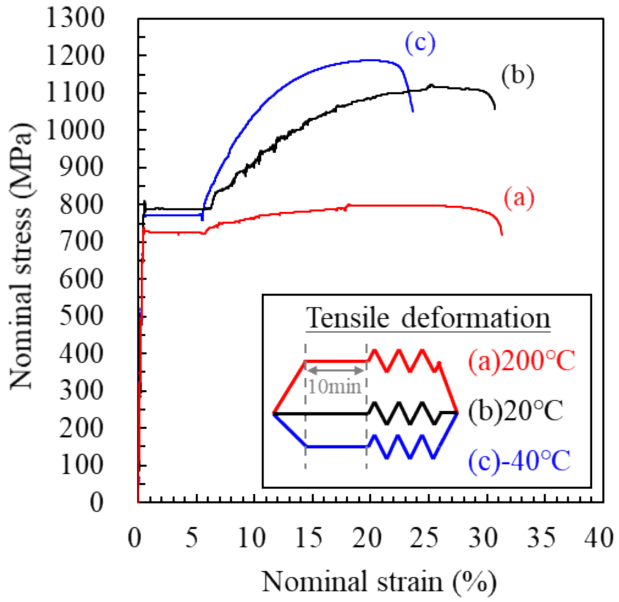

Fig. 1. Nominal stress-strain curves obtained from tensile tests at various temperatures.

Table 1 $V\gamma$ after tensile tests until fracture at various temperatures.

The tensile test temperature until fracture	$V\gamma$ after the tensile test until fracture
200 °C	22.3%
20 °C	1.2%
-40 °C	0.2%

Fig. 2 shows nominal stress-strain curves obtained from tensile tests until 10 % strain at various temperatures and then subsequently deformed until fracture at 20 °C. The highest strength-elongation was obtained by a condition of the tensile test was deformed at 200 °C until 10 % strain and at 20°C until fracture. Table 2 shows Vγ after tensile tests until 10 % strain at various temperatures and Vγ after the subsequent tensile tests until fracture at 20 °C. Vγ before tensile tests was 29 % and 25% of Vγ remained with the tensile deformation at 200 °C until 10 % strain, and then, most of the retained austenite was transformed to martensite the tensile deformation at 20 °C until fracture. Therefore, the highest strength-elongation balance was obtained by utilizing the TRIP (TRansformation Induced Plasticity) effect of the retained austenite after the tensile deformation of 10 % strain.

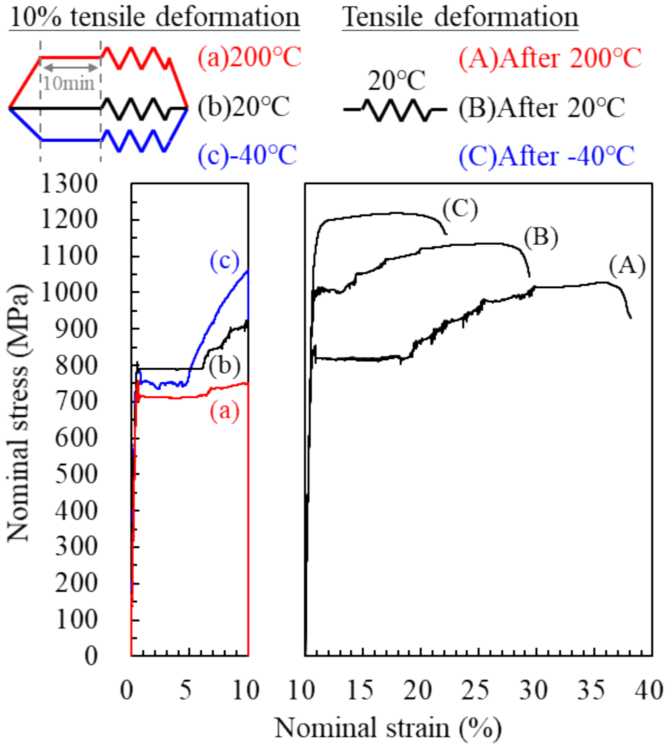

Fig. 2. Nominal stress-strain curves obtained from tensile tests until 10 % strain at various temperatures and until fracture at 20 °C.

Table 2 Vγ after tensile tests until 10 % strain at various temperatures and Vγ after the subsequent tensile tests until fracture at 20 °C.

The tensile test temperature until 10 % strain	Vγ after the tensile test until 10 % strain	Vγ after the tensile test until fracture
200 °C	25.0%	1.8%
20 °C	16.8%	1.1%
-40 °C	7.9%	0.4%

It should be noted that it is important in the medium Mn steel to utilize the TRIP effect of retained austenite after tensile deformation to the limit by slip deformation without transforming from austenite to martensite at relatively high temperatures, that is, to control the retained austenite stability by optimizing the tensile deformation temperature.

References

1) S. Chen, J. Hu, X. Zhang, H. Dong and W. Cao: J. Iron Steel Res. Int., **22** (2015) pp.1126-1130.
2) R. Rana, P. J. Gibbs, E. De Moor, J. G. Speer and D. K Matlock: Steel Res. Int., **86** (2015) pp.1139-1150.
3) Koh-ichi Sugimoto, Hikaru Tanino and Junya Kobayashi: Mater. Sci. Eng. A, **688** (2017) pp.237-243.
4) D. M. Field and D. C. Van Alen: Met. Mater. Trans. A, **49** (2018) pp.1152-1166.
5) Z. H. Cai, H. Ding, R. D. K. Misra and Z. Y. Ying: Acta Mater., **84** (2015) pp.229-236.

Effect of ultra-grain refinement on deformation behavior of Fe-24Ni-0.3C metastable austenitic steel

Wenqi Mao
Japan Atomic Energy Agency

In the present work, specimens of Fe-24Ni-0.3C (wt.%) metastable austenitic steel having different mean grain sizes, one with 0.5 μm (ultrafine-grained, UFG) and one with 35 μm (coarse-grained, CG), were fabricated by cold rolling and subsequent annealing processes. The effect of ultra-grain refinement on the deformation behavior and deformation-induced martensitic transformation (DIMT) in this material was investigated by tensile tests with a hybrid in situ neutron diffraction and digital image correlation (DIC) technique and microstructure observation with electron backscattering diffraction (EBSD). The UFG specimen exhibited a significantly higher yield strength of 680 MPa which is 3.7 times higher than that of the CG specimen, due to the ultra-grain refinement strengthening. Surprisingly, a large uniform elongation of 82% was maintained in the UFG specimen which was almost the same as that of the CG specimen. In addition, results of tensile tests and DIC analysis revealed that the Portevin-Le Chatelier (PLC) behavior of this material was obviously changed by the grain refinement. Before the DIMT onset, the PLC behavior changed from type A+B to type A as the grain size was reduced from 35 μm to 0.5 μm. After the DIMT occurrence, although both the UFG and CG specimens exhibited type C PLC effect, the UFG specimen exhibited stronger stress oscillation and larger localized deformation. The detailed mechanism of the effect of the ultra-grain refinement will be discussed based on the results of in situ neutron diffraction and EBSD observation, which will be shown in the poster.

Global and local deformation behavior of ferrite + martensite + austenite steel analyzed by *in-situ* X-ray diffraction and digital image correlation (DIC) method

Avala Lavakumar[1,2*], Myeong-heom Park[1] and Nobuhiro Tsuji[1,3]

[1] Department of Materials Science and Engineering, Kyoto University, Yoshida-honmachi, Sakyo-ku, Kyoto 606-8501, Japan.
[2]Institute for Materials Chemistry and Engineering, Kyushu University, Fukuoka, 816-8580, Japan
[3]Elements Strategy Initiative for Structural Materials (ESISM), Kyoto University, Yoshida-honmachi, Sakyo-ku, Kyoto 606-8501, Japan.
*email: avala.lavakumar.4e@kyoto-u.ac.jp

Keywords: TRIP steel, Strain partitioning, Stress partitioning, Digital Image correlation, *in-situ* XRD

Introduction

Steels showing transformation-inducedplasticity (TRIP) have attracted significant interest for automotiveapplications due to their superior mechanical balance between strength and ductility[1,2]. In general, TRIP-assisted steels contain a complex microstructure that includes soft ferrite and austenite, in addition to the hard bainite and/ormartensite[3]. The origin of goodstrength and ductility in TRIP-assisted steels is believed to be attributed to the metastable austenite, because it transforms to deformation-induced martensite under tensile deformation[4]. On the other hand, due todifferent mechanical strength levelsof phase constituents, typically, plastic strains are highly concentrated in the softer phase, and the elastic (lattice) strains are more in the harder phase under mechanical loading[5]. This significantly affects the stress and strain distribution between the phases and the overall deformation mechanisms of the alloy during deformation. Although TRIP-assisted multiphase steels show excellent mechanical properties, the detailed deformation behavior of constituent phases due to the TRIP effect has not yet been fully clarified because of their complicated microstructure.Recently, the i*n-situ* synchrotron high-energy x-ray diffraction (HE-XRD) and Digital Image Correlation (DIC) method has been widely adopted for investigating internal stress and strain partitioning between individual phases in the microstructures[6,7]. With the support of these advanced techniques, it is expected that the deformation nature of each phase in the multiphase steels can be evaluated. The objective of the present study is to investigate the mechanical behavior of individual microstructural phasesduring deformation and to discuss its role on the global mechanical properties of a TRIPassisted multi-phase steel.

Materials and methods

In the present study, a multi-phase steel alloy with a chemical composition of Fe-1.6Mn-1.4Si-1.0Ni -0.5Al-0.2C (mass %) was used. Atwo-step heat treatment process consisting of intercritical annealing at 830ºC for 120 seconds followed by isothermal holding at 400ºC for 120 seconds was applied to fully ferritic microstructure specimens to develop ferrite + austenite + martensite microstructure. The microstructure observation and phase identification were carried out with a field-emission scanning electron microscope (FE-SEM) and EBSD analysis, respectively. To evaluate mechanical properties tensile test was carried out at room temperature at an initial strain rate of $8.3 \times 10^{-4} s^{-1}$ with specimen dimensions having a gauge length of 10 mm, a width of 2.5 mm, and thickness of 1 mm. In order to investigate local strains, the microscopic Digital Image Correlation (μ-DIC) technique was used. For this, the surface of a tensile specimen is dispersed with nano-sized SiO_2 particles, which acts as a marker for strain measurement using DIC software (Vic-2D^{TM} 2009 powered by correlated solutions, Inc.). After that, an SEM micrograph of identical areas in an un-deformed specimen was compared with those in the tensile-deformed one using the DIC analysis.

Results

Figure 1 shows (a) EBSD image quality (IQ) + phase map and (b) True stress-strain curve of the 1.6Mn-1.4Si-1.0Ni -0.5Al-0.2C (mass %) steel, of which microstructure was composed of 74% ferrite, 14% martensite and 12% austenite. Since EBSD IQ map generally expresses the quality of Kukuchi-patterns, martensite with a high density of lattice defects resulted in low Kikuchi-pattern quality having a darker contrast in IQ maps. This ferrite + austenite + martensite steel exhibited excellent mechanical properties having a high (true) ultimate tensile strength of 1272 MPa and excellent (true) total elongation of 25%. It is expected that the deformation-induced martensite transformation could happen during deformation as a consequence of the TRIP effect in the present steel, and it significantly contributes to superior mechanical properties.

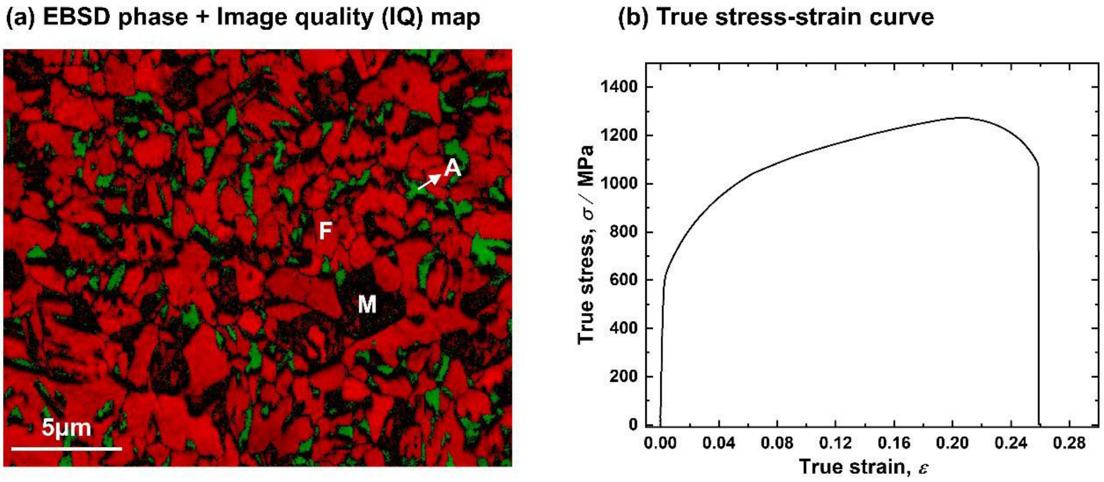

(a) EBSD phase + Image quality (IQ) map

(b) True stress-strain curve

Fig. 1. (a) SEM-EBSD IQ + phase map showing the ferrite, austenite, and martensite (b) True stress-strain curve of the studied steel at room temperature of Fe-1.6Mn-1.4Si-1.0Ni -0.5Al-0.2C (mass %) steel.

(a) Strain distribution maps

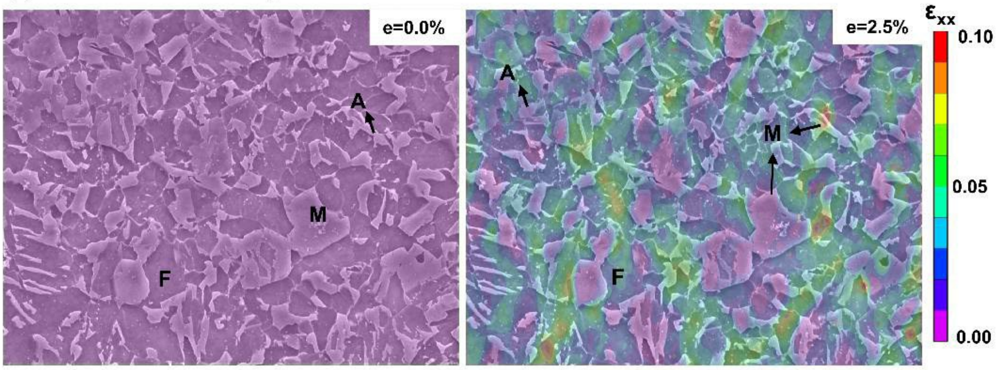

(b) Phase + Image quality (IQ) maps

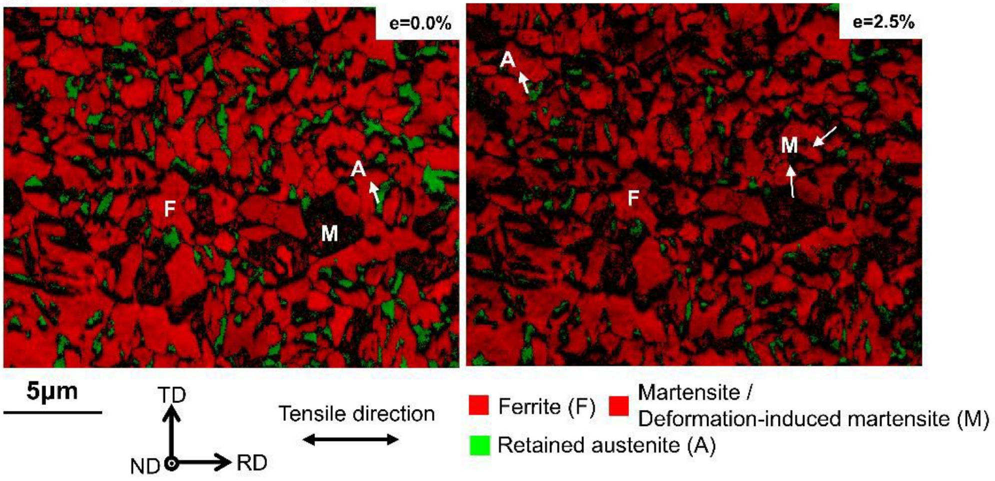

Fig. 2 (a) Strain distribution maps **(b)** IQ + phase maps showing at a specific region within the gauge length of the specimen after tensile deformation of 0% and 2. 5%

Figure 2a exhibit the DIC local strain distribution maps and corresponding EBSD IQ + phase maps shown in **Figure 2b**, at the center position of the gauge part of tensile specimen deformed to 0.0% and 2. 5%. By comparing **Fig. 2a** and **Fig. 2b**, it is possible to differentiate the local plastic strain in ferrite, martensite, and austenite. Tensile direction is parallel to a horizontal direction of images, and the level of strain (ε_{xx}) in strain distribution maps was expressed by the different colors according to the key strain bars, shown on the right side of **Fig. 2a**. In the strain distribution map (**Fig. 2a**), the local strain is heterogeneously distributed among the microstructural phases at the tensile strain of 2.5%. It was realized that high strain localized regions correspond to mostly ferritic regions; however, distribution of local plastic strain in martensite (initially existed in the microstructure) regions had a smaller strain, which suggests martensite is less deformed under tensile loading as compared to ferrite. Besides, austenite also showed higher local strain distribution as compared to martensite, but still, it is less than ferritic grains. The local strain in austenite areas is complex in nature since during deformation, austenite is changed into deformation-induced martensite. It can be seen in IQ +Phase map that a large portion of austenite grains was transformed to deformation-induced martensite at tensile deformation of 2.5%. This means the initial fraction of austenite (12% at e = 0.0%) was drastically reduced to 7 % at a tensile strain of 2. 5%. IQ +Phase maps reveal the locations of deformation-induced martensite regions; thus, it can bepossible to calculate the plastic strain even in newly formed martensite regions. It was observed that deformation-induced martensite regionsshowed higher local strain distribution than initial martensite regions. Therefore, such kind of strain partitioning to the softer ferrite and austenite from the stronger martensite at higher tensile strains can be considered as the reason for the enhanced strain hardening in the current ferrite + austenite + martensite steel.

Conclusions

The ferritic + martensitic + austenite steel showed excellent mechanical properties with high strength (1272 MPa) and large ductility (25 %). µ-digital image correlation (DIC) analysis were used to quantitatively analyze the progress of deformation-induced martensitic transformation and the distribution of local plastic strain distribution between different phases during tensile deformation. As a result, it was clarified that the mechanical interaction between the different phases, especially the interaction between the deformation-induced martensite phase and the other phases, led to the increase of work hardening in this ferrite + martensite + austenite steel, which suppressed the plastic instability leading to the large tensile elongation.

Acknowledgment

This study was financially supported by JST CREST (JPMJCR1994), Elements Strategy Initiative for Structural Materials (ESISM, No. JPMXP0112101000), and KAKENHI (Grant-in-Aid for Scientific Research from the Japan Society for the Promotion of Science; No. 15H05767 and 20K14608), all through the Ministry of Education, Culture, Sports, Science and Technology (MEXT), Japan. The synchrotron radiation experiments (beam time No. 2018B1760) at SPring-8 were performed with the approval of the Japan Synchrotron Radiation Research Institute (JASRI). The author (A.L) has been supported by the Japanese Government (MEXT) Scholarship. All the supports are gratefully appreciated.

References

1. Tsuji, N. *et al.* Strategy for managing both high strength and large ductility in structural materials–sequential nucleation of different deformation modes based on a concept of plaston. *Scr. Mater.* **181**, 35–42 (2020).
2. Matsumura, O., Sakuma, Y. & Takechi, H. Enhancement intercritical of elongation annealed by retained austenite steel. *Trans. ISIJ* (1987).
3. Sugimoto, K. I., Kobayashi, M. & Hashimoto, S. I. Ductility and strain-induced transformation in a high-strength transformation-induced plasticity-aided dual-phase steel. *Metall. Trans. A, Phys. Metall. Mater. Sci.* (1992). doi:10.1007/BF02646127
4. Pereloma, E., Gazder, A. & Timokhina, I. Retained Austenite: Transformation-Induced Plasticity. in *Encyclopedia of Iron, Steel, and Their Alloys* (2016). doi:10.1081/e-eisa-120049200
5. Lavakumar, A. *et al.* In-situ neutron diffraction study on the deformation of a TRIP-assisted multi-phase steel composed of ferrite, austenite and martensite. *IOP Conf. Ser. Mater. Sci. Eng.* **580**, 12036 (2019).
6. Tomota, Y. *et al.* Tensile behavior of TRIP-aided multi-phase steels studied by in situ neutron diffraction. *Acta Mater.* **52**, 5737–5745 (2004).
7. Tasan, C. C. *et al.* Integrated experimental – numerical analysis of stress and strain partitioning in multi-phase alloys. *Acta Mater.* **81**, 1–19 (2014).

Three-dimensional observation of small fatigue cracks growth process in a beta titanium alloy Ti-22V-4Al using multiscale synchrotron radiation computed tomography

Gaoge Xue[1,*], Takashi Nakamura[2], Nao Fujimura[2], Hiroyuki Oguma[3], Akihisa Takeuchi[4], Masayuki Uesugi[4] and Kentaro Uesugi[4]

[1] Division of Mechanical and Space Engineering, Hokkaido University, Sapporo, Hokkaido 060-8628, Japan
[2] Division of Mechanical and Aerospace Engineering, Hokkaido University, Sapporo, Hokkaido 060-8628, Japan
[3] Research Center for Structural Materials, National Institute for Materials Science, Tsukuba, Ibaraki 305-0047, Japan
[4] Japan Synchrotron Radiation Research Institute (JASRI), SPring-8, Hyogo 679-5198, Japan

*email: setsu_xue@eis.hokudai.ac.jp

Keywords: Titanium, small crack, nondestructive inspection, crack growth

1. Introduction

Due to their high specific strength, beta titanium alloys have received considerable attention in the aerospace industry [1)]. Consequently, research on their fatigue behavior has become critical, with recent findings indicating that fatigue cracks initiate at a crystallographic level associated with the small crack regime [2)]. The synchrotron radiation computed tomography (SR-CT) is an emerging method to non-destructively observe this fatigue behavior during the crack growth process. One of the widely used SR-CT methods for this purpose is the micro-CT with a micrometer-order of spatial resolution and a millimeter-order of field-of-view (FOV). For small fatigue cracks, however, a higher spatial resolution is required to analyze microscopic details. A high-energy phase-contrast X-ray nanotomography (nano-CT) with a spatial resolution of approximately 100 nm has been recently proposed, attracting considerable attention [3)]. Nano-CT can visualize small cracks and the surrounding microstructure, but its relatively narrow FOV presents challenges in locating the crack in the specimen bulk and monitoring its growth process. Consequently, the advantages of the micro- and nano-CT must be integrated to understand small crack growth and the interaction between small cracks and the local microstructure.

In the present study, SPring-8, a third-generation synchrotron radiation facility in Hyogo, Japan, was used to observe the small crack growth in a beta titanium alloy specimen. SPring-8's BL20XU beamline provides freely switchable multiscale tomography between the micro- and nano-CT.

2. Methodology

Material

The test material was a commercial metastable titanium alloy (Ti-22V-4Al) with a chemical composition (mass %) of Al (4.15), V (21.17), Fe (0.15), O (0.14), C (0.013), and H (0.0124). Its heating process involved a solution treatment at 1023 K for 1 h, followed by water quenching, then aging at 823 K for 4 h, and finally, air cooling. The heating rates of the solution and aging treatments were greater than 2000 K/h and 1000 K/h, respectively, which provided a coarse and acicular alpha-phase precipitated microstructure as shown in Fig. 1. The heat-treated alloy exhibited 850 MPa in 0.2% proof stress and 967 MPa in tensile strength. A straight-sectioned specimen was developed with a 0.7 mm diameter and 3 mm length; it was polished by emery papers until #2000 to remove the hardened layer.

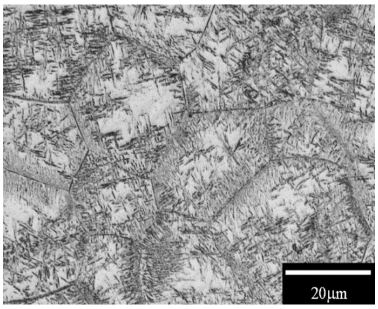

Fig. 1 SEM images of the heat-treated Ti-22V-4Al microstructure illustrating a coarse and acicular alpha-phase precipitation.

Imaging conditions and procedure

A micro- and nano-CT were conducted on the BL20XU beamline at SPring-8 $^{4)}$. In both the imaging modes, a 30.0 keV X-ray was employed, and the sample was rotated about its longitudinal axis from 0° to 180° with 0.1° increments, which provided 1800 radiographs per scan. The exposure time for measuring the X-ray intensity was 0.025 s and 4.0 s for the micro- and nano-CT, respectively, while the pixel size was 0.6 μm and 0.0387 μm, respectively.

An in-situ small crack growth test was carried out at the beamline hutch. A micro-CT imaging was followed by a fatigue test, and both were repeated at each interval of the loading cycle (ΔN). For the fatigue test, a maximum stress of 650 MPa was applied using a 10 Hz sine wave with a stress ratio of R = 0.1. The crack initiation process was captured by assuming ΔN = 500 until the completion of 2000 loading cycles, and it was readjusted to 1000 until specimen fracture. During the CT imaging processes, a tensile load of 50% maximum stress was applied to open the crack. A schematic of the CT system applied on a 1 mm diameter bulk specimen is shown in Fig. 2.

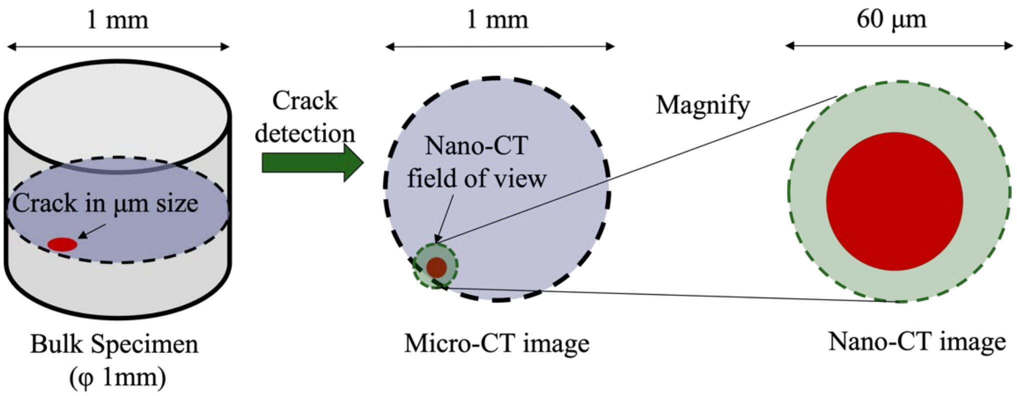

Fig. 2 Schematic of the applied imaging system.

3. Result and discussion

Micro-CT

Four cracks were observed at the specimen surface at the 1000th cycle, and one more was identified at the 1500th cycle. These five cracks were coded as C-1 to C-5, with C-1 leading to the final fracture at 9751 cycles. A comparison between the crack propagation rates ($\mathrm{d}a/\mathrm{d}N$) of all the five cracks against the stress intensity factor range (ΔK) is presented in Fig. 3. The $\mathrm{d}a/\mathrm{d}N$-ΔK curves exhibit a good agreement. However, with a decrease in ΔK, the deviation in $\mathrm{d}a/\mathrm{d}N$ increases. Tokaji et al. also conducted a ΔK-decreasing test using a compact tension specimen of Ti-22V-4Al $^{5)}$, represented by the dashed line in Fig. 3. In the high-ΔK regime (over 4-5 MPa√m), the $\mathrm{d}a/\mathrm{d}N$-ΔK in the present study was consistent with that of the large cracks. By contrast, in the low-ΔK regime, most of the $\mathrm{d}a/\mathrm{d}N$ of the small cracks were greater than those of the large cracks at the same ΔK. Therefore, the aforementioned results suggest that a smaller crack follows the least-resistance path, and the local microstructural factors can hinder its growth.

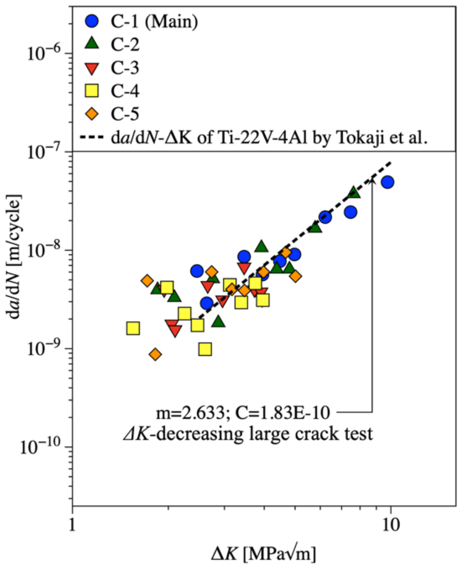

Fig. 3 Relationship between the crack propagation rate (da/dN) and the stress intensity factor range (ΔK).

Nano-CT

Fig. 4 presents the nano-CT images of a surface crack at initiation. Microstructural details, such as the grain boundary and alpha-phase precipitation, are evident in the longitudinal section views in Fig. 4 (a) and (b). The crack initiated from the inside of the beta grain rather than the grain boundary. Meanwhile, Fig. 4 (c) shows the nano-CT image projected on a plane perpendicular to the loading axis. The opened crack is indicated by the shadow feature. It is observed that the crack propagation was restrained by the grain boundary as highlighted by the red arrow. This phenomenon has been referred to as the grain boundary blocking effect [6)], and indicates that the mutual interaction between the crack and the local microstructure can be captured.

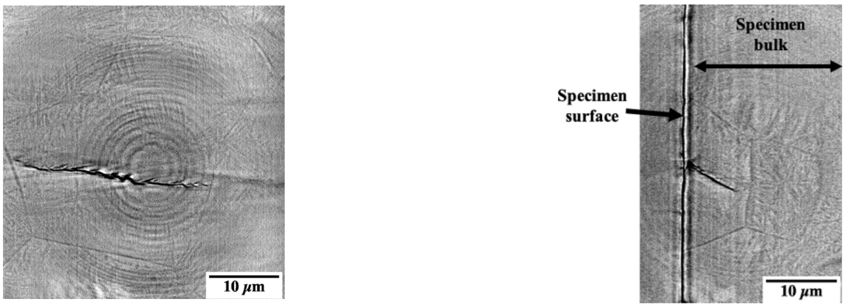

(a) Longitudinal section (parallel to crack length direction)

(b) Longitudinal section (parallel to crack depth direction)

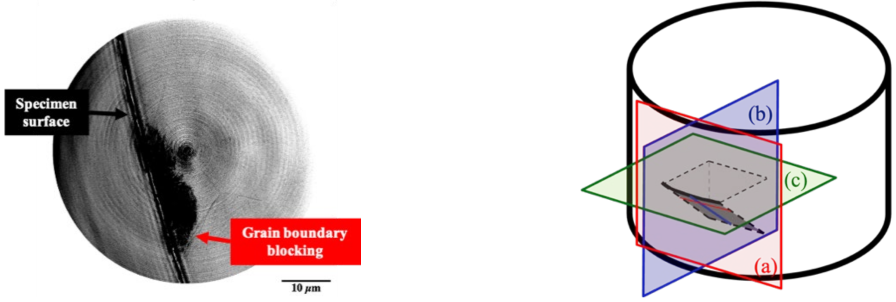

(c) Crack projected on a plane perpendicular to the loading axis

(d) Schematic of sectioning and projection view

Fig. 4 Nano-CT images of a surface crack.

4. Conclusion

This paper presents an investigation of the small crack initiation and propagation behavior observed by multiscale X-ray tomography involving the micro-CT and nano-CT methods. The following can be concluded:

1. The crack initiation and propagation were investigated by the micro-CT. Multiple cracks were initiated at the 1000th and 1500th cycles, equivalent to approximately 10% of the fatigue life (fracture observed at the 9751st cycle).
2. The propagation rates of the five detected cracks illustrated a good agreement with the da/dN–ΔK curve, indicating that the crack-shape evolution was negligibly related to the da/dN–ΔK. Moreover, with a decrease in the ΔK, the deviation in the crack propagation rate increased.
3. Both the microstructural details of the beta titanium alloy and the mutual interactions between the crack and its surrounding microstructure were clearly recognized by the nano-CT. The crack was initiated inside the beta grain, which lacked an alpha-phase precipitation. In addition, the grain boundary blocking effect could also be captured, thereby demonstrating that the microstructure plays a significant role in the small-crack behavior within beta titanium alloys.

Acknowledgement

We would like to express our sincere gratitude to the Daido Steel Co., Ltd. for providing the experimental material. The synchrotron radiation experiments were performed at the BL20XU, SPring-8 (proposal nos. 2020A0172) with the approval of the Japan Synchrotron Radiation Research Institute (JASRI). This research was supported by the f3 Engineering Education and Research Center at the Faculty of Engineering, Hokkaido University, and an Ambitious Doctoral Fellowship from the Hokkaido University. This research was funded by the Japan Society for the Promotion of Science, Japan (grant number: Scientific Research (A, 18H03748 and 21H04529)).

References

1) Boyer RR, Briggs RD. The use of β titanium alloys in the aerospace industry. *J Mater Eng Perform* 2005; 14:681–5.
2) Xue G, Nakamura T, Fujimura N, Takahashi K, Oguma H. Initiation and propagation processes of internal fatigue cracks in β titanium alloy based on Fractographic analysis. *Appl Sci* 2020; 11:131.
3) Takeuchi A, Suzuki Y. Recent progress in synchrotron radiation 3D-4D nano-imaging based on X-ray full-field microscopy. *Microscopy* 2020; 69:259–79.
4) Takeuchi A, Uesugi K, Uesugi M, Yoshinaka F, Nakamura T. Nondestructive multiscale X-ray tomography by combining microtomography and high-energy phase-contrast nanotomography. *Microsc Microanal* 2018; 24:108–9.
5) Tokaji K, Takafuji S, Ohya K, Kato Y, Mori K. Fatigue behavior of beta Ti-22V-4Al alloy subjected to surface-microstructural modification. *J Mater Sci* 2003; 38:1153–9.
6) Tanaka K, Akiniwa Y, Nakai Y, Wei RP. Modelling of small fatigue crack growth interacting with grain boundary. *Eng Fract Mech* 1986; 24:803–19.

The formation process of multiple facets in internal fatigue fractures of (α+β) Ti-6Al-4V

Takuya Yamazaki[1*], Hironori Morishita[1], Takashi Nakamura[2], Nao Fujimura[2] and Kosuke Takahashi[2]

[1] Division of Mechanical and Space Engineering, Hokkaido University, Sapporo, Hokkaido 060-8628, Japan
[2] Division of Mechanical and Aerospace Engineering, Hokkaido University, Sapporo, Hokkaido 060-8628, Japan

*Email: zaki-elms173@eis.hokudai.ac.jp

Keywords: Very high cycle fatigue; Crack initiation; Fractography Synchrotron radiation; NDI

Introduction

In very high cycle fatigue of Ti-6Al-4V, fractures are known to occur from inside the material(1). A typical rough area(2) is frequently observed on the fracture surface. On this rough area, many tiny flat surfaces, known as multiple facets, are evident. These facets are a peculiar characteristic of internal fractures. It is generally known that the facet in Ti-6Al-4V corresponds to the α-phase and that it can become the fatigue fracture origin(3). However, the circumstances under which these cracks originate from the facets have not yet been clarified. Additionally, identifying the facet of the main crack origin among multiple facets can be challenging. Thus, the focus of this study was on the formation mechanism of multiple facets, as well as the growth process of the internal crack in the rough area. Uni-axial fatigue tests were conducted, and fractography was utilized to classify the fracture morphology based on the location and size of the rough area. Moreover, synchrotron radiation computed tomography (SR-CT) was performed to observe the facet formation process nondestructively.

Material

(α+β) Ti-6Al-4V was used in this study(4). The 20-mm diameter × 1000 mm round bars were subjected to solution treatment (1203 K × 3.6 ks → A.C.) and aging treatment (978 K × 7.2 ks → A.C.). After heat treatment, the mechanical properties are tensile strength: 943 MPa, 0.2% proof stress: 860 MPa, elongation: 17 %, and Vickers hardness: 316 Hv. The microstructure is a dual-phase structure consisting of a primary α phase and (α+β) phase (a β phase containing a needle-shaped α phase). The average grain size is 9.4 µm for α grains and 9.1 µm for (α+β) grains. In this test, two specimens with diameters of 4.0 mm and 0.7 mm were used. The former specimen was used to obtain basic fatigue data and the latter was used to observe the internal cracks by SR-CT.

Fatigue properties

Uniaxial fatigue tests were conducted for the 4 mm-diameter specimen(5) and the 0.7 mm-diameter specimen under the stress ratio of 0.1 in an atmospheric environment. The *S-N* plots are shown in Fig. 1. Circles (○) indicate the surface fracture, triangles (△) indicate the internal fracture, and diamonds (◇) indicate the combined fracture(5) in which the surface and internal cracks propagate and coalesce. The open marks are the 4.0 mm-diameter specimen results and the solid marks are the 0.7 mm-diameter specimen results. There was no significant difference in the *S-N* properties of the two specimens; therefore, the fatigue properties of this material are sufficiently evaluated using the 0.7-mm diameter specimen for SR-CT. Furthermore, four internal fractures occurred at 600 MPa, for which the fatigue life varies from 3.63×10^7 cycles to 8.94×10^7 cycles. To determine whether the fatigue life affects the fracture surface morphology, we sequentially conducted fracture surface observation on these four specimens.

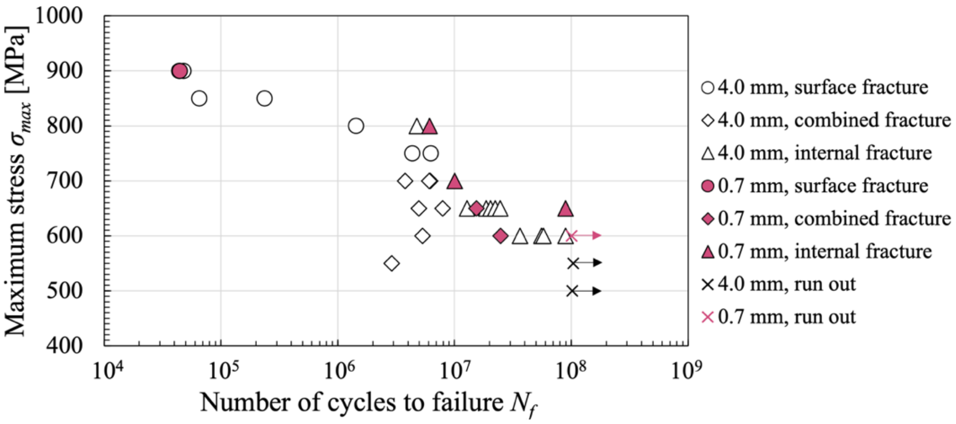

Fig. 1 *S-N* plots of the material used.

Fracture surface observation

To clarify the internal crack growth process, the fracture surface of the internal fractures of the 4-mm specimens was observed by scanning electron microscopy (SEM). We can observe the rough area, which contains multiple facets on the fracture surface (Fig. 2). The distance between the multiple facets in the rough area was about 20 µm.

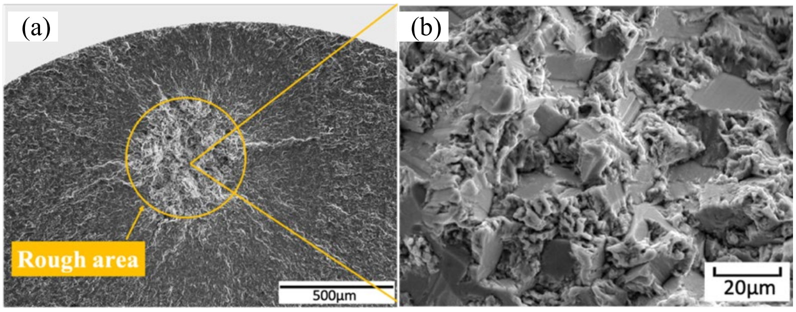

Fig. 2 (a) Fracture surface of the internal fracture of Ti-6Al-4V. σ_{max} = 600 MPa, R = 0.1, N = 8.94 x 10^7 cycles. (b) Magnified view of the area surrounding the origin of the fracture shown in (a).

To quantitatively analyze the rough area, we conducted three-dimensional SEM focusing on the flat surface located outside the rough area. The concept of area ratio, which is the ratio of the flat surface area to the rough area, was introduced in the present study to describe the transition process between these distinct morphologies. The procedures are as follows:

First, a facet located at the center of the rough area was determined as the starting point for the measurement, and three-dimensional SEM images of the rectangular area (50 µm × 150 µm) were taken from the starting point to the specimen surface. Then, the area of the flat region within a height difference of 5 µm was measured, and the area ratio was determined as the ratio of this flat region to the rectangular area (50 µm × 150 µm image).

Fig. 3 shows the relationship between the area ratio and ΔK for four fracture surfaces of the internal fracture (corresponding to (△) in Fig. 1). Here, ΔK was calculated by Equation (1):

$$\Delta K = \frac{1}{\pi} \Delta\sigma\sqrt{\pi a} \ ^{(6)} \qquad (1)$$

where a corresponds to the distance between the starting point and the center of the rectangular area.

The obtained four curves are almost identical regardless of the differences in the fatigue life. ΔK_{trans}, which describes the transition from the rough area to the flat surface, was determined by the ΔK value at the 50% area ratio. As seen in Table 1, the ΔK_{trans} is almost the same regardless of the differences in the fatigue life. This means that the transition from the rough area to the flat surface is dominant by ΔK of the internal crack reaches a certain value. Namely, the transition can be a fracture mechanics phenomenon. Moreover, considering that the rough area and the flat surface correspond to the microstructure-sensitive features and the microstructure-insensitive features, respectively, the transition is regarded as a border between the so-called Stage 2a and Stage 2b regions of the crack propagation process. Therefore, the characteristic fracture surface of the rough area is formed under the typical Stage 2a crack growth process.

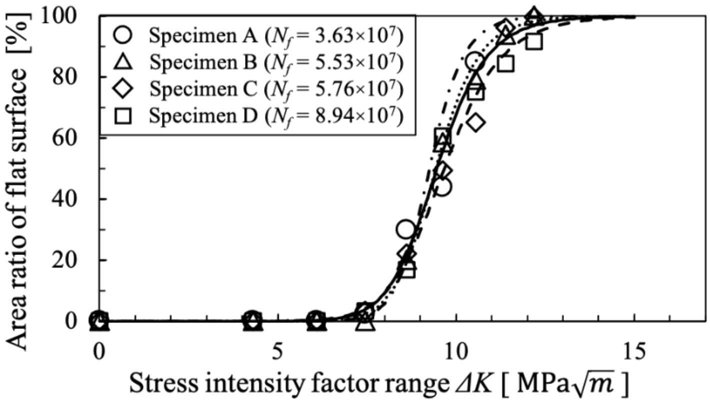

Fig. 3 Relationship between ΔK and the area ratio of the flat surface on the fracture surfaces.

Table 1 ΔK_{trans} at 50% of the area ratio of flat surface.

Specimen	A	B	C	D
ΔK_{trans} (MPa√m)	9.47	9.44	9.68	9.26

Observation of internal cracks using synchrotron radiation X-rays

In the previous section, it was noted that the rough area is classified into the typical Stage 2a process. However, the formation mechanism of multiple facets is not known yet. Two factors can possibly explain the multiple facets: one is that many of the internal cracks initiate from facets independently propagate and coalesce with each other, and the other is that multiple facets are formed one after another during the propagation from a single crack. To clarify which factor is suitable, we conducted nondestructive observation of the internal cracks using SR-CT. A 0.7-mm specimen subjected to cyclic loading of $N = 5.0 \times 10^7$ cycles with maximum stress $\sigma_{max} = 600$ MPa and a stress ratio $R = 0.1$ was prepared and nondestructive observation was performed using SPring-8 (BL20XU). This fatigue test condition corresponds to the condition under which the internal fracture was observed in the 4 mm specimens. The principle and technique of observation was based on Yoshinaka's method(3), and the observation was conducted using SR-CT. The observation conditions are shown in Table 2.

Table 2 SR-CT observation conditions.

X-ray energy	Step angle	Exposure time	Pixel size	Field of view
30 keV	0.1 °	0.025 s	0.5 μm	1×1 mm

As a result of the observation, 14 internal cracks were detected in the 0.7-mm specimen. The detected internal cracks were numbered Crack 1, 2, ..., 14, in the order of decreasing projected area. The distribution of the crack positions is shown in Fig. 4. The shortest distance between the internal cracks in the specimen was about 210 μm. In comparison to the distance between the multiple facets in the rough area (about 20 μm), the cracks in this specimen were located far from each other and were unlikely to coalesce during propagation. The longitudinal cross-sectional images of the largest detected cracks, Crack 1 and Crack 2, are shown in Fig. 5. The black line represents the crack. The dark area in Fig. 5 indicates the α phase, and the brighter area indicates the (α+β) phase. Both of these cracks are generated in the α phase, and are considered to correspond to the facets. The size of these cracks was comparable to the size of a grain. In other words, these cracks do not contain multiple facets. These results indicate that multiple cracks are not formed by the coalescence of cracks initiated and propagated independently from many facets; they are induced by the Stage 2a crack propagation process initiated from a single facet.

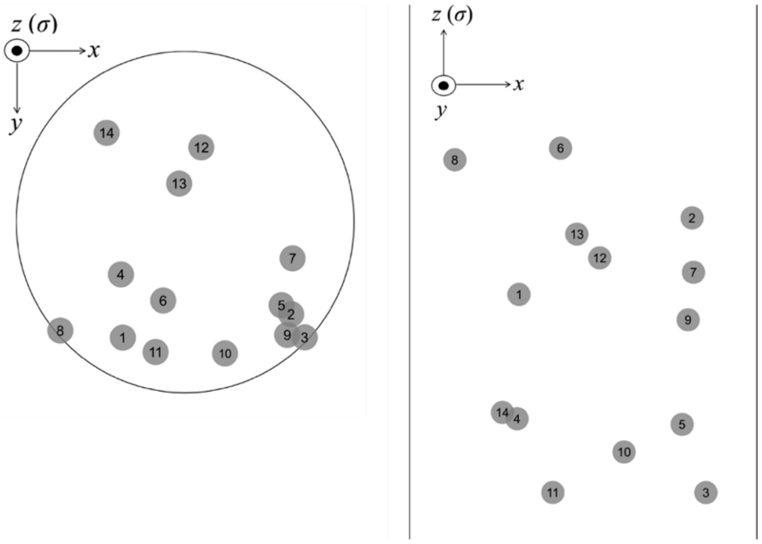

(a) Cross-sectional view. (b) Longitudinal view.

Fig. 4 Crack initiation sites in the observation region.

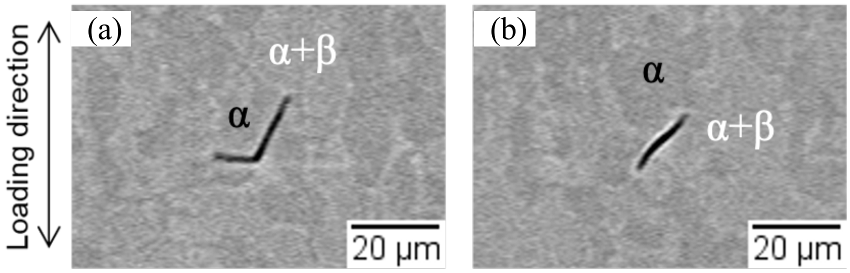

(a) Crack 1 ($\sqrt{area}$ $=12.4$ μm) (b) Crack 2 ($\sqrt{area} = 12.0$ μm)

Fig. 5 The longitudinal cross-sectional images of Crack 1 and Crack 2 (σ_{max}=600 MPa, N_f=5.0×10^7).

Conclusion

The rough area of the fracture surface of internal fractures was quantitatively investigated by SEM fractography. Nondestructive observation of the internal microcracks was performed using SR-CT. The main results are:

1. The transition from the rough area to the flat surface is determined by the ΔK value, and the rough area corresponds to the Stage 2a region in the fracture process.
2. The distance between the micro-internal cracks detected by SR-CT is too large for the cracks to be connected to each other. Thus, multiple cracks are not formed by the coalescence of the microcracks initiated and propagated independently from many facets; they are induced by the Stage 2a crack propagation process initiated from a single facet.

Acknowledgement

This work was performed at SPring-8, Japan Synchrotron Radiation Research Institute (BL20XU, Project No. 2020A0172). This research was funded by the Japan Society for the Promotion of Science under the Scientific Research grant (A, 21H04529).

References

1) S. Nishijima and K. Kanazawa*: Mater. Struct.* **22** (1999) pp. 601-607.
2) X. Liu, C. Sun and Y. Hong: *Mater. Sci. Eng. A* **622** (2015) pp. 228-235.
3) S.K. Jha, C.J. Szczepanski, P.J. Golden, W.J. Porter III and R. John: *Int. J. Fatigue* **42** (2012) pp. 248-257.
4) F. Yoshinaka, T. Nakamura, A. Takeuchi, M. Uesugi and K. Uesugi: *Mater Struct.* **42** (2019) pp. 2093-2105.
5) H. Oguma and T. Nakamura: *Journal of the Society of Materials Science,Japan.* **60** (2011) pp. 1072-1078.
6) I.N. Sneddon: *Proc Roy Soc, London, Ser. A.* **187** (1946) pp. 229-260.

Estimation of Fatigue life for internal cracks using crack growth rates measured in a vacuum environment

Sourav Kumar Modi[1, *], Paras Mehendiratta[1], Takashi Nakamura[2], Nao Fujimura[2] and Kosuke Takahashi[2]

[1] Division of Mechanical and Space Engineering, Hokkaido University, Sapporo, Hokkaido 060-8628, Japan
[2] Division of Mechanical and Aerospace Engineering, Hokkaido University, Sapporo, Hokkaido 060-8628, Japan
*Email: souravkumarmodi@frontier.hokudai.ac.jp

Keywords: crack growth, fatigue, high strength steel, inclusions, ODA, vacuum

1. Introduction

Recent times have stressed the importance of an in-depth understanding of the properties of fatigue cracks for high-strength steel. This is because the fractures originate from inside the material in very high-cycle region, typically when the number of cycles exceeds 10^7. Furthermore, the stress at which this occurs is significantly lower than the stress that causes surface fractures in the high-cyclic fatigue (HCF) region. As it is extremely difficult to directly observe the internal fracture process that mostly occurs because of the internal cracks initiating from the non-metallic inclusions in the order of a few micrometers (1), the exact mechanism of the internal fractures is not entirely known. The study of internal fracture surfaces has shown the formation of an optically dark area (ODA) (2) around these inclusions in longer fatigue lives. Several researchers have attempted to explain the effects of these inclusions by drawing similarities between the internal cracks and surface cracks in a vacuum, as the internal cracks are also cut off from the outside environment (3, 4). Additionally, earlier experiments have shown that ODA-like regions form in the fracture surfaces of fatigue tests performed in a vacuum (5).

This study aims to understand the process of internal fatigue crack initiation and propagation by estimating the fatigue life of internal cracks using the surface crack growth rates of high-strength steel SNCM 439 measured in a vacuum environment. The fatigue lives were calculated by integration with the assumption that the fatigue cracks propagated according to the Paris power law.

Finally, a comparison between the estimated and actual fatigue lives from the internal fractures helps elucidate the mechanism of internal fractures resulting from a fatigue crack.

2. Experimental procedure

2.1 Experiment material

The material used in the experiments was JIS SNCM 439. Normalizing (1133 K for 3.6 ks followed by air cooling), quenching (1123 K, oil cooled after holding for 3.6 ks), and low-temperature-tempering (433 K, after holding for 7.2 ks, it was subjected to air cooling) were performed for heat treatment.

2.2 Experiment specimen and fatigue test conditions

The following two experiments were conducted using two types of specimens from different lots of the materials:

(a) Experiment 1 – Push–pull fatigue test: Fatigue tests at $R = -1$ were performed to obtain the S-N curve focusing on subsurface fatigue fractures initiating from non-metallic inclusions (6).

(b) Experiment 2 – Fatigue crack growth test: MT specimens were used according to the ASTM E647-00 manual for ΔK decreasing tests in a vacuum environment (5) to examine the crack growth and arrest properties.

These experiments are referred to as Experiments 1 and 2 for convenience.

3. Experimental results

3.1 *S-N* curve

The results of the fatigue tests performed in Experiment 1 are shown in Fig. 1. After 10^5 cycles, subsurface fractures became prominent in the specimens, and the fatigue life increased compared to the surface fractures. However, below 650 MPa stress, these failures seemed to stop, which likely shows that a fatigue limit exists in this VHCF region, as also suggested by Murakami (7). Most of the actual fractures originated from TiN type of inclusions having sizes ranging between 4.96 and 9.25 µm. However, in the specimens subjected to 1100 MPa and 750 MPa, the cracks started from the Al_2O_3 type of inclusions, having sizes of 21.6 µm and 31.26 µm, respectively.

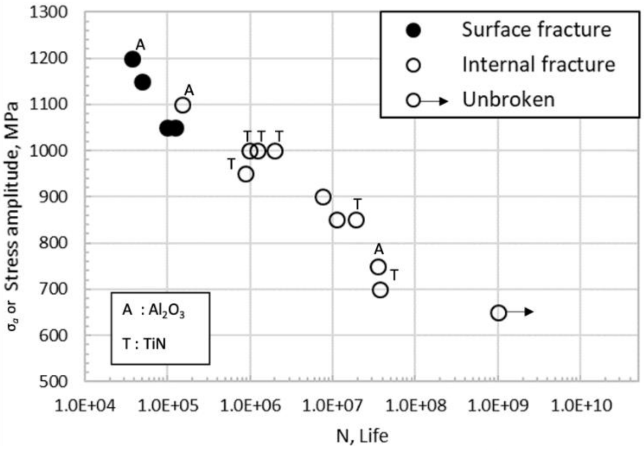

Fig. 1 *S-N* curve of SNCM439^(6)^.

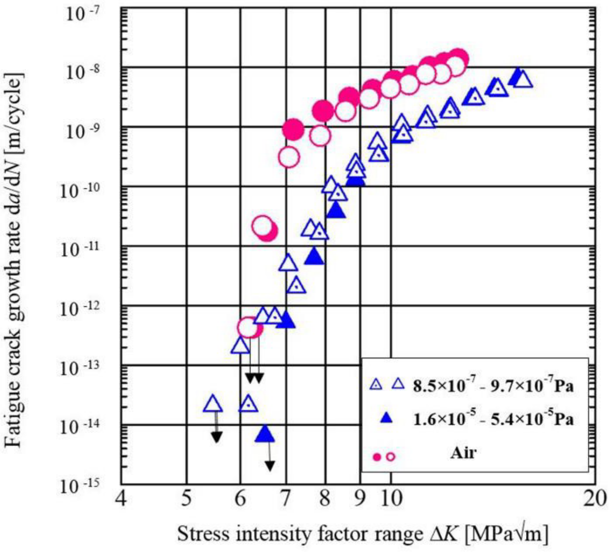

Fig. 2 Relationship between d*a*/d*N* and Δ*K*.
(both air and vacuum) ^(5)^.

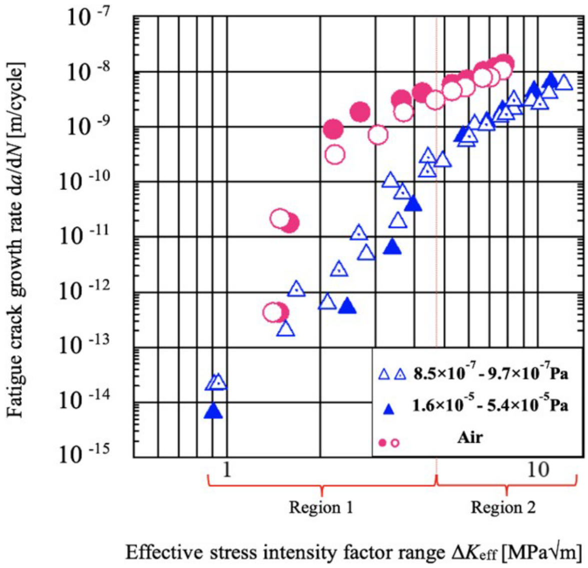

Fig. 3 Relationship between d*a*/d*N* and ΔK_{eff}
(both air and vacuum) ^(5)^.

3.2 Crack growth rate

To examine the properties of the crack growth, the stress intensity factor range Δ*K* is calculated using Equation (1) in which only the positive value of K_{min} is used. Therefore, for the stress ratio, $R = -1$, the value of K_{min} becomes 0. The effective stress intensity factor range ΔK_{eff} is calculated using K_{max} and K_{op}, as expressed in Equation (2), where K_{op} refers to the stress intensity factor at the crack opening.

$$\Delta K = K_{max} - K_{min}, K_{min} = 0 \qquad (1)$$

$$\Delta K_{eff} = K_{max} - K_{op} \qquad (2)$$

Fig. 2 presents the d*a*/d*N* versus Δ*K* values in air and vacuum environments. Clearly, there is a significant difference between the fatigue crack growth rates in air and in a vacuum, leading us to assume that the slower crack growth rates observed in the vacuum can explain the longer life observed in subsurface fractures. Fig. 3 presents the d*a*/d*N* versus ΔK_{eff} values observed in the air and vacuum. We chose the d*a*/d*N* versus ΔK_{eff} curve in the vacuum to perform the life evaluation, as it is generally thought that most of the fatigue life is spent in a small-crack regime where there is not much crack closure effect; therefore, it is important to remove the crack closure effect by using ΔK_{eff} instead of Δ*K*. In addition, evidently the effective threshold $\Delta K_{eff,th}$ is lower in a vacuum than in air, which seems appropriate for explaining the subsurface properties. As shown in Fig. 3, there are two major regions depending on the rate of change in crack growth rate in the vacuum environment. The division of these regions is performed only for the simplicity of curve fitting and easier estimation of the life of the cracks; there is no physical meaning whatsoever of this division as far as the material's properties are concerned.

4. Process of fatigue life estimation

We use the power law to integrate the life in each of these two regions and add them together to obtain the fatigue life at a particular stress level. The Paris power law (as expressed in Equation (3) was used, as well as two sets of material constants C and m from the da/dN versus ΔK_{eff} curve in a vacuum. Therefore, Equation (3) was used to fit the curve and obtain the values of C and m in Regions 1 and 2, respectively.

$$\frac{da}{dN} = C\,(\Delta K_{\text{eff}})^m \text{, where } C \text{ and } m \text{ are the Paris constants derived.} \tag{3}$$

The stress intensity factor or ΔK for any subsurface penny-shaped crack or inclusion is expressed by Equation (4). However, in our study, this equation is used to relate the value of the crack length with ΔK_{eff} instead of ΔK.

$$\Delta K_{\text{eff}} = \frac{2}{\pi}\Delta\sigma\sqrt{\pi a} \tag{4}$$

For Region 1

In Region 1 of the da/dN and ΔK_{eff} curves in Fig. 3, the values of material constants C and m according to Equation (3) are 2.066×10^{-14} and 6.015, respectively. Equations (3) and (4) are then used after rearranging to obtain Equation (5), which can be integrated to obtain the estimated life in Region 1.

$$\int_0^N dN = \int_{a_i}^{a_f} \frac{\pi^m da}{2^m C \Delta\sigma^m (\pi a)^{\frac{m}{2}}} \tag{5}$$

Equation (5) is used to obtain the fatigue life at each $\Delta\sigma$ or σ (as σ, min=0 for R= -1). At each $\Delta\sigma$, a_i is the initial crack length based on the different sizes of the assumed non-metallic inclusions (considering inclusions as penny shaped, a_i is half of the initial length). Meanwhile, a_f is the crack length at which the calculated ΔK_{eff} is at the boundary of Regions 1 and 2 of the da/dN versus ΔK_{eff} curves in a vacuum (Fig. 3). The value of ΔK_{eff} was regarded as 4.54 MPa$\sqrt{m}$ as per the boundary shown in Fig. 3.

For Region 2

For Region 2, the values of C and m were 2.163×10^{-12} and 3.27, respectively. Similar to Region 1, Equation (5) is integrated to obtain the fatigue life. The lower limit of the crack length is the upper limit of Region 1, and the upper limit was fixed at 2 mm based on the specimen of Experiment (1). However, this upper limit does not significantly affect the life, as observed during the calculations.

The abovementioned process was applied to determine the estimated life in different cases, depending on the actual size of the inclusion available in the high-strength steel.

Table 1 Estimated fatigue life.

Stress limit	Inclusion size µm (type)	Actual life, Nf	Estimated life, Np			Np/Nf
			Region 1	Region 2	Total	
1100	21.6 (Al_2O_3)	1.52E+05	1.94E+04	6.46E+04	8.39E+04	55.26 %
1000	6.92 (TiN)	9.89E+05	9.22E+05	7.75E+04	9.99E+05	101.08 %
1000	6.95 (TiN)	1.22E+06	9.13E+05	7.75E+04	9.91E+05	80.95 %
1000	4.96 (TiN)	1.99E+06	1.84E+06	7.75E+04	1.92E+06	96.19 %
950	8.42 (TiN)	8.83E+05	8.38E+05	8.54E+04	9.24E+05	104.54 %
850	9.25 (TiN)	1.91E+07	1.37E+06	1.05E+05	1.48E+06	7.75 %
750	31.3 (Al_2O_3)	3.56E+07	1.87E+05	1.33E+05	3.20E+05	0.90 %
700	6.75 (TiN)	3.68E+07	5.65E+06	1.31E+05	5.78E+06	15.71 %

5. Results and discussion

The fatigue lives estimated along with the actual internal fatigue life from the S-N curve of SNCM 439 are listed in Table 1. Clearly, the predicted life is quite close to the actual fatigue life at higher stress amplitudes, but the difference continues to increase with a reduction in the stress amplitude. In the lower stress region, the estimated life compared to the actual life is less than 16% of the actual life. In general, the difference was found to be larger for the specimens where the Al_2O_3 type inclusion was the fracture source. This difference may be due to the different mechanisms of crack initiation in the Al_2O_3 and TiN inclusions. In TiN inclusions, cracks originate earlier than Al_2O_3 inclusions, indicating that the actual life is the same or larger for Al_2O_3 inclusions despite their larger size (8).

One of the possible reasons for this variation between the estimated and actual fatigue lives is that the crack growth rates observed in the large crack growth experiments performed in vacuum using ΔK_{eff} could be higher than the crack growth rate of internal cracks. Slow internal crack growth rates have been suggested by several researchers (9, 10). This implies that the internal crack growth rates could be 10–100 times slower than the large crack growth rates in vacuum in the lower ΔK_{eff} or ΔK regions.

Another possible reason for this variation between the estimated and actual fatigue lives is that the life predicted in this study did not include crack initiation, which could constitute most of the fatigue life (11).

6. Summary

The main findings of this study are as follows:

1. The estimated fatigue life in this method is efficient for higher stress amplitude regions, where the actual ΔK values are not quite small.
2. The estimated fatigue life from this method is not efficient for the lower stress amplitude region, where the actual ΔK values are small. A possible reason for the deviation could be the difference in the crack propagation rates observed in the surface crack in a vacuum, and the actual crack propagation rate, along with the possibility of a large crack initiation life that was not considered.
3. The real mechanism of internal crack initiation and slow growth near inclusions cannot be understood by examining only the effect of a vacuum-like environment around the internal cracks. Therefore, additional studies on the crack initiation life are essential for a better understanding of the internal crack properties starting from inclusions.

References

1) Zhang, J.M., S.X. Li, Z.G. Yang, G.Y. Li, W.J. Hui and Y.Q. Weng, “Influence of inclusion size on fatigue behavior of high strength steels in the gigacycle fatigue regime”, International Journal of Fatigue, Vol. 29, No. 4 (2007), pp. 765-771.

2) Murakam, Y., T. Nomoto and T. Ueda, “Factor influencing the mechanism of superlong fatigue failure in steels”, Fatigue & Fracture of Engineering Materials & Structures, Vol. 22, No. 7 (1999), pp. 581-590.

3) Grinberg, N.M., “The effect of vacuum on fatigue crack growth”, International Journal of Fatigue, Vol. 4, No. 2 (1982), pp. 83-95.

4) Yoshinaka, F. and T. Nakamura, “Effect of vacuum environment on fatigue fracture surfaces of high strength steel”, Mechanical Engineering Letters, Vol. 2 (2016), pp. 15-00730, No. 15-00730, DOI: 10.1299/mel.15-00730.

5) Mehendiratta, P., R. Ishihara, T. Nakamura, N. Fujimura and K. Takahashi, “Effects of vacuum environment on the fatigue crack growth properties of high strength steel-behavior of long crack by ΔK decrease test”, JSME M&M2018 Conference, OS0801, (2018).

6) 水門恵理，中村孝，小熊博幸， 池田慎太郎，“SNCM439 の超高サイクル疲労特性に及ぼす焼もどし温度の影響”，日本機械学会論文集（A 編），Vol. 76, No. 764 (2010), pp. 440-442.

7) Murakami, Y. and M. Endo, “Effects of defects, inclusions and inhomogeneities on fatigue strength”, International Journal of Fatigue, Vol. 16, No. 3 (1994), pp. 163-182.

8) Spriestersbach, D., P. Grad and E. Kerscher, “Influence of different non-metallic inclusion types on the crack initiation in high-strength steels in the VHCF regime”, International Journal of Fatigue, Vol. 64 (2014), pp. 114-120.

9) Furuya, Y., “Small internal fatigue crack growth rate measured by beach marks”, Materials Science & Engineering, Vol. 678 (2016), pp. 260-266.

10) Hong, Y., Z. Lei, C. Sun and A. Zhao, “Properties of crack interior initiation and early growth for very-high-cycle fatigue of high strength steels”, International Journal of Fatigue, Vol. 58 (2014), pp. 144-151.

11) Marines-Garcia, I., P.C. Paris, H. Tada, C. Bathias and D. Lados, “Fatigue crack growth from small to large cracks on very high cycle fatigue with fish eye failures”, Engineering Fracture Mechanics, Vol. 75, No. 6 (2008), pp. 1657-1665.

Influence of shearing condition on delayed fracture at sheared edge in 1470 MPa grade steel

Satoshi Maeda[1,*], Masaki Tada[1], Yuki Toji[1] and Shinjiro Kaneko[1]

[1]Steel Research Laboratory, JFE Steel Corporation, 1, Kawasaki-cho, Chuo-ku, Chiba, 260-0835, Japan
*email: sa-maeda@jfe-steel.co.jp

Keywords: Hydrogen embrittlement, Delayed fracture, Sheared edge

1. Introduction

Recently, application of high strength steel sheets to automobiles is expanding in order to achieve both collision safety andweight reduction for fuel efficiency. Therefore understanding delayed fracture caused by hydrogen embrittlement is important. Regarding delayed fracture at sheared edge, even when no stress is applied, it is known that cracks are generated when hydrogen is introduced [1]. However the details of such cracks are not clear. In this report, the influences of shearing conditions on cracks at sheared edge were investigated.

2. Experimental procedure

1470 MPa cold-rolled steel sheet were sheared under various shearing conditions, including the clearance, blank holder, and shear angle. The sheared samples were immersed in NH_4SCN acid to induce cracks on the sheared edge. These cracks were observed by microscope. Residual stress measurements and FEM analysis were performed to consider the direction and depth of the cracks.

3. Results and discussion

Fig. 1 shows images of the sheared edge after immersion for each shearing condition. Multiple cracks were observed under all conditions. The direction of cracks changed depending on the shear angle and the blank holder. When the shear angle was 0° with the blank holder, ND cracks were observed. Otherwise, without the blank holder, TD cracks were observed near the burr side in addition to ND cracks. At the shear angle of 2°, the direction of cracks were oblique from the upper left to the lower right, and there was little difference between the results with and without blank holder. Measurement of residual stress at sheared edge revealed the correlation between the direction of cracks and the value of ND and TD residual stress.

In order to investigate the depth of the cracks at sheared edge, the cross section of the crack was observed. The depth of the cracks from surface was approximately 200 μm. The results of FEM analysis indicated that a compressive stress region existed inside the tensile stress at sheared edge, and the depth of the tensile stress region was corresponding to the depth of the crack. These results suggested that crack propagation was suppressed by the inside compressive stress.

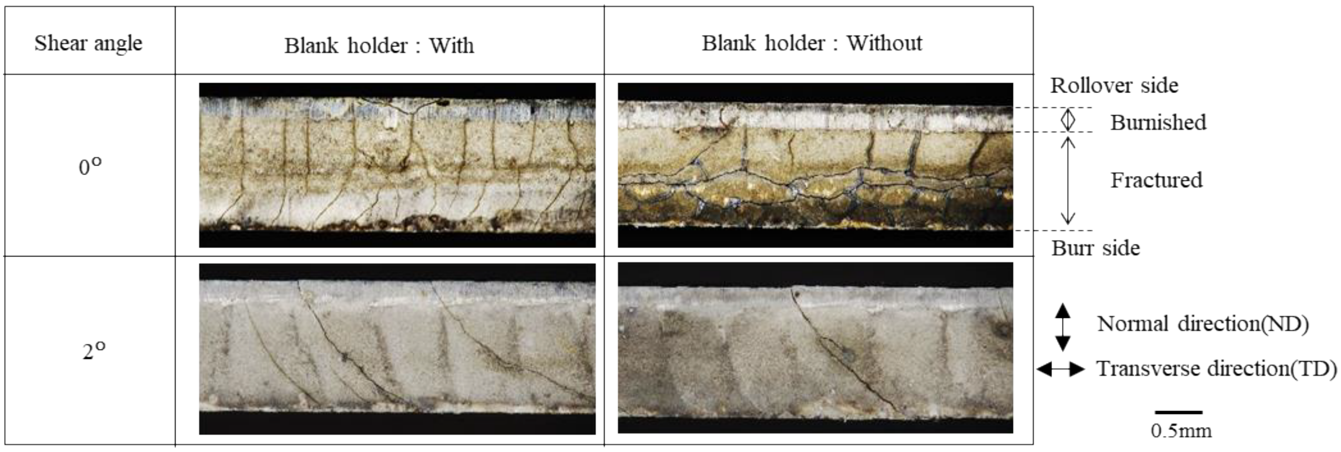

Fig. 1 Influence of shear angle and blank holder on crack at sheared edge (clearance = 14%)

4. References

1) Y. Nakagawa, K. Mori, T. Maeno and R. Umemiya: Journal of the JSTP, **59**(2018), pp. 221-227

Enhanced plastic fatigue durability of Fe-Mn-Cr-Ni-Si bidirectional-TRIP steel

Fumiyoshi Yoshinaka[1,*], Takahiro Sawaguchi[1], Susumu Takamori[1], and Satoshi Emura[1]

[1] Research Center for Structural Materials, National Institute for Materials Science, Tsukuba, Ibaraki 305-0047, Japan
*email: YOSHINAKA.Fumiyoshi@nims.go.jp

Keywords: high-Mn steel, fatigue, plastic deformation, martensitic transformation, electron backscattering diffraction

Metal fatigue is the main failure mechanism of the mechanical and structural components under cyclic deformation conditions. Fig. 1 (a) shows the schematic of typical fatigue fracture process. Fatigue fracture is caused by crack initiation and propagation. Under cyclic loading, local irreversible dislocation motion occurs even if the stress is below the yield stress. The accumulation of irreversible components of slip, which is also aided by gas adsorption on the newly developed surface due to deformation, results in the formation of irregularities on the metal surface called intrusion and extrusion. Crack initiation is triggered by the stress/strain concentration at the root of intrusion. Fig. 1 (b) shows the fatigue crack initiation from the artificial defect processed by the femtosecond laser on the high-Mn steel. Slip bands were formed by cyclic loading and the crack initiated along the well-developed one. As shown in the figure, the development of slip band and crack initiation are continuous, and it is difficult to distinguish them clearly. After the crack initiation, crystallographic shear crack growth on the slip plane is observed (stage I). As the crack becomes sufficiently long, it propagates macroscopically linearly in the direction perpendicular to the loading axis due to multiple slip (stage II). Although the crack growth behavior differs depending on its length, fatigue crack growth is always caused by plastic deformation at the crack tip. Namely, although fatigue damage is observed as crack initiation and propagation, its true nature is plastic deformation.

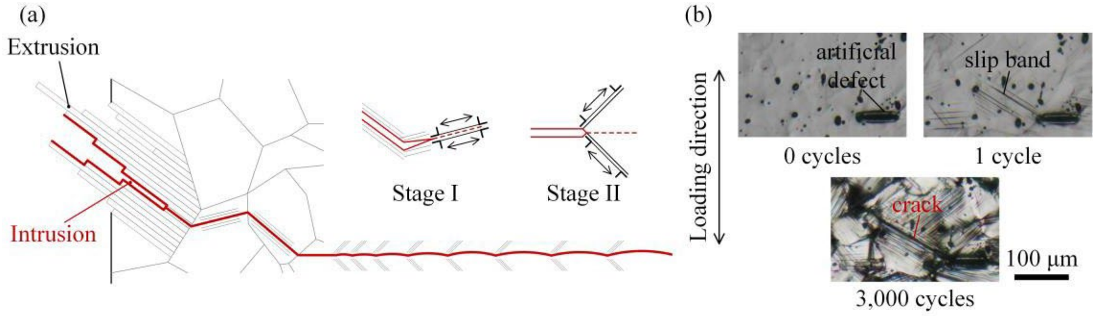

Fig. 1 (a) Schematic of fatigue fracture process and (b) Crack initiation and stage I crack propagation.

The term "metal fatigue" usually refers to high cycle fatigue (HCF), in which low loads below the yield stress are applied repeatedly, resulting in fracture with number of cycles over 10^5 cycles. In contrast, fatigue in which fracture occurs in a relatively small number of cycles (typically less than 10^4 cycles) due to large loading accompanied by macroscopic plastic deformation is called low-cycle fatigue (LCF) or plastic fatigue. LCF is one of the limit states in seismic design of steel structures. A vast amount of LCF data has been accumulated, and several empirical laws on LCF has been proposed, including the Manson-Coffin law 1), 2). It is reported that the plastic fatigue life N_f is not significantly affected by chemical composition 2. However, in recent years, it has been reported that some austenitic steels and high entropy alloys exhibit excellent plastic fatigue endurance 3)-7). This peculiarity can be understood by the fact that the essence of fatigue is plastic deformation. The plastic deformation mechanism of austenitic alloys is sensitive to the stacking defect energy (SFE), which depends on chemical composition (and deformation temperature). The smaller the SFE is, the more easily the dislocations extended, and the typical deformation mechanism changes from extended dislocation glide to deformation twins and ε-martensitic transformation 8). The variety of deformation mechanisms in FCC alloys is therefore considered to give rise to different LCF properties.

TRIP steel is a material that exhibits excellent ductility through deformation accompanying phase transformation 9). There are several types of deformation-induced transformations; the transformation from initial FCC γ-austenite to BCC α'-martensite (γ→α'-martensitic transformation), the two-stage γ→ε→α'-martensite transformation in which HCP ε-martensite is formed as an intermediate phase due to low SFE, and the γ→ε-martensitic transformation when ε is sufficiently stable. In addition to these, a bidirectional γ→ε→γ transformation, in which the ε-martensite generated by the γ→ε-martensitic transformation is reversely transformed into γ-austenite, has recently been reported 10)-12). The TRIP steels that utilize this bidirectional transformation are called bidirectional-TRIP (B-TRIP) steels. The present authors believe that this reversible bidirectional transformation can mitigate the accumulation of fatigue damage (irreversible component of slip), and have been working on the development of B-TRIP steels with excellent fatigue endurance 13), 14).

The Fe-15Mn-10Cr-8Ni-4Si B-TRIP steel is a material that developed for application in a seismic damper 15). Seismic damper is a device that absorbs seismic energy transmitted to buildings through cyclic elastoplastic deformations. Due to the principle of operation, low cycle fatigue is unavoidable for seismic dampers, and their design life is determined by the plastic fatigue life. The Fe-15Mn-10Cr-8Ni-4Si B-TRIP steel have excellent fatigue endurance that can withstand multiple giant earthquakes, and has already been installed in some buildings as seismic dampers. Recently, Fe-15Mn-11Cr-7.5Ni-4Si B-TRIP alloy was also developed as a modified alloy with improved weldability 13). Fig. 2 shows the design concept of the B-TRIP steels. Firstly, the Gibbs free energy difference between γ-austenite and ε-martensite $\Delta G^{\gamma\to\varepsilon}$ is set to be 0 to activate the bidirectional γ→ε→γ transformation. The details of the calculation of $\Delta G^{\gamma\to\varepsilon}$ is shown in our recent paper 16). In this paper, we combined thermodynamic parameters reported in 17), 18). The other condition is to inhibit the formation of α'-martensite. The γ→α' or γ→ε→α'-martensitic transformations are irreversible process during fatigue deformation; the α'-martensite interferes with the occurrence of the bidirectional γ→ε→γ transformation.

The present paper reports the plastic fatigue durability of newly developed B-TRIP steels through comparison with the other austenitic steels reported in literature from the view point of deformation mechanism and $\Delta G^{\gamma\to\varepsilon}$. Additionally, the potential of the design concept of fatigue resistant alloy utilizing B-TRIP is pursued via analysis of deformation microstructure of the B-TRIP steels.

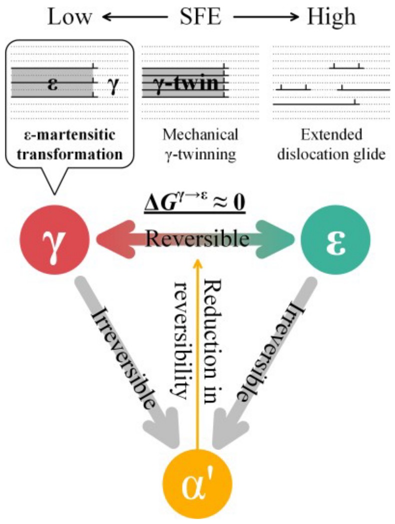

Fig. 2 Design concept of the B-TRIP steels.

The Fe-15Mn-(10+2X)Cr-(8-X)Ni-4Si B-TRIP steels with systematically increasing amounts of Cr and decreasing amounts of Ni were made, where X = 0, 0.5, 1, 2. Hereinafter, these are referred to as X0, X05, X1, and X2, depending on the value of X. X0 and X05 alloys correspond to the B-TRIP alloys mentioned above. The purpose of these alloys with varying Cr and Ni was to improve hot cracking susceptibility by changing the solidification mode, but the present study focuses on their fatigue properties. The alloy was melted in an argon atmosphere. The ingot was forged and rolled at 1,000 °C, and heat-treated at 1,000 °C for 1h, followed by water quenching. All materials had a fully-austenitic microstructure. The strain-controlled uniaxial fatigue tests were conducted on the specimens with the parallel part of φ8 × 13 mm. The triangle waves were applied at strain rate of 0.4%/s under strain ratio of -1 and total strain amplitude εt, a of 1%.

Fig. 3 (a) shows the fatigue life N_f of the Fe-15Mn-(10+2X)Cr-(8-X)Ni-4Si B-TRIP steels and other TRIP/TWIP steels from literature 3),4),6),7),19)-21). As shown in the figure, TRIP/TWIP steels had a longer N_f than general austenitic steel (JIS SUS316 stainless steel). Especially, B-TRIP steels showed superior plastic fatigue durability compared to other TRIP/TWIP steels. Fig. 3 (b) shows the relationship between $\Delta G^{\gamma\to\varepsilon}$ and N_f. The N_f took the high value at around $\Delta G^{\gamma\to\varepsilon}$ of 0 J/mol. When $\Delta G^{\gamma\to\varepsilon}$ is about 0, the phase stability between γ-asutenite and ε-martensite is balanced and the bidirectional transformation is more likely to occur. In other words, the fact that N_f took the maximum value when $\Delta G^{\gamma\to\varepsilon}$ is around 0 indicates the effectiveness of B-TRIP in improving the fatigue life. However, the N_f of B-TRIP steels decreased with increasing X value i.e., increasing Cr/Ni ratio, even though their $\Delta G^{\gamma\to\varepsilon}$ got close to 0 with increasing X.

Fig. 4 shows the EBD phase maps of X0–X2 after fatigue fracture. The measurement sample was the section parallel to the loading axis obtained in the parallel part. The post-mortem microstructures consisted of a small amount of retained γ-austenite, large amount of deformation-induced ε-martensite, and very limited amount of α'-martensite. Fig. 4 (e) shows the area fraction of each phase. Since there was a possibility that the small amount of α'-martensite could not be accurately measured by the wide-area EBSD with relatively large step size of 1 μm, the measurement using ferritescope (FS in Fig. 4 (e)) was also conducted on the section perpendicular to the loading axis obtained in the parallel part. As shown in the figure, the amount of ε-martensite increased with increasing Cr/Ni ratio, and that of α'-martensite also increased slightly.

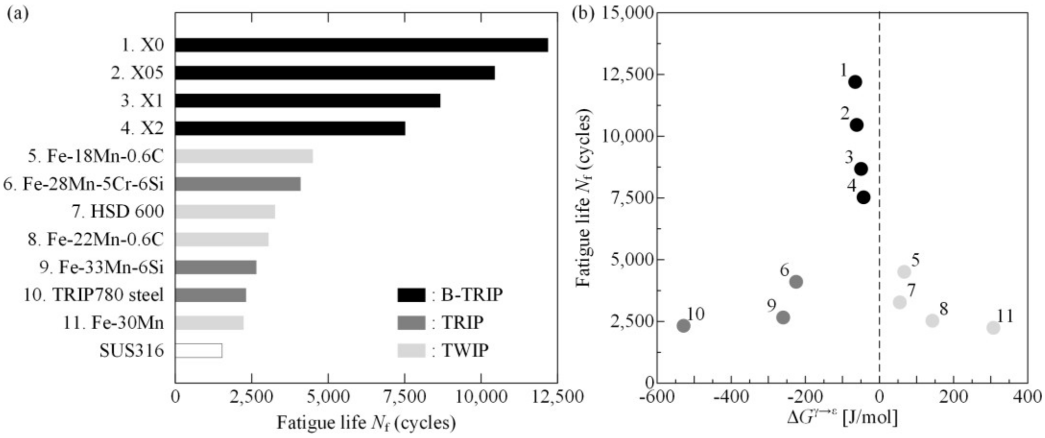

Fig. 3 (a) Fatigue life N_f of B-TRIP steels and TRIP/TWIP steels[3),4),6),7),19)-21)], and (b) Relationship between $\Delta G^{\gamma\to\varepsilon}$ and N_f.

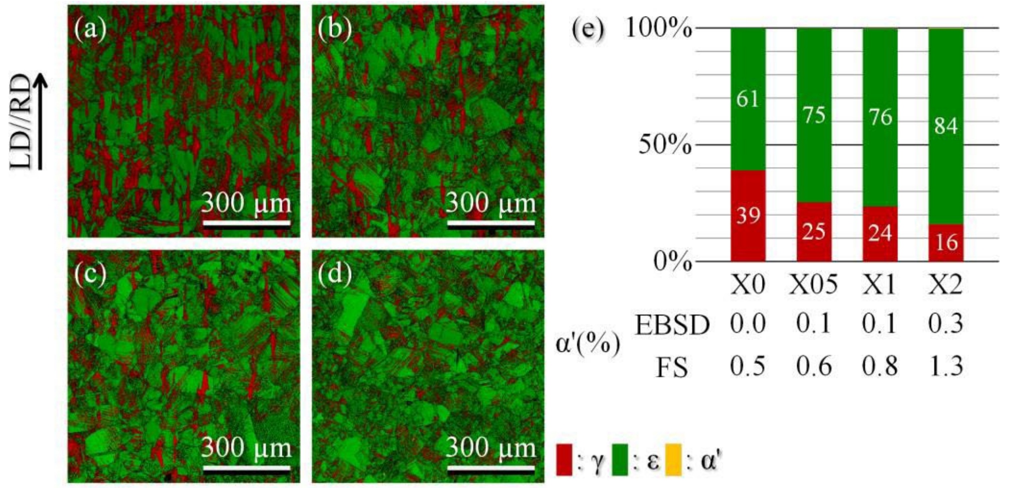

Fig. 4 EBSD phase maps for (a) X0, (b) X05, (c) X1, and (d) X2, and (e) phase fraction after fatigue fracture.

Fig. 5 (a) shows the α'-martensite formed at the grain boundary. As this example, the region with stress/strain concentration seemed to be the formation site of α'-martensite. Crack tip would be the significant stress/strain concentration part in the fatigue fracture. So, the measurement of α'-martensite using ferritescope was conducted on the fracture surface. The measurement region was at around the fracture origin site. As shown in Fig. 5 (b), larger amount of α'-martensite was formed on the fracture surface compared to the bulk (Fig. 4 (e)). Namely, although the difference in the amount of α' martensite formed during bulk plastic deformation is small, this small difference in ease of the transformation is accentuated in the local field at the crack tip. Therefore, the formation of local α'-martensite in the vicinity of the crack may be responsible for the decrease in fatigue life despite the fact that the value of $\Delta G^{\gamma\to\varepsilon}$ approaches the ideal value (0 J/mol) as the Cr/Ni ratio increases. As an effect of phase transformation on the fatigue crack, transformation induced crack closure and/or the stress relaxation due to TRIP effect have been well recognized as mechanisms for retardation in crack growth [22)]. In the present steels, however, the harmful effect of the α'-martensitic transformation might have exceeded the benefits of the transformation. The α'-martensite is irreversible phase against cyclic loadings, and the formation of it reduces the frequency of bidirectional transformation. Especially, the significant formation of α'-martensite at the crack tip might locally

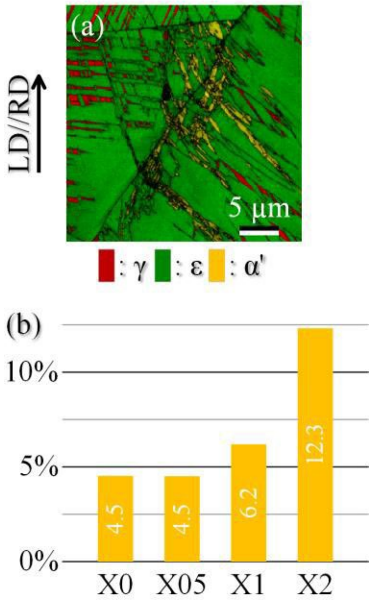

Fig. 5 (a) EBSD phase maps for X2, and (b) phase fraction for α'-martensite measured on the fracture surface.

invalidate the fatigue damage mitigation mechanism due to B-TRIP. As the crack length increases, the stress/strain intensity at the crack tip becomes sever and the α'-martensitic transformation is more likely to occur mechanically. The formed martensite results in the acceleration of crack growth, leading to more severe stress/strain intensity. During the crack initiation, the same situation might occur for the development of intrusion and the stress/strain concentration at the intrusion root.

The superior plastic fatigue durability of the Fe-Mn-Cr-Ni-Si B-TRIP steels against other steels including general TRIP/TWIP steels indicates the effectiveness of the fatigue life improvement mechanism via bidirectional transformation due to near zero $\Delta G^{\gamma\to\varepsilon}$. However, even when $\Delta G^{\gamma\to\varepsilon}$ approaches 0, the increase in Cr/Ni from X0 to X2 produced reduction in N_f due to easy occurrence of α'-martensitic transformation for larger Cr. The measurement result that the mount of α'-martensite was large on the fracture surface indicates that the stress/strain concentration (or intensity) at crack tip accelerated the transformation. The significant formation of α'-martensite at the crack tip might locally invalidate the fatigue damage mitigation mechanism due to B-TRIP. Additionally, the chain reaction in which the increase in the crack length due to accelerated crack growth by the α'-martensitic transformation leads to further α'-martensitic transformation may occur. In addition to set $\Delta G^{\gamma\to\varepsilon}$ to be 0, therefore, the α'-martensitic transformation needs to be significantly suppressed even at the crack tip to maximize the effects of B-TRIP on the fatigue crack initiation and growth. The characterization of α'-martensite formed at the crack tip and clarification of its effect on the crack behavior is necessary in the future work.

Acknowledgement

The authors acknowledge the support of a Grant-in-Aid for Early-Career Scientists (19K14853) from the Japan Society for the Promotion of Science, Japan. A part of this work was supported by the Adaptable and Seamless Technology transfer Program through Target-driven R&D (A-STEP) from Japan Science and Technology Agency (JPMJTR203B).

References

1) L. Xue: Int. J. Fatigue. **30** (2008) 1691-1698.
2) K. Hatanaka: JSME Int. J. Ser. 1 Solid. Mech. Strength. Mater. **33** (1990) 13-25.
3) W. Tasaki, T. Sawaguchi, I. Nikulin, K. Sekido and K. Tsuchiya: Mater. Trans. **57** (2016)1707-1713.
4) C. Shao, P. Zhang, R. Liu, Z. Zhang, J. Peng and Z. Zhang:Acta. Mater. **103** (2016) 781-795.
5) C. Shao, P. Zhang, R. Liu, Z. Zhang, J. Peng, Q. Duan and Z. Zhang:Acta. Mater. **118** (2016) 196-212.
6) M. W. Klein, M. Smaga and T. Beck: Metals. **8** (2018) 832.
7) T. Hilditch, H. Beladi, P. Hodgson and N. Stanford: Mater. Sci. Eng. A. **534** (2012) 288-296.
8) A. Saeed-Akbari, J. Imlau, U. Prahl and W. Bleck: Metall. Mater. Trans.A. **40** (2009) 3076-3090.
9) F. Yoshinaka, T. Sawaguchi, S. Takamori and S. Emura: Mater. Sci. Eng.A. **833** (2022) 142583.
10) S. Vakili, A. Zarei-Hanzaki, AS Anoushe, HR Abedi, MH Mohammad-Ebrahimi, M. Jaskari, S. Sohn, D. Ponge and LP. Karjalainen: Acta. Mater. **185** (2020) 474-492.
11) W. Lu, CH. Liebscher, G. Dehm, D. Raabeand Z. Li: Adv. Mater. **30** (2018) 1804727.
12) YK. Lee: Metall. Mater. Trans. A **32** (2001) 229-237.
13) F. Yoshinaka, T. Sawaguchi, T. Nakamura, G. Arakane, Y. Inoue, S. Motomura and A. Kushibe: Scr. Mater. **197** (2021) 113815.
14) F. Yoshinaka, T. Sawaguchi, I. Nikulin, S. Takamori and N. Nagashima: Procedia Struct. Integr. **19** (2019) 214-223.
15) I. Nikulin, T. Swaguchi, A. Kushibe, Y. Inoue, H. Otsuka and K. Tsuzaki: Int. J. Fatigue **88** (2016) 132-141.
16) T. Sawaguchi, I. Nikulin, K. Ogawa, S. Takamori, F. Yoshinaka, Y. Chiba, H. Otsuka, Y. Inoue and A. Kushibe: Acta. Mater. **220** (2021) 117267.
17) DT. Pierce, JA. Jiménez, J. Bentley, D. Raabe, C. Oskay and JE. Witting:Acta. Mater. **68** (2014) 238-253.
18) S. Curtze, VT. Kuokkala, A. Oikari, J. Talonen and H. Hänninen: Acta. Mater. **59** (2011) 1068-1076.
19) F. Yoshinaka and T. Sawaguchi: Int. J. Fatigue **130** (2020) 105271.
20) CW. Shao, P. Zhang, YK Zhu, ZJ Zhang, JC Peng and ZF. Zhang: Acta. Mater. **134** (2017) 128-142.
21) P. Guo, L. Qian, J. Meng, F. Zhang and L. Li: Mater. Sci. Eng. A. **584** (2013) 133-142.
22) Z. Mei and J. Morris Jr: Eng. Franc Mech. **39** (1991) 569-573.

Hydrogen embrittlement susceptibility of a 1.5GPa class dual phase steel evaluated by using U-bend specimens

Rama Srinivas Varanasi*[1], Motomichi Koyama[1,2], Yuki Shibayama[1,3], Saya Ajito[1], Tomohiko Hojo[1], Eiji Akiyama[1]

1 Institute for Materials Research, Tohoku University, 2-1-1 Katahira, Aoba-ku, Sendai, 980-8577 Japan.
2 Elements Strategy Initiative for Structural Materials (ESISM), Kyoto University, Yoshida-honmachi, Sakyo-ku, Kyoto 606-8501, Japan
3 Graduate School of Engineering, Tohoku University, 6-6-01-2 Aramaki Aza Aoba, Aoba-ku, Sendai, Miyagi, 980-8579 Japan.

*email: rama.varanasi@tohoku.ac.jp

Keywords: Hydrogen embrittlement, Dual phase steel, U-bend test, Delayed fracture, crack propagation

The advanced high strength steels which are used in automotive applications are prone to hydrogen-induced delayed fracture. Higher the tensile strength, greater the risk of hydrogen induced delayed fracture [1], necessitating the evaluation of hydrogen embrittlement behavior. To this end, the U-bend test is a robust true-false test method [2]. In the present work, we evaluate the hydrogen embrittlement susceptibility of a 1.5 GPa-class ferrite/martensite dual-phase (DP) steel using a U-bend test. U bending was first applied to the DP steel. Subsequently, the specimen was loaded by bolt-tightening. The applied load was controlled by varying the degree of bolt-tightening. The loaded specimen was electrochemically charged with hydrogen in a 3 wt.% NaCl aqueous solution with NH_4SCN. The hydrogen charging current density was increased in a step-wise manner until a fracture occurred. Herein, we discuss the effects of plastic strain, applied stress, and hydrogen concentration on hydrogen embrittlement susceptibility. Furthermore, the influence of microstructure on local damage is clarified.

The initial microstructure of the DP steel (~25% ferrite) consists of a banded microstructure. Pre-existing cracks were observed adjacent to the MnS inclusions in the cross-section along the rolling direction in the as-received sample. The fracture surfaces of the specimen after hydrogen-induced delayed fracture showed a quasi-cleavage fracture, and the crack initiation site reached the top surface of the U-bend specimen with increasing applied load. Earlier observations conducted on tempered martensitic steel revealed sub cracks in the fractured specimens with the absence of surface cracks [2]. On the contrary, in the fractured specimen of DP steel, we observe that there exists a competitive growth of surface cracks and international cracks. The formation of surface cracks is explained by the role of plastic strain and microstructure. In the DP steel, we observe that the crack propagated unhindered in the martensitic region. However, crack deflection and blunting occurred when the crack is in the vicinity of ferrite. Furthermore, our investigation revealed that the pre-existing cracks due to MnS inclusions have a negligible influence on the crack propagation.

Acknowledgement

This article is based on results obtained from a project commissioned by the New Energy and Industrial Technology Development Organization (NEDO).

References

[1] Y. Shibayama, T. Hojo, M. Koyama, H. Saitoh, A. Shiro, R. Yasuda, T. Shobu, T. Matsuno, E. Akiyama, Effects of Stress and Plastic Strain on Hydrogen Embrittlement Fracture of a U-bent Martensitic Steel Sheet, ISIJ International. 61 (2021) 1322–1329. https://doi.org/10.2355/isijinternational.ISIJINT-2020-569.
[2] Y. Shibayama, T. Hojo, E. Akiyama, An Evaluation Method for Hydrogen Embrittlement of High Strength Steel Sheets Using U-bend Specimens, ISIJ Int. 61 (2021) 1104–1111. https://doi.org/10.2355/isijinternational.ISIJINT-2020-260.

First-Principles Investigation on the Beneficial Effect of Interstitial Carbon on Steel Corrosion

Mariko Kadowaki[1], Arkapol Saengdeejing[2], Izumi Muto[3], Ying Chen[2], Yu Sugawara[3], and Nobuyoshi Hara[3]

[1] Research Center for Structural Materials, National Institute for Materials Science, Tsukuba, Ibaraki 305-0047, Japan
[2] Fracture and Reliability Research Institute, Tohoku University, Sendai, Miyagi 980-8579, Japan
[3] Department of Materials Science, Tohoku University, Sendai, Miyagi 980-8579, Japan
*email: KADOWAKI.Mariko@nims.go.jp

Keywords: carbon steel, corrosion resistance, martensite, polarization measurements, first-principles calculations

1. Aim and Scope

Martensitic carbon steels are used as structural materials in applications such as automobiles and other vehicles because of their excellent mechanical properties. Interstitial carbon atoms are located in the octahedral sites in the body-centered tetragonal (bct) crystal structure, and bring high strength to martensite. In addition to the role in providing strength, interstitial carbon has been known to improve the corrosion resistance of steel materials[1)]. In particular, the resistance against dissolution reaction of steels ($Fe \rightarrow Fe^{2+}+2e^-$) has been reported to be improved by interstitial carbon [2-4)]. However, the detailed mechanisms for the superior dissolution resistance provided by the interstitial carbon have not yet been clarified.

In this research, we focused on the work function of martensitic carbon steels. Work function, W, is defined as the energy difference between the vacuum level and the Fermi level of materials, and can be represented in the following formula:

$$W = E_{\mathrm{Vacuum}} - E_{\mathrm{Fermi}} \quad (1)$$

where E_{Vacuum} is the vacuum level and E_{Fermi} is the Fermi level of materials. In other words, work function is the energy needed to remove an electron from a solid substance to the surrounding vacuum. Since the work function and ionization energy of metals are the same [5)], the electrochemical properties of metals, such as the resistance against dissolution reaction ($M \rightarrow M^{z+}+ze^-$), are considered to be principally associated with their work function. It has been widely reported that the metals with high work function indicate superior resistance against dissolution reaction [6, 7)]. Therefore, it is expected that the presence of interstitial carbon may affect the work function of martensitic carbon steels. However, there has been no report in the literature focusing on this point of view. In this study, by conducting both experiments and first-principles calculations, the relationship between the amount of interstitial carbon, the corrosion resistance, and the work function of martensitic carbon steels was analyzed.

2. Experimental and Computational Methods

The specimens were the steels with three carbon contents: 0.001 mass%, 0.44 mass%, and 0.88 mass% C. The specimens were heat-treated at 1223 K, and then, quenched in water to form martensitic structure. The immersion test and potentiodynamic anodic polarization measurements of the specimens were conducted in 50 mM $C_8H_5KO_4$ at pH 4.0. In reality, the actual application of carbon steels almost always involves outdoor corrosion environments which can be characterized as predominantly near-neutral pH environments. Because of this reason, the solution at pH 4.0 was used. Prior to potentiodynamic anodic polarization, the specimens were polarized at -1.2 V for 600 s to remove any air-formed film.

In addition to the electrochemical measurement, first-principles calculations based on density functional theory (DFT) were carried out. For the calculation, the Vienna Ab initio Simulation Package (VASP) was used with the projector augmented wave (PAW) method [8)] and GGA-PBE potential [9)]. For the calculations, slab-model supercells with bct crystal structure were used. The supercells were constructed with a slab (metal) region and a vacuum region. The slab region was composed of 12 layers of iron atoms, and the crystallographic orientation of each layer was arranged to be (110) or (100). It is widely known that the interstitial carbon is located in the octahedral site, not the tetrahedral site in the martensite [10)]. Because of this reason, for the first-principles calculations, the carbon atoms were arranged to be in the octahedral sites in the slab region.

3. Results

The corrosion behavior of 0.001, 0.44, and 0.88 mass% C martensitic specimens were investigated in 50 mM $C_8H_5KO_4$ solution at pH 4.0. The specimens were immersed into the solution for 5 h, and the corrosion morphology was compared. It was clarified that the surfaces of all specimens were actively dissolved. The corrosion damage decreased with increasing in the interstitial carbon content. In addition to the immersion tests, potentiodynamic anodic polarization measurements of the specimens were also conducted. From the polarization measurements, it was clarified that the anodic current density decreased with increasing in the interstitial carbon content. According to above results, it was confirmed that the anodic dissolution reaction of martensite ($Fe \rightarrow Fe^{2+} + 2e^-$) was suppressed with increasing in interstitial carbon.

To clarify the reason for the superior anodic dissolution resistance obtained by interstitial carbon, first-principles calculations were conducted. Slab-model supercells consisting of a bct Fe (martensite)/vacuum interface were used, and the effect of interstitial carbon on the work function of martensite at (110) and (100) planes was analyzed. The results of the calculations indicated that for both (110) and (100) planes, the work function linearly increased with increasing interstitial carbon content. The work function is defined as the energy needed to remove an electron (e^-) from metal surface. In other words, it is expected that the specimens with high work function indicate superior resistance against dissolution reaction ($Fe \rightarrow Fe^{2+} + 2e^-$). The martensitic specimen with higher interstitial carbon content showed higher work function, and it appeared to be one of the predominant reasons for the superior dissolution resistance.

4. Conclusions

1) The dissolution resistance of martensitic carbon steel was improved by the presence of interstitial carbon.
2) The increase in the work function provided by interstitial carbon is one of the predominant reasons for superior dissolution resistance.

Acknowledgement

This work was performed under the support of a Grant-in-Aid for JSPS Research Fellow (grant No. JP18J20518). The authors acknowledge the Center for Computational Materials Science of the Institute for Materials Research, Tohoku University for the support of the supercomputing facilities.

References

1) F. J. Martin, E. J. Lemieux, and T. M. Newbauer: *Electrochem. Solid-State Lett.*, **10** (2007) C76.
2) M. Kadowaki, I. Muto, Y. Sugawara, T. Doi, K. Kawano, and N. Hara: *J. Electrochem. Soc*. **164** (2017).
3) M. Kadowaki, A. Saengdeejing, I. Muto, Y. Chen, H. Masuda, H. Katayama, T. Doi, K. Kawano, H. Miura, Y. Sugawara, and N. Hara: *Corros. Sci.*, **163** (2020) 108251.
4) M. Kadowaki, A. Saengdeejing, I. Muto, Y. Chen, T. Doi, K. Kawano, Y. Sugawara, and N. Hara: *J. Electrochem. Soc*., **168** (2021) 111503.
5) A. Kahn: *Mater. Horiz.*, **3** (2016) 7.
6) S. Yin, D. Y. Li, and R. Bouchard: *Metall. Mater. Trans. A*, **38A** (2007) 1032.
7) S. Yin, D. Y. Li, and R. Bouchard, *Wear*, **263** (2007) 801.
8) G. Kresse and J. Furthmüller: *Phys. Rev. B*, **54** (1996) 11169.
9) G. Kresse and D. Joubert: *Phys. Rev. B*, **59** (1999) 1758.
10) M. Souissi, Y. Chen, M. H. F. Sluiter, and H. Numakur:, *Comput. Mater. Sci.*, **124** (2016) 249.

Crack propagation behavior in rotational bending fatigue test of soft-nitrided JIS SCM420 steel

Naoya Ihara[1,*], Takashi Iwamoto[1] and Kimihiro Nishimura[2]

[1] JFE Steel Corp., 1-chome, Kawasakidori, Mizushima, Kurashiki, Okayama 712-8511, Japan
[2] JFE Techno-Research Corp., 1 Kokancho, Fukuyama, Hiroshima 721-0931, Japan
*email: n-ihara@jfe-steel.co.jp

Keywords: steel, nitriding, fatigue, crack propagation

1 Introduction

Soft nitriding is a heat treatment process for hardening the surface of structural steels and is applied to increase fatigue strength. It has been reported that the rotational bending fatigue strength of carburized steels is controlled by crack stagnation behavior 1). The mechanism of stagnation has been considered to be the increase in residual stress by stress-induced or strain-induced transformation of retained γ to martensite during the fatigue process. Although some reports have examined the fatigue strength and structure of the compound layer formed on the surface of soft-nitrided steels 2,3), their crack propagation behavior has not been clarified. In this study, the crack propagation behavior of soft-nitrided steel was investigated in a rotating bending fatigue test, focusing on crack stagnation behavior.

2 Experimental procedure

Normalized JIS SCM 420 steel after soft nitriding treatment was used in this study. A rotating bending fatigue test was conducted with a specimen with a 1R notch. The fatigue limit was defined by the maximum stress at which the test could be continued for more than 10^7 cycles. The crack propagation behavior between 10^5 and 10^7 cycles were studied. Microstructure observation by optical microscopy and EBSP analysis were also carried out.

3 Results and Discussion

The change in the crack length during the fatigue test at the fatigue limit of 400 MPa is shown in Fig. 1. The crack has clearly stagnated at a length of about 200 μm at the fatigue limit, which indicates that crack stagnation is controlling for fatigue strength. The calculated stress intensity factor in this process increases with the depth from the notch, implying that crack stagnation cannot be explained only by the change in the stress intensity factor. An EBSP analysis confirmed that retained γ did not exist in the soft-nitrided normalized SCM 420. Fig. 2 shows an optical micrograph around the crack and the corresponding KAM (Kernel Averaged Misorientation) map. Since a large amount of plastic strain was detected around the crack, it is inferred that crack stagnation in soft-nitrided steel can be explained by a plastic-induced closure mechanism.

4 Conclusion

The crack propagation behavior of soft-nitrided JIS SCM 420 was investigated in a rotating bending fatigue test. Crack stagnation occurred and was considered to be controlling for fatigue strength. It is suggested that the fatigue limit is explained by the crack stagnation behavior due to plastic-induced closure.

References

1) T. Ochi, S. Kozawa, M. Kubota: Tetsu to Hagané. **97** (2011) 9 (486-492).
2) S. Takagi, Y. Tonozuka, N. Nakamura, T. Itou: Tetsu to Hagané. **104** (2018) 10 (594-601)
3) Y. Hiraoka, A. Ishida, O. Umezawa: Netsusyori, **57**(2017) 2 (64-72)

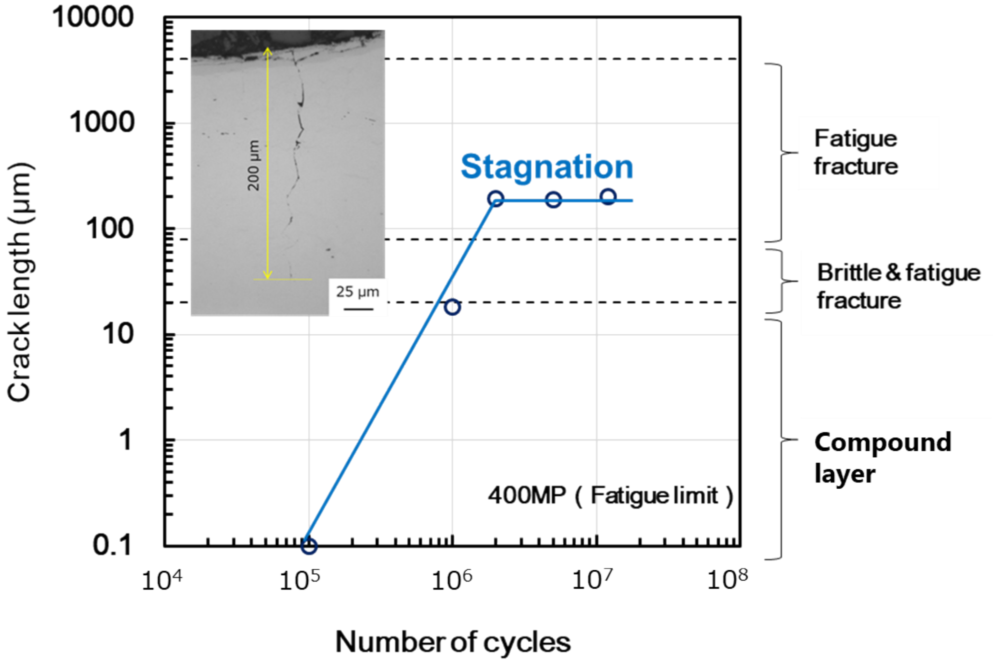

Fig. 1 Change in crack length with number of cycles at fatigue limit in rotating bending fatigue test of soft-nitrided JIS SCM420. An example of a stagnated crack (1.2×10^7 cycles) is also shown in the figure.

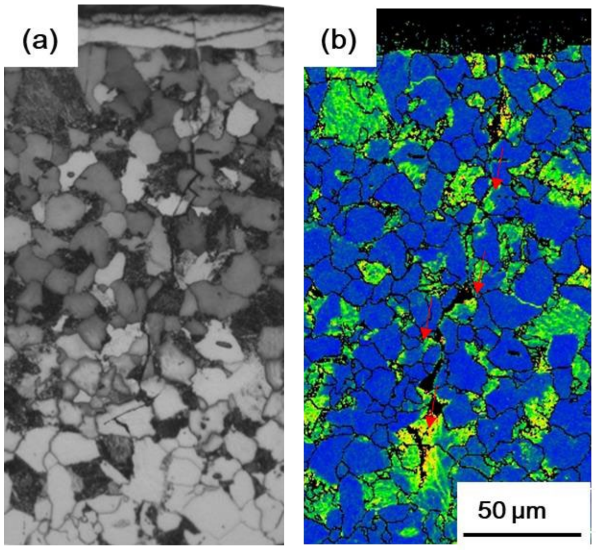

Fig. 2 (a) Optical micrograph and (b) KAM map determined from EBSP analysis of soft-nitrided JIS SCM420 after rotating bending fatigue test.